UNIVERSITY OF OKLAHOMA

GRADUATE COLLEGE

CYCLIC MISCIBLE INJECTION IN UNCONVENTIONAL RESERVOIRS: UPSCALING, SOAKING, CONTAINMENT, AND ASPHALTENE DEPOSITION

A DISSERTATION

SUBMITTED TO THE GRADUATE FACULTY

in partial fulfillment of the requirements for the

Degree of

DOCTOR OF PHILOSOPHY

By

RAKI SAHAI
Norman, Oklahoma
2024

Downloaded from SHAREOK. Persistent Handle URL: https://hdl.handle.net/11244/340299

CYCLIC MISCIBLE INJECTION IN UNCONVENTIONAL RESERVOIRS: UPSCALING, SOAKING, CONTAINMENT, AND ASPHALTENE DEPOSITION

A DISSERTATION APPROVED FOR THE
MEWBOURNE SCHOOL OF PETROLEUM AND GEOLOGICAL ENGINEERING

BY THE COMMITTEE CONSISTING OF

Dr. Rouzbeh G. Moghanloo, Chair

Dr. Matthew Pranter

Dr. Deepak Devegowda

Dr. Benjamin (Bor-Jier) Shiau

Dr. Curtis Whitson

© Copyright by Raki Sahai 2024
All Rights Reserved.

I dedicate this dissertation to my wife, Priya, for her love, support, patience, and understanding throughout this over-six-year journey.

My kids, Nivaan and Nea, for their unconditional love.

And my parents for their unconditional love, support, and encouragement.

Acknowledgments

First and foremost, I would like to express my sincere gratitude to my advisor, Dr. Rouzbeh G. Moghanloo, for his ongoing guidance, support, and tutelage during my Ph.D. research. I am very grateful for his supervision, insightful comments throughout the research, and unwavering support and belief in me. This journey would not have been possible without you.

Besides my advisor, I would like to thank Dr. Devegowda, Dr. Shiau, Dr. Pranter, and Dr. Whitson for serving on the dissertation committee and providing valuable input during the General Exam. Dr. Whitson, thank you for sharing your experience and being available for numerous discussions on shale reservoir development, research, and life.

Mathias Carlsen and K. Patel for the discussions on this research topic and for providing the data that helped complete the research. Additionally, I would like to acknowledge discussions with Damon Bennett and Erich Kerr on this topic and shale development in general. Special thanks to the Mewbourne School of Petroleum & Geological Engineering staff, especially Katie Shapiro, for being always there to help.

Finally, I would like to thank my family and friends for their motivation and support.

Table of Contents

List of Tables.....ix

List of Figures.....xii

Abstract.....xxi

Chapter 1 Introduction.....1

1.1 Development of Shale Reservoirs.....3

1.2 Review and Current Status of EOR in Shale Reservoirs.....5

1.3 Research Objectives and Scope.....6

1.4 Dissertation Organization.....7

Chapter 2 Enhanced Oil Recovery in Unconventional Shale Reservoirs.....9

2.1 Literature Review.....10

2.1.1 Laboratory Studies.....10

2.1.2 Simulation Studies.....22

2.1.3 Caveats.....32

2.2 Field Trials/Pilots.....33

2.2.1 Bakken.....34

2.2.2 Eagle Ford.....40

2.3 Learnings & Issues Realized From the Field Trials.....46

Chapter 3 Upscaling Laboratory Results to Field Scale.....50

3.1 Fluid Flow in Porous Media.....50

3.2 Diffusion in Porous Media and Effective Diffusion Coefficients.....54

3.3 Mathematical Model Formulation.....57

3.3.1 Basic Formulation 60
3.3.2 Injection Phase 69
3.3.3 Soaking Phase 71
3.3.4 Production Phase 73
3.3.5 Base Model Validation 75
3.4 Scaling parameters to upscale lab results to field results 76
3.5 Sensitivity Analysis 79
3.5.1 Effect of Diffusion Coefficient D_e 79
3.5.2 Effect of Alpha 80
3.5.3 Effect of B_i 81
3.5.4 Effect of length 'L' 82
3.5.5 Effect of time on small block size (L = 0.01 m) as a function of two different D_e values 84
3.6 Upscaling Equation 86
3.7 Discussion 88
3.8 Key Takeaways 89
Chapter 4 Does the Soaking Phase Matter? 91
4.1 Effect of Soaking Times 91
4.2 Fracture Distribution 93
4.3 Sensitivity Analysis 93
4.3.1 Effect of Soaking Time on Different Size Matrix Blocks 94
4.3.2 Effect of Diffusion Coefficient D_e on Different Size Matrix Blocks 95
4.4 Discussion 97

4.5 Key Takeaways 98

Chapter 5 The Issues of Containment and Asphaltene Deposition 100

5.1 Containment of Injected Gas 100

5.2 Asphaltene Deposition with Miscible Gas Injection 102

5.3 Case Studies from Two Huff-and-Puff Pilots in the Eagle Ford 105

5.3.1 Pilot in the Eagle Ford Gas Condensate Window 106

5.3.2 Pilot in the Eagle Ford Volatile Oil Window 110

5.4 Numerical Modeling of the Ritchie Farms Huff-and-Puff EOR Pilot 111

5.4.1 History Matching 116

5.4.2 Forecast with Miscible Cyclic Huff-and-Puff EOR 123

5.5 Sensitivities 141

5.5.1 Carbon Dioxide (CO_2) 141

5.5.2 Dimethyl Ether (DME) 142

5.5.3 Sensitivities with CO_2 and DME 145

5.6 Discussion 163

5.6.1 Schematic of cyclic process with DME 166

5.7 Key Takeaways 168

Chapter 6 Conclusions and Recommendations 170

6.1 Conclusions 170

6.2 Recommendations for Future Work 175

Nomenclature 177

References 179

List of Tables

Table 2.1: Summary of the Eagle Ford Fluid Properties (modified from Ganjdanesh et al., 2019b) 23

Table 2.2: Peng-Robinson EOS Parameters and Fluid Composition for the Black Oil Model (Ganjdanesh et al., 2019b) 23

Table 2.3: Peng-Robinson EOS Parameters and Fluid Composition for the Volatile Oil Model (Ganjdanesh et al., 2019b) 24

Table 2.4: Peng-Robinson EOS Parameters and Fluid Composition for the Gas Condensate Model (Ganjdanesh et al., 2019b) 24

Table 2.5: Produced Field Gas Composition (Ganjdanesh et al., 2019b) 25

Table 2.6: Summary of Bakken and Eagle Ford Reservoir Properties (Pospisil et al., 2020) 34

Table 2.7: Summary of Pilot Tests in the Bakken Play 38

Table 2.8: Huff-and-Puff Data from seven Eagle Ford Pilots in the East Volatile Oil area (Modified from Thoms, 2020) 44

Table 2.9: Eagle Ford Huff-and-Puff Fluid Type and GOR Targets based on Current Projects (modified from Kostarelos, 2019).....45

Table 3.1: Black Oil Composition from Eagle Ford (Orangi et al., 2011) and Effective Diffusion Coefficients Calculated by Incorporating Tortuosity Effects (Cronin et al., 2019).....57

Table 3.2: Comparison of Model Outputs Against the Results of Akita and Moghanloo (2018) 76

Table 5.1: 12-Component Composition for the Two Nearby Eagle Ford Wells, 5H and 92H (modified from Kerr et al., 2020).....113
Table 5.2: EOS Parameters of the 12-Component Fluid Model (modified from Kerr et al., 2020) 113
Table 5.3: Binary Interaction Coefficients for the Different Components 113
Table 5.4: Hydraulic fracture properties used for the three wells (154H, 156H, and 158H), with three different fracture geometries per well (Kerr et al., 2020) 117
Table 5.5: Composition of the Field Gas 123
Table 5.6: Scenarios to Evaluate the Effect of Different Cycle Times.....125
Table 5.7: Results for the Different Scenarios for One Stage Modeled for the Three Wells 130
Table 5.8: Scenarios to Evaluate the Effect of Injection Rate 133
Table 5.9: Scenarios to Evaluate the Effect of Injection Rates.....134
Table 5.10: Scenarios to Evaluate the Effect of Soaking Time 135
Table 5.11: Results for the Different Scenarios to Evaluate the Effect of Soaking Time – same number of cycles.....138
Table 5.12: Results for the Different Scenarios to Evaluate the Effect of Soaking Time – same 26 months of total huff-and-puff duration; different number of cycles..139
Table 5.13: Scenarios to Evaluate the Effect of Soaking Time 146
Table 5.14: Binary Interaction Coefficients between DME and other components (Cho et al. (2018)).....146
Table 5.15: Scenarios to Evaluate the Effect of Injectant Type.....153
Table 5.16: Scenarios to Evaluate the Effect of Water Solubility 155

Table 5.17: Results for the Different Scenarios 156
Table 5.18: Binary Interaction Coefficients between DME and other components (Tsanas (2018)) 158
Table 5.19: Scenarios to Evaluate the Effect of BICs 159
Table 5.20: Results for the Different Scenarios 159
Table 5.21: Scenarios to Evaluate the Effect of Soaking Time 161
Table 5.22: Results for the Different Scenarios to Evaluate the Effect of Soaking Time – same number of cycles 162
Table 5.23: Results for the Different Scenarios to Evaluate the Effect of Soaking Time – same 26 months of total huff-and-puff duration; different number of cycles .. 163

List of Figures

Figure 1.1: A 30-70% increase in oil recovery is expected from huff-and-puff EOR injection in the black oil window of the Eagle Ford formation (modified from Thomas et al., 2016). 1

Figure 1.2: Production response from one of the single-well pilots in the Eagle Ford (modified from Hoffman, 2018). 3

Figure 1.3: Delineation of conventional and unconventional resources based on fluid mobility (modified from Cander, H. (2012)). 4

Figure 2.1: The three rock sample geometries used for the experiments (1) 11.2 mm diameter round rod, (2) 11.2 mm diameter by 1-3 mm thick "coins," and (3) 1-3.4 mm crushed particles (Hawthorne et al., 2019). 12

Figure 2.2: Effect of surface area on the total oil hydrocarbon recovery rates for high-permeability Middle Bakken (left) and Lower Bakken Shale (right) rock samples. Experiments were conducted with three different geometries: (1) 11.2 mm diameter by 40 mm long round rods, (2) 11.2 mm diameter by 1-3 mm thick "coins," and (3) 1-3.4 mm crushed particles (Hawthorne et al., 2019). 12

Figure 2.3: Recovery factor as a function of four different sample sizes, with recovery increasing with decreasing sample size (modified from Dang, 2019). 13

Figure 2.4: Three different matrix samples, each with the same minimum length dimension of dx, are expected to have similar recoveries.....14

Figure 2.5: Distribution of acoustic events with distance perpendicular to the fracture plane. Data from all tests exhibit a good fit to a Lorenz/Cauchy distribution curve shown in red (Damani et al., 2018). 15

Figure 2.6: A comparison of lab fracture density from SEM analysis (Bhagat, 2012) with geological field observations (Vermilye & Scholz, 1998; Zhang & Stephansson, 2010) suggests that lab observations can be used to constrain field-scale SRV. 17

Figure 2.7:Microseismic results from Barnett shale showing evidence of a complex fracture network created (Warpinski et al., 2008). 18

Figure 2.8: Hydraulic fracture distribution from four cored Eagle Ford wells (modified from Raterman et al., 2018).....18

Figure 2.9: MMP values for typical Bakken crude oil with different gases (Hawthorne et al., 2017).....19

Figure 2.10: Impact of soaking time on huff-and-puff recovery for the Eagle Ford samples (Dang, 2019).....21

Figure 2.11: Pressure-Temperature (PT) diagrams for the black oil, volatile oil, and gas condensate reservoir fluids for the Eagle Ford (Ganjdanesh et al., 2019b).....24

Figure 2.12: Phase behavior/PT diagram of Black Oil Fluid at Initial Condition, Before Injection, and After Injection near the Hydraulic Fracture Face (left); Comparison of Cumulative Oil Production with and without Gas Injection for Black Oil Reservoir (right) (modified from Ganjdanesh et al., 2019). 26

Figure 2.13: Phase behavior/PT diagram of Volatile Oil Fluid at Initial Condition, Before Injection, and After Injection near the Hydraulic Fracture Face (left); Comparison of Cumulative Oil Production with and without Gas Injection for Volatile Oil Reservoir (right) (modified from Ganjdanesh et al., 2019).....28

Figure 2.14: Phase behavior/PT diagram of Gas Condensate Fluid at Initial Condition, Before Injection, and After Injection near the Hydraulic Fracture Face (left); Comparison of Cumulative Oil Production with and without Gas Injection for Gas Condensate Reservoir (right) (modified from Ganjdanesh et al., 2019). ..29

Figure 2.15: Pressure-Temperature (PT) diagrams for the gas condensate reservoir fluid at the initial condition, before injection, and after injection of the produced field gas or rich gas (Ganjdanesh et al., 2019).....31

Figure 2.16: Sensitivity Analysis with an Eagle Ford Volatile Oil EOR project (Atan et al. (2018)). 32

Figure 2.17: Location of Pre-2018 Bakken EOR Tests (Hamling et al., 2021).....36

Figure 2.18: First three commercial EOG huff-and-puff EOR units with varying well spacing (Grinestaff et al., 2020).....41

Figure 2.19: Eagle Ford EOR Pilots as of 2020 (Leahey et al., 2020).....42

Figure 2.20: Estimated Incremental Oil Recoveries (Leahey et al., 2020). 43

Figure 2.21: EUR increase with huff-and-puff EOR Versus annual injected volumes per well. 44

Figure 2.22: Illustration of an Eagle Ford EOR Project that experienced significant interwell communication, with four parent and five child wells (Torres et al., 2019). ...48

Figure 3.1: Transport mechanisms as a function of Peclet number 51

Figure 3.2: Schematic of a hydraulically fractured horizontal well in a shale reservoir; the inset shows the region of investigation from the hydraulic fracture face to the no-flow boundary. 59

Figure 3.3: Element of volume as a cuboid (Crank, 1975). 61

Figure 3.4: Concentration (C) vs. distance curves for an instantaneous plane source. Numbers on curves are values of Dt (Crank, 1975). 66

Figure 3.5: Schematic of a hydraulically fractured horizontal well in a shale reservoir during the HUFF or INJECTION stage; the inset shows the region of investigation with the injected gas exiting the hydraulic fracture and mixing with the remaining oil in the matrix. The movement of the injected gas is from the hydraulic fracture face to the no-flow boundary. 69

Figure 3.6: Concentration profiles vs. Distance 'x' and Position Ratio 'X' from the hydraulic fracture face (i.e., x=0) for the Injection phase. 70

Figure 3.7: Concentration profiles vs. Distance 'x' and Position Ratio 'X' for the Soaking phase. 73

Figure 3.8: Schematic of a hydraulically fractured horizontal well in a shale reservoir during the PUFF or PRODUCTION stage; the inset shows the region of investigation with the remaining oil, which has become miscible with the injected gas exiting the matrix. The movement of the solvent mixed with oil is from the matrix to the hydraulic fracture. 73

Figure 3.9: Concentration profiles vs. Distance 'x' and Position Ratio 'X' for the Production phase. 74

Figure 3.10: Schematic of matrix and fracture network at laboratory and field scales, and the corresponding values of α and B_i. 78

Figure 3.11: Impact of varying D_e from 1×10^{-7} to 1×10^{-9} m^2/s on L_p, M_t, and the Recovery Factor Ratio. 80

Figure 3.12: The impact of varying α from 0.1 to 10 on recoveries at core and reservoir scales and the Recovery Factor Ratio. 81

Figure 3.13: Impact of varying B_i from 1 to 100 on L_p, M_t, and the Recovery Factor Ratio. 82

Figure 3.14: Comparison of penetration length after the Soaking phase for blocks of 0.01, 0.1, 1, and 10 m. 83

Figure 3.15: Comparison of Recovery Factor Ratio for matrix blocks of lengths 0.01, 0.1, 1, and 10 m, as a function of D_e. 83

Figure 3.16: Comparison of the total amount of gas diffused (M_t) for matrix blocks of length 0.01, 0.1, 1, and 10 m, as a function of D_e. 84

Figure 3.17: Comparison of the concentration front for L = 0.01 m sample after 3, 15, and 30 minutes of injection-soaking-production phases. Results are shown for D_e of $1x\ 10^{-8}$ and $1x10^{-9}$ m^2/s. 86

Figure 3.18: Recovery Factor Ratio vs. B_i/α graphs for $\alpha = 0.1$ (top) and $\alpha = 1$ and 10 (bottom). 87

Figure 4.1: Impact of soaking time on huff-and-puff recovery for the Eagle Ford samples (Dang, 2019). 92

Figure 4.2: Comparison of soaking to injection penetration length ratios for the different matrix blocks (0.01, 0.1, 1, and 10 m) as a function of various soaking times. Injection and production cycle times were kept constant at 30 days each. 95

Figure 4.3: Comparison of soaking to injection penetration length ratios for the different matrix blocks (0.01, 0.1, 1, and 10 m) as a function of various effective diffusion

coefficient values. Injection, soaking, and production cycle times were kept constant at 30 days each. 96

Figure 5.1: Reservoir simulation history-matched model for EP Energy's Maltsberger EOR project consists of 13 horizontal wells and multiple long interwell fractures (Ganjdanesh et al., 2019b). 107

Figure 5.2: Observed and simulated results for three initial huff-and-puff cycles for EP Energy's Maltsberger W09 well – a) Gas Injection Rates and Cumulative Injected Gas Volume, b) Oil Production Rate, and c) Bottomhole Pressures(Ganjdanesh et al., 2019b). 109

Figure 5.3: Reservoir simulation grid for the Ritchie Farm pilot, showing a single stage for the three wells (154H, 156H, and 158H), each with nine clusters with asymmetric fracture geometries. 115

Figure 5.4: Oil-Water and Gas-Liquid Relative Permeability curves used for the matrix.118

Figure 5.5: History match results for 154H – oil rate and cumulative oil production comparison (top left), gas rate and cumulative gas comparison (top right), water rate and cumulative water production comparison (bottom left), and bottom hole pressure comparison (bottom right). 119

Figure 5.6: History match results for 156H – oil rate and cumulative oil production comparison (top left), gas rate and cumulative gas comparison (top right), water rate and cumulative water production comparison (bottom left), and bottom hole pressure comparison (bottom right). 120

Figure 5.7: History match results for 158H – oil rate and cumulative oil production comparison (top left), gas rate and cumulative gas comparison (top right), water

rate and cumulative water production comparison (bottom left), and bottom hole pressure comparison (bottom right).....121
Figure 5.8: Pressure distribution at the end of history match, with 1 stage modeled for each of the three wells (coarse grid model). 122
Figure 5.9: Pressure distribution at the end of history match, with 1 stage modeled for each of the three wells (fine grid model). 124
Figure 5.10: Oil mole fraction at the end of scenario 2 (left), oil production rate & gas injection rate for the single stage (top right), C1 mole fraction in the oil phase (middle right), and oil viscosity for a grid block (pink square grid block) within the SRV.....127
Figure 5.11: Oil mole fraction at the end of scenario 2 (left), oil production rate & gas injection rate for the single stage (top right), C1 mole fraction in the oil phase (middle right), and oil viscosity for a grid block (pink square grid block) just outside the SRV. 128
Figure 5.12: Oil mole fraction at the end of scenario 2 (left), oil production rate & gas injection rate for the single stage (top right), C1 mole fraction in the oil phase (middle right), and oil viscosity for a grid block (pink square grid block) in the matrix. 129
Figure 5.13: Cumulative oil production for the different scenarios. 130
Figure 5.14: Cumulative oil production for the different scenarios. 134
Figure 5.15: Oil viscosity changes for the different scenarios. 136
Figure 5.16: Oil Rate for Ritchie Farms (1 stage) for the different scenarios. 137
Figure 5.17: Cumulative oil production for the different scenarios. 138

Figure 5.18: Oil production by puff cycle for the different scenarios for Ritchie Farms 156H. 140

Figure 5.19: Pressure-Temperature diagram for DME, n-propane, and n-butane (Salimi et al., 2022). 143

Figure 5.20: Oil rate, cumulative oil production, bottom hole pressure for Ritchie Farms 158H, and cumulative water production for the different scenarios. 148

Figure 5.21: C1 mole fraction in oil (top right) and oil viscosity (bottom right) at six different grid blocks (left) for scenario 2 (Field Gas). 149

Figure 5.22: CO_2 mole fraction in oil and oil viscosity at six different grid blocks for scenario 9 (CO_2) (left), and DME mole fraction in oil and oil viscosity at six different grid blocks for scenario 10 (DME) (right).....150

Figure 5.23: C1 mole fraction in oil and gas phases and oil viscosity for the first Field Gas injection cycle from perforation (distance = 0) to matrix (distance = 135 ft). 151

Figure 5.24: CO_2 mole fraction in oil and gas phases and oil viscosity for the first CO_2 injection cycle from perforation (distance = 0) to matrix (distance = 135 ft). 151

Figure 5.25: DME mole fraction in oil and gas phases and oil viscosity for the first DME injection cycle from perforation (distance = 0) to matrix (distance = 135 ft). 152

Figure 5.26: Variation of the reference Henry's Law Constant with temperature for various gases (Li & Nghiem, 1986). 154

Figure 5.27: Cumulative water production, cumulative oil production, DME mole fraction in oil, and oil viscosity for scenarios 10, 11, and 12. 157
Figure 5.28: Oil rate, cumulative oil production, DME mole fraction in oil, and oil viscosity for scenarios 10 and 13. 160
Figure 5.29: Cumulative oil production for the different scenarios. 162
Figure 5.30: Schematic of the cyclic process with DME 167

Abstract

Despite numerous cyclic miscible injection studies and field pilot tests being carried out in unconventional shale reservoirs over the last 15 years, governing mechanisms are yet to be fully understood, as there is a discrepancy between experimental results and field observations. Generally, the pilot field tests demonstrate much lower recoveries than what was originally predicted by laboratory and simulation studies. Hence, this research aims to develop a systematic approach to upscale the lab results across spatial scales, improve injectant performance, and optimize the process to achieve better recoveries. Disparate topics impacting the performance of cyclic miscible injection, including upscaling, soaking, containment, and asphaltene deposition, are addressed.

A new mathematical model is developed using classical equations to mimic the cyclic huff-and-puff miscible process. Traditionally, constant pressure or constant flow rate boundary conditions are used to describe flow between the fracture network and matrix during the injection and soaking phases, which is not realistic. The complex fracture network in this study is characterized as an ensemble of rock pillars separated by fracture discontinuities to represent field conditions better. Two scaling factors are developed to upscale the laboratory results to the field scale, and an upscaling equation is derived to better predict the recovery factors across spatial scales.

Next, the significance of the soaking phase in the cyclic process is evaluated as a function of the micro-fracture distribution within the complex fracture network and the mixing of the various injectants with the remaining oil. By better understanding various

injectants penetration depths and mixing/swelling recovery mechanisms, recommendations are made to tailor the huff-and-puff process to improve oil recovery.

Finally, Dimethyl Ether (DME), a novel liquid solvent, shows potential transformative benefits compared to typical gas injectants. Compositional modeling and simulation of a volatile oil pilot in the Eagle Ford show promising results with DME due to a more efficient recovery mechanism and improved accessibility to the remaining oil, resulting in a much better recovery improvement than gas injectants. The advantages of DME application are complemented by significantly lower implementation costs compared to CO_2 and typical hydrocarbon solvents.

A better understanding of the cyclic miscible injection processes and further optimization can extend the life of unconventional shale wells by unlocking a significant amount of hydrocarbon resources currently left behind undrained.

Chapter 1

Introduction

Despite the recent volatility in commodity prices, oil production from unconventional shale reservoirs has steadily increased annually since 2010, except for 2020 (EIA, 2023). As the shale development matures, the industry has been actively seeking new ways to unlock incremental value beyond primary depletion. In particular, the miscible gas injection EOR via the huff-and-puff technique has garnered interest in recent years. Although EOG Resources was the first operator to claim commercial success in the Eagle Ford using the miscible gas huff-and-puff technique in 2016 (**Figure 1.1**), several experimental and pilot tests have been reported in the literature since 2008, summarized by Alfarge et al., 2017.

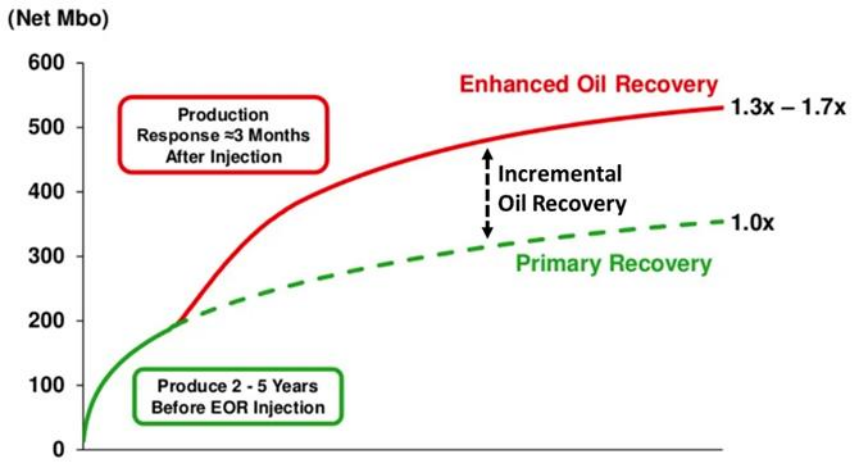


Figure 1.1: A 30-70% increase in oil recovery is expected from huff-and-puff EOR injection in the black oil window of the Eagle Ford formation (modified from Thomas et al., 2016).

Although multiple wells on a pad (or field) may be part of the huff-and-puff EOR implementation, the application is a single-well technique in which the miscible gas is injected, and the remaining oil is produced from the same well. The method involves injecting a miscible

gas into a well (referred to as the injection or huff phase), shutting in the well for some amount of time to allow the injected gas to mix with the remaining oil (soaking phase), and then producing back hydrocarbons from the same well (production or puff phase). These are three distinct phases for each huff-and-puff cycle, each lasting anywhere from 15 to 90 days, and then the cycle is repeated multiple times to recover the remaining oil in the shale matrix. Over the last few years, several field trials have been implemented in the Bakken, Eagle Ford, Permian, and STACK/SCOOP. Various fluids have been tested in these trials, ranging from water and CO_2 in the initial pilots in the Bakken (Hoffman & Evans, 2016) to mainly using produced gas in recent tests.

Although injectivity of the gas has not been a problem in the field trials, the recoveries reported have been lower than those predicted by laboratory experiments and simulation studies. In these field trials, the wells usually see a production uplift from the first few huff-and-puff cycles; however, the production soon falls back to pre-huff-and-puff rates (**Figure 1.2**). Additionally, the hydrocarbon recoveries from successive huff-and-puff cycles have been observed to reduce over previous cycles, as shown in **Figure 1.2** and other reports in the literature. EOG has reported the expected recoveries to be in the range of 30-70% (of primary recovery), but the results from three to five years of huff-and-puff implementation have typically only been in the range of 10-40% (Enverus Prism, 2024), only about half of the original expectations reported. Several factors, such as containment of the injected gas, limited mixing/miscibility with the remaining oil (limited accessibility), and asphaltene deposition, are being discussed in the industry to understand the limits of the huff-and-puff application.

Furthermore, a commonly asked question for candidate selection is whether wells with better primary recovery make better candidates for huff-and-puff application. A few studies have

been performed to investigate this issue (Akita & Moghanloo, 2018; Carlsen et al., 2019; Fu et al., 2019; Mydland et al., 2020); however, the mechanics of huff-and-puff application in shale reservoirs is not well understood. This study continues to build on these industry-wide efforts. It focuses on the impact of the stimulated reservoir volume (SRV), created during the hydraulic fracturing of the well for primary production, on the accessibility and efficacy of the huff-and-puff EOR treatment using miscible gases.

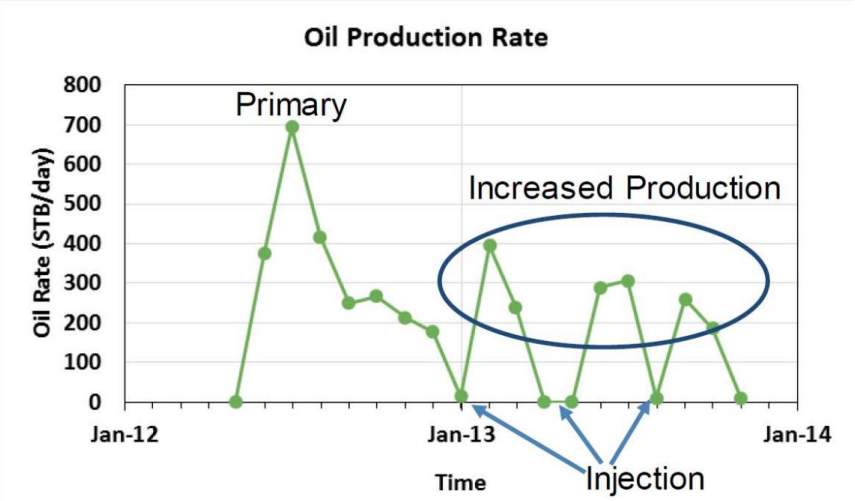


Figure 1.2: Production response from one of the single-well pilots in the Eagle Ford (modified from Hoffman, 2018).

1.1 Development of Shale Reservoirs

The shale revolution refers to the phenomenon that emerged in terms of domestic gas and oil supply in the United States. The knowledge of the presence of large amounts of hydrocarbons in shale reservoirs is not new. The shale revolution is not driven by a recent discovery of a new type of formation; instead, the recent advances in drilling and stimulation technology allowed geologists and engineers to exploit the shale formation in a cost-effective way. The natural gas was extracted from shallow shale reservoirs in Fredonia, New York, in 1825, three decades before Col. Edwin Drake drilled the first commercial conventional well in 1859. However, the first

commercial development of naturally fractured Devonian shales started in 1915. For most of the 20th century, shale formation was considered a “seal” for conventional reservoirs. It was not until the US crude oil and natural gas production started to decline in the 1970s that the interest in shale reservoirs developed in the mid-1970s (Sahai, 2022).

Cander (2012) defined unconventional reservoirs as resources in which technology must be used to increase the mobility ratio (k/μ) to achieve commercial flow rates (**Figure 1.3**). Unlike conventional petroleum deposits, unconventional petroleum systems act as self-sourced and self-sealed reservoirs, with trap and migration having no effect on hydrocarbon accumulation. However, with low porosity and sub-micro- to nano-Darcy permeability, horizontal wells and multistage hydraulic fracturing are required to exploit the shale reservoirs economically. The production mechanisms are dominated by the small pore throat sizes and gas adsorbed to the kerogen matrix in these organic-rich reservoirs. The shale formations are commonly believed to be naturally fractured, creating complex fracture networks during hydraulic fracturing and influencing reservoir drainage areas during production.

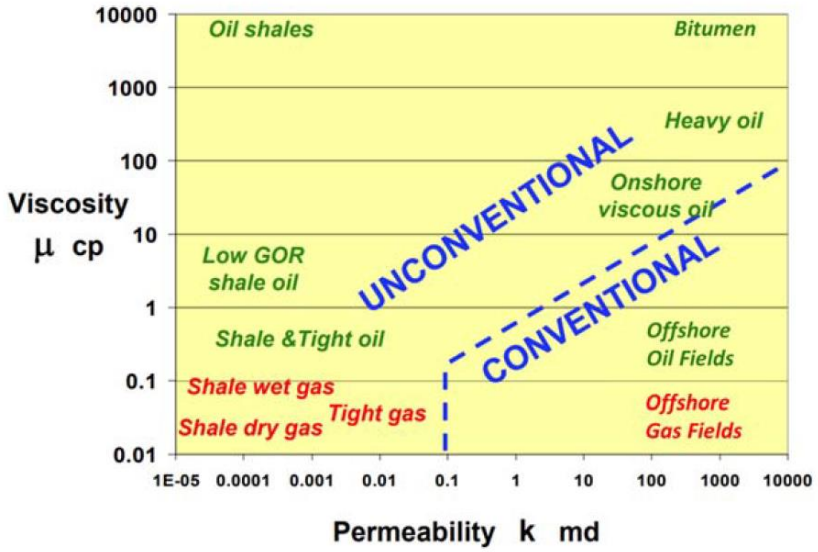


Figure 1.3: Delineation of conventional and unconventional resources based on fluid mobility (modified from Cander, H. (2012)).

The production from shale wells is characterized as having a high peak production rate due to the large surface area created with hydraulic fracturing, followed by a steep decline as high as ~70% per annum, and finally, long-term tail production with low rates due to tight shale matrix. As a result, a large number of "new wells" have to be developed annually to offset the production decline from older base wells. The recovery from these older shale oil wells is estimated at 5-10% (Hoffman, 2018), leaving over 90% of oil in place after primary depletion for enhanced oil recovery (EOR) methods.

1.2 Review and Current Status of EOR in Shale Reservoirs

Due to the tight flow characteristics, conventional miscible and immiscible flooding EOR techniques using injector and producer well pairs do not apply to unconventional shale reservoirs. As a result, over the past decade, the industry has shifted to cyclic miscible gas huff-and-puff EOR from the same well. Since 2008, numerous laboratory experiments and numerical reservoir simulation studies have shown the potential of huff-and-puff EOR application to increase recovery beyond primary depletion in the liquids-rich shale reservoirs.

With EOG Resources claiming success with the miscible gas cyclic huff-and-puff EOR in the Eagle Ford, several majors and large independents have pilots across different shale plays. Gas injectivity has not been a problem; however, the lack of containment of the injected gas, preventing pressure buildup in the reservoir and achieving miscibility conditions, has led to lower oil recoveries than those forecasted with experimental work and modeling studies. Also, the results from the pilot tests have varied responses across different shale plays, highlighting the need for better subsurface characterization and other complexities that need to be better understood.

1.3 Research Objectives and Scope

The EOR using miscible gas injection has a lengthy and successful history in conventional reservoirs. However, the physics governing the cyclic huff-and-puff EOR process in shale reservoirs is not yet well understood. Understanding the physics could help the industry optimize the EOR process, leading to significant gains in hydrocarbon recovery from liquids-rich shale reservoirs. As covered in the literature review (**Chapter 2**), several laboratory experiments, simulation studies, and field trials have been conducted over the past 15 years. Data and learnings from these works can further enhance our understanding of the fundamental physics impacting the EOR process.

Laboratory experiments and simulation studies are carried out during the feasibility and appraisal stage of project planning and overstated hydrocarbon recoveries can result in inaccurate economic assessment. Therefore, the main task of this research is to develop an upscaling methodology and help optimize the process to improve recoveries from the huff-and-puff miscible gas EOR method at the field scale.

The specific objectives include:

1) To develop a mathematical model to simulate the huff-and-puff process by leveraging the existing laboratory studies and classical analytic equations
2) To evaluate the accessibility of the injected gas during the injection, soaking, and production cycles in the presence of natural and hydraulic fractures
3) Based on the results from the model, develop a correlation or series of correlations that help to understand the recoveries at the field scale. Such a correlation(s) can help with better candidate selection and a more accurate technical evaluation during the feasibility and post-treatment lookback evaluation.

4) Evaluate the role of soaking time as a function of stimulated reservoir volume
5) To investigate the feasibility of other injectants, such as liquid solvents, that could eliminate one of more issues realized with the gas-based cyclic miscible huff-and-puff process.
6) Finally, develop recommendations that can help optimize the huff-and-puff process by focusing on the variables that enhance oil recovery.

The scope of the mathematical model is limited to classical analytical solutions to evaluate the penetration of the injected gas-oil mixture as a pseudo-single phase through diffusion after the mixing has occurred. On the other hand, the feasibility of other injectants includes using three-phase numerical reservoir simulation to investigate multiple cycles of the huff-and-puff process.

1.4 Dissertation Organization

This dissertation is presented in six chapters.

- Chapter 1 provides an introduction to the research study. The development of the shale reservoirs and the current status of huff-and-puff EOR in shale reservoirs are presented first, followed by the research objectives and scope.
- Chapter 2 outlines the literature related to the various experimental work and simulation studies performed since 2008 pertaining to the research. This is followed by a summary of the various field trials and pilots in the Bakken and Eagle Ford, along with the lessons learned.
- Chapter 3 presents the formulation of the mathematical model for understanding the recoveries expected from the huff-and-puff EOR process. After validating the results of the mathematical model against published analytical results, the model is extended to complex

fracture networks. Finally, the upscaling schemes are developed to translate recovery from core to reservoir scale based on the sensitivities performed for the various inputs.

- Chapter 4 extends the mathematical model developed in Chapter 3 to investigate the role of the soaking phase in the cyclic huff-and-puff EOR process in shale reservoirs.
- Chapter 5 presents two case studies from the Eagle Ford, followed by a numerical modeling study evaluating the performance of three different injectants with respect to containment and recoveries. This is followed by a discussion of asphaltene deposition during the miscible gas injection process.
- The summary and recommendation are presented in Chapter 6, along with recommendations for future research studies.

Key takeaways are presented at the end of each chapter.

Chapter 2

Enhanced Oil Recovery in Unconventional Shale Reservoirs

As shale plays mature and the location inventories shrink, the operators have been looking into techniques to extend well recoveries beyond primary recovery from the hydraulically fractured shale wells. With the recoveries from the primary depletion expected to be less than 10% (Clark, 2009; Sheng, 2018), a large percentage of unrecovered hydrocarbons in the liquids-rich shale plays could be recovered with the application of the EOR methods. Conventional EOR techniques such as miscible flooding (gas injection) and thermal injection using injector-producer pairs (or patterns) are not feasible in ultra-tight low permeability shale reservoirs.

Over the past decade, several field trials have been conducted to test a cyclic miscible gas injection EOR technique involving a single wellbore for both injection and production phases. The cyclic process, referred to as "Huff-and-Puff," involves three distinct phases – injection, soaking, and production. During the injection (or huff) phase, the gas is injected into the tight rock, which mixes and achieves miscibility with the remaining oil during the soaking (or shut-in) phase, and then flows back during the production (or puff) stage.

Although miscible gas huff-and-puff EOR has now been field-tested in several shale plays in the U.S. (Eagle Ford, Bakken, Permian, and SCOOP/STACK), pilots in the Eagle Ford Shale seem to have responded the best to this technology with EOG Resources claiming incremental recoveries expected to be 30-70% of the primary recovery (**Figure 1.1**). The injectivity of the gas has not been a problem; however, the recoveries reported after three to five years of huff-and-puff have been at the low end of this expected range.

Over the past decade, several studies have investigated the potential of miscible gas injection to increase the hydrocarbon recovery from liquids-rich shale reservoirs. This chapter starts with a review of the various laboratory experiments and simulation studies, followed by a summary of the field trials and pilots in the Bakken and Eagle Ford plays. Finally, some of the learnings from the field trials are summarized along with technical issues that remain to be addressed.

2.1 Literature Review

Since 2008, numerous laboratory experiments and numerical reservoir simulation studies have shown the potential of huff-and-puff EOR application to increase recovery beyond primary depletion in liquids-rich shale reservoirs. This literature review is not meant to be all-inclusive but highlights the scope and findings of various experimental and simulation studies pertinent to this research.

2.1.1 Laboratory Studies

Several laboratory experiments have been carried out over the past decade to investigate the propensity of the injected gas to mix with the remaining oil in core samples and to understand how much additional oil can be recovered by repeating multiple huff-and-puff cycles. A few different types of experiments pertinent to this study are (A) experiments performed to evaluate the impact of sample size on huff-and-puff EOR recovery, (B) the creation of a secondary fracture network during the hydraulic fracture stimulation, (C) the effect of injection pressure and injected gas composition on huff-and-puff EOR efficacy, and (D) investigation of soaking times on overall huff-and-puff cyclic process.

2.1.1.1 Experiments related to the impact of sample size

EERC Experiments

Energy and Environmental Research Center (EERC) has conducted several experiments since 2013 to investigate the applicability of EOR in the Bakken shale samples and found the EOR recovery mechanisms to be different from those in conventional reservoirs. To examine the effect of sample size on the huff-and-puff recoveries, Hawthorne et al. (2019) performed tests using three different types of sample geometries – 11.2 mm diameter round rod, 11.2 mm diameter by 1-3 mm thick coins, and 1-3.4 mm crushed particles – all from the same formation (Figure **2.1**). They found that the recoveries from the coins and crushed particles were nearly complete in one hour (though the 1-3.4 mm crushed particles were slightly faster than the coins), while only 28% recovery was possible from the round rod during the same time (**Figure 2.2 – left**). Similar and more distinct observations were made from the three sample sizes prepared from the Lower Bakken Shale with lower permeability and diffusion coefficients (**Figure 2.2 – right**), which shows different recoveries at the end of 24 hours (ranging from 38% for the rod to 89% for the crushed particles.



Figure 2.1: The three rock sample geometries used for the experiments (1) 11.2 mm diameter round rod, (2) 11.2 mm diameter by 1-3 mm thick "coins," and (3) 1-3.4 mm crushed particles (Hawthorne et al., 2019).

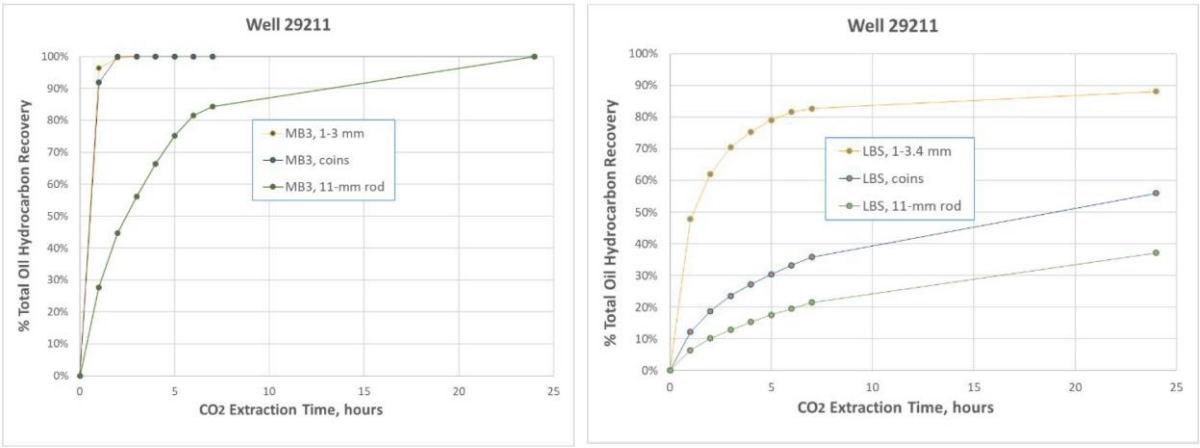


Figure 2.2: Effect of surface area on the total oil hydrocarbon recovery rates for high-permeability Middle Bakken (left) and Lower Bakken Shale (right) rock samples. Experiments were conducted with three different geometries: (1) 11.2 mm diameter by 40 mm long round rods, (2) 11.2 mm diameter by 1-3 mm thick "coins," and (3) 1-3.4 mm crushed particles (Hawthorne et al., 2019).

Oklahoma University (OU) Experiments

Similar experiments were carried out by Dang (2019) to investigate the impact of sample size on hydrocarbon recovery. The experiments included injecting CO_2 while keeping the pressure 1,000 psi above the MMP (Minimum Miscibility Pressure) of 2,500 psi. The experiment tested

recovery for four sample sizes – 0.9-2 mm, 2-4.7 mm, 4.7-6.7 mm, and 6.7-8 mm. Smaller samples were found to have higher recovery with fewer huff-and-puff cycles. After five huff-and-puff cycles, the final recovery from these samples varied by ~18% (**Figure 2.3**).

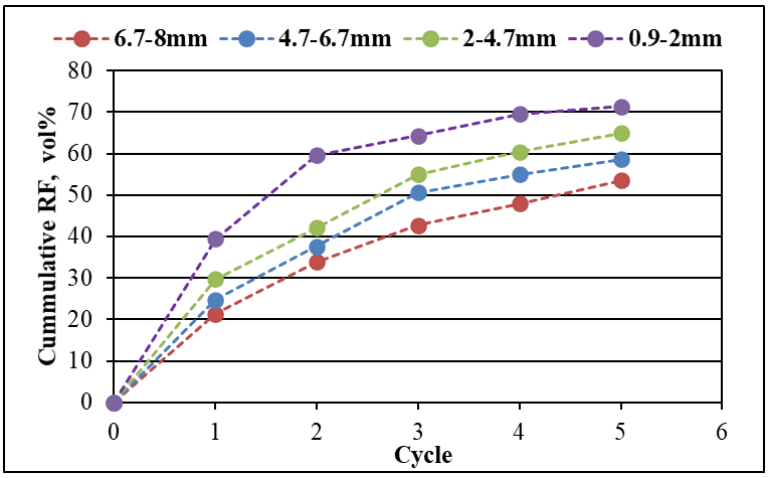


Figure 2.3: Recovery factor as a function of four different sample sizes, with recovery increasing with decreasing sample size (modified from Dang, 2019).

Researchers concluded from both of these experiments at EERC and OU that the smaller sample results in higher recovery due to a larger exposed surface area. However, it is postulated that higher oil recovery is also a function of the smallest length dimension ("critical length"), which the injected gas has to penetrate to mix with the remaining oil in the sample. In other words, three different-sized samples of the matrix in the shape of a cube, column, and slab (**Figure 2.4**) would result in the same recovery factor as long as they have the same minimum length dimension, "dx" (based on Fick's law). Mydland et al. (2020) presented numerical simulation results using a single porosity model with diffusion to demonstrate similar concepts.

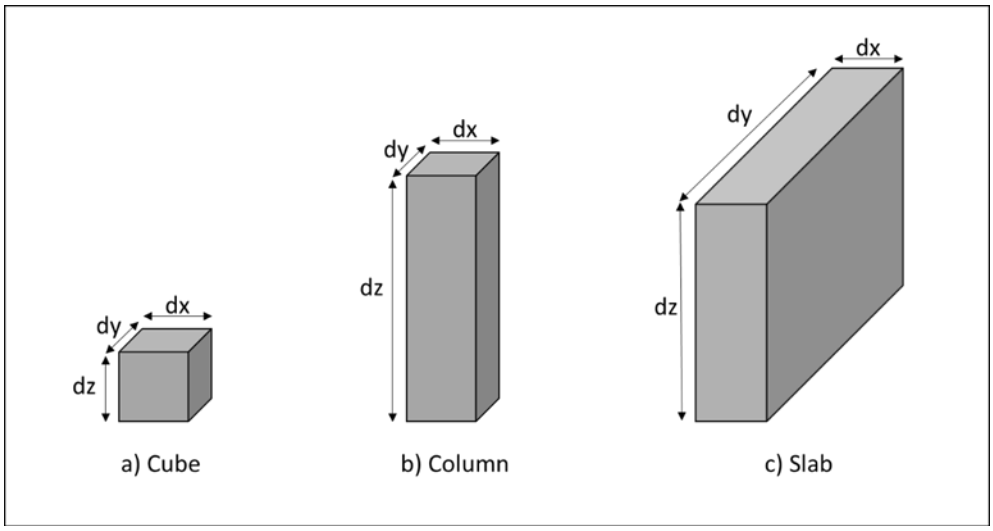


Figure 2.4: Three different matrix samples, each with the same minimum length dimension of dx, are expected to have similar recoveries.

2.1.1.2 Fracture distribution observed in laboratory experiments

Hydraulic fracture propagation and associated rock failure mechanism depend on multiple factors, including in situ reservoir stresses and the interaction of fracturing fluid with the reservoir fluid during hydraulic fracturing. Damani et al. (2018) conducted six experiments on triaxially stressed core samples of low porosity, low permeability Tennessee sandstone to investigate the effect of in situ and injection fluid on hydraulic fracture mechanisms by recording the acoustic emissions.

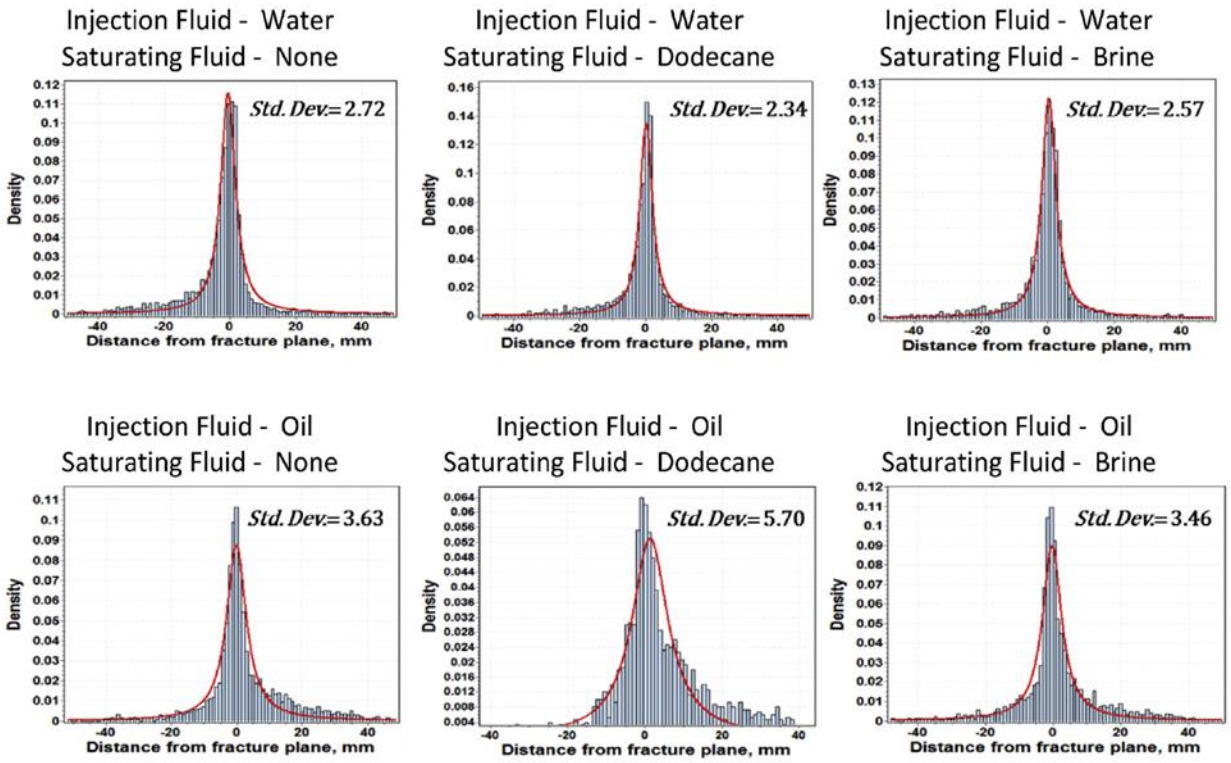


Figure 2.5: Distribution of acoustic events with distance perpendicular to the fracture plane. Data from all tests exhibit a good fit to a Lorenz/Cauchy distribution curve shown in red (Damani et al., 2018).

Figure 2.5 shows the distribution of acoustic emission events (i.e., fracture density in the process zone adjacent to the primary fracture) as a function of distance from the primary fracture plane. Additionally, in all six tests, the density (frequency) of secondary fractures appears to decrease as we move away from the main perforation in either direction. A statistical analysis of fracture density perpendicular to the induced hydraulic fracture showed a good fit to the Lorenz/Cauchy distribution:

$$\boldsymbol{f(x) = \frac{1}{\pi\gamma}\left[\frac{\gamma^2}{(x-x_0)^2+\gamma^2}\right]} \qquad \textbf{…Equation 2.1}$$

where f(x) is the probability density function for an event to lie at distance x from the fracture plane, x_0 is the location of the peak of the distribution (referred to as the location parameter), and γ is the half-width at half maximum (referred to as the scale parameter). In all six tests, the location

parameter is zero. The value of the scale parameter determines the statistical dispersion of the distribution. Therefore, the larger the scale parameter, the more spread out the distribution. The scale parameter differs for the six tests; however, the scale parameter and the standard deviation are lower for water injection tests. The maximum value or the peak of the Cauchy distribution is given by $1/\pi\gamma$. For the top-left chart in Figure **2.5**, the location parameter is zero with a scale parameter of three. So, Eq. (16) for this test can be written as:

$f(x) = \frac{0.9549}{x^2+9}$ with the maximum value of probability density function of 10.61%.

Figure 2.6 compares the lab and actual field observations related to primary fracture length (Fault Length on the x-axis) to fracture width or distance between the secondary fractures (Process Zone Width on the y-axis). As the SEM, lab, and field measurements all fall along the 1:50 scaling line (scaling parameter), it suggests that the lab observations related to secondary fracture distributions can be upscaled to represent the field scale SRV.

Similar observations have been made in the various field studies corroborating the creation of complex fracture networks. Mineback studies (Jeffrey & Settari, 1995; Warpinski & Teufel, 1987) and fracture diagnostic techniques such as microseismic monitoring (**Figure 2.7**) have indicated fracture propagation away from the maximum stress direction due to the low in situ differential stress (i.e., the difference between the maximum and the minimum horizontal stress) and/or presence of natural fractures. The presence of joints and faults can affect the fracture geometry of hydraulic fractures by arresting the fracture growth, increasing fluid leak-off, and enhancing the creation of multiple fractures. A recent study from Eagle Ford showed hydraulic fracture complexity when the wells were cored after the hydraulic fracture treatment (**Figure 2.8**). In this study, the hydraulic fractures were observed in a subparallel set at approximately one fracture per foot along the wellbore, and nearly all were aligned with the principal horizontal stress.

The core data indicated that the hydraulic fracture intensity decreased with height and lateral distance (Raterman et al., 2018).

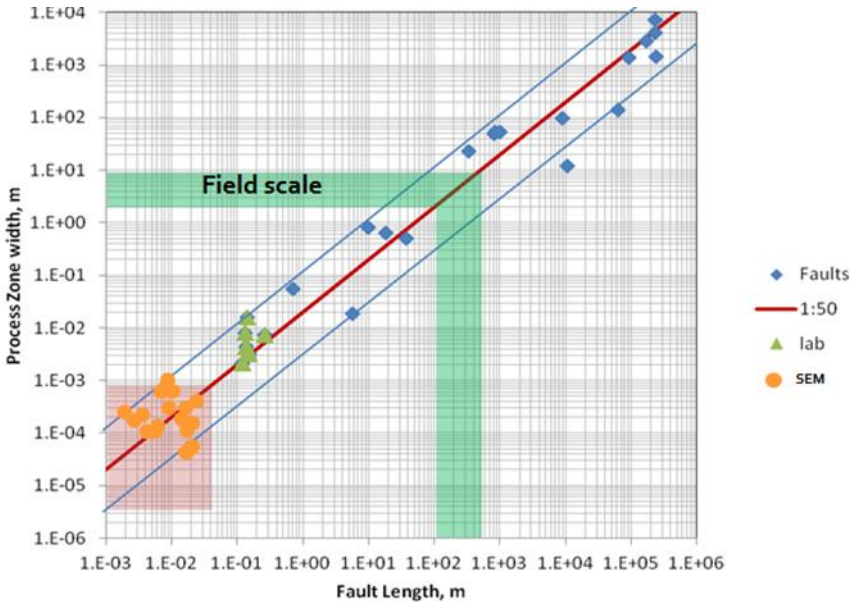


Figure 2.6: A comparison of lab fracture density from SEM analysis (Bhagat, 2012) with geological field observations (Vermilye & Scholz, 1998; Zhang & Stephansson, 2010) suggests that lab observations can be used to constrain field-scale SRV.

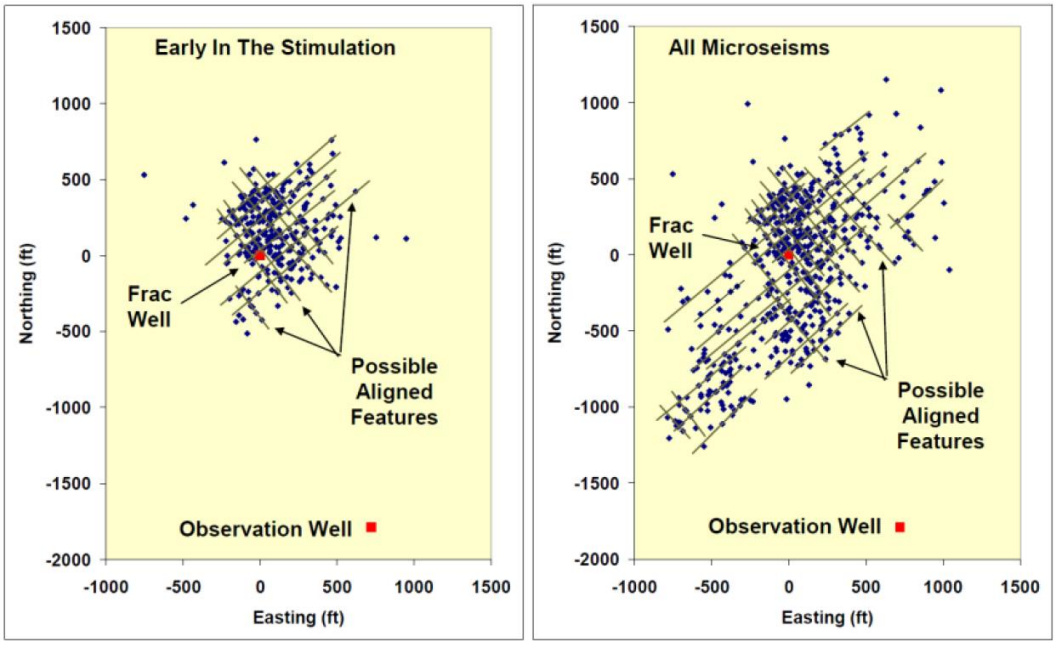


Figure 2.7:Microseismic results from Barnett shale showing evidence of a complex fracture network created (Warpinski et al., 2008).

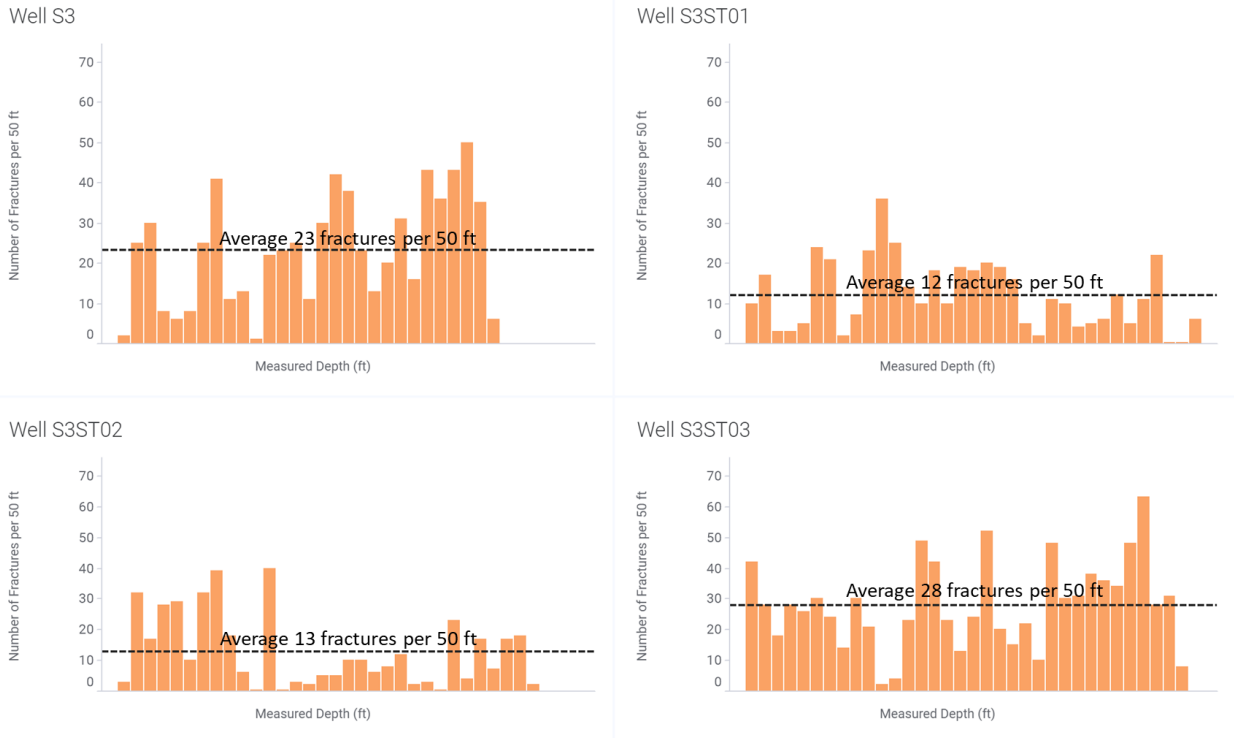


Figure 2.8: Hydraulic fracture distribution from four cored Eagle Ford wells (modified from Raterman et al., 2018).

2.1.1.3 Experiments related to injection pressure and injected gas composition

The selection of the injectant gas during the feasibility study depends on the ability of gas to (i) mobilize remaining oil, and (ii) cost and availability. Most lab experiments relate the injection pressure to Minimum Miscibility Pressure (MMP), representing the pressure at which the injected gas will become miscible with the remaining oil in the matrix. The MMP is a function of the composition of the injection gas and remaining oil in the matrix. **Figure 2.9** shows the MMP results for different gases with Bakken crude oil determined by the capillary-rise vanishing interfacial tension (VIT) method at 230°F (Hawthorne et al., 2017). For Bakken crude oil, the MMP values range from 1,358 psi for ethane to 4,512 psi for methane. Subsequent studies (Hawthorne et al., 2019; Min, 2019) have shown additional recoveries with rich gas over lean gas.

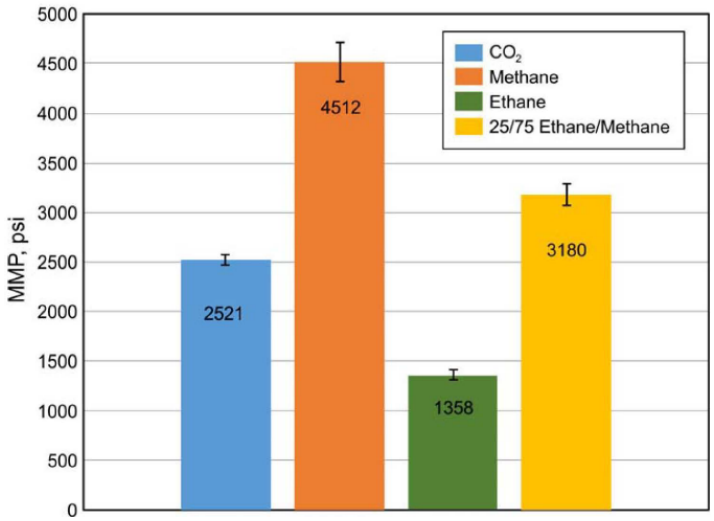


Figure 2.9: MMP values for typical Bakken crude oil with different gases (Hawthorne et al., 2017).

The experimental work of Min (2019) also showed that the injection pressure relative to the MMP determines the fraction of hydrocarbons that can be mobilized and recovered during the production phase. Min reported that with injection pressure 1,000 psi above MMP, hydrocarbons up to C25 were recovered in the lab. However, with a pressure of 1,000 psi below MMP,

hydrocarbons only up to C19 were recovered. This corroborates the laboratory findings of EERC with the Bakken oils, where the higher pressures were found to mobilize more oil regardless of MMP (Hawthorne et al., 2018). In the field, this could result in differences in the composition of the produced stream after various huff-and-puff cycles if the pressures in the matrix at the end of injection and soaking phases vary due to differences in cycle times, pressure containment, etc.

Conversely, it has been debated that the primary recovery mechanism during huff-and-puff in ultra-tight shale matrix is diffusion because of low Peclet numbers rather than advection. As a result, the miscibility pressure pertinent to this process is First Contact Miscible (FCM), which could be over 1,000 psi higher than the MMP (Carlsen et al., 2020). The FCM MMP can be measured using the Vanishing Interfacial Tension (VIT) method (Hawthorne et al., 2016; Mukherjee, 2020) or Swelling Test (Carlsen et al., 2020). In the VIT method, the observed interfacial tension is associated with the capillary rise in a small glass capillary tube, and the pressure at which capillary rise disappears is considered as FCM MMP. In the Swelling Test, the FCM MMP represents the maximum pressure on a pressure-composition (p-x) diagram at which the reservoir fluid and injection gas forms a single phase when mixed in any proportion.

2.1.1.4 Experiments related to soaking time

Both lab experiments (Dang, 2019; Min et al., 2020) and simulation studies (Song & Yang, 2013) have shown higher recoveries with longer soaking time **above MMP (Figure 2.10)**, which supports that the injected gas is transported within the matrix by diffusion, which is a relatively slower process than advection. From an economics standpoint, although shutting in the well for a

longer duration would directly impact near-term production and economics, it would require fewer cycles overall if extended soaking time results in higher oil recovery from the shale matrix.

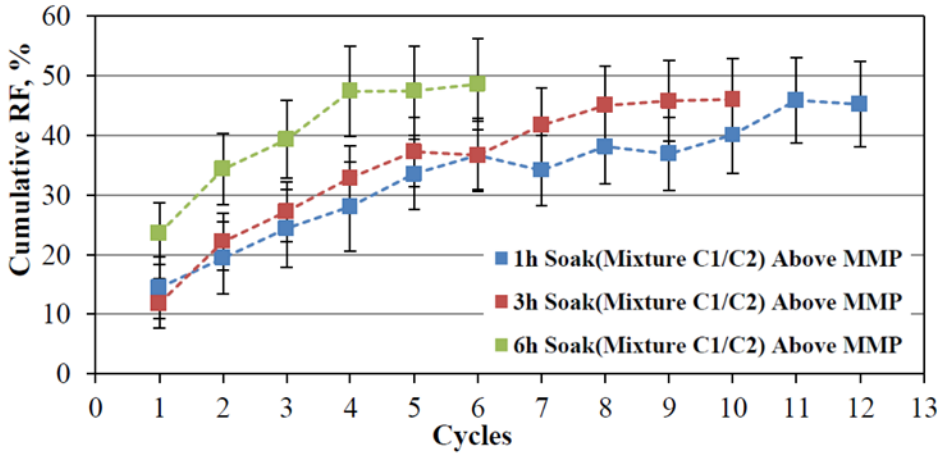


Figure 2.10: Impact of soaking time on huff-and-puff recovery for the Eagle Ford samples (Dang, 2019).

Furthermore, Song and Yang (2013) and Perez and Devegowda (2020) have shown that soaking time beyond a certain threshold did not yield any additional recovery, so there is an optimum soaking time based on the rock and fluid properties. Afari et al. (2022) studied the effect of soaking time using numerical simulation and concluded that soaking has minimal to no impact on additional oil recovery but qualified those results by stating that the effective diffusion coefficient was not high enough to impact oil recovery. So, in general, there is no consensus yet on the impact of soaking time on huff-and-puff recoveries.

2.1.2 Simulation Studies

Similar to the various laboratory studies, several simulation studies have been performed, especially to understand the efficacy of injectant gas composition on the different reservoir fluid types.

2.1.2.1 Phase Behavior of Different Reservoir Fluid Types with Same Gas Injectant

To compare the performance of huff-and-puff gas injection in different reservoir fluid types, Ganjdanesh et al. (2019b) developed a Peng-Robinson Equation of State (EOS) model using the fluid samples from the three Eagle Ford wells within a few miles from each other. Since the only gas available for injection to the operator was the produced field gas from offsetting producers, the study evaluated the phase behavior and miscibility of the injected field gas with the different reservoir fluid types (black oil, volatile oil, and gas condensate).

A compositional simulator was used to build single well models for each reservoir fluid type, with a lateral length of 4,500 ft and fracture spacing of 50 ft. The reservoir thickness was modeled to be 130 ft with the average matrix porosity and permeability of 5% and 334 nD, respectively. An embedded discrete fracture model (EDFM) was used to model the fracture network. A summary of the Eagle Ford reservoir fluid properties, fluid composition, Pressure-Temperature (PT) diagram, and EOS parameters for the three reservoir fluid types are presented in **Table 2.1** through **Table 2.4** and **Figure 2.11**. The gas condensate fluid modeled was a rich gas with a condensate gas ratio (CGR) or yield of 147 stb/mmscf.

The field production data for the primary depletion phase was used to history match the model. The history matched fracture half-length varied between 50-175 ft, fracture height ranging from 50-90 ft, and fracture conductivity ranges between 3-30 md-ft. This was followed by

modeling ten (10) Huff-and-Puff cycles using the produced field gas, which comprised ~77% methane and 19% ethane/propane (**Table 2.5**). The field data of the initial Huff-and-Puff cycles was used to fine-tune the history-matched model further. The Huff-and-Puff cyclic injection using the produced field gas showed the best additional uplift with the black oil system (30-40%), followed by gas condensate (15-20%) and then the volatile oil systems (10%), and is discussed below.

Table 2.1: Summary of the Eagle Ford Fluid Properties (modified from Ganjdanesh et al., 2019b)

Reservoir Fluid Analysis	**Black Oil**	**Volatile Oil**	**Gas Condensate**
Well depth, ft	8,082	9,800	9,175
Static Reservoir Pressure, psi	4,726	5,843	5,858
Reservoir Temperature, °F	215	258	256
Saturation (Bubble/Dew Point) Pressure, psi	2,120	3,641	4,314
Separator Tests			
Stock Tank Oil Gravity, °API	42.5	48.3	51.2
Oil Specific Gravity	0.813	0.786	0.781
Solution GOR, scf/stb	538	2,412	6,814
Gas Specific Gravity at std. conditions	0.838	0.925	0.876

Table 2.2: Peng-Robinson EOS Parameters and Fluid Composition for the Black Oil Model (Ganjdanesh et al., 2019b)

Comp.	P_c, atm	T_c, K	Acentric Factor	Molecular Weight	Volume Shift	V_c for Viscosity	Parachor	Composition, Mole Frac.
C_1+N_2	45.3731	190.838	0.00808	16.029	-0.19396	0.09977	77.213	0.32550
$C_{2-3}+CO_2$	46.1742	331.954	0.12209	35.858	-0.1285	0.16637	124.744	0.14906
C_{4-6}	33.5282	461.193	0.23442	70.443	-0.04667	0.30629	224.9726	0.10303
C_{7-10}	25.2	538	0.418	114	0.0346	0.447	330	0.14634
C_{11-20}	17.8	722	0.76	199	0.119	0.753	544	0.19183
C_{21-45}	13.7	843	1.24	383	-0.0693	0.938	999	0.07997
C_{46-80}	12	1120	1.15	745	-0.29	1.48	1840	0.00427

Table 2.3: Peng-Robinson EOS Parameters and Fluid Composition for the Volatile Oil Model (Ganjdanesh et al., 2019b)

	P_c, atm	T_c, K	Acentric Factor	Molecular Weight	Volume Shift	V_c for Viscosity	Parachor	Composition, Mole Frac.
CO_2+H_2S	72.957	304.902	0.224	43.880	-0.06259	0.09405	78.021	0.01023
N_2	33.500	126.200	0.040	28.014	-0.17589	0.08980	41.000	0.00098
C_1	45.400	190.600	0.008	16.043	-0.19402	0.09900	77.300	0.50614
C_2	48.200	305.400	0.098	30.070	-0.14314	0.14800	108.900	0.11486
C3	41.900	369.800	0.152	44.097	-0.11270	0.20300	151.900	0.05987
C_{4-6}	33.304	463.021	0.240	69.966	-0.04758	0.30972	228.699	0.10675
C_{7-10}	29.590	535.699	0.383	112.988	-0.16457	0.61271	327.683	0.11655
C_{11-32}	20.119	702.845	0.809	235.471	-0.20948	0.92785	669.614	0.07921
C_{33-80}	11.020	1002.334	1.102	581.589	-0.05259	1.89294	1487.045	0.00541

Table 2.4: Peng-Robinson EOS Parameters and Fluid Composition for the Gas Condensate Model (Ganjdanesh et al., 2019b)

	P_c, atm	T_c, K	Acentric Factor	Molecular Weight	Volume Shift	V_c for Viscosity	Parachor	Composition, Mole Frac.
N_2+C_1	45.341	190.279	0.008	16.077	-0.19399	0.09895	77.119	0.64630
C_{2-3}+CO_2	48.605	328.344	0.131	35.303	-0.12963	0.16186	120.963	0.18104
C_{4-6}	33.642	457.134	0.233	68.412	-0.05319	0.30432	223.519	0.07721
C_{7-10}	25.543	552.025	0.393	111.195	0.03860	0.57868	323.211	0.05560
C_{11-20}	18.110	680.801	0.649	192.155	0.09620	0.88320	527.386	0.03367
C_{21-30}	14.261	839.202	0.961	333.494	0.05441	0.72721	849.178	0.00515
C_{31-80}	12.810	1009.275	1.127	501.418	-0.00831	1.17805	1260.502	0.00104

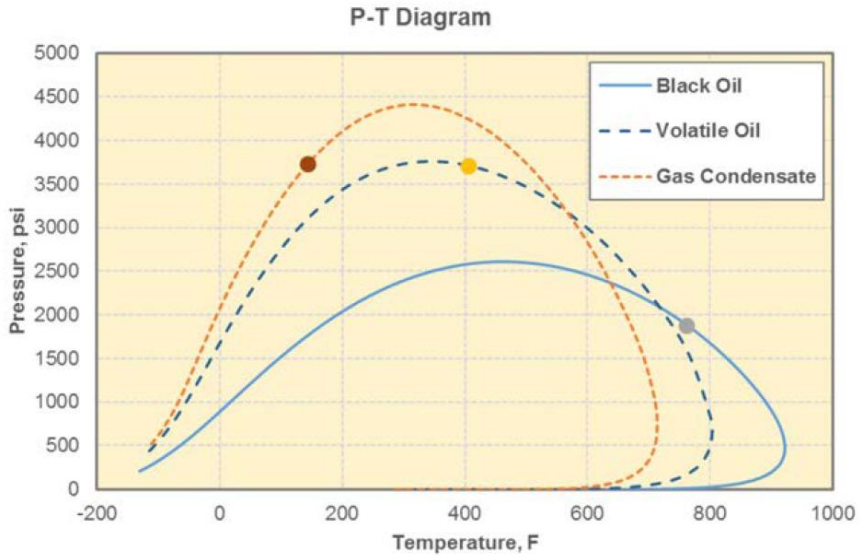


Figure 2.11: Pressure-Temperature (PT) diagrams for the black oil, volatile oil, and gas condensate reservoir fluids for the Eagle Ford (Ganjdanesh et al., 2019b).

Table 2.5: Produced Field Gas Composition (Ganjdanesh et al., 2019b)

Component	Composition, mole fraction
C_1	0.768
C_{2-3}	0.190
C_{4-6}	0.042
C_{7+}	0.000

Black Oil

The black oil fluid system exists as a single-phase undersaturated oil in the reservoir with an initial reservoir pressure (4,726 psi) higher than bubble-point pressure (2,120 psi) and a C7+ mole fraction greater than 42%. The reservoir temperature is significantly lower than the critical temperature.

With primary production, as the reservoir pressure near the hydraulic fracture face (and within the reservoir) drops below the bubble-point pressure, the light and intermediate components from the remaining oil in the matrix form a gas phase. The two-phase flow of hydrocarbons in the gas and oil phases impedes the flow of heavier components in the oil phase, making a less efficient process. When the injected field gas mixes with the remaining reservoir fluid, the vaporization process results in a low-viscosity single-phase mixture near the fractures, thereby recovering additional oil.

Figure 2.12 (left) compares the phase behavior/PT diagram of the black oil fluid at the initial conditions to before injection (after the period of primary production) and after injection. The green line shows the reservoir temperature of the black oil reservoir. The critical temperature of the fluid is higher than the reservoir temperature at the initial condition and before injection (primary production being an isothermal process); however, it decreases below the reservoir temperature with the gas injection. With primary production, as the composition of the reservoir

fluid changes with pressure, the phase diagram of the black oil fluid changes slightly when the pressure drops below the bubble-point (before injection phase diagram). With the gas injection, the mixture of the remaining reservoir fluid and injected field gas forms a gas condensate mixture with a bubble-point pressure of about 4,600 psi. The bottom hole pressure at the end of gas injection should be greater than the bubble-point pressure to ensure high incremental oil recovery.

Figure 2.12 (right) compares the cumulative oil production with and without gas injection for the black oil reservoir. The black oil fluid model showed the highest hypothetical incremental oil recovery (30-40%) after ten cycles of Huff-and-Puff miscible injection.

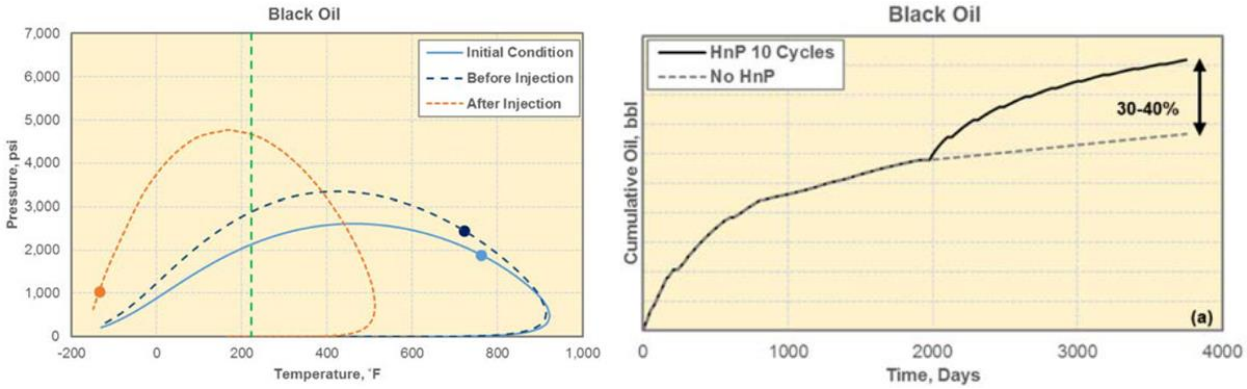


Figure 2.12: Phase behavior/PT diagram of Black Oil Fluid at Initial Condition, Before Injection, and After Injection near the Hydraulic Fracture Face (left); Comparison of Cumulative Oil Production with and without Gas Injection for Black Oil Reservoir (right) (modified from Ganjdanesh et al., 2019).

Volatile Oil

The volatile oil fluid system also exists as a single-phase undersaturated oil in the reservoir with the initial reservoir pressure (5,843 psi) higher than bubble-point pressure (3,641 psi), and a C7+ mole fraction greater than 20%. The reservoir temperature is closer to the critical temperature, compared to the black oil system. The volatile oil fluid contains fewer heavy molecules and more intermediate components than black oil. The degree of undersaturation (difference between initial

reservoir pressure and bubble-point pressure) is lower than that of the black oil system. With primary production, as the reservoir pressure near the hydraulic fracture face (and gradually within the reservoir) drops below the bubble-point pressure, most of the oil flashes into gas, producing less liquid content.

Figure 2.13 (left) compares the phase behavior/PT diagram of the volatile oil fluid at the initial conditions to before injection (after the period of primary production) and after injection. The green line shows the reservoir temperature of the volatile oil reservoir. The critical temperature of the fluid is slightly higher than the reservoir temperature at the initial condition and before injection (primary production being an isothermal process); however, it decreases below the reservoir temperature with the gas injection. As the injected field gas mixes with the remaining reservoir fluid, the reservoir fluid system gradually shifts from a volatile oil to a gas condensate system. The phase diagram expands as the reservoir fluid mixes with the injected gas and the saturation pressure increases as the ratio of the injected gas increases in the fluid mixture. At the end of the gas injection, the fluid mixture dew point is about 7,000 psi. The miscibility of the produced gas and the volatile oil is dominated by vaporization. However, the low percentage of intermediate components in the produced gas highly reduces the efficiency of the vaporization process.

Figure 2.13 (right) compares the cumulative oil production with and without gas injection for the volatile oil reservoir. The volatile oil model showed the lowest oil recovery (10%) after ten cycles of Huff-and-Puff miscible injection.

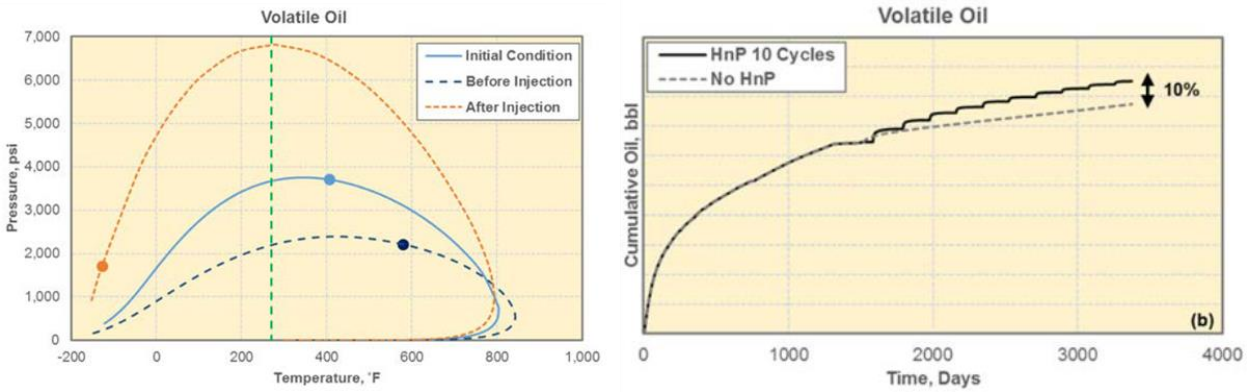


Figure 2.13: Phase behavior/PT diagram of Volatile Oil Fluid at Initial Condition, Before Injection, and After Injection near the Hydraulic Fracture Face (left); Comparison of Cumulative Oil Production with and without Gas Injection for Volatile Oil Reservoir (right) (modified from Ganjdanesh et al., 2019).

Gas Condensate

The gas condensate fluid system exists as a single-phase gas in the reservoir with the initial reservoir pressure (5,858 psi) higher than the dew-point pressure (4,314 psi), and a C7+ mole fraction of about 9.5%. The reservoir temperature is higher than the critical temperature of the original reservoir fluid but less than the cricondentherm. The degree of undersaturation (difference between initial reservoir pressure and dew-point pressure) is significantly less than in the black oil and volatile oil systems. With primary production, heavier components condense into a liquid phase as the reservoir pressure near the hydraulic fracture face (and gradually within the reservoir) drops below the dew-point pressure. Since the condensate saturation barely builds up above 10 percent, the gas flows preferentially to condensate, and large amounts of intermediate and heavy components accumulate and remain unrecoverable in the matrix.

Figure 2.14 (left) compares the phase behavior/PT diagram of the gas condensate fluid at the initial conditions to before injection and after injection. The green line shows the reservoir temperature of the gas condensate reservoir. The critical temperature of the gas condensate fluid

is slightly lower than the reservoir temperature at the initial condition; however, the critical temperature increases above the reservoir temperature during primary production. The phase diagram shifts towards a volatile oil behavior during primary production with the accumulation of medium and heavy hydrocarbons. As the injected field gas mixes with the remaining reservoir fluid, the heavier components that accumulate in the matrix during primary production re-vaporize into the gas phase and become mobile. With the injection of the produced field gas, the phase envelope expands, shifting back towards the gas condensate state. The dew-point pressure of the new mixture is higher than the in situ mixture. The size of the phase envelope after injection and the dew point of the new mixture are functions of the injected gas quality.

Figure 2.14 (right) compares the cumulative oil production with and without gas injection for the gas condensate reservoir. The gas condensate model showed an oil recovery of 15-20% after ten cycles of Huff-and-Puff miscible injection, a slightly higher recovery than the volatile oil model.

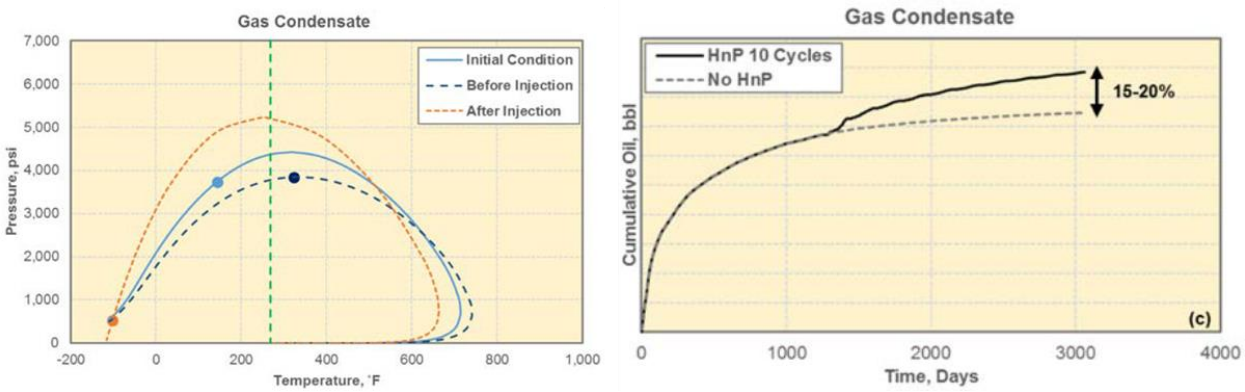


Figure 2.14: Phase behavior/PT diagram of Gas Condensate Fluid at Initial Condition, Before Injection, and After Injection near the Hydraulic Fracture Face (left); Comparison of Cumulative Oil Production with and without Gas Injection for Gas Condensate Reservoir (right) (modified from Ganjdanesh et al., 2019).

2.1.2.2 Effect of injected gas composition on oil recovery

In **Section 2.1.2.1**, although the volatile oil system showed the lowest oil recovery compared to the black oil and gas condensate system, simulation studies by Atan et al. (2018) have shown that the composition of the injected gas has a significant impact on the performance and recovery uplift observed from miscible gas Huff-and-Puff process. Atan et al. (2018) suggested that a richer injectant gas is needed to shrink the phase envelope and decrease the saturation pressure. The efficiency of the vaporization process in the volatile oil system will be much higher with lowering the mixture saturation pressure.

In the case of gas condensate reservoirs, Ganjdanesh et al. (2019b) evaluated the impact of using the produced field gas (77% C1, 19% C2+C3, 4% C4+) and a rich gas (70% C2, 30% C3). **Figure 2.15** shows the phase diagram at the initial condition, before injection, and after the injection of the produced field gas or rich gas. With primary production, the phase diagram shifts towards a volatile oil behavior during primary production with the accumulation of medium and heavy hydrocarbons. When the produced field gas is mixed with the remaining oil, the phase diagram switches back to the gas condensate but with a higher dew point pressure (above 5,000 psi) than the initial condition (4,314 psi). With the rich gas, the mixture has the same change in phase behavior as that with the produced field gas but with a lower dew point pressure (~3,000 psi) than the initial condition. With a lower dew point pressure, the onset of the condensate accumulation is delayed. The incremental oil recovery with the rich gas was greater than 25 percent by shrinking the phase diagram and decreasing the dew-point pressure.

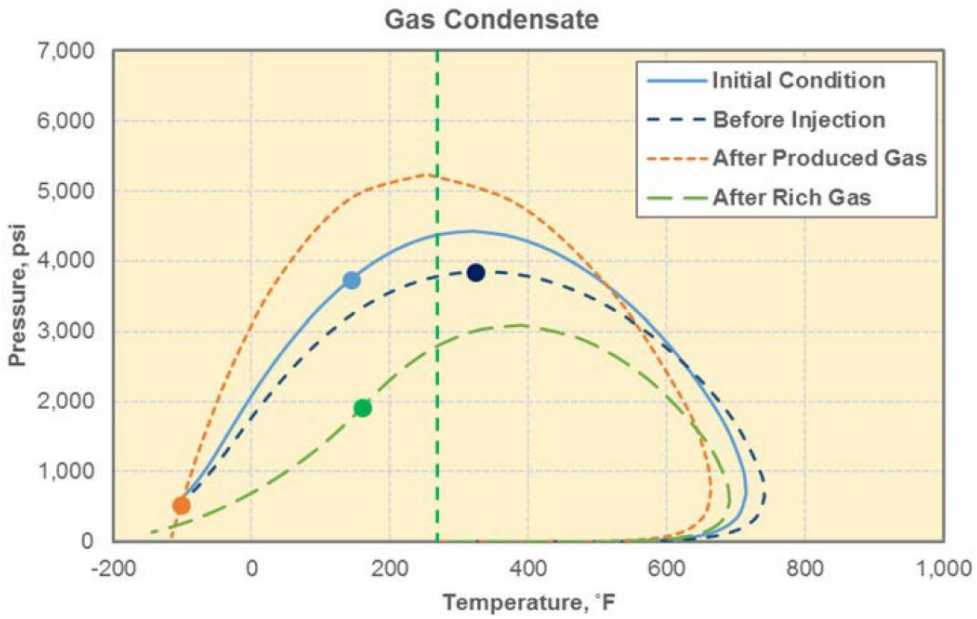


Figure 2.15: Pressure-Temperature (PT) diagrams for the gas condensate reservoir fluid at the initial condition, before injection, and after injection of the produced field gas or rich gas (Ganjdanesh et al., 2019).

2.1.2.3 Sensitivity Analysis

Atan et al. (2018) performed a sensitivity analysis with a volatile oil EOR project from the Eagle Ford to evaluate the impact of individual parameters on the huff-and-puff recovery (**Figure 2.16**). While the SRV size showed the largest impact between the low and high cases, the containment of the injected gas and injected gas composition provides the highest risk and opportunity in a huff-and-puff miscible gas process.

- The highest risk in the huff-and-puff process is the containment of the injected gas, as extreme leakage will prevent achieving the miscibility conditions with the remaining oil and lead to the cycling of the injected gas.

- The biggest opportunity is to optimize the injectant gas composition. Using a richer gas improves the efficiency and recovery of the remaining oil compared to the produced field gas, and an optimized process can achieve an incremental oil recovery of 41%.

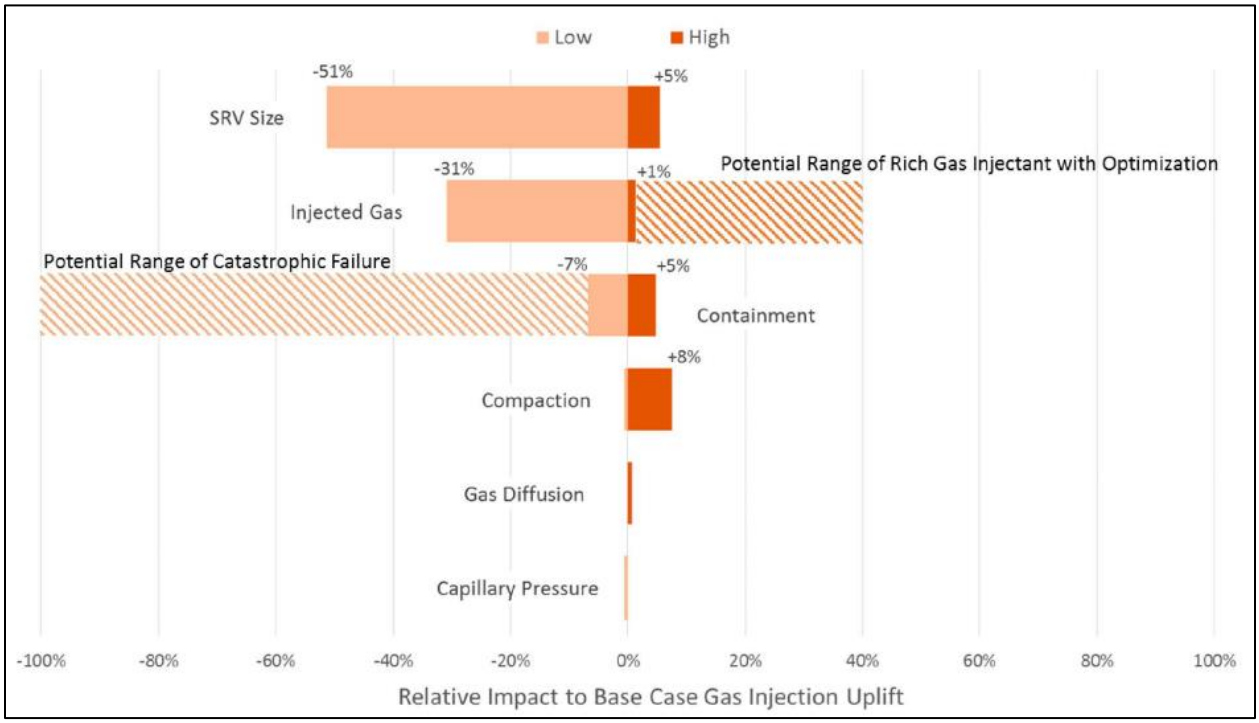


Figure 2.16: Sensitivity Analysis with an Eagle Ford Volatile Oil EOR project (Atan et al. (2018)).

2.1.3 Caveats

Although these experimental and simulation studies have helped understand the impact of the various factors on recovery, it is worth mentioning a few issues (or caveats):

1) Many of these experiments were performed by injecting gas(es) through small cores or crushed rock particles. Recoveries from these samples have been reported in the 60-95% (Alfarge et al., 2018). This could be attributed to the increased contact area between the shale matrix and the injected gas in these experiments.

2) The small core samples used in the laboratory experiment may not fully capture the tortuosity and disconnected pores in the shale matrix. So, the diffusion coefficients calculated in the laboratory would represent "bulk" diffusion coefficients rather than "effective" diffusion coefficients, which could be one to two orders of magnitude smaller. Some simulation studies have used the same diffusion coefficient reported from the laboratory experiments and could overpredict recoveries from the shale matrix.
3) In the simulation studies, models can overpredict the recoveries with huff-and-puff due to using coarser grid blocks and bulk diffusion coefficients. Additionally, a lack of (or incorrect) characterization of natural and/or hydraulic fractures and features can overestimate the containment of the injected gas in these models.
4) Lastly, there is a scale difference between the core sample in the laboratory and formation in the field, which could result in differences in the interpreted recovery mechanism(s) and the expected recoveries. The core flooding and fluid characterization studies provide initial design parameters for further analysis. However, caution must be exercised when extrapolating the laboratory results to the field scale.

2.2 Field Trials/Pilots

As of Q1 2024, about fifty liquid-rich projects (500+ wells) have been permitted for huff-and-puff EOR in shale reservoirs (Enverus Prism, 2024; Shale Ingenuity, 2022), with the majority of them in the Eagle Ford. This review focuses on the subsurface and other technical aspects of the huff-and-puff application but acknowledges the importance of logistics and economics in defining the overall success of the project. Additionally, since most of these are in the Bakken and Eagle Ford basins, the following sections cover the pilots in these two plays in detail. A summary of the reservoir properties for the Bakken and Eagle Ford is included in **Table 2.6**.

Currently, ten EOR projects are permitted in the Permian Basin, two in the Scoop/Stack and three in the Powder River, all in different planning and implementation stages. With minimal data available publicly on these pilots, they are not covered in this review.

Table 2.6: Summary of Bakken and Eagle Ford Reservoir Properties (Pospisil et al., 2020)

Play	Max Thickness (ft)	Depth (ft)	Reservoir Temp. (°F)	Pressure Gradient (psi/ft)	Lithology	Porosity (%)	Permeability
Bakken	9,160	9,600-10,400	240	0.6-0.73	Shaly siltstone, limestone, dolomite	1-15	0.01-20 mD
Eagle Ford	300	1,500-12,000	270	0.5-0.8	Marlstone, limestone, shaly siltstone	4-12	50-1,500 nD

2.2.1 Bakken

Eleven EOR field pilot tests have been performed in the Bakken play, including the recent Liberty Resources' East Nesson EOR Project, which started injection in 2H21. These pilot tests are summarized in **Table 2.7** based on the information published by Grinestaff (2019), Hamling et al. (2021), Hoffman et al. (2016), Pospisil et al. (2020), and Sorensen (2022). Although the pre-2018 tests across ND and MT (**Figure 2.17**) were performed by multiple operators using different injectants (both water and gas) in stimulated and unstimulated vertical and horizontal wells, they have the following similar conclusions and learnings:

1) Although the permeability of Bakken is suspected to be low (micro-Darcy range), injectivity does not appear to be a problem in the Bakken formation, irrespective of the injectant fluid (water or gas).

2) Containment or conformance control was found to be a major issue, with the injectant breakthrough observed in offset wells within days or weeks.
3) Different cycle times of injection, soaking, and production were utilized in these early trials; however, based on available post-treatment data for a few pilots, additional oil recovery has been minimal to almost insignificant.

Additionally, the XTO pilot in the unstimulated vertical well indicated changes in the produced hydrocarbon stream, which suggests that the CO_2 did penetrate the matrix and mobilized part of the remaining oil.

Based on the learnings from these early pre-2018 trials, Liberty Resources, in collaboration with EERC, DOE, and other service companies, planned two trials in ND using a rich gas. In the Stomping Horse project (2018-19 pilot), several issues encountered in the pre-2018 trials, including the gas containment within the Drill Spacing Unit (DSU), were resolved. With the conformance control, the bottom hole pressure buildup was achieved. However, the pressure buildup was insufficient to achieve miscibility above MMP (Pospisil et al., 2020; Sorensen, 2022). In the East Nesson project, a rapidly switching 2-phase slug (co-injection of gas and water) was utilized to control injectant breakthrough in offset wells while allowing the pressure buildup to increase beyond MMP (Pospisil et al., 2022). Additionally, co-injection of the fluid lowered the injection pressure at the surface (<1,300 psi) while increasing formation pressure to ~4,450 psi (a net pressure increase of 3,500 psi), well above the estimated MMP of 2,430 psi for produced rich gas. Pospisil et al. (2022) reported the production response after the first cycle, which was 7,000 bbls over the baseline trend for the DSU. When available publicly, results from additional

production cycles can be compared against the laboratory results and simulation studies and evaluate the accessibility and sweep efficiency of the injectant within the DSU.

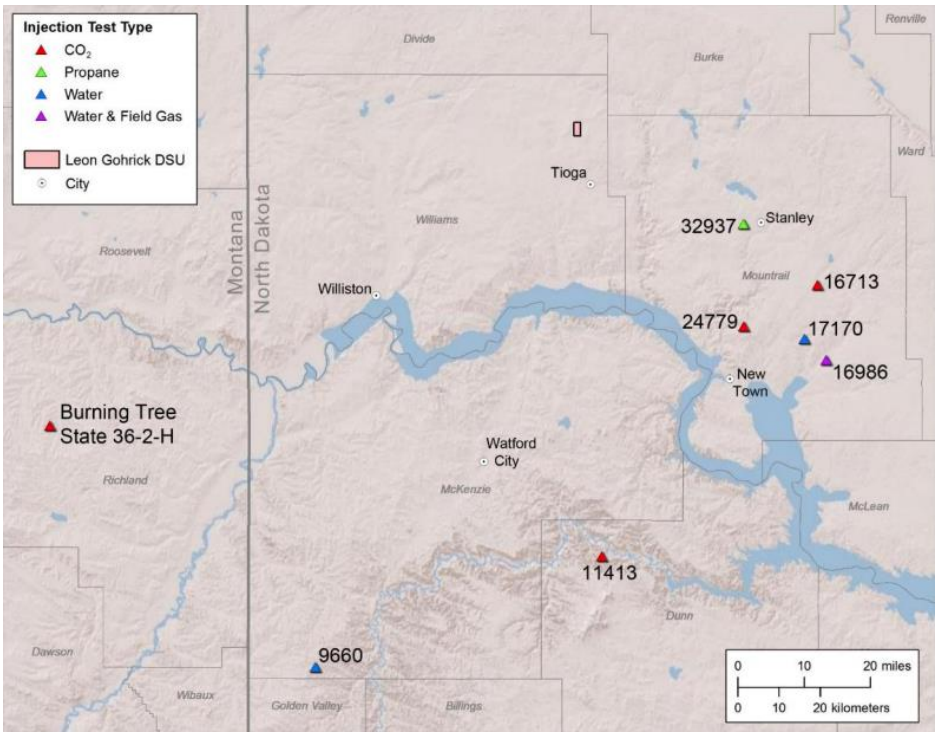


Figure 2.17: Location of Pre-2018 Bakken EOR Tests (Hamling et al., 2021).

The pre-2018 trials consisted of older vintage wells with an early generation of completion design and sparse detailed operational data, so the learnings from these pilots cannot be easily applied to optimize huff-and-puff EOR for recent vintage wells with modern completions.

Although the injectant breakthrough was successfully controlled in the East Nesson project, the natural fracture network across the play is not yet well understood and continues to be variable impacting conformance control, sweep efficiency of the injectant, and the overall success of the EOR process. Also, the natural fracturing intensity varies between counties within ND and MT – Parshall and Sanish area containing more natural fractures than the Elm Coulee area, which

is more dolomitic with slightly higher porosity within Middle Bakken. The differences in geologic makeup and hydrocarbon fluid variability within the same play would require a tailored approach to make the huff-and-puff application effective across different parts of the play.

Table 2.7: Summary of Pilot Tests in the Bakken Play

Well	Operator	State	Test Year	Formation	Injectant	Well & IOR Type	Max. Inj Rate	Max. Pressure (psi)	Avg. Injection Rate	Avg. Pressure (psi)	Cumulative Injected Volume	Notes
#9660	Meridian	ND	1994	Upper Bakken	Freshwater	Horizontal	500 bpd	5000 bhp	200 bpd	3000 bhp	13,260 bbl water	50-day injection, 82-day soak; test unsuccessful
#16713	EOG	ND	2008	Middle Bakken	CO_2	Huff-and-Puff/ Hz well with 6 packers (open hole completion?)	700 bpd	1500 sdp	580 bpd	1000 sdp 6950 bhp	30.7 MMscf CO_2	After 11 days of injection, a breakthrough occurred in an offset well 1-mile away.
Burning Tree	Continental, Enerplus, XTO	MT	2009	Middle Bakken	CO_2	Single-stage horizontal well	3000 Mscfd	1848 bhp	1000 Mscfd	N/A	45 MMscf CO_2	45-day injection, 64-day soak; no incremental oil from public data
#17170	EOG	ND	2012	Middle Bakken	Produced Water	Huff-and-Puff/ Hz well with 7-packers (open hole completion?)	3000 bpd	4000 bhp	1500 bpd	1000 bhp	39,177 bbl water	30-day injection, 10-day soak
#16986	EOG	ND	2014	Middle Bakken	Field gas with some produced water	Horizontal, waterflood for ~2 years before being converted into gas injector	1500 MMscfd	5000 bhp	1500 Mscfd	4500 bhp	88.7 MMscf field gas	With gas injection, produced water was used to manage gas mobility or build system pressure with less gas volume; it appeared to communicate with the production well.
#24779	Whiting	ND	2014	Middle Bakken	CO_2	Unstimulated Vertical Well	31 gpm	3500 bhp	10.5 gpm	3500 bhp	3.4 MMscf CO_2	Test designed to see if unstimulated formation would accept CO_2; planned 10 MMscf of injection – a breakthrough in offset Three Forks well after 3.4 MMscf of CO_2 injection
N/A	N/A	MT	2014	Bakken	Water	Waterflood – 1 injection well	N/A	N/A	1700 bwpd (3 months), then 1000 bwpd (5 months)	N/A	N/A	Offset wells were monitored for rate and pressure responses. The closest offset well (880 ft away) saw a water breakthrough after 1 week but had no impact on the oil rate.
#32937	Hess	ND	2017	Middle Bakken	Propane C_3H_8	Stimulated Vertical Well	227 Mscfd	5500 sdp	105 Mscfd	4000 sdp	19.9 MMscf C_3H_8	Test designed to see if the injection of propane results in incremental recovery from offset wells; offset well shows a sharp increase in production after 2 months.

#11413	XTO	ND	2017	Middle Bakken	CO_2	Unstimulated Vertical Well	12 gpm	9480 bhp	9 gpm	9400 bhp	1.7 MMscf CO_2	4-day injection, 15-day soak; changes in produced hydrocarbon production suggest CO_2 did penetrate the matrix and mobilized oil
#30619, #30620 (Stomping Horse)	Liberty		2018-19	Middle Bakken	Rich Gas (70% CH_4, 20% C_2H_6, 10% C_3H_8)	Cyclic multi-well huff-and-puff	689-703 Mscfd	1000-1200 sdp	950-1080 Mscfd	N/A	160 MMscf across 5 wells	Six different injection cycles were achieved, injectivity was readily established, conformance was maintained within DSU, and pressure buildup occurred but did not achieve MMP (need more working fluid)
East Nesson	Liberty	ND	2021-22	Bakken	Produced Rich Gas, in conjunction with water and surfactants			1300 whp	1.5 MMscfd; 1.3 Mbwpd		46 MMscf rich gas; 40 Mbbls water; 2400 gal surfactant	2-phase fluid injection with 33-day first injection cycle (9/9/21-10/11/21); rapidly switching stacked slug flow injection regime rather than conventional WAG injection; high-pressure buildup occurred and pressure maintained ~4,450 psi maintained with the co-injection (MMP ~2,430 psi); minor gas breakthrough observed at one offset well but controlled & contained by increasing the water slug ratios

bhp: bottom-hole pressure
sdp: surface discharge pressure
whp: well-head pressure

2.2.2 Eagle Ford

Compared to Bakken, higher recoveries from the huff-and-puff EOR process have been reported in Eagle Ford, so more field trials and pilots have been implemented in Eagle Ford. However, unlike the field trials in Bakken, where the information has been publicly shared by the North Dakota Industrial Commission (NDIC) and the Energy & Environmental Research Center (EERC), the information for pilots in Eagle Ford is not publicly available. The industry and academia have relied on Texas Railroad Commission (TRRC) H-12 and H-13 application forms, lease filings, injection/production data reported to the State, GIS images, and aerial surveys to track the implementation of huff-and-puff EOR operations and to identify the onsite compression.

The Eagle Ford has over eleven years of EOR history across 36 pads injecting produced gas. Although EOG Resources first tested the gas injectivity on a single well in the Steen Scruggs unit in November 2012, the actual commercial implementation did not start until 2014 with the Henkaus unit. Within two years, the EOR application was expanded to include the three adjacent units on each side (**Figure 2.18**). The wells have different inter-well spacing and completion designs and saw a 167 to 200 bopd increase compared to the pre-EOR (or base) rate.

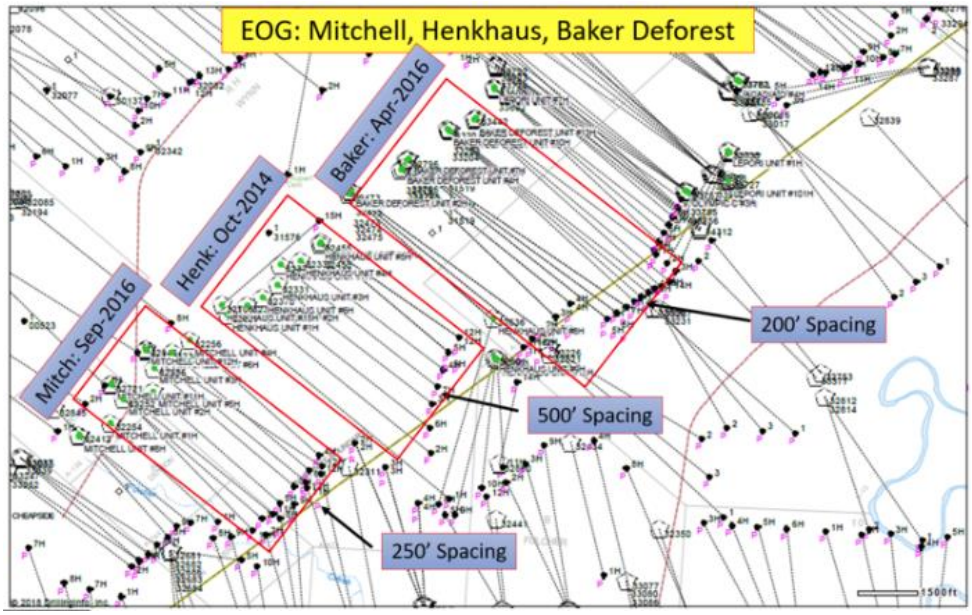


Figure 2.18: First three commercial EOG huff-and-puff EOR units with varying well spacing (Grinestaff et al., 2020).

Since then, the huff-and-puff EOR projects have progressed to injecting into 7-10 wells simultaneously, with recent projects utilizing 4+ compressors, 20-30 wells, and 40-50 MMscfd (Kostarelos, 2019). **Figure 2.19** shows the locator map of the various huff-and-puff pilots and projects across the Eagle Ford. Although these pilots have been focused across the Black Oil and Volatile Oil windows of the play, better recoveries have been observed in the East Volatile Oil areas of Karnes and Gonzales, being deeper (higher pressures) and higher quality oil. **Figure 2.20** shows the average increase in oil EUR per well for 15 units (or leases) with 147 wells. Compared to primary recovery, the average uplift is estimated at ~12 Mbbl per 1000' or 36%. If we look at the 12 EOG units alone, the average uplift is 41%, which is at the lower end of the expected recovery range (30-70%) reported by EOG in 2016 (Leahey et al., 2020). However, Leahey et al. did caveat these estimates that if certain wells in the unit (or lease) were not converted, these estimates are conservative.

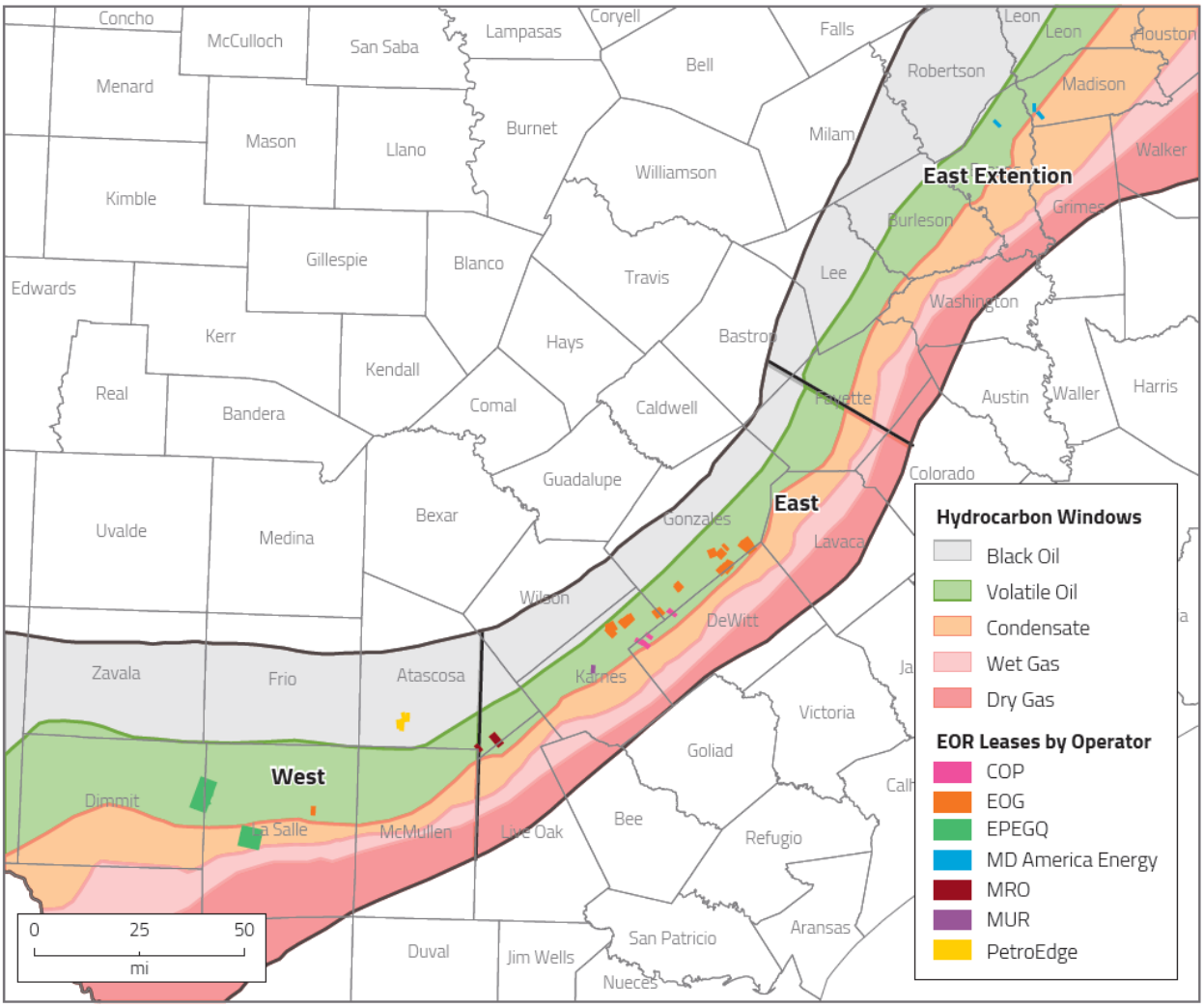


Figure 2.19: Eagle Ford EOR Pilots as of 2020 (Leahey et al., 2020)

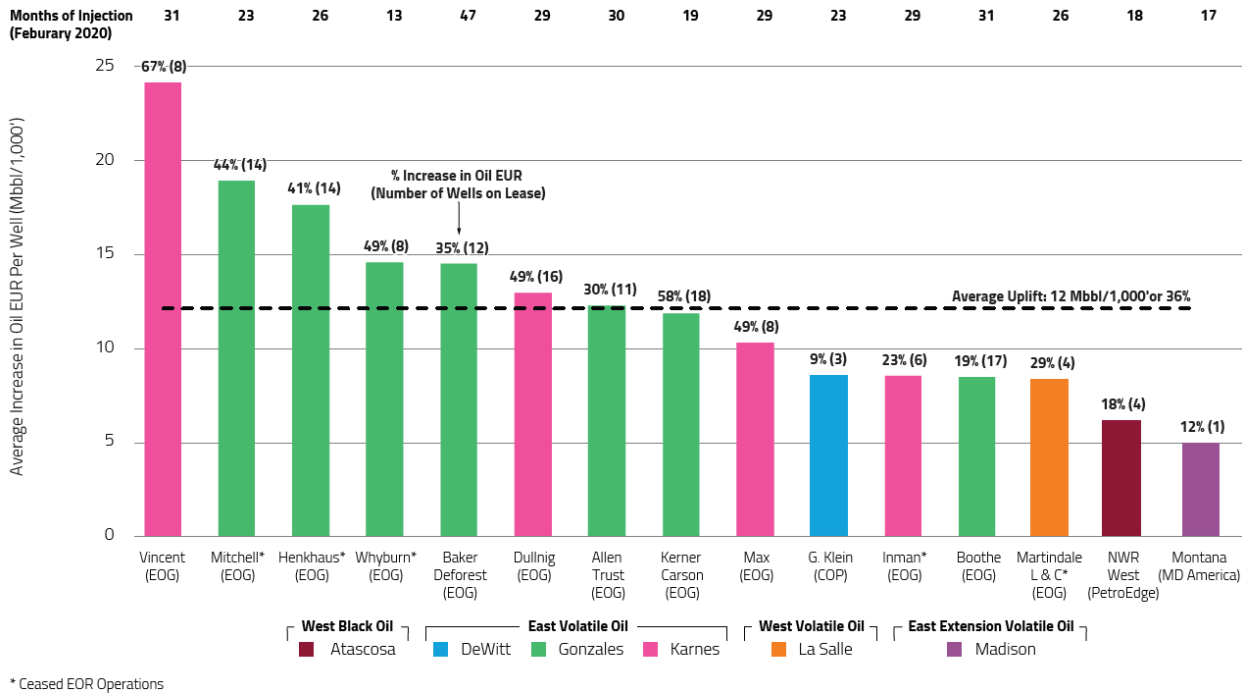


Figure 2.20: Estimated Incremental Oil Recoveries (Leahey et al., 2020).

Table 2.8 summarizes the huff-and-puff gas injection data for seven EOG units within the East Volatile Oil window, where the EOR activity is concentrated. This data shows that the operator had trialed various cycle times for soaking and overall huff-and-puff cycle, and the injected gas rate has averaged ~15 MMscf/d. A few different metrics are included in the table; however, a linear relationship was found between annual injected volumes and oil EUR increase (**Figure 2.21**). **Table 2.9** shows the current status of huff-and-puff pilots in the Eagle Ford as a function of different fluid windows.

There have been several discussions about sourcing the gas (self-sourced from treatment wells vs. gas bought from the surrounding area) in the Eagle Ford, which impacts the working fluid and the overall project economics.

Table 2.8: Huff-and-Puff Data from seven Eagle Ford Pilots in the East Volatile Oil area (Modified from Thoms, 2020)

Unit	Number of wells	Injection Start	Total Days per Cycle (Injection/Soak/Production)	Soak/Injection Cycle Ratio	Production/(Soak + Injection) Cycle Ratio	Cycles per Year	Average Injected Volume (MMcf/d/well)	Annual Injected Volumes Per well (MMcf)	EUR Increase Compared to Pre-EOR (%)
Braune	11	Sep-17	41 (3/6/32)	2.00	3.56	9	14.047	329	N/A
Boothe	17	Jun-17	85 (6/16/63)	2.67	2.86	4	14.981	365	19%
Mitchell	14	Sep-16	67 (12/7/48)	0.58	2.53	5	7.261	474	44%
Allen Trust	11	Aug-17	39 (5/11/23)	2.20	1.44	10	10.059	487	30%
Dullnig	16	Feb-18	66 (4/3/23)	0.75	3.29	5	25.591	510	49%
Kerner Carson	18	Sep-18	30 (5/3/22)	0.60	2.75	6	17.769	532	58%
Vincent	8	Jul-17	52 (7/6/39)	0.86	3.00	7	11.818	567	67%

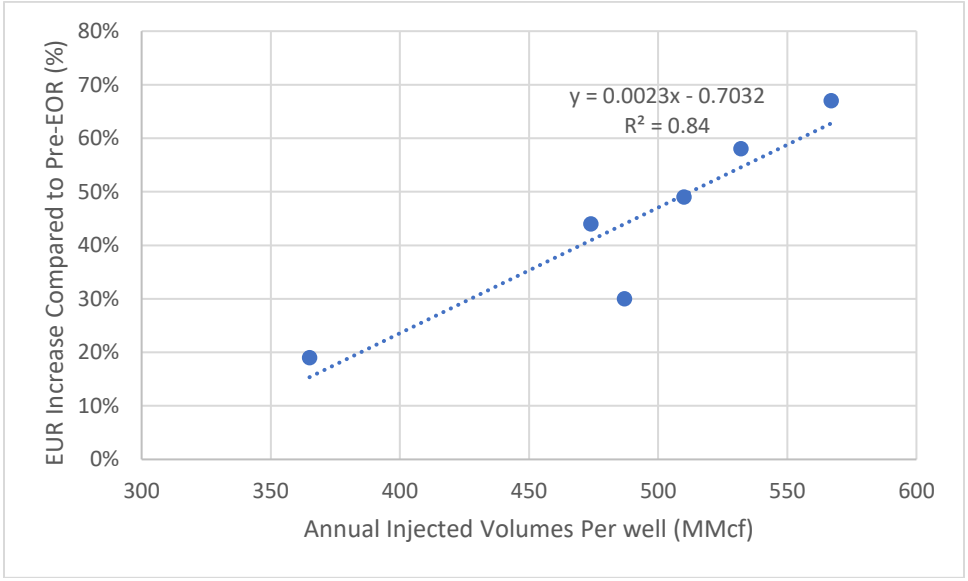


Figure 2.21: EUR increase with huff-and-puff EOR Versus annual injected volumes per well.

Compared to the Bakken, the Eagle Ford formation is believed to be relatively quiet in terms of natural fractures, though some pilots have reported gas leakage to the offset producers. One of the Eagle Ford operators was able to contain the injected gas by re-pressurizing pad edge wells with water injection, especially during the injection cycles, which has resulted in ~10% additional incremental recovery (Kerr et al., 2020).

Although the amount of gas injected is one of the primary costs impacting the overall economics, the optimal injection rate is still unknown. However, some modeling studies (Rogers et al., 2020) have shown that higher injection rates could result in better sweep efficiency and higher incremental recoveries.

Table 2.9: Eagle Ford Huff-and-Puff Fluid Type and GOR Targets based on Current Projects (modified from Kostarelos, 2019)

Region	GOR Range (scf/STB)	Sp. Gravity (°API)	Fluid Type	Huff-and-Puff Status
1	0 – 100	10.0 – 30.0	Oil	–
2	100 – 500	30.0 – 41.4	Oil	**Non Proven**
3	500 – 1,000	41.4 – 45.8	Oil	**Pilot**
4	1,000 – 1,500	45.8 – 48.2	Oil	**Proven**
5	1,500 – 2,000	48.2 – 49.8	Oil	
6	2,000 – 3,000	49.8 – 52.0	Volatile Oil	
7	3,000 – 4,000	52.0 – 53.5	Rich Condensate	**Pilot**
8	4,000 – 5,000	53.5 – 54.6	Rich Condensate	
9	5,000 – 8,000	54.6 – 56.7	Condensate	**Not Proven**
10	8,000 – 15,000	56.7 – 59.4	Condensate	
11	15,000 – 50,000	59.4 – 63.6	Condensate	–
12	>50,000	>63.3	Dry Gas	–

A few technical papers have recently been published in which the operators have tried to history match (via numerical simulation) the pilot performance. These initial papers have highlighted the various inputs that had to be tweaked to get a decent match to the actual post-EOR

data. Nevertheless, the history-matching process results in a non-unique solution, and the complete physics governing the recoveries is still not fully known.

As mentioned, the pilots in the Eagle Ford Shale seem to have responded the best to huff-and-puff EOR, with EOG claiming incremental recoveries expected to be 30-70% of the primary recovery (**Figure 1.1**). The injectivity of the gas has not been a problem; however, the recoveries reported after three to five years of huff-and-puff have been at the low end of this expected range at 10-40% (Enverus Prism, 2024). The range has also been found to be a function of the spatial location of the pilot within the Eagle Ford, with pilots in the NE part of the play showing better recoveries.

2.3 Learnings & Issues Realized From the Field Trials

The miscible gas Huff-and-Puff EOR trials have had varying degrees of success in the shale plays. The production response from the Eagle Ford wells has been significantly better than those observed in the recent Bakken trials, resulting in more pilots in the volatile oil window of Eagle Ford. The main learnings from the field trials are:

1) Gas injectivity into tight shale reservoirs is not a problem. However, pressure buildup has been an issue in getting the reservoir pressure above MMP to achieve miscibility. This could be associated with the issue of containment of the injected gas within the DSU.
2) The recovery mechanism(s) controlling the Huff-and-Puff process are not well understood. Although laboratory experiments have indicated diffusion as the primary mechanism, it has been debated that the actual recovery in the field possibly comes from the combination of diffusion and advection processes.

3) The fracture network, consisting of hydraulic and natural fractures, seems to have benefits and disadvantages for the Huff-and-Puff process. At one end, the fracture network appears to help transport the injected gas further within the tight shale matrix. However, complex fracture networks have also been attributed to the lack of containment of the injected gas within the DSU, resulting in early breakthroughs into offset wells.

   Robust reservoir characterization is critical to understanding and mapping the fracture network, which can be used to create realistic geocellular models, run more realistic reservoir simulations, and predict more accurate Huff-and-Puff recovery. A lack of understanding of the major fractures and features could result in an early breakthrough of injected gas, ultimately leading to cycling gas from treatment to offset location(s).

4) Accessibility (or sweep efficiency) of the injectant within the shale matrix is believed to be less than the laboratory experiments and simulation models predicted. If the Huff-and-Puff recovery is driven by diffusion, extended soaking times may be needed as diffusion is relatively slow compared to advection. Additionally, no tools currently exist that can track the penetration of the injected gas into the shale matrix at the field scale.

5) The importance of accurate fluid characterization of the remaining oil and understanding the two-phase phenomenon during Huff-and-Puff cannot be underscored.

6) Cycle time optimization – one of the biggest challenges in field trials has been to define the optimum duration of the injection, soaking, and production cycles. Operators have tried several trial-and-error approaches for cycle time optimization and found that small volumes of gas injection will do very little in increasing oil recoveries. Conversely, large volumes of gas are needed for the process to generate additional recoveries. As shown in Figure **2.21**, a linear relationship was found between annual injected volumes and oil EUR

increase from the Huff-and-Puff application in Eagle Ford, with yearly volumes being a function of both the cycle times and the gas injection rate.

7) Interwell communication during primary recovery can be due to long natural fractures with high conductivity or connected SRVs (Stimulated Reservoir Volume) generated by the hydraulic fracture stimulation treatments. These fractures or connected SRVs can prevent good pressure buildup in the reservoir during the huff-and-puff EOR process and reduce the miscibility of the injected gas with the remaining oil, thereby reducing sweep efficiency and effectiveness of the overall EOR process.

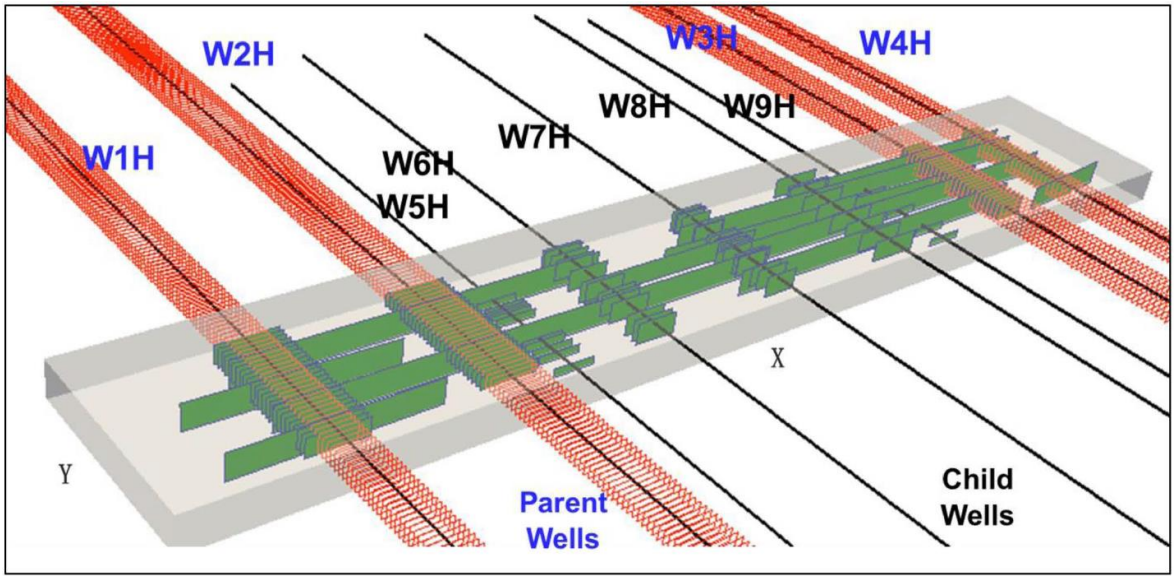


Figure 2.22: Illustration of an Eagle Ford EOR Project that experienced significant interwell communication, with four parent and five child wells (Torres et al., 2019).

Figure 2.22 illustrates an EOR project in the black oil window of the Eagle Ford shale operated by EP Energy (Torres et al., 2019). A nine-well sector model, consisting of four parent wells and five child wells, was simulated using the EDFM (Embedded Discrete Fracture Model) technique to understand the impact of interwell interference on the effectiveness of the huff-and-puff application. The study demonstrated the need to consider pressure containment strategies

when designing a pilot, as laboratory studies do not account for complex fracture networks and the interwell connectivity encountered in the field. For the Huff-and-Puff process to be effective and economically viable, the reservoir characteristics must allow the operator to pressure up the depleted reservoir and contain the injected gas within the DSU for an adequate period to enable the gas to mix with the remaining oil. In the modeled part of the field, pressure leak occurrence was inevitable due to interwell communication. It required the operator to try alternate pressure containment strategies, such as converting two low-profit producing wellbores into water injection wells to create a barrier.

Several factors affect the efficacy of the miscible gas huff-and-puff EOR process in the shale reservoirs and need to be evaluated during the feasibility study. Some of the questions currently being asked by the operators/industry are:

1) Why is the incremental oil recovery from the huff-and-puff process limited? Can miscible gas injection be further optimized to improve recovery? Could there be a better injectant/solvent that is less mobile than gas to mitigate the containment issues?
2) Is the soaking phase really necessary? Operators tend to move quickly with the soak period between the “huff” and “puff” cycles because shutting a well is considered too costly with a loss in production. Yet, using theoretical calculations, the researchers have found that soaking times could have massive recovery gains, even when accounting for downtime.
3) Do wells with good primary recovery become better candidates for huff-and-puff EOR application?

Chapter 3

Upscaling Laboratory Results to Field Scale

As covered in previous chapters, after three to five years of huff-and-puff EOR implementation, the recovery from the field pilots has been on the low end of the recovery range expected from the experimental and simulation studies. This chapter includes formulating a mathematical model using classical equations to mimic the cyclic huff-and-puff miscible process and upscale the laboratory results to a field scale.

3.1 Fluid Flow in Porous Media

In general, the fluid flow (or transport) in porous media occurs through advection (Darcy's law) and diffusion (Fick's law) processes. The mass flux of a substance in a particular direction is defined as the quantity of that substance moving across a unit area of porous media perpendicular to the flow direction and is given by:

$$\boldsymbol{Flux\ q} = \frac{\boldsymbol{amount\ that\ passes\ through\ cross-section}}{\boldsymbol{cross-sectional\ area \times time\ duration}} = \frac{\boldsymbol{m}}{\boldsymbol{A\Delta t}} = \boldsymbol{cu + j} \qquad \textbf{…Equation 3.1}$$

where, the terms 'cu' and 'j' represent the advective and diffusive flux, respectively. The advection describes the transport of a substance through the (macroscopic) bulk flow of fluid. In contrast, diffusion refers to the net movement of particles due to concentration differences (movement from high concentration to low concentration) through random molecular motions. These two mass transfer mechanisms are a function of the Peclet number. The Peclet number (Pe) is a dimensionless number representing the ratio of the advection rate to the diffusion rate in an advection-diffusion transport system (Rapp, 2017).

$$Pe = \frac{Advection\ transport\ rate}{Diffusion\ transport\ rate} = \frac{uL_c}{D} \qquad \textbf{...Equation 3.2}$$

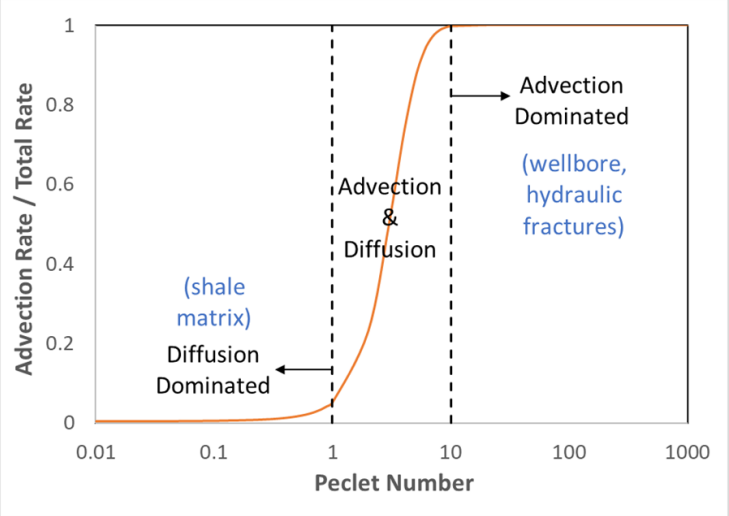


Figure 3.1: Transport mechanisms as a function of Peclet number

The Pe number is less than one in diffusion-dominated regimes, whereas the Pe number greater than one represents advection-dominated systems (**Figure 3.1**). **The Pe number is close to zero in the ultra-low permeability shale matrix, and transport by advection is often neglected based on the Peclet number criterion.** Cronin et al. (2019) illustrated that the Pe value for the Eagle Ford oil matrix (Pe ≈ 0.02) is four orders of magnitude smaller than conventional oil reservoirs (Pe ≈ 30), so mass transfer by advection is negligible compared to diffusion in the shale matrix. Several lab experiments over the past decade have also shown diffusion to be the dominant transport mechanism in shale reservoirs (Kovscek et al., 2008; Vega et al., 2010; Hawthorne et al., 2013; Tovar et al., 2014; Alharthy et al., 2015; Fu et al., 2019).

During the huff-and-puff application, the path of the injected fluid from the surface (wellhead) to the shale matrix and the associated mass transport mechanisms can be characterized as follows:

- Wellbore: Advection-dominated due to high conductivity/turbulent flow within the tubular.
- Fracture network (primary and secondary fractures, both natural and hydraulically created): Advection-dominated due to the high conductivity of the propping agents and/or creation of a proppant arch above the proppant bed (Warpinski, 2009).
- Ultra-tight shale matrix: Diffusion-dominated due to Peclet numbers much smaller than 1.

The recovery of remaining oil from the shale matrix using miscible gas huff-and-puff is not an advection-driven displacement process but a diffusion-driven mixing process. During the injection phase, the mechanisms occurring include (1) advection in the wellbore and the fracture network due to pressure gradient across the highly conductive flow path, which results in the injected gas filling up the fractures, and (2) diffusion from the hydraulic/natural fracture face into the shale matrix due to concentration difference. The pressure difference between the fractures and the matrix initially drives the gas into the matrix, and then the miscible front moves into the matrix due to diffusion. Diffusion is a temperature-dependent process, driven by concentration and pressure gradients along the path traveled.

During the soaking phase, with the well shut in for some time, there is minimal transport due to advection. However, diffusion from the fracture network to the shale matrix continues due to concentration difference (driving force). Based on Fick's first law, the velocity of the front during diffusion is a function of concentration difference, the diffusion coefficient, and the pore-throat of the matrix (small length). Unlike advection, where the front moves as a function of time (as described by Buckley Leverett equation for immiscible displacement), the front moves as a function of √time during the diffusion process (as defined by Lucas-Washburn equation, which

relates **penetration length 'L_p'** of fluid through porous structure exhibiting diffusive behavior as $L_P = \sqrt{Dt}$). During the injection and soaking phases, the solvent (i.e., the injected gas) diffuses from the fractures into the matrix. In contrast, the remaining oil simultaneously diffuses into the fractures, and the process is referred to as the **counter-current diffusion process**. During the production phase, the well is flowed back, and the **co-current diffusion process** from the matrix into the fracture network results in the recovery of the remaining oil.

The pressure required to achieve the miscibility of the injected gas with the remaining oil during the diffusion process is referred to as the minimum miscibility pressure (MMP), and it is a function of the composition of the injected gas and remaining oil in the matrix. The miscibility of injected gas with the remaining oil results in viscosity reduction as the oil swells and is pushed out of the matrix into the fracture network. **The MMP measurement pertinent to the huff-and-puff process is the First-Contact Miscible (FCM) MMP measured by the swelling test.** The FCM MMP is usually over 1,000 psi higher than the Multiple-Contact Miscible (MCM) MMP measured by a slim tube test for displacement processes (Mydland et al., 2020; Carlsen et al., 2020). The FCM remains important because the effective diffusion coefficients are a function of the amounts and compositions of the phases that form by mixing the various fluids components (Cronin et al., 2019). The impact of phase behavior as a huff-and-puff recovery mechanism is not the primary focus of this part of the research, and the **mathematical model developed is based on the transport of single-phase, single-component injectant into the hydraulically fractured shale reservoirs assuming the FCM process to achieve miscibility.**

3.2 Diffusion in Porous Media and Effective Diffusion Coefficients

Mass diffusion is the process by which matter is transported from one part of a system to another due to random molecular motions. This process was first recognized by Adolph Fick (1855), who mathematically defined diffusion in isotropic substances as the rate of transfer of diffusing substance through unit area of cross-section being proportional to the concentration gradient measured normal to the cross-section:

$$\boldsymbol{Flux\ q_{diffusion} = -D\frac{dC}{dx}} \qquad \textbf{…Equation 3.3}$$

Equation 3.3 is also called Fick's First Law of Diffusion. This relation is analogous to Ohm's Law (for a steady flow of electric current) and Fourier's Law (for heat conduction). The negative sign in **Equation 3.3** arises because diffusion occurs in the direction opposite to that of increasing concentration (driving force).

Compared to the bulk molecular diffusion, diffusion of solvent (i.e., injected gas) in porous media is hindered due to the tortuous nature of the pores and reduced cross-section area with the heterogeneous pore size distribution. With diffusion being the primary recovery mechanism for the huff-and-puff process, accurately estimating diffusion coefficients is essential to understanding the mass transfer rate. Grathwohl (2012) described a method to account for tortuosity, pore constrictivity, absorption, and surface diffusion into an effective diffusion coefficient per phase 'D_e':

$$\boldsymbol{D_e = \frac{D\varepsilon_t\delta}{\tau_f}} \qquad \textbf{…Equation 3.4}$$

- Tortuosity τ_f (dimensionless): is an intrinsic property of a porous medium and is defined as the ratio of actual flow path length to the straight distance between the ends. For homogenous isotropic media, the tortuosity is a function of porosity, with values between 1 and $\sqrt{3}$. However, for most grain packing arrangements, the tortuosity is closer to 1.15 (van Brakel & Heertjes, 1974).

These measurements are usually based on straight capillary tubes randomly distributed in three orientations. In the tight unconventionals, especially the shale, the pore morphology is far from those of these ideal smooth straight tubes. For tight sand formations such as Mesaverde, with pore throats larger than 10 nm, the tortuosity values calculated by Ziarani and Aguilera (2012) ranged primarily between 1 and 8. Additional studies by Ziarani et al. (2020) using SEM images and MICP data have shown the tortuosity to range between 7 and 40. For shales, Ziarani et al. (2020) have reported the tortuosity values to be significantly higher, ranging from orders of 10 to as high as 100. Backeberg et al. (2017) studied the tortuosity in shale using X-ray computational tomography (CT). They reported an average tortuosity factor of 25 in the direction parallel to the sedimentary lamination and one to two orders of magnitude higher perpendicular to the lamination.

Since tortuosity is challenging to measure directly, correlations are often used to obtain a first approximation. Tortuosity can be expressed using the empirical relation proposed by Waxman and Smits:

$$\boldsymbol{\tau_f = \emptyset_m F = a\emptyset_m^{1-m}} \quad \text{…Equation 3.5}$$

- Pore Constrictivity δ (dimensionless): is the ratio of the diameter of the diffusing particle to the pore diameter. Its value is always less than one and can be estimated using the various empirical relations published in the literature. For homogeneous isotropic media with perfectly round grain packing, the pore constrictivity is calculated to be about 0.75 (van Brakel & Heertjes, 1974). The constrictivity is defined not for a single pore but as the parameter of the entire pore space considered within the porous medium. Additionally, it depends on the influence of the pore walls on the fluid occupying the pores.
- Effective transport-through porosity ε_t (dimensionless) accounts for the reduced cross-sectional area available for diffusion in the porous media. Due to the wide range of pore size distribution (heterogeneous pores) and the presence of non-connected pores, its value can be smaller than the porosity of the matrix.

Fu et al. (2019) pointed out that, besides effective diffusion coefficients changing for different cycles with changing hydrocarbon composition, the effective diffusion coefficients also vary across the different litho-facies and rock types contacted by the treatment well during primary depletion. The "history-matched" oil diffusion coefficients were reported to be in the range of ten to the power of negative seven but varied based on the changing composition of the remaining oil. The effective diffusion coefficients of gas components were five to ten times larger than that of oil components. In contrast, Cronin et al. (2019) computed the effective diffusion coefficients in the range of ten to the power of negative eleven by utilizing the Sigmund-Wilke correlation and incorporating tortuosity effects (**Table 3.1**).

Table 3.1: Black Oil Composition from Eagle Ford (Orangi et al., 2011) and Effective Diffusion Coefficients Calculated by Incorporating Tortuosity Effects (Cronin et al., 2019)

Component	z_i	$D_i = D_{ii}/\tau$ (10^{-5} ft^2/D)	$D_i = D_{ii}/\tau$ (10^{-11} m^2/s)
N_2	0.00073	4.8606	5.2264
CO_2	0.01282	3.4219	3.6795
CH_4	0.31231	5.8116	6.2491
C_2H_6	0.04314	3.1092	3.3433
C_3	0.04148	2.0378	2.1911
i-C_4	0.01350	1.4912	1.6034
n-C_4	0.03382	1.4867	1.5986
i-C_5	0.01805	1.1545	1.2414
n-C_5	0.02141	1.1488	1.2353
n-C_6	0.04623	0.92590	0.99559
C_{7+}	0.16297	0.68147	0.73276
C_{11+}	0.12004	0.42799	0.46020
C_{15+}	0.10044	0.28796	0.30963
C_{20+}	0.07306	0.14273	0.15347

Although separate effective diffusion coefficients are used for oil and gas phases in commercial reservoir simulators, they are assumed to be constant values for each phase (Cronin, 2020; Ghasemi et al., 2017). Since the diffusion coefficient varies by component and with changing composition, the net effective diffusion coefficient is expected to change with each huff-and-puff cycle spatially and temporally. During reservoir simulation, the diffusion coefficients are usually set as tuning parameters and assigned a wide range (two to four orders of magnitude) during automated history matching to observe how sensitive the results are for a particular constant diffusion coefficient. However, with the history matching process resulting in a non-unique solution, using a constant diffusion coefficient may not represent the diffusion process accurately. It may lead to inaccurate prediction of the diffusion front and the resultant hydrocarbon recovery.

3.3 Mathematical Model Formulation

This section covers the mathematical model developed to emulate the huff-and-puff EOR process in shale reservoirs using miscible gas. The mass flux for a one-dimensional single-phase model is calculated using the classical analytic equations for mass and heat diffusion. The process

is assumed to be diffusion-dominated based on the Peclet number criterion in the tight shale matrix. The injection and soaking phases are modeled as counter-current diffusion processes, while the production phase represents a co-current diffusion process.

Consider the one-dimensional diffusion of gas injected in a hydraulically fractured shale well during gas huff-and-puff EOR, as shown in **Figure 3.2**. The base case consists of a hydraulically fractured well within the matrix with no secondary fractures/natural fractures. Assuming a no-flow boundary (or line of symmetry) in the middle of two transverse fractures, the region of investigation considered here is from the hydraulic fracture face (x=0) to the no-flow boundary (x=L), with L representing half of the fracture spacing between two adjacent primary fractures. With typical cluster spacing of 25-60 ft (Evans et al., 2018) used in the Eagle Ford huff-and-puff pilots to date, developed between 2010 and 2018 (Enverus Prism, 2024), L of ~32.8 ft (10 m) was assumed for the base case. As the injected gas moves in a positive x direction (from x=0 to x=L), the region can be considered a semi-infinite medium to model the process analytically. Existing analytical solutions for heat and mass transfer is used to simulate the solvent (i.e., injected gas) influx from the fractures into the matrix during the huff and soaking periods (a counter-current diffusion process) and solvent-with-oil flux from matrix to fractures during the puff period (a co-current diffusion process). For the injection phase, the geometry of the hydraulic fracture face is assumed to be a plane sheet, and Fick's second law of diffusion is solved for the chosen initial and boundary conditions. The matrix is considered a slab placed inside a limited volume of well-stirred/well-mixed fluid for the soaking and production phases, and heat diffusion equations are solved for non-uniform initial conditions created at the end of the injection and soaking phases, respectively.

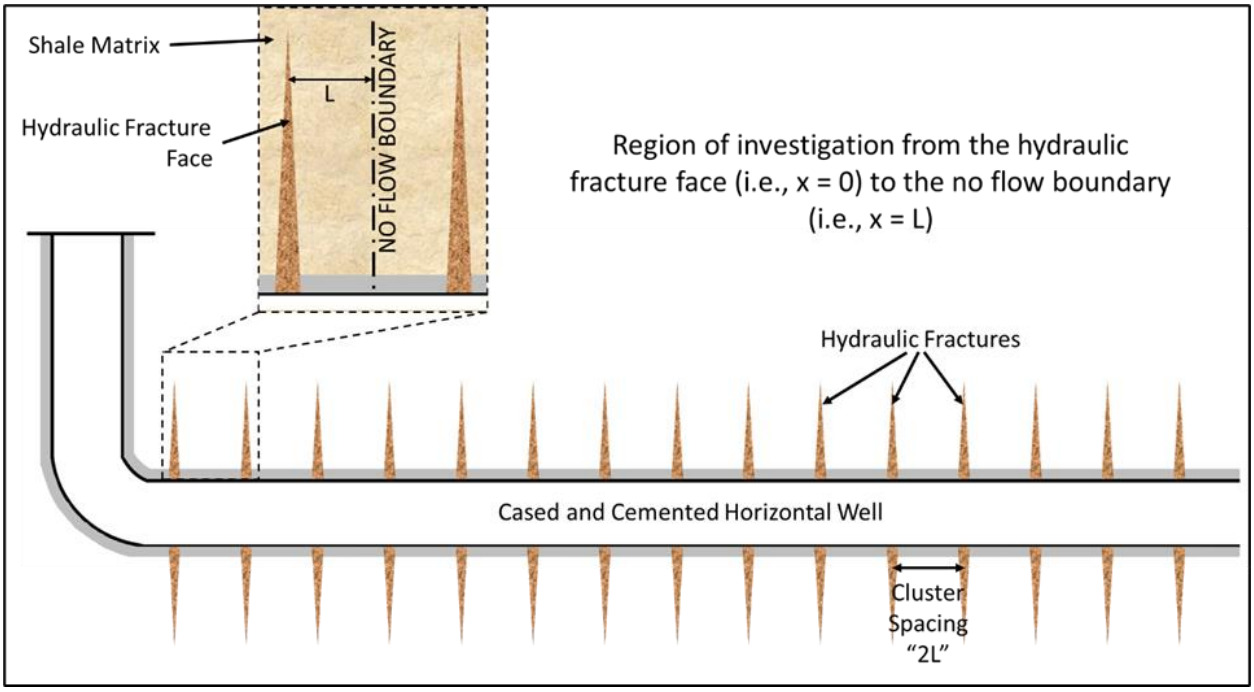


Figure 3.2: Schematic of a hydraulically fractured horizontal well in a shale reservoir; the inset shows the region of investigation from the hydraulic fracture face to the no-flow boundary.

The key modeling assumptions include:

- The matrix block is assumed to be **homogenous** and **isotropic**, with no natural fractures or damaged region between the hydraulic fractures and the matrix (for the **base model**).
- The fluid in the wellbore and fractures is assumed to be well-stirred/well-mixed such that the concentration gradients are negligible, and any pressure gradients in the region of investigation are ignored.
- The existing analytical solutions assume a **1-D flow in the x-direction**.
- The hydrocarbon in the matrix is considered **single-phase** and under **isothermal conditions**. The model predicts the movement of the injectant in the x-direction to estimate the penetrated length.

- The analytical solution is based on **a single component**, assuming that miscibility has already occurred under FCM conditions.

- **Mass transfer in the matrix occurs by diffusion alone. Based on the Peclet number criterion, the advective transport in the matrix is so slow that it is neglected.**

- The diffusion coefficient is an **effective value**, and for this formulation, is assumed to be constant and does not change with changing pressure and fluid composition. However, the runs are made using a range of D_e values to capture the dynamic nature of the diffusion coefficient during the huff-and-puff process.

3.3.1 Basic Formulation

According to Fick's first law of diffusion, for diffusion in an isotropic medium, the rate of transfer of diffusing substance through unit area is proportional to the concentration gradient measured normal to the section:

$$\boldsymbol{F = -D\frac{\partial C}{\partial x}} \quad \textbf{(along the x-axis)} \qquad \textbf{….Equation 3.6}$$

The negative sign in **Equation 3.6** arises because diffusion occurs in the direction opposite to that of increasing concentration.

To derive the fundamental differential equation of diffusion in an isotropic medium, let us consider an element of volume as a cuboid whose sides are parallel to the coordinate axes and are of lengths 2 dx, 2 dy, 2 dz (**Figure 3.3**). Let the center of the element be at P(x, y, z), where the concentration of the diffusing substance is C. Let ABCD and A'B'C'D' be the faces perpendicular to the x-axis.

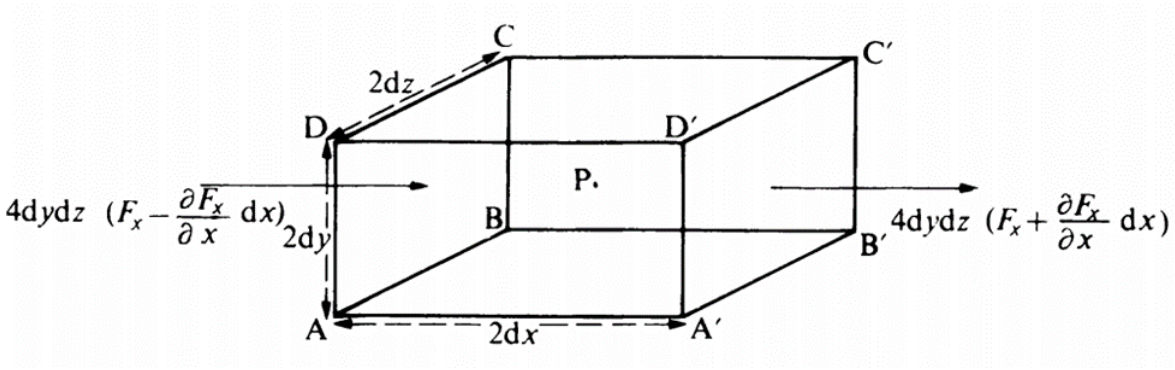


Figure 3.3: Element of volume as a cuboid (Crank, 1975).

The rate at which diffusing substance enters the element through the face ABCD in the plane x – dx is given by:

$$4\,dy\,dz\left(F_x - \frac{\partial F_x}{\partial x}dx\right)$$

Similarly, the rate of loss of diffusing substance through the face A'B'C'D' is given by:

$$4\,dy\,dz\left(F_x + \frac{\partial F_x}{\partial x}dx\right)$$

The contribution to the rate of increase of diffusing substance in the element from these two faces is equal to:

Diffusing substance entering through ABCD – Loss of diffusing substance through A'B'C'D'

$$\left[4\,dy\,dz\left(F_x - \frac{\partial F_x}{\partial x}dx\right)\right] - \left[4\,dy\,dz\left(F_x + \frac{\partial F_x}{\partial x}dx\right)\right]$$

$$\left[4\,dy\,dz\left(-2\frac{\partial F_x}{\partial x}dx\right)\right]$$

$$-8dx\,dy\,dz\,\frac{\partial F_x}{\partial x}$$

Similarly, for the other faces:

$$-8\,dx\,dy\,dz\,\frac{\partial F_y}{\partial y} \quad \text{and} \quad -8\,dx\,dy\,dz\,\frac{\partial F_z}{\partial z}$$

But the rate at which the amount of diffusing substance in the element increases is also given by

$$8\,dx\,dy\,dz\,\frac{\partial C}{\partial t}$$

Therefore,

$$8\,dx\,dy\,dz\,\frac{\partial C}{\partial t} = -8\,dx\,dy\,dz\,\frac{\partial F_x}{\partial x} - 8\,dx\,dy\,dz\,\frac{\partial F_y}{\partial y} - 8\,dx\,dy\,dz\,\frac{\partial F_z}{\partial z}$$

$$\boldsymbol{\frac{\partial C}{\partial t} + \frac{\partial F_x}{\partial x} + \frac{\partial F_y}{\partial y} + \frac{\partial F_z}{\partial z} = 0} \qquad \textbf{….Equation 3.7}$$

If the diffusion coefficient D is constant, then from **Equation 3.6**

$$\frac{\partial F_x}{\partial x} = -D\frac{\partial^2 C}{\partial x^2}$$

$$\frac{\partial F_y}{\partial y} = -D\frac{\partial^2 C}{\partial y^2}$$

$$\frac{\partial F_z}{\partial z} = -D\frac{\partial^2 C}{\partial z^2}$$

$$\boldsymbol{\frac{\partial C}{\partial t} = D\left(\frac{\partial^2 C}{\partial x^2} + \frac{\partial^2 C}{\partial y^2} + \frac{\partial^2 C}{\partial z^2}\right)} \qquad \textbf{…Equation 3.8}$$

Equation 3.8 can be simplified by assuming the diffusion is one-dimensional, i.e., there is a concentration gradient only along the x-axis.

$$\boldsymbol{\frac{\partial C}{\partial t} = D\frac{\partial^2 C}{\partial x^2}} \qquad \textbf{…Equation 3.9}$$

which is referred to as Fick's second law of diffusion, with diffusion in one dimension and constant D.

If we initially assume the medium to be infinite, i.e., $-\infty < x < +\infty$, and the substance to spread gradually on both sides. Anticipating such similarity in the solution, we can write:

$$c(x,t) = t^{-\alpha}F(\eta) \quad with\, \eta = \frac{x^2}{4Dt}$$

where,

$t^{-\alpha}$ = 'size factor,' representing the temporal decay of the maximum concentration values (at x = 0), and the dimensionless exponent α is expected to be positive.

$F(\eta)$ = 'shape factor' giving a similar curve profile. This function has a 'stretched coordinate' so that the same value of $F(\eta)$ is obtained for increasing values of x as time goes on (constant x^2/t). This is to take into account the spreading of the substance. Exponent 2 of x is an educated guess that renders the functional dependency compatible with the equation. This choice is rooted in that t appears as a first-order derivative while x enters the equation as a second-order derivative. The factor D in the denominator of η is there to make the ratio dimensionless; η, therefore, has no units, and its function $F(\eta)$ takes on a universal character. Finally, factor 4 is introduced for pure mathematical convenience.

Next, we calculate the derivatives of c needed to solve the diffusion equation:

$$\frac{\partial c}{\partial t} = -\alpha t^{-\alpha-1}F(\eta) + t^{-\alpha}\frac{dF}{d\eta}\frac{\partial \eta}{\partial t} = -\alpha t^{-\alpha-1}F(\eta) - \eta t^{-\alpha-1}\frac{dF}{d\eta}$$

$$\frac{\partial c}{\partial x} = t^{-\alpha}\frac{dF}{d\eta}\frac{\partial \eta}{\partial x} = \frac{x t^{-\alpha-1}}{2D}\frac{dF}{d\eta}$$

$$\frac{\partial^2 c}{\partial x^2} = \frac{\partial}{\partial x}\left(\frac{\partial c}{\partial x}\right) = \frac{t^{-\alpha-1}}{2D}\frac{dF}{d\eta} + \frac{xt^{-\alpha-1}}{2D}\frac{d^2F}{d\eta^2}\frac{\partial \eta}{\partial x} = \frac{t^{-\alpha-1}}{2D}\frac{dF}{d\eta} + \frac{t^{-\alpha-1}}{D}\eta\frac{d^2F}{d\eta^2}$$

Substituting $\frac{\partial c}{\partial t}$ and $\frac{\partial^2 c}{\partial x^2}$ in the diffusion equation yields:

$$-\alpha t^{-\alpha-1}F(\eta) - \eta t^{-\alpha-1}\frac{dF}{d\eta} = D\left(\frac{t^{-\alpha-1}}{2D}\frac{dF}{d\eta} + \frac{t^{-\alpha-1}}{D}\eta\frac{d^2F}{d\eta^2}\right)$$

$$-\alpha t^{-\alpha-1}F(\eta) - \eta t^{-\alpha-1}\frac{dF}{d\eta} = \frac{t^{-\alpha-1}}{2}\frac{dF}{d\eta} + \eta t^{-\alpha-1}\frac{d^2F}{d\eta^2}$$

The time factors cancel out, and the partial differential equation is reduced to an ordinary differential equation, with variable η:

$$-\alpha F(\eta) - \eta\frac{dF}{d\eta} = \frac{1}{2}\frac{dF}{d\eta} + \eta\frac{d^2F}{d\eta^2}$$

$$\eta\frac{d}{d\eta}\left(\frac{dF}{d\eta} + F\right) + \frac{1}{2}\left(\frac{dF}{d\eta} + 2\alpha F\right) = 0$$

Since the exponent α is still free, we will now choose it so that two groups in the parentheses are identical, i.e., $\alpha = \frac{1}{2}$. A possible solution is one that obeys

$$\frac{dF}{d\eta} + F(\eta) = 0$$

which is:

$$F(\eta) = Ae^{-\eta}$$

where, A is an arbitrary constant of integration.

Putting all the pieces together, we arrive at the following solution:

$$\boldsymbol{c(x,t)\ or\ C = At^{-\frac{1}{2}}exp\left(-\frac{x^2}{4Dt}\right)} \qquad \textbf{…Equation 3.10}$$

This expression is symmetrical with respect to x = 0. It tends to zero as x approaches infinity positively or negatively for t > 0. For t = 0, it vanishes everywhere except at x = 0, where it becomes infinite.

The total amount of substance M diffusing in a cylinder of infinite length and unit cross-section is given by:

$$M = \int_{-\infty}^{+\infty} C\, dx$$

and if the concentration distribution is that of **Equation 3.10**, we see:

$$\frac{x^2}{4Dt} = \zeta^2 \quad and \quad dx = \sqrt{4Dt}\, d\zeta$$

that:

$$M = A\sqrt{4Dt} \int_{-\infty}^{+\infty} \exp(-\zeta^2)\, d\zeta$$

Since $\int_{-\infty}^{+\infty} \exp(-\zeta^2)\, d\zeta = \sqrt{\pi}$

$$M = A\sqrt{4\pi Dt}$$

$$\rightarrow A = \frac{M}{\sqrt{4\pi Dt}}$$

Substituting this value of A in , we obtain:

$$\boldsymbol{C = \frac{M}{\sqrt{4\pi Dt}}\, exp\left(-\frac{x^2}{4Dt}\right)} \qquad \textbf{…Equation 3.11}$$

which is the solution that describes the spreading by diffusion of an amount of substance M deposited at time t=0 in the plane x=0. Figure **3.4** shows typical distributions at three successive times.

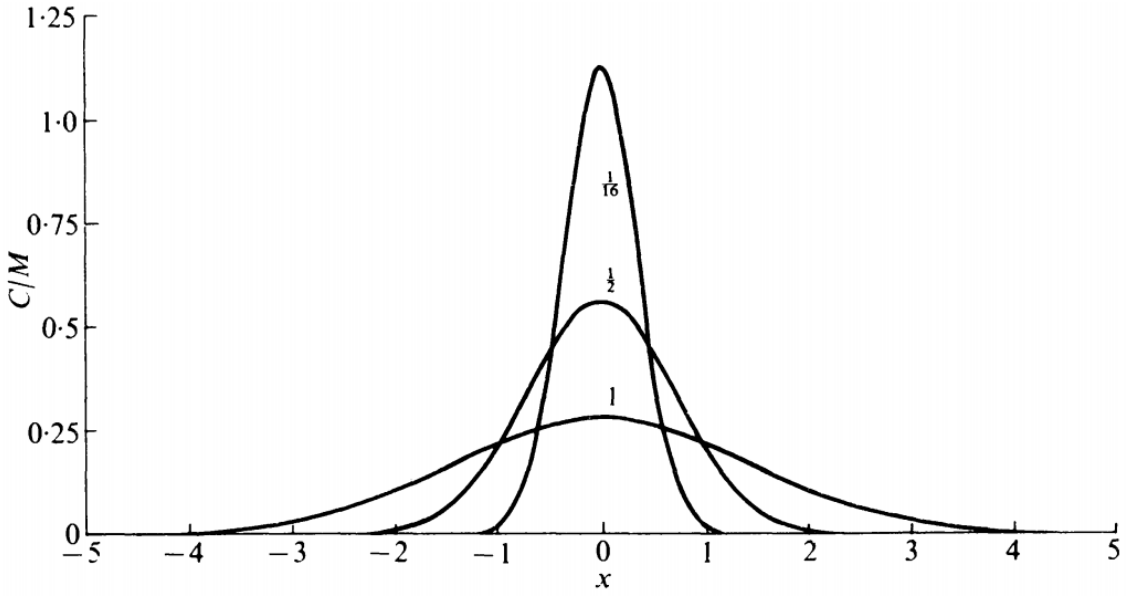


Figure 3.4: Concentration (C) vs. distance curves for an instantaneous plane source. Numbers on curves are values of Dt (Crank, 1975).

In this case, we are dealing with a semi-infinite medium, i.e., all the diffusion occurs in the direction of positive x with an impermeable boundary at x = 0. So, we can consider the solution for negative x to be reflected in the plane x = 0 and superposed on the original distribution in the region x > 0. Since the original solution was symmetrical about x = 0, the concentration profile for the semi-infinite cylinder is given by:

$$\boldsymbol{C = \frac{M}{\sqrt{\pi D t}} exp\left(-\frac{x^2}{4Dt}\right)} \qquad \textbf{…Equation 3.12}$$

Next, we can apply the Laplace transform to find the solution of **Equation 3.9** in a semi-infinite medium:

$$\boldsymbol{\frac{\partial C}{\partial t} = D\frac{\partial^2 C}{\partial x^2}} \qquad \text{…Equation 3.13}$$

satisfying the boundary condition

$C = C_0, x = 0, t > 0$

and the initial condition

$C = 0, x > 0, t = 0$

On multiplying both sides of **Equation 3.9** by e^{-pt} and integrating with respect to t from 0 to ∞:

$$\int_0^\infty e^{-pt} \frac{\partial^2 C}{\partial x^2} \mathrm{dt} - \frac{1}{D} \int_0^\infty e^{-pt} \frac{\partial C}{\partial t} dt = 0$$

If we assume that the orders of differentiation and integration can be interchanged, then

$$\int_0^\infty e^{-pt} \frac{\partial^2 C}{\partial x^2} \mathrm{dt} = \frac{\partial^2}{\partial x^2} \int_0^\infty C\, e^{-pt} dt = \frac{\partial^2 \bar{C}}{\partial x^2}$$

Integrating by parts, we have

$$\int_0^\infty e^{-pt} \frac{\partial C}{\partial t} dt = [C\, e^{-pt}]_0^\infty + p \int_0^\infty C\, e^{-pt} dt = p\, \bar{C}$$

which reduces to

$$\boldsymbol{D \frac{\partial^2 \bar{C}}{\partial x^2} = p\, \bar{C}} \qquad \textbf{…Equation 3.14}$$

By treating the boundary conditions in the same way

$$\boldsymbol{\bar{C} = \int_0^\infty C_0 e^{-pt} dt = \frac{C_0}{p}, \quad x = 0} \qquad \text{…Equation 3.15}$$

Thus, the Laplace transform reduced the partial differential equation **Equation 3.9** to the ordinary differential equation **Equation 3.14.** The solution of this ODE satisfying **Equation 3.15** and for which $\bar{C}$ remains finite as x approaches infinity is

$$\bar{C} = \frac{C_0}{p} e^{-qx}$$

where $q^2 = p/D$, and the corresponding function is

$$\boldsymbol{C = C_0\, erfc \frac{x}{2\sqrt{Dt}}}$$ **…Equation 3.16**

where $erfc\ z = 1 - ef\ z$

This shows that the solution for diffusion into a semi-infinite medium, having zero initial concentration and the surface of which is maintained constant, involves only the single dimensionless parameter:

$$\boldsymbol{\frac{x}{2\sqrt{Dt}}}$$

which shows that:

- The distance of penetration of any given concentration is proportional to the square root of time
- The time required for any point to reach a given concentration is proportional to the square of its distance from the surface and varies inversely as the diffusion coefficient
- The amount of diffusing substance entering the medium through the unit area of its surface varies as the square root of time.

3.3.2 Injection Phase

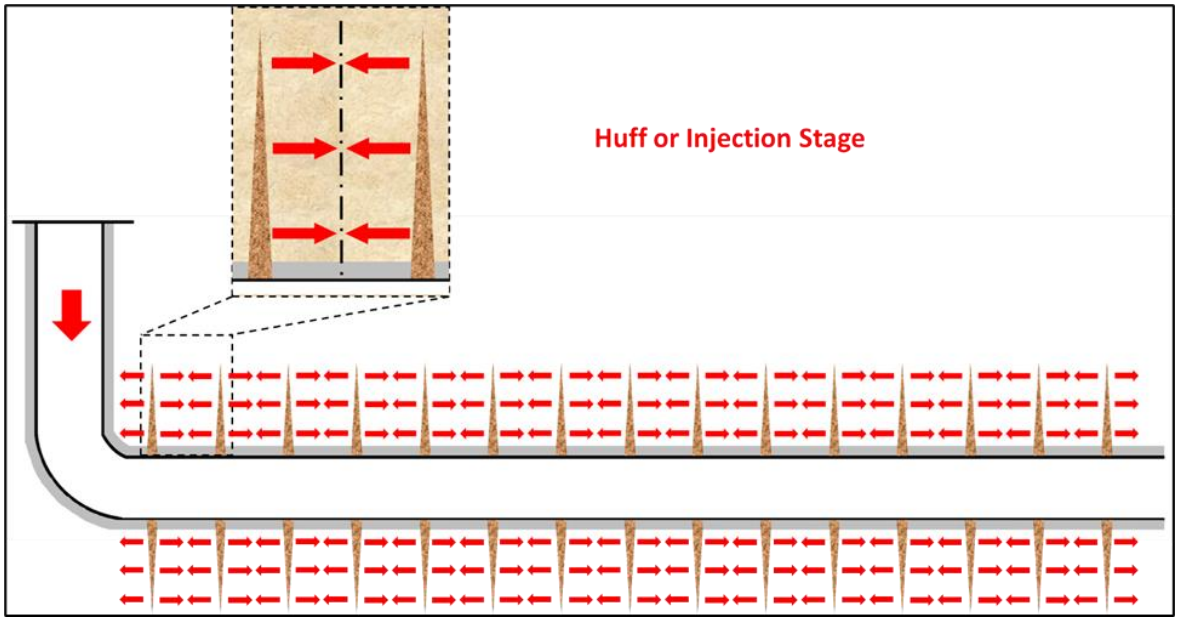


Figure 3.5: Schematic of a hydraulically fractured horizontal well in a shale reservoir during the HUFF or INJECTION stage; the inset shows the region of investigation with the injected gas exiting the hydraulic fracture and mixing with the remaining oil in the matrix. The movement of the injected gas is from the hydraulic fracture face to the no-flow boundary.

During the injection (or huff) stage, the first stage of the cyclic process, gas is injected into the hydraulically fractured shale well (**Figure 3.5**), which has been in primary production for a few years. Before the start of the injection phase, the region of investigation ($0 < x < L$) is initially at a uniform concentration of C_0. During the injection phase, the hydraulic fracture face can be assumed to be at a constant mixture (of injected gas and oil) with concentration C_1. The mixture is concentrated initially along the face of the hydraulic fracture before it enters the matrix and mixes with the remaining oil. This can be represented as a plane sheet (two thin parallel planes at $x = 0$ and $x = L$), and Fick's second law of diffusion can be analytically solved for chosen initial and boundary conditions. The concentration profile for the semi-infinite cylinder in shown in **Equation 3.12**. The analytical solution for the concentration profile (diffusion front) for the plane sheet model is given by (Carslaw & Jaeger, 1959; Crank, 1975):

$$C_{inj}(X,T) = C_0 + (C_1 - C_0)\left(1 - \frac{4}{\pi}\sum_{n=0}^{\infty}\frac{(-1)^n}{2n+1}\exp\left\{\frac{-D(2n+1)^2\pi^2 t}{4L^2}\right\}cos\left[\frac{(2n+1)\pi x}{2L}\right]\right)$$

…Equation 3.17

where, Cinj is the amount of moles of gas injected into the system.

For the first injection cycle, we assume C_0 and C_1 of 0% and 100%, respectively. The effective diffusion coefficient D_e is varied from 1.0 x 10^{-7} to 1.0 x 10^{-10} m^2/s. Although the duration of the injection phase in the field trials varied from 15 to 60 days, the duration of all the runs in this study was fixed at 30 days.

To quickly compare the results for the various sensitivities, two dimensionless variables are introduced in the analysis (described in **Section 3.4)**:

$$Dimensionless\ Time\ T = \frac{Dt}{L^2}$$

$$Position\ Ratio\ X = \frac{x}{L}$$

Figure 3.6 shows the concentration profile for one of the runs with L of 10 m and D_e of 1.0 x 10^{-7} m^2/s, resulting in the penetration length L_p of 1.85 m and position ratio of 18.5%.

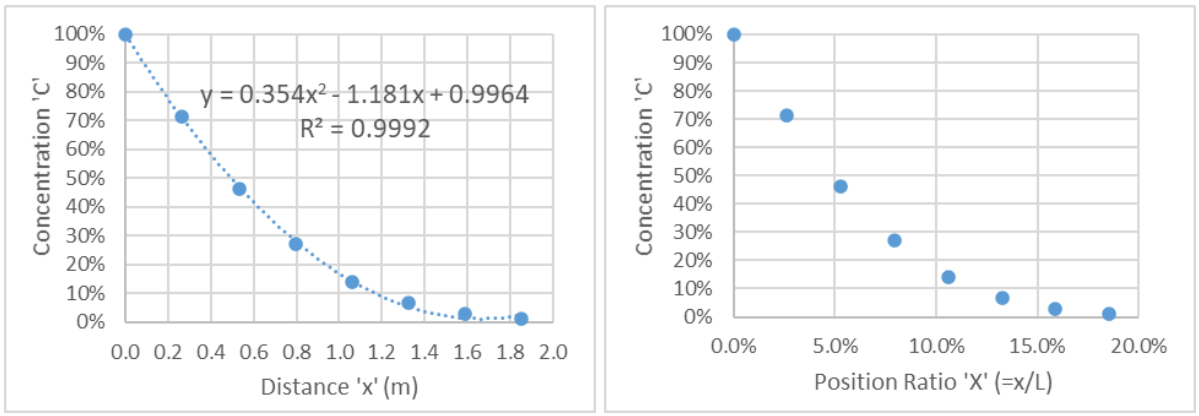


Figure 3.6: Concentration profiles vs. Distance ‘x’ and Position Ratio ‘X’ from the hydraulic fracture face (i.e., x=0) for the Injection phase.

In the present mass diffusion problem, in addition to determining the penetration length, we are also interested in the amount of substance diffused during the time t. If M_t denotes the total amount of diffusing substance (injected gas) entering the sheet at time t, and M_∞ the corresponding quantity after some infinite time (at equilibrium), then (Carslaw & Jaeger, 1959; Crank, 1975):

$$\frac{M_t}{M_\infty} = 1 - \sum_{n=0}^{\infty} \frac{8}{(2n+1)^2\pi^2} \exp\left\{-\frac{D(2n+1)^2\pi^2 t}{4l^2}\right\} \quad \textbf{…Equation 3.18}$$

For the base run shown in **Figure 3.6**, the total amount of gas diffused is 0.057 moles.

In the later part of this study, to investigate the diffusion of the injected gas in the matrix as a function of the micro-fracture distribution, the length L was varied by four orders of magnitude from 0.01 m to 10 m. The L in these runs represents half of the fracture spacing between adjacent fractures. The position ratio X and M_t for these different runs allowed us to quickly compare the penetration length L_p (as a percentage relative to L) and the amount of substance diffused during 30 days.

3.3.3 Soaking Phase

Next, the concentration profile for the soaking phase is solved with the matrix modeled as a slab with a limited volume of homogeneous solution within hydraulic fractures at the end of the injection phase. Following the huff (or injection period), the solvent influx from the fractures to the matrix continues during the soaking period. However, **the solvent volume available for the counter-current diffusion process (from the fractures to the matrix) varies between the experimental setup in the laboratory and the field**. **To account for scale differences between the core and reservoir scale, we introduce two additional dimensionless parameters:**

$$\textbf{Alpha } \alpha = \frac{\textbf{Volume of Fracture Network } V_f}{\textbf{Volume of Matrix } V_m} = \frac{1}{K}$$

$$\textbf{Mass transfer coefficient } Bi = \frac{k_c}{D_e} L_c$$

The concentration profile at the end of the injection phase is used as the initial condition for the soaking phase. The analytical solution for the concentration profile for the slab model is given by (Mikhailov & Ozisik, 1984):

$$C_{soak}(X,T) = \frac{\theta_0 + K \int_0^1 X^{1-2m} F(X) dX}{1 + K/[2(1-m)]} - \sum_{i=1}^{\infty} E_i \left[\theta_0 - \mu_i \int_0^1 X^{1-m} \frac{J_{-m}(\mu_i X)}{J_{-m}(\mu_i)} F(X) dX\right] \frac{X^m J_{-m}(\mu_i X)}{J_{-m}(\mu_i)} e^{-\mu_i^2 \tau} \quad \textbf{…Equation 3.19}$$

where, m = 0.5 for a slab (value specific to shape), X and T are the dimensionless position ratio and dimensionless time (both described above), and F(X) is a function of the concentration profile at the end of the injection phase. The Ei function is the culmination of the two scaling parameters α and Bi, and is mathematically defined as:

$$E_i = \frac{2}{\mu_i}\left[1 + \frac{2m}{\mu_i}\left(\frac{\mu_i}{B_i} - \frac{K}{\mu_i}\right) + \left(\frac{\mu_i}{B_i} - \frac{K}{\mu_i}\right)^2 + \frac{2K}{\mu_i}\right]^{-1} \quad \textbf{…Equation 3.20}$$

where, m = 0.5 for a slab (value specific to shape), B_i is the mass transfer coefficient, K is the inverse of α, and eigenvalues μ_i are the non-zero positive roots of the transcendental equation

$$\tan q_n = -\alpha q_n$$

where, $\mu_i = q_n$. The roots μ_i of this transcendental equation depend on the value of α. For all the runs, a soaking time of 30 days was used.

Figure 3.7 shows the concentration profile for one of the runs with L of 10 m, D_e of 1.0 x 10^{-7} m^2/s, Injection L_p of 1.85 m, and Soaking L_p of 2.56 m.

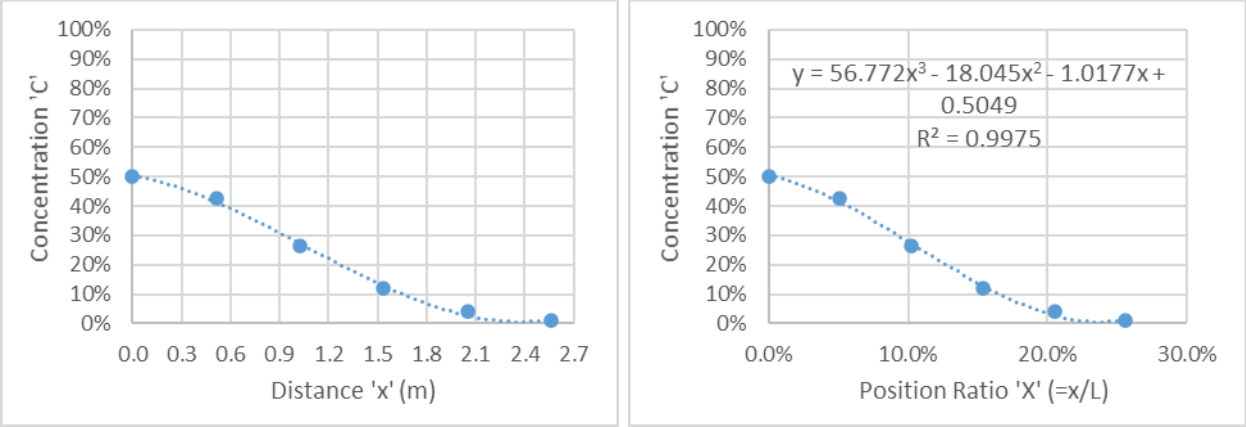


Figure 3.7: Concentration profiles vs. Distance ‘x’ and Position Ratio ‘X’ for the Soaking phase.

3.3.4 Production Phase

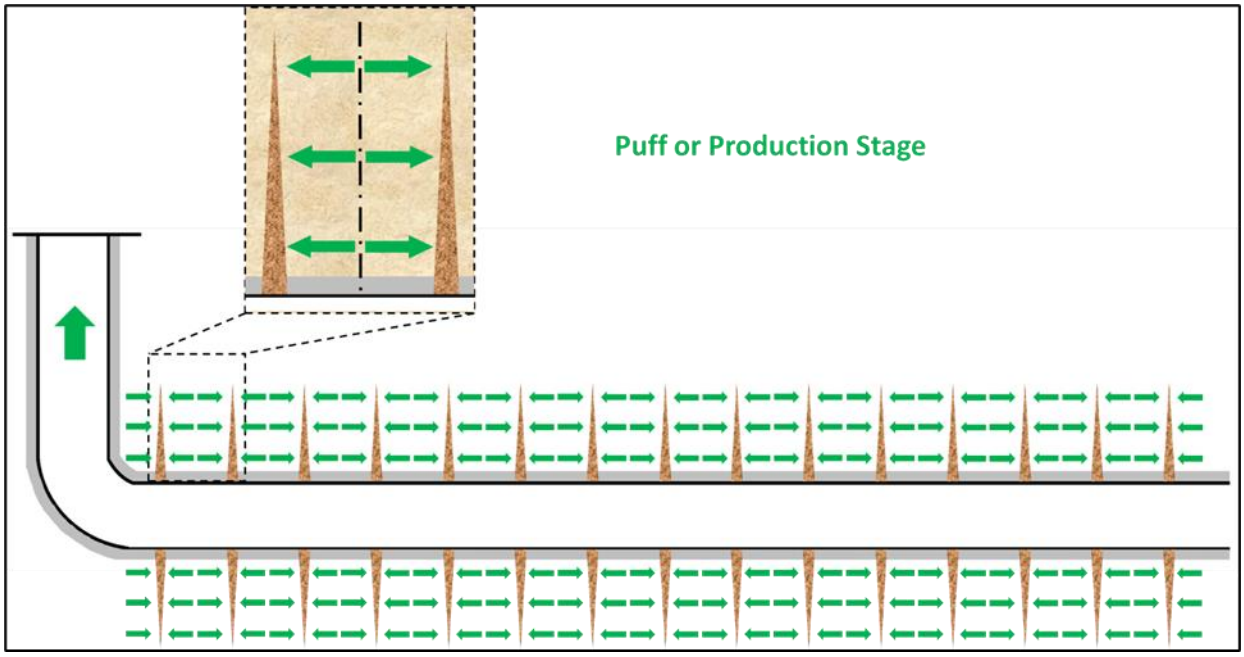


Figure 3.8: Schematic of a hydraulically fractured horizontal well in a shale reservoir during the PUFF or PRODUCTION stage; the inset shows the region of investigation with the remaining oil, which has become miscible with the injected gas exiting the matrix. The movement of the solvent mixed with oil is from the matrix to the hydraulic fracture.

Lastly, the concentration profile for the production phase is solved with the matrix again modeled as a slab. Following the soaking period, the solvent mixed with oil (single-phase) flows from the matrix to the fracture (a co-current diffusion process) (**Figure 3.8**). **Equations 3.19** and

3.20 are solved for the production phase. The concentration profile at the end of the soaking phase is used as the initial condition for the production phase. The effective diffusion coefficient for this phase is assumed to be an order of magnitude lower than that used for injection and soaking phases to capture the mass flux reduction during this phase due to the two-phase phenomenon in the shale matrix. For all the runs, a production time of 30 days was used.

Figure 3.9 shows the concentration profile for one of the runs with L of 10 m, D_e of 1.0 x 10^{-7} m^2/s, Injection L_p of 1.85 m, and Soaking L_p of 2.56 m.

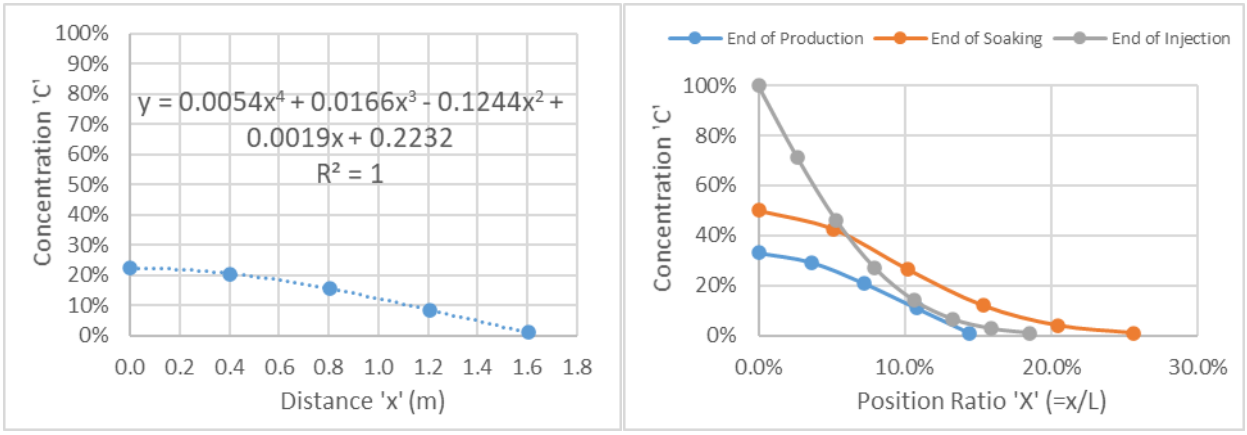


Figure 3.9: Concentration profiles vs. Distance ‘x’ and Position Ratio ‘X’ for the Production phase.

Because of the scale difference between the core and reservoir, two values recoveries can be reported based on the length scale under consideration:

1) In the laboratory experiment, because of the small core diameter, the penetrated length after the soaking stage might be the total length (diameter) of the core. The recovery factor can be calculated as the ratio of the area under the blue curve over the area under the orange curve, which is 49%.

2) On the other hand, in the field, the recovery factor can be calculated as the area under the blue curve over the total length of the sample, which is 12.6%.

The difference in the two recoveries is due to the scale difference between core and reservoir. A Recovery Factor Ratio is calculated as a fraction of recovery at the field scale (numerator) to that at the laboratory scale (denominator).

3.3.5 Base Model Validation

After developing the mathematical model, the first step was to validate the model outputs against the published results. The model outputs were first qualitatively compared to the works published by Crank (1975) and Mikhailov & Ozisik (1984) for the concentration profile, and the outputs were found to be reasonably close. Next, the results for the base case were compared to the outputs for one of the cases (L = 70m, $\alpha = 0.11$, $D_e = 1 \times 10^{-7}$ m^2/s, t = 30 days) published by Akita and Moghanloo (2018), and the outputs were found to be within +/-3% for the injection and soaking phases, and +/- 8% for the production phase (**Table 3.2**). The main reasons for some of the differences are:

- A slight variance in L_p values is due to significant figures reported by Akita and Moghanloo (2018).
- In this study, the non-zero positive roots of the transcendental equation were kept static for the soaking and production phases. In contrast, based on their study objectives, Akita and Moghanloo solved a different transcendental equation for the production phase, resulting in a difference in outputs.

Table 3.2: Comparison of Model Outputs Against the Results of Akita and Moghanloo (2018)

Phase	Output Variable	Akita & Moghanloo (2018)	Base Model Outputs	Difference Between the Outputs (%)
Injection	L_p (m)	1.800	1.855	3.03
	M_t (moles)	0.008141	0.008137	0.04
	C_{avg} (%)	0.452	0.439	2.99
Soaking	L_p (m)	2.600	2.574	0.99
	M_t (moles)	0.557914	0.559565	0.30
	C_{avg} (%)	0.797	0.799	0.30
Production with $B_i=\infty$	M_t (moles)	0.310973	0.333214	7.15
	RF – Core Scale (%)	55.74	59.55	6.84
	RF – Reservoir Scale (%)	2.07	2.19	5.78
Production with a smaller value of B_i	B_i (dimensionless)	0.01	0.11	-
	M_t (moles)	0.338573	0.312981	7.56
	RF – Core Scale (%)	60.69	55.93	7.83
	RF – Reservoir Scale (%)	2.25	2.06	8.74

*Inputs used in both the models: L = 70m, α = 0.11, D_e = 1 x 10^{-7} m^2/s, t = 30 days each for injection-soaking-production phases

Once the base model was developed and outputs validated against the published results, the model was expanded to represent field conditions better by incorporating fracture distribution observed in the laboratory and field (**Section 2.1.1.2**). The matrix is characterized as an ensemble of rock pillars separated by fracture discontinuities, with the fracture spacing expected to follow the Lorenz/Cauchy distribution (**Equation 2.1**). The L is varied by four orders of magnitude from 0.01 m to 10 m; however, the smallest length dimension for each matrix block is expected to dictate the one-dimensional diffusion process.

3.4 Scaling parameters to upscale lab results to field results

Although the well is shut in during the soaking period, the solvent influx from the fractures to the matrix continues. However, **the solvent volume available for the diffusion process varies between the laboratory setup and the field due to scale differences between the core and**

reservoir (**Figure 3.10**). To account for these differences, two dimensionless scaling parameters are introduced:

- **Alpha 'α':** is the ratio of the volume of the fracture network to the volume of the matrix. Because of the scale difference between the core and reservoir, the volume of solution in the fracture network to the total volume of the matrix varies by one to two orders of magnitude. We can explain this by analogy with dipping a piece of paper in a cup full of water (core at lab scale) vs. dipping a thick book in the same cup (large matrix block at field scale). In other words, α can be defined as the fraction of the total solute finally taken up by the matrix, and is inversely proportional to K defined in the existing analytical solutions for the heat and mass transfer in the slab model.

$$\boldsymbol{Alpha\ \alpha = \frac{Volume\ of\ Fracture\ Network\ V_f}{Volume\ of\ Matrix\ V_m} = \frac{1}{K}} \qquad \textbf{…Equation 3.21}$$

  For this study, three values of α are used – 0.1, 1, and 10 – to investigate the effect of scale differences on the recovery through the huff-and-puff process. The value of 0.1 would represent the field scale, while values from 1 to 10 would represent the lab scale.

- **Mass transfer coefficient 'B_i'** (referred to as Biot number in heat transfer calculations): is a dimensionless quantity used to describe the overall mass transfer effectiveness during the counter-current and co-current diffusion processes and is a function of concentration change between the fracture network and the matrix. As discussed, diffusion is a path-dependent process driven by the concentration and pressure gradients. Any alteration to the path reduces the overall mass transfer effectiveness. We hypothesize that the mass transfer coefficient varies between the laboratory and field scales due to the presence of a "damaged zone" around hydraulic fractures at the field scale, limiting the mass transfer. The damaged

zone could be from gel damage residue, proppant crushing due to stress cycling, wettability alteration, connectivity loss/coordination number reduction (Davudov & Moghanloo, 2018), asphaltene deposition, hydraulic fracture water imbibition, and other factors such as changes in geomechanical properties.

$$\textbf{Mass transfer coefficient } B_i = \frac{k_c}{D_e} L_c \qquad \textbf{...Equation 3.22}$$

With the D_e values varied from 1.0 x 10^{-7} to 1.0 x 10^{-10} m^2/s, L_c (i.e., L) varied from 0.01 m to 10 m (four orders of magnitude), and k_c varied from 1.0 x 10^{-6} to 1.0 x 10^{-8}, the resultant B_i values were varied from 0.01 to 100 (five orders of magnitude). Smaller values of B_i represent lab scale with good connectivity between the fracture and the matrix, resulting in uniform mass transfer. Larger values of B_i represent field conditions where the non-uniform mass transfer occurs due to damaged zone and other factors.

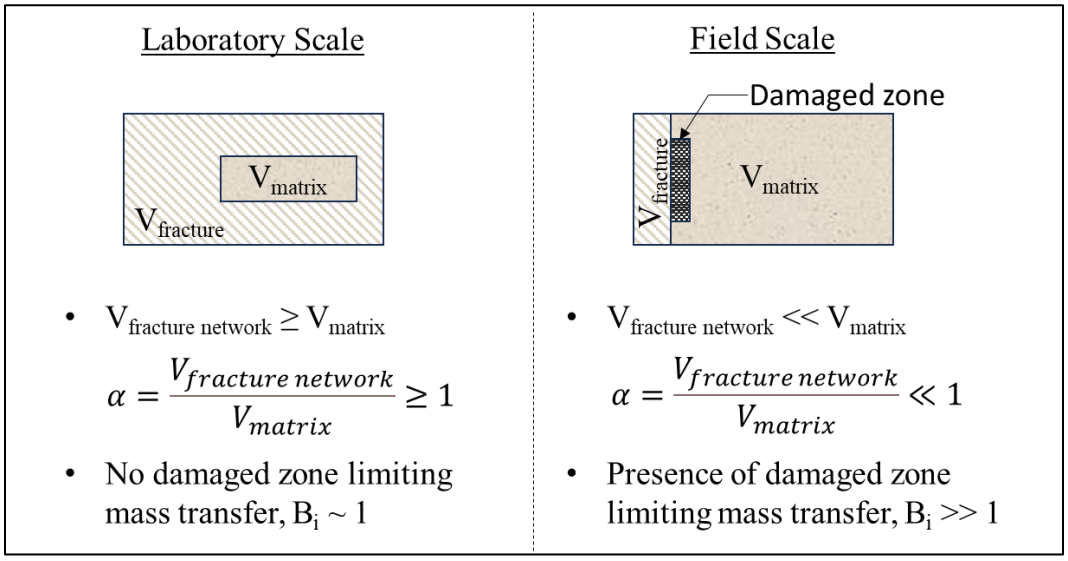


Figure 3.10: Schematic of matrix and fracture network at laboratory and field scales, and the corresponding values of α and B_i.

3.5 Sensitivity Analysis

After validating the model output (**Section 3.1.5**), several sensitivities were performed to understand the impact of diffusion coefficients D_e, α, and B_i on penetration lengths, M_t, and the recoveries. The results are summarized below.

3.5.1 Effect of Diffusion Coefficient D_e

As covered above, experimental and numerical modeling studies have reported a wide range of "constant" diffusion coefficients in the literature for the huff-and-puff EOR process. **Figure 3.11** shows the impact of D_e on penetration lengths (as % of length L), M_t, and Recovery Factor Ratio for the base case with L = 10 m, $\alpha = 0.1$. and D_e values of 1×10^{-7}, 1×10^{-8}, 1×10^{-9} m^2/s. The penetration lengths and the Recovery Factor Ratio values were found to have an exponential relationship with D_e when plotted on semi-log plots.

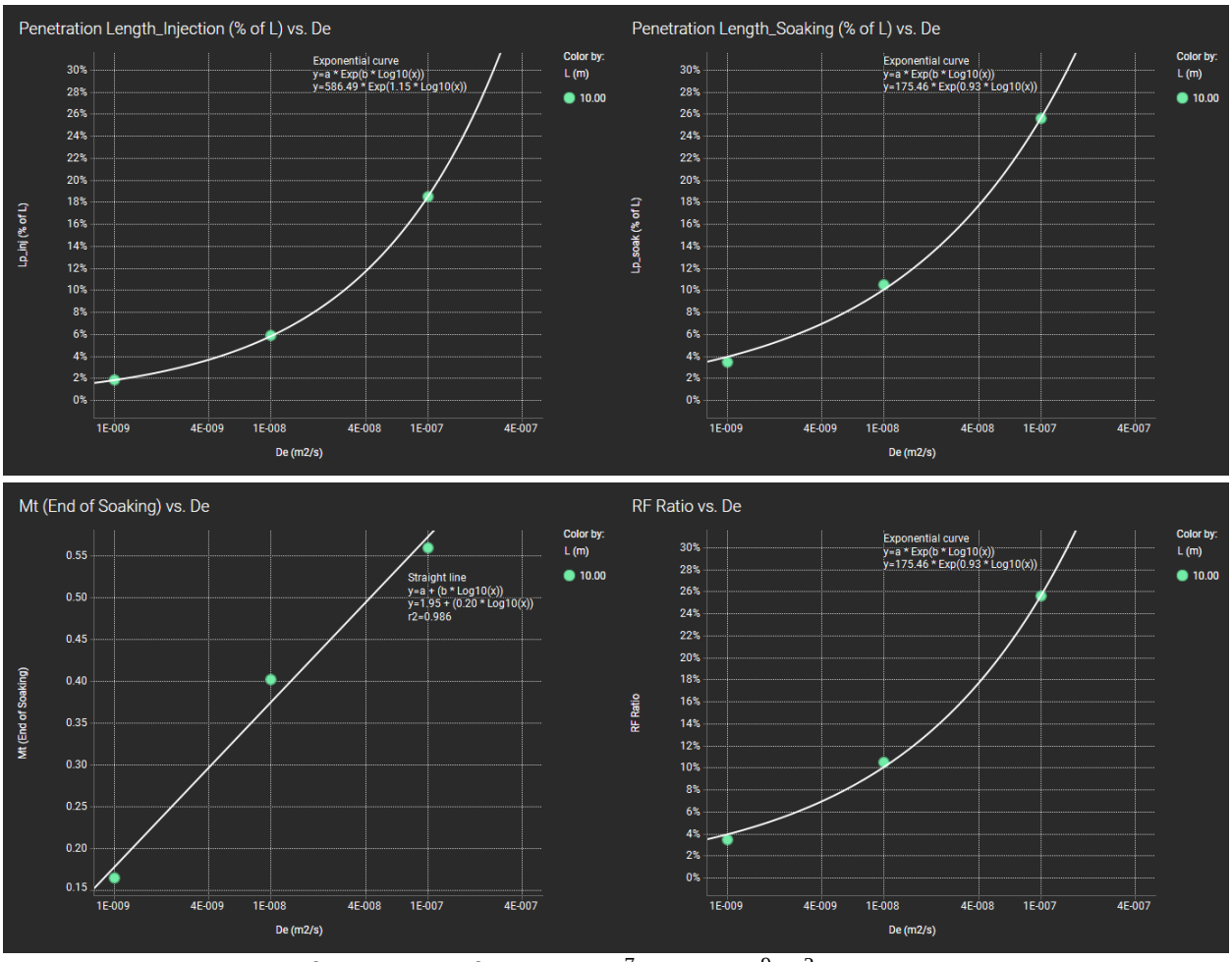


Figure 3.11: Impact of varying D_e from 1 x 10^{-7} to 1 x 10^{-9} m^2/s on L_p, M_t, and the Recovery Factor Ratio.

3.5.2 Effect of Alpha

A few sensitivities were conducted to investigate the impact of α, one of the two scaling parameters, on recoveries. **Figure 3.12** shows the effect of changing α from 0.1 to 10 (two orders of magnitude) on the recoveries at the core scale, reservoir scale, and the Recovery Factor Ratio for the base case with L = 10 m, D_e = 1 x 10^{-9} m^2/s, and B_i of 100. The recoveries were found to have a logarithmic relationship to α at both the core and reservoir scales. However, similar to the results in **Figure 3.11**, the Recovery Factor Ratio for all three cases was ~3% due to low D_e.

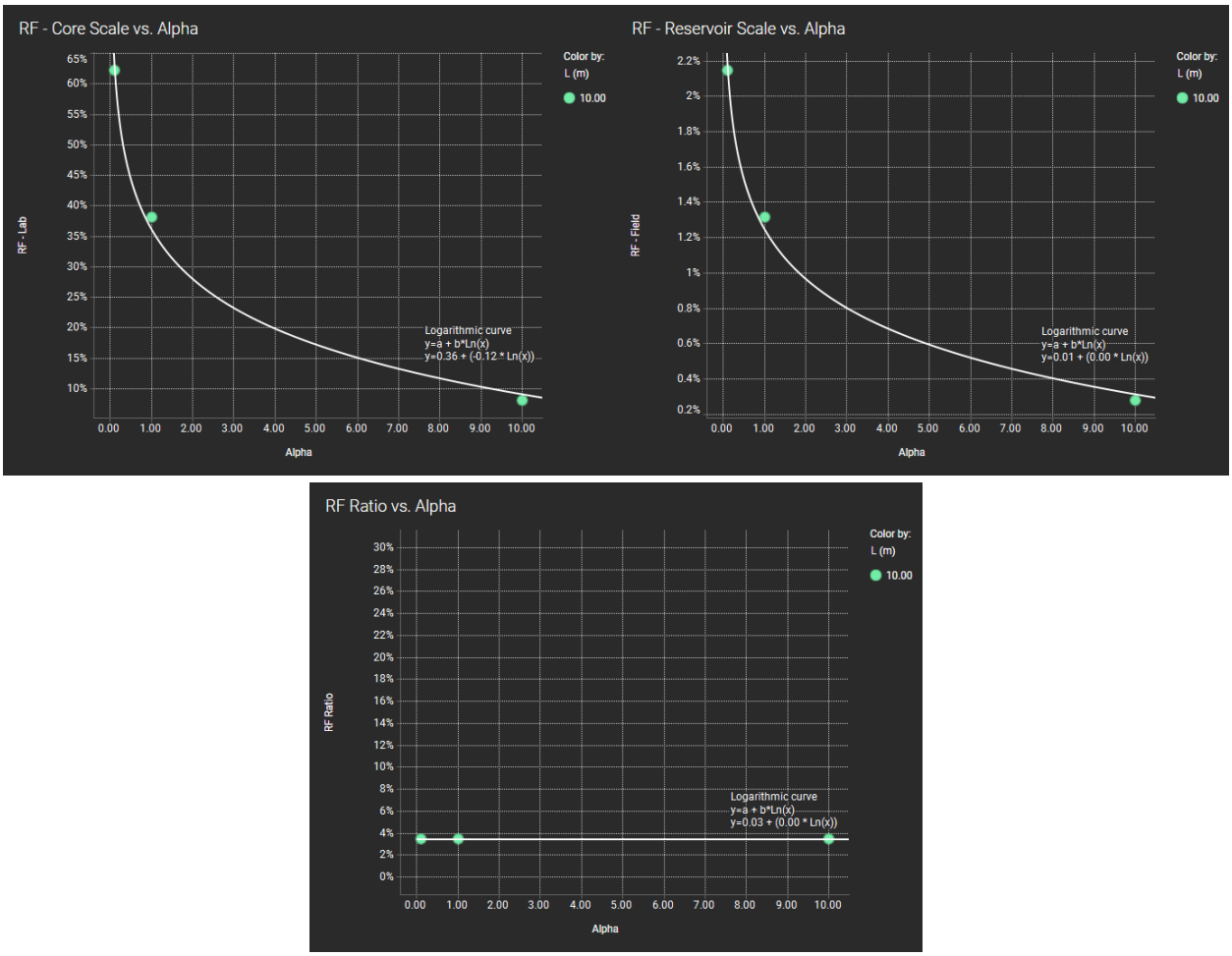


Figure 3.12: The impact of varying α from 0.1 to 10 on recoveries at core and reservoir scales and the Recovery Factor Ratio.

3.5.3 Effect of B_i

Next, the impact of B_i, the second scaling parameter, on the penetration lengths, M_t, and the Recovery Factor Ratio was evaluated by varying B_i values from 1 to 100. **Figure 3.13** shows similar results and exponential relationships observed when running sensitivities for varying D_e (**Figure 3.11**). Similar results were observed because the two parameters are inversely related, and changing the value of B_i required updated values of D_e to keep L_c and k_c constant (**Equation 3.22**).

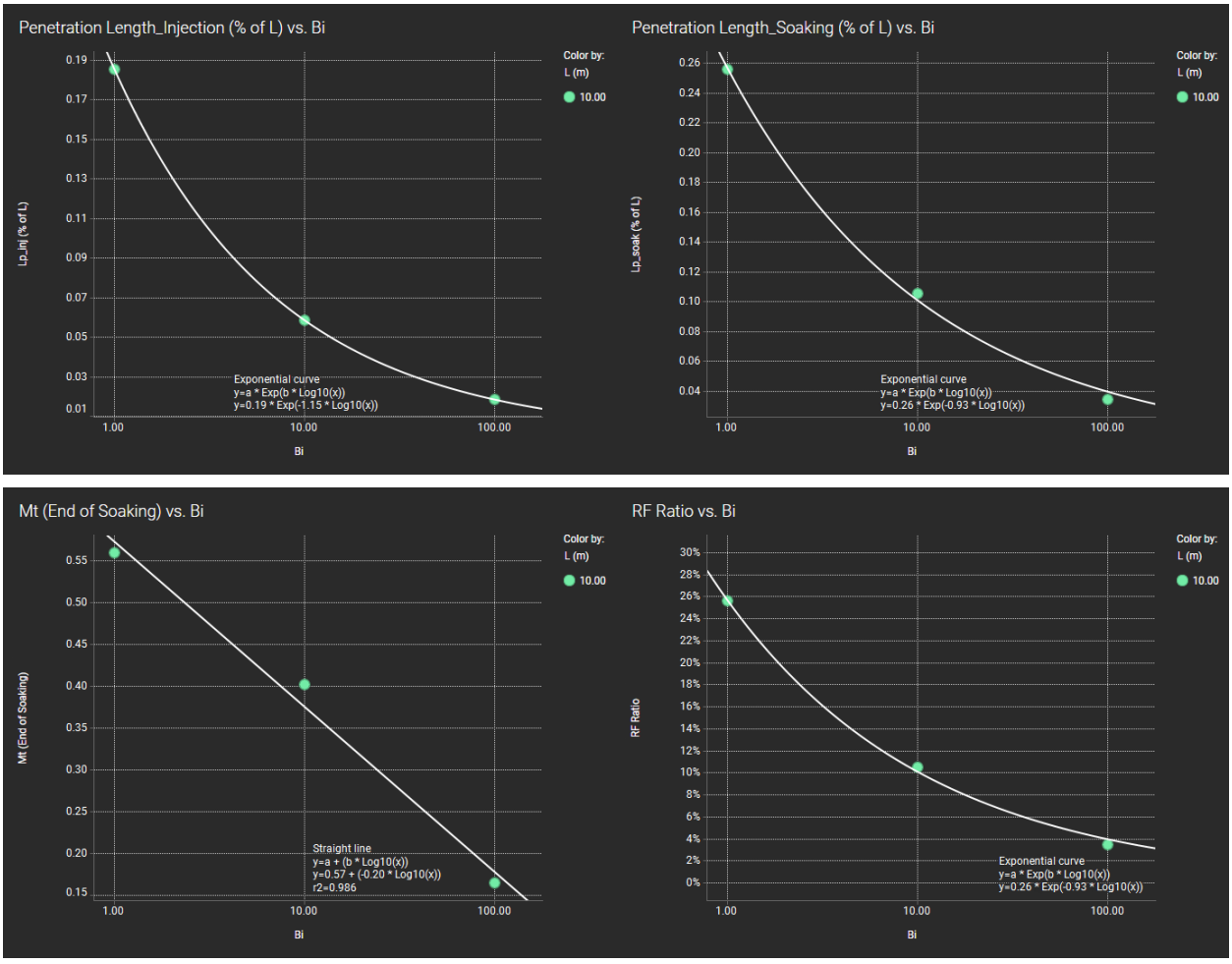


Figure 3.13: Impact of varying B_i from 1 to 100 on L_p, M_t, and the Recovery Factor Ratio.

3.5.4 Effect of length 'L'

For the second phase of this study, the L is varied from 10 m (base case) to 0.01 m (four orders of magnitude) to understand the movement of the diffusion front (accessibility) on smaller matrix blocks created during hydraulic fracturing and expected to follow the Lorenz/Cauchy's distribution. **Figure 3.14** shows a linear trend between penetration length (as a function of L) after soaking and Recovery Factor Ratio, which helps validate the model for smaller matrix blocks. **Figure 3.15** compares the recoveries expected from matrix blocks of different sizes, which vary

as a function of D_e. After 30 days of each injection-soaking-production phase, the recoveries from the smaller matrix blocks (L = 0.01 m and 0.1 m) are expected to be significantly higher (approaching 100%) than the larger blocks. However, as shown in **Figure 3.16**, the total amount of gas diffused (M_t) would be higher for the larger blocks.

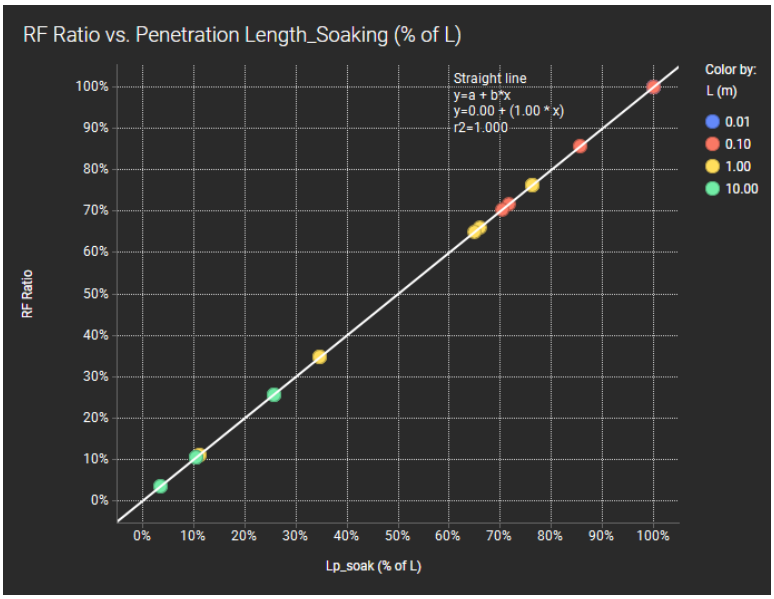


Figure 3.14: Comparison of penetration length after the Soaking phase for blocks of 0.01, 0.1, 1, and 10 m.

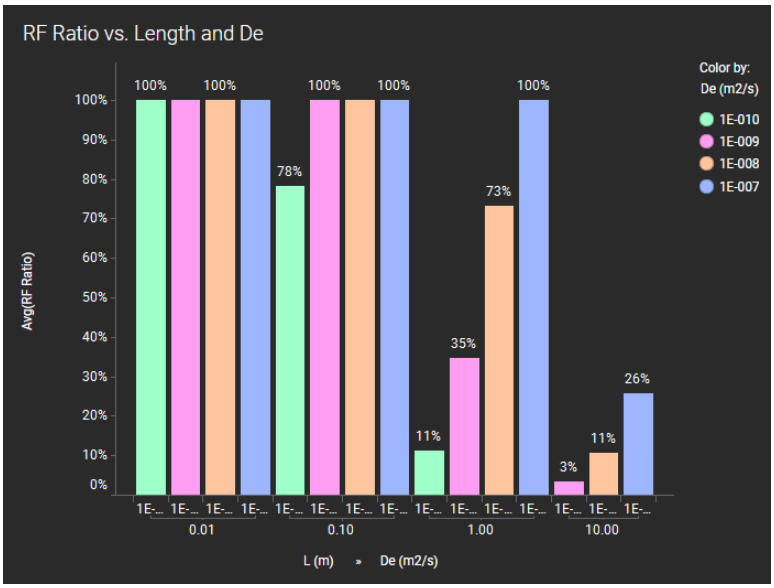


Figure 3.15: Comparison of Recovery Factor Ratio for matrix blocks of lengths 0.01, 0.1, 1, and 10 m, as a function of D_e.

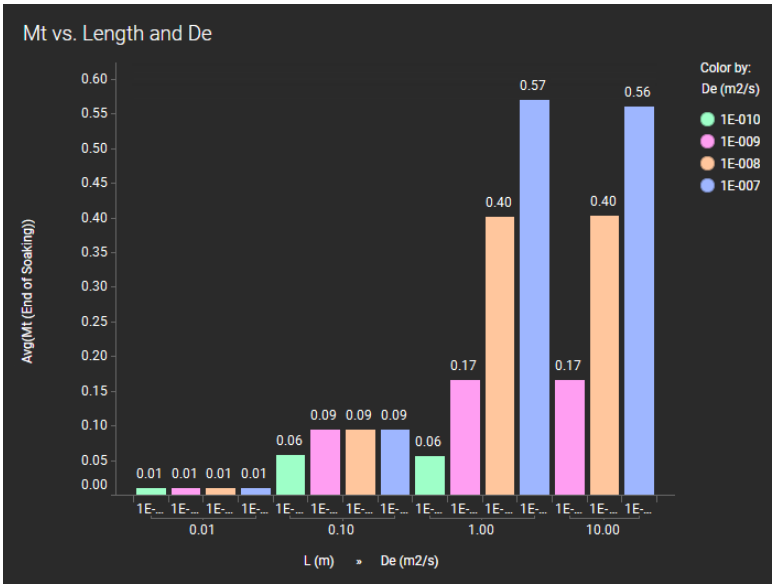
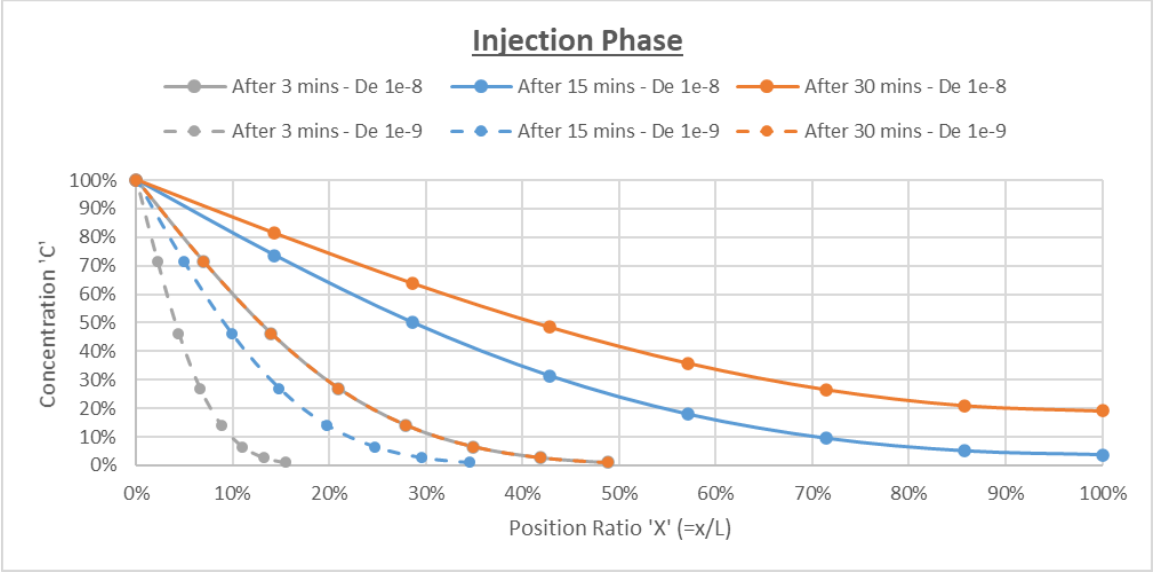
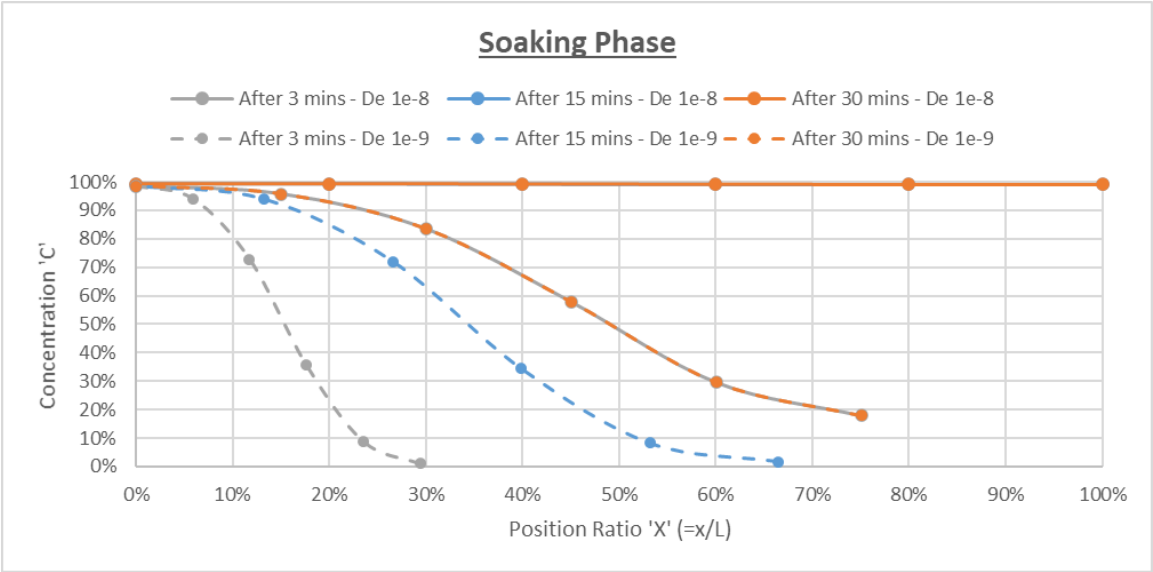


Figure 3.16: Comparison of the total amount of gas diffused (M_t) for matrix blocks of length 0.01, 0.1, 1, and 10 m, as a function of D_e.

3.5.5 Effect of time on small block size (L = 0.01 m) as a function of two different D_e values

As shared in the previous section, the penetration length for the smaller blocks (L = 0.01 m and 0.1 m) is 100% after the injection and soaking phases of 30 days each. **Figure 3.17** shows the movement of the diffusion front after 3, 15, and 30 minutes of injection and soaking. A comparison is made for D_e values of $1x\ 10^{-8}$ and $1x10^{-9}$ m^2/s. Lab experiments by Hawthorne et al. (2019) corroborate these mathematical modeling results.


Injection Phase
After 3 mins - De 1e-8
After 15 mins - De 1e-8
After 30 mins - De 1e-8
After 3 mins - De 1e-9
After 15 mins - De 1e-9
After 30 mins - De 1e-9
Concentration 'C'
100%
90%
80%
70%
60%
50%
40%
30%
20%
10%
0%
0%
10%
20%
30%
40%
50%
60%
70%
80%
90%
100%
Position Ratio 'X' (=x/L)


Soaking Phase
After 3 mins - De 1e-8
After 15 mins - De 1e-8
After 30 mins - De 1e-8
After 3 mins - De 1e-9
After 15 mins - De 1e-9
After 30 mins - De 1e-9
Concentration 'C'
100%
90%
80%
70%
60%
50%
40%
30%
20%
10%
0%
0%
10%
20%
30%
40%
50%
60%
70%
80%
90%
100%
Position Ratio 'X' (=x/L)

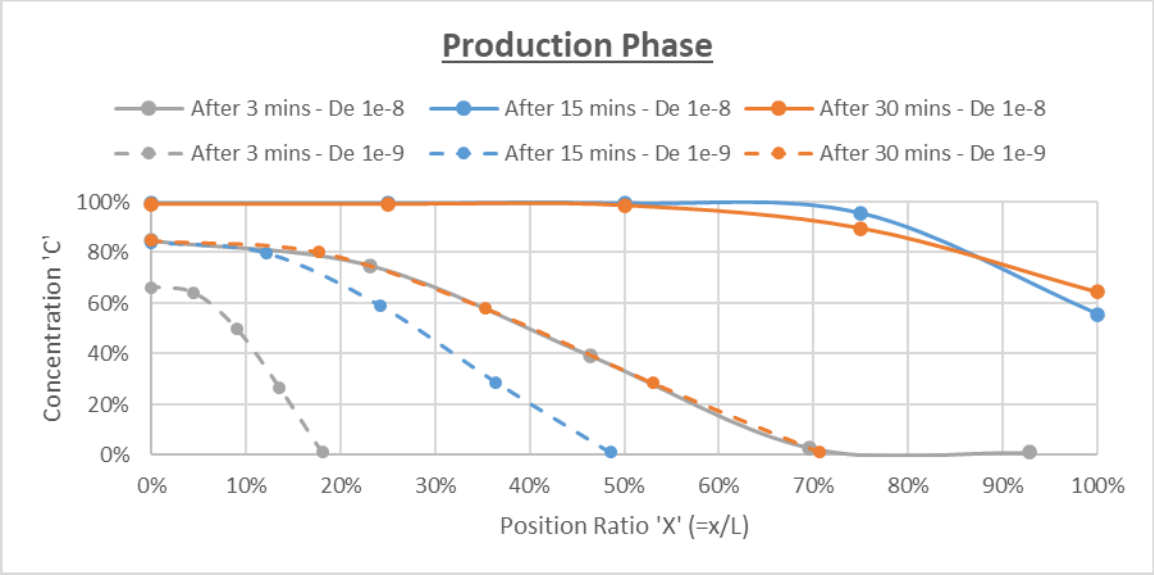


Figure 3.17: Comparison of the concentration front for L = 0.01 m sample after 3, 15, and 30 minutes of injection-soaking-production phases. Results are shown for D_e of 1x 10^{-8} and 1x10^{-9} m^2/s.

3.6 Upscaling Equation

Based on the results from this study, an upscaling equation was derived to predict recoveries in the field more accurately. As mentioned, the fracture geometry created near-wellbore was found to have a first-order effect on the efficacy of the huff-and-puff process in the field. Additionally, a combination of the two scaling parameters – α and B_i – were found to impact recovery. In particular, the recovery factor ratio was found to be a function of $\frac{B_i}{\alpha}$ term, and two upscaling equations were derived based on the value of α.

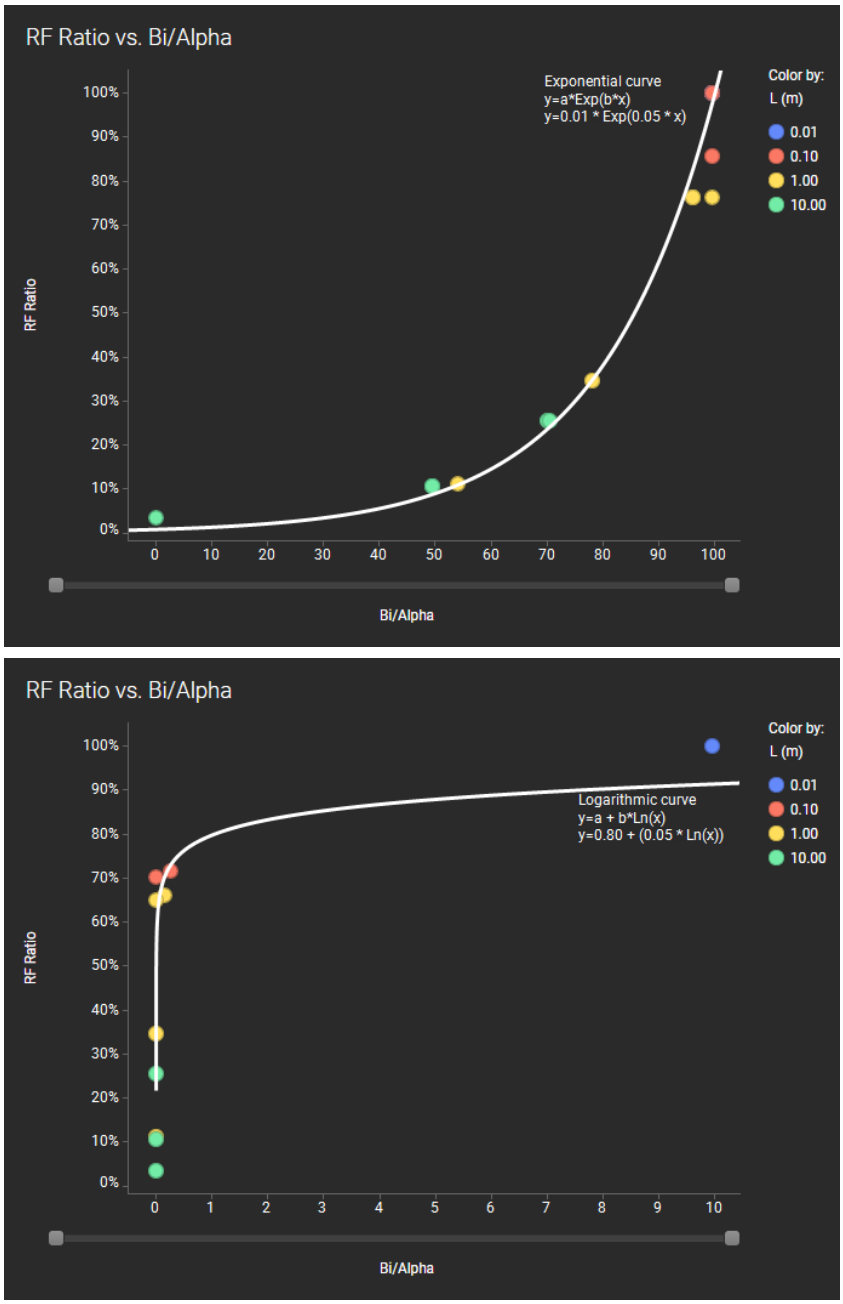


Figure 3.18: Recovery Factor Ratio vs. B_i/α graphs for $\alpha = 0.1$ (top) and $\alpha = 1$ and 10 (bottom).

- For $\alpha = 0.1$, the data suggests that the lab-scale results can be upscaled to field-scale recoveries by using an exponential relationship (**Figure 3.18 – top**):

$$\text{Recovery Factor Ratio} = \frac{\text{Recovery at reservoir scale}}{\text{Recovery at core scale}} = 0.01\ \text{Exp}\left(0.05\ \frac{B_i}{\alpha}\right)$$

- For values of α ranging from 1 to 10, a logarithmic relationship exists between the recoveries at the reservoir scale to the core scale (**Figure 3.18 – bottom**):

$$\text{Recovery Factor Ratio} = \frac{\text{Recovery at reservoir scale}}{\text{Recovery at core scale}} = 0.80 + \left(0.05 \times \text{Ln}\left(\frac{B_i}{\alpha}\right)\right)$$

3.7 Discussion

For the mathematical modeling, the huff-and-puff process is assumed to be primarily diffusion-driven. However, the Peclet number (Pe) is not expected to be constant and could vary due to lithology and fabric changes within the rock. This could result in advection-based fluid flow in addition to diffusion. The advection-based flow would result in additional penetration length, which is not captured in the results above.

The experimental work carried out by Damani et al. (2018) was based on the low-porosity, low-permeability Tennessee sandstone samples and not directly with the shale samples. Each shale formation has different geological and geomechanical characteristics, resulting in different secondary fracture distributions. In addition, the degree of natural fracturing contrasts between different shale formations, resulting in varied fracture complexity during hydraulic fracturing treatment. As a result, the Lorenz/Cauchy distribution may differ for each shale play with a higher standard deviation or may fit a different distribution such as Gaussian or triangular. So, the minimum length dimension dx (i.e., L) is varied over four orders of magnitude to capture the impact of different block thicknesses on recoveries and upscaling the results from the lab to field scale.

Fu et al. (2019) reported that the composition of lighter oil components declined in the produced oil from the first to the last gas injection cycle, while the composition of the intermediate and heavier components increased. This observation suggests we may be recovering the remaining

oil from the same penetration length within the small matrix block, bounded by secondary fractures near the wellbore. To recover the remaining oil from larger matrix blocks, we possibly have to repeat multiple huff-and-puff cycles for a longer duration.

Recoveries were calculated for just one cycle of injection-soaking-production phases of 30 days each. In reality, the multiple cycles are repeated as part of the huff-and-puff implementation. Additionally, for this part of the research, the First Contact Miscible process was assumed for a pseudo-single-phase hydrocarbon, which excludes two-phase phenomena. The use of Fick's law to describe the concentration-based diffusion only applies to single-phase fluid systems and excludes the effect of any cross-phase diffusion.

3.8 Key Takeaways

A mathematical model is developed using classical analytic equations to understand the recoveries expected from the huff-and-puff process at the core and reservoir scale. Based on the Peclet number criterion in the tight shale matrix, the process is assumed to be diffusion-dominated, and the penetration of a limited injectant volume in different-sized grid blocks is evaluated.

- The penetration of the injectant into the matrix during the injection, soaking, and production phases is evaluated and compared as a function of parameters such as Diffusion Coefficient, matrix block size, and duration of the different phases of the cyclic process.
- Discrepancies observed in the recoveries between the lab scale and field scale can be resolved by incorporating the two scaling parameters – Alpha α and Mass Transfer Coefficient B_i
- An upscaling equation is derived in terms of $\frac{B_i}{\alpha}$ to predict recovery factors better

- Two upscaling schemes are identified to translate recovery factors from core to reservoir scale based on the values of α, and exponential and logarithmic trends were observed for $\alpha = 0.1$ and $\alpha > 0.1$, respectively.

The impact of complex fracture networks created during hydraulic fracturing on the efficacy of the huff-and-puff EOR process is investigated:

- The Lorenz/Cauchy distribution observed in the laboratory experiments by Damani et al. (2018) for fracture density can be scaled to the field using the 1:50 upscaling relationship.
- Secondary fractures emanating from the primary fracture follow a Lorenz/Cauchy distribution and result in decreasing recoveries away from the wellbore. Initial cycles appear to tap into the tightly spaced fractures/smaller matrix blocks near the wellbore. As cycles are repeated, the larger blocks away from the wellbore are accessed with comparatively slower recovery. To optimize the recovery/process, the operators should look into extending the injectant-remaining oil contact time by modifying the duration of injection/soaking/production phases in subsequent cycles.

Chapter 4

Does the Soaking Phase Matter?

This chapter extends the work from the previous chapter. It utilizes the Lorenz/Cauchy distribution observed to investigate the impact of fracture spacing on gas injection scenarios with and without soaking times. The mathematical model previously developed represents the infiltration of the injected gas into the shale matrix by modeling mass diffusion of a limited volume of well-stirred fluid into a porous medium (matrix). To better represent field conditions, the matrix is characterized as an ensemble of rock pillars separated by fracture discontinuities randomly distributed, and the recovery was explored as a function of the micro-fracture distribution.

4.1 Effect of Soaking Times

One of the operating parameters that is not well understood after numerous field trials is the optimum duration of the different phases (injection, soaking, and production). In the Eagle Ford trials, the soaking times have varied from ~3 to 16 days, with the soaking to injection cycle ratio of 0.6 to ~2.7 (Thoms, 2020), with mixed recovery uplift values. Much speculation exists in the industry about whether the benefits of the soaking phase are sufficient to offset the time lost during soaking when the well is shut in.

Gamadi et al. (2013) studied the effects of soaking pressure and soaking time with the cyclic nitrogen injection with Eagle Ford and Marcos core plugs at the laboratory scale. Their results showed that the oil recovery increased with soaking time but depended more on soaking

pressure to achieve miscibility. Yu et al. (2016) pointed out that oil recovery increased with longer soaking times with the Eagle Ford cores; however, an optimum soaking time existed beyond which no additional recovery was observed. In contrast, Sheng (2017) studied the effect of soaking time using a numerical simulation model for the Middle Bakken and showed minimal to no additional oil recovery with soaking but reported model convergence issues with the inclusion of diffusion. Afari et al. (2022) recently presented similar results with CO_2 huff-and-puff for the Middle Bakken. However, the authors qualified those results by stating that the value of the diffusion coefficient used was not high enough to impact the oil recovery. Finally, Dang (2019) performed experiments with crushed samples from Eagle Ford and 72/28 C1/C2 mixture above MMP. **Figure 4.1** shows the results from Dang's experimental work with longer soaking times resulting in a higher incremental recovery.

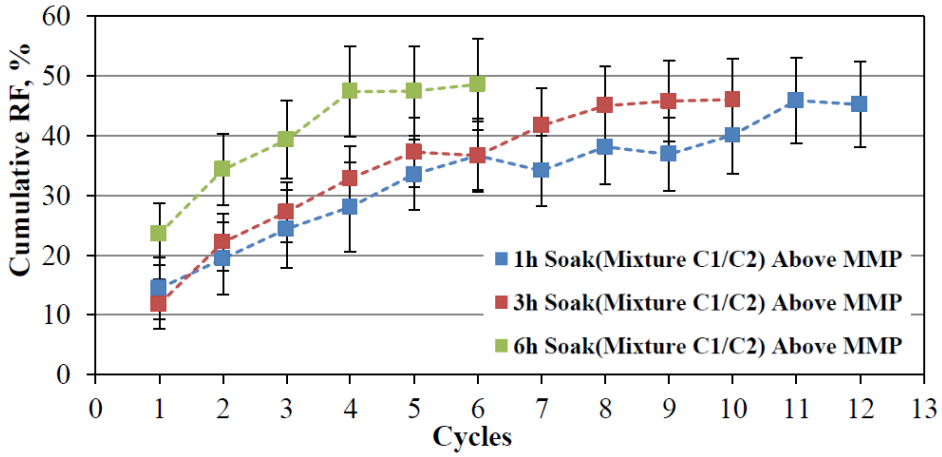


Figure 4.1: Impact of soaking time on huff-and-puff recovery for the Eagle Ford samples (Dang, 2019).

4.2 Fracture Distribution

Damani et al.(2018) have shown that the fractures emanating from the primary fractures follow a Lorenz/Cauchy distribution (**Section 2.1.1.2**), with secondary fracture density decreasing away from the wellbore. Smaller matrix blocks are expected to be created near-wellbore due to higher complexity, and matrix blocks gradually increasing in size are expected with decreasing fracture density away from the wellbore. As mentioned in **Section 3.5.4**, for the second phase of this study, the L was varied from 10 m (base case) to 0.01 m (four orders of magnitude) to understand the movement of the diffusion front (accessibility) on different matrix blocks created during hydraulic fracturing treatment.

4.3 Sensitivity Analysis

Chapter 3 included the model validation results and the various sensitivities to evaluate the impact of stimulated reservoir volume on the efficacy of huff-and-puff recoveries. This chapter extends the previous work to investigate the effect of the soaking phase on the huff-and-puff EOR recoveries in the presence of a secondary fracture network. The following two sensitivities were carried out using the model developed.

- The effect of the soaking phase on the different-sized matrix blocks was investigated as a function of various soaking times while keeping the injection and production cycle times constant.
- The effect of the soaking phase on the different-sized matrix blocks as a function of diffusion coefficients, which changes with pressure and composition with each huff-and-puff cycle, spatially and temporally.

4.3.1 Effect of Soaking Time on Different Size Matrix Blocks

To evaluate the effect of the soaking phase on huff-and-puff recoveries, the model outputs were compared for the different-sized matrix blocks (0.01, 0.1, 1, and 10 m) at different soaking times of 1, 15, 30, and 90 days. The injection and production times were kept constant at 30 days, along with an effective diffusion coefficient of 1×10^{-9} m^2/sec and alpha of 0.1 (representing field scale), so the results for the soaking phase can be compared in isolation. **Figure 4.2** shows the results with the penetration length ratio, i.e., the penetration lengths after the soaking phase to that after the injection phase, for the different matrix blocks:

- Both the 0.01 and 0.1 m cases achieve a penetration length ratio of 100% within one day of soaking. A penetration length ratio of 100% suggests that the soaking phase does not help with any additional recoveries.
- Both the 1 and 10 m cases show an increasing penetration length ratio with longer soaking times.

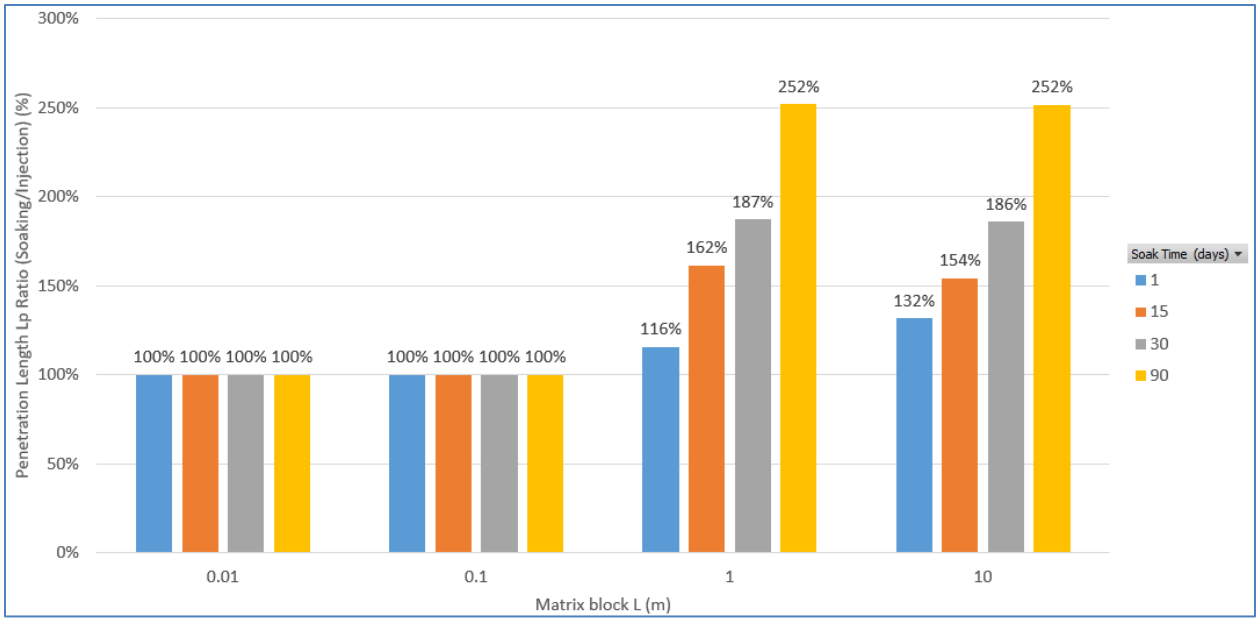


Figure 4.2: Comparison of soaking to injection penetration length ratios for the different matrix blocks (0.01, 0.1, 1, and 10 m) as a function of various soaking times. Injection and production cycle times were kept constant at 30 days each.

4.3.2 Effect of Diffusion Coefficient D_e on Different Size Matrix Blocks

Next, the effect of soaking time on the different matrix blocks was evaluated as a function of effective diffusion coefficients. The effective diffusion coefficients were varied by four orders of magnitude, from 1 x 10^{-7} through 1 x 10^{-10} m^2/sec. The cycle times for each phase (injection, soaking, and production) were kept constant at 30 days. **Figure 4.3** shows the penetration length

ratio for the different matrix blocks as a function of varying diffusion coefficient values. A few observations can be made:

- All 0.01 m cases have a penetration length ratio of 100%, irrespective of the D_e. The penetration length ratio of 100% suggests that the soaking phase does not help with any additional recoveries.
- Similar results were observed for the 0.1 m cases, except when the D_e approaches 1 x 10^{-10} m^2/sec and the soaking phase starts to help increase accessibility.
- All 1 and 10 m cases have a penetration length ratio of over 100%, except for the 1 m case with a higher D_e value (1 x 10^{-7} m^2/sec). Values of over 100% indicate that the soaking phase increases the accessibility for larger block sizes of 1 and 10 m.

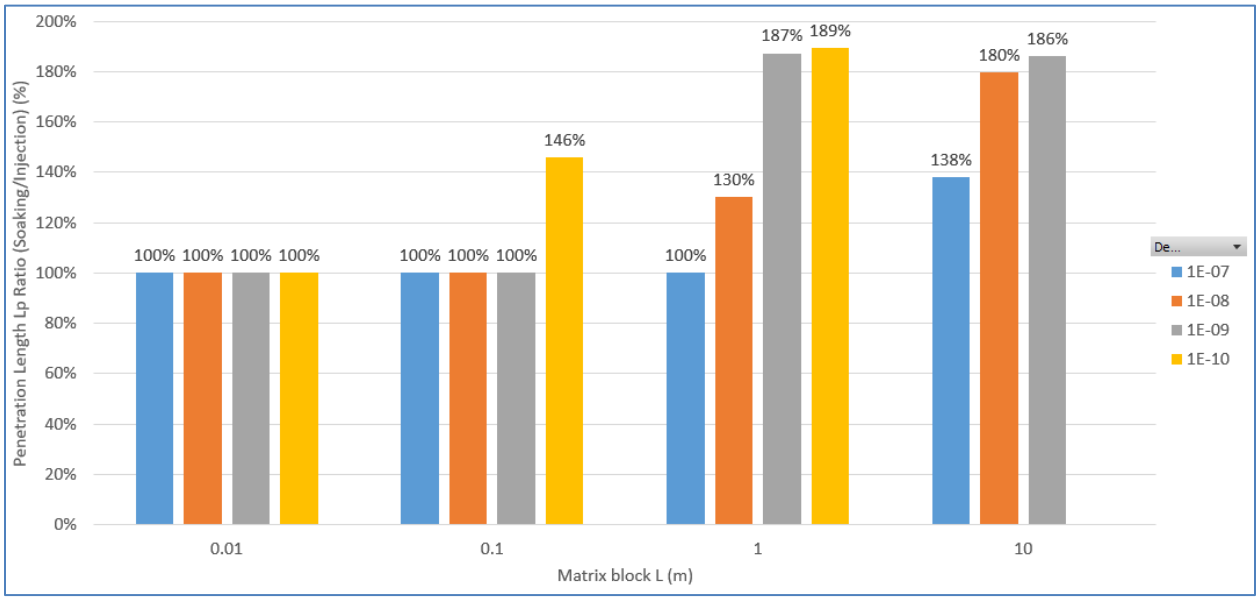


Figure 4.3: Comparison of soaking to injection penetration length ratios for the different matrix blocks (0.01, 0.1, 1, and 10 m) as a function of various effective diffusion coefficient values. Injection, soaking, and production cycle times were kept constant at 30 days each.

4.4 Discussion

For the formulation of the mathematical model, it is assumed that the miscible conditions already exist with reservoir pressure higher than the minimum miscibility pressure (MMP). The MMP measurement pertinent to the huff-and-puff process in tight shale reservoirs is the First Contact Miscible (FCM) MMP measured by the swelling test. The FCM MMP is usually 1,000 psi or greater higher than the Multiple Contact Miscible (MCM) MMP measured by slim tube test for displacement EOR process in conventional reservoirs (Mydland et al., 2020; Carlsen et al., 2020).

Additionally, we have assumed the huff-and-puff process to be primarily diffusion-driven in the different-sized matrix blocks. However, the authors acknowledge that advection may play a small role as a transport mechanism due to pressure gradients, and the impact on recovery is not included in the results. With respect to diffusion, for the production (or puff) phase, the diffusion coefficient used was one order of magnitude lower than that for the injection and soaking stages to account for the two-phase phenomenon. However, the diffusion coefficient value was still assumed constant for each phase, which is a limitation of all the models. In reality, the diffusion coefficients change during the huff-and-puff cycles with changes in pressure and composition, which is hard to simulate in a model.

Lastly, the formulation and the model outputs are based on 1-D flow. If we extend the 1-D solution to 3-D, the penetration lengths would be less. This would make the impact of the soaking phase even more significant with the larger fracture blocks.

Bin et al. (2020) have argued that the Huff-and-Puff oil recoveries depend on “residence time,” i.e., soaking and production time, and not soaking time alone. A couple of counter-arguments would be: (1) the experiments were performed using 7-8 mm crushed samples with

significant surface area, and the response would be different with different-sized samples, especially larger-sized samples, and (2) the fluid flow during the soaking and production phases are governed by counter-current and co-current diffusion processes, respectively, and so the soaking and production times should not be lumped together in analysis.

Perez & Devegowda (2020), based on molecular dynamics simulation with a 72:28 C1:C2 mixture as an injectant, observed an upper limit (threshold) to the penetration of the injectant during the soaking phase. However, penetration length is expected to be a function of the injectant composition (results covered in **Section 5.5**), so additional recoveries could be expected with optimization of the injectant composition. Furthermore, Perez and Devegowda (2020) observed a **counterflow of hydrocarbon molecules from the organic kerogen to the microfracture during the soaking period**, resulting in the additional benefit of the soaking phase.

4.5 Key Takeaways

Much speculation exists in the industry about whether the benefits of the soaking phase are sufficient to offset the time lost during soaking when the well is shut in. This chapter extends the model developed in Chapter 3 to investigate the relevance of the soaking phase in the huff-and-puff process.

- Fracture geometry created near the wellbore, i.e., fracture spacing and distribution, has a first-order effect on the efficiency of the huff-and-puff process in the field. However, Damani et al.(2018) have shown that the fractures emanating from the primary fractures follow a Lorenz/Cauchy distribution, with secondary fracture density decreasing away from the wellbore.

- The soaking phase was found to be significantly less impactful on the smaller matrix blocks closer to the wellbore. However, larger matrix blocks away from the wellbore show increasing penetration lengths with longer soaking times.
- Since the initial huff-and-puff cycles are suspected to be tapping into and recovering the remaining oil from smaller matrix blocks near the wellbore, the operators can possibly skip or limit the soaking phases from the initial cycles to optimize the process. However, as the large matrix blocks away from the wellbore are the main contributor to production in subsequent cycles, increasing the duration of soaking stages for the subsequent cycles is recommended.

Chapter 5

The Issues of Containment and Asphaltene Deposition

The shale reservoirs, in general, are characterized by low porosity (typically less than 5%) and ultra-low permeability (usually less than 1,000 nD). Due to these tight flow characteristics, conventional miscible and immiscible flooding techniques using injector and producer well pairs do not apply to unconventional shale reservoirs. As a result, over the past decade, the industry has shifted to cyclic miscible gas huff-and-puff EOR from the same well. The results from the pilot tests in the various shale plays have highlighted additional complexities in the huff-and-puff process that need to be better understood. This chapter discusses two of these complexities: a) containment of the injected gas, and b) asphaltene deposition during the miscible gas injection process.

Although gas as an injectant has been used because of its high injectivity compared to water and can develop miscibility with the reservoir oil, other injectants need to be explored. A new liquid solvent injectant is introduced and evaluated as an alternative, which shows several technical and economic benefits over gas injectants, including minimizing these two complex issues.

5.1 Containment of Injected Gas

As covered in Chapter 2, one of the factors limiting the successful implementation of this technique in the field is the containment (or confinement) of injected gas within the drainage area of the pilot well(s) (Baldwin et al., 2020; Carlsen et al., 2019; Eltahan, 2020; Ganjdanesh et al., 2019a; Ganjdanesh et al., 2019b; Grinestaff, 2019; Jacobs, 2019; Jin, 2019; Kerr et al., 2020;

Rogers et al., 2020; Salahshoor, 2020; Torres et al., 2019). The gas containment is essential for pressure buildup in the reservoir to achieve miscibility with the remaining oil.

Limited laboratory studies have been carried out with fractured core samples to investigate the impact of gas breakthroughs on oil recovery. In the case of pilots, horizontal (and not vertical) containment has been observed as an issue (Jacobs, 2019). The inter-well communication could be due to:

1. The unoptimized hydraulic fracture stimulation, with uneven distribution of fluid and proppant between clusters within a stage, resulting in long, tensile hydraulic fractures and prolonged communication between wells (Jacobs, 2019), and/or
2. As observed in the Eagle Ford shales, the reactivation of long natural and/or closed hydraulic fractures with gas injection in the form of shear slip, shear dilation, or local propagation based on the stress- and other pressure-dependent properties (Torres et al., 2019).

While a large surface area is critical for the injected gas to contact the residual oil, there have been cases where these long fractures allow the early breakthrough of the gas into neighboring wellbores. The injected gas moves so fast through these long-connected fractures that it becomes difficult for the injected gas to mix with the stranded oil in the matrix. Lack of containment due to early breakthroughs of the injected gas limits the miscibility of the fluids, thereby reducing recovery of the remaining mobile oil.

Common approaches taken by the operators are to either shut in the offset wells during the injection period (Carlsen et al., 2019; Kerr et al., 2020) or convert the exterior wells on the pad into water injection wells to act as a water curtain (Baldwin et al., 2020; Torres et al., 2019). Another method utilized by one of the operators in Bakken includes using a rapidly switching 2-

phase slug of gas and water to control the injectant breakthrough in offset wells while allowing the pressure buildup to increase beyond MMP (Section 2.2). Section 5.3 includes two case studies from the Eagle Ford shale, where the operator applied different strategies to minimize the horizontal containment issue.

5.2 Asphaltene Deposition with Miscible Gas Injection

The crude oil is considered a colloidal system, with the asphaltenes and resins constituting the dispersed state, while the aromatics and saturates are present in the continuous phase. Generally, the presence of asphaltenes in the *in situ* reservoir fluid is not considered an issue as it exists in a balanced state with resins. Due to the opposite charges, the resins have a strong propensity towards asphaltenes and hold the asphaltene micelles in suspension through attraction forces, thereby enhancing the stability of the colloidal system. The asphaltenes and resins remain in thermodynamic equilibrium until one of the conditions, i.e., pressure, temperature, or oil composition, changes. However, when the injected gas becomes miscible with the remaining oil, the composition of the oil (percentage of saturates, aromatics, resins in the liquid phase of oil, and asphaltenes that exist as solids in the oil) changes, which disrupts the balance of the crude oil colloidal system, thereby resulting in the deposition of the asphaltenes in the reservoir (Ashoori et al., 2017; Xiong et al., 2023). The precipitation and irreversible retention of asphaltenes can lead to formation damage and pore plugging, thereby causing permeability impairment and oil recovery reduction (Shen & Sheng, 2016; Sofla et al., 2024).

In terms of composition, even though heavy oils have a significant asphaltene content, precipitation chances are reduced due to the large concentration of resin available to stabilize the

asphaltene particles. Asphaltene precipitation issues are more common in light to medium oils, which contain low asphaltene concentrations (de Boer et al., 1995).

The process of asphaltene precipitation and deposition with the miscible gas injection is well-studied and documented in conventional reservoirs using core flooding experiments, X-ray, SEM imaging, etc. (Behbahani et al., 2013; Behbahani et al., 2014; Hamadou et al., 2008; Sim et al., 2005; Srivastava et al., 1997; Turta et al., 1997). Laboratory experiments in the conventional reservoir cores have shown a significant permeability reduction due to asphaltene deposition. The asphaltene deposition was a function of pre-injection core permeability, CO_2 gas concentration (as most of the experiments were carried out with CO_2 as the miscible gas), and the quantity and size of asphaltene particles in the reservoir oil. Maroudas (1996) found that particles with a size greater than $1/3^{rd}$ of the size of pore throats could severely block the pore throats, and it aligns with the 1/3-1/7 rule of thumb reported in the literature for potential permeability reduction with different reservoir core samples (Partz et al., 1989; Sim et al., 2005).

In the shale reservoirs, the pore throat sizes are much smaller, and large asphaltene aggregates may cause more severe plugging problems. Additionally, the oil produced from shale reservoirs is of light to medium gravity, which tends to have more severe asphaltene precipitation issues. Both of these reasons could lead to asphaltene deposition during the miscible gas injection in shale reservoirs, though the severity would depend on the type of gas injected. Some may argue that the fluid samples collected at the surface are not representative of *in situ* fluids as the production occurs after molecular sieving (or filtration) through tiny pore throats, so the *in situ* oil may be less susceptible to asphaltene precipitation.

In recent years, a few studies have been carried out to investigate the effects of asphaltene precipitation during huff-and-puff miscible gas injection in shale reservoirs. Shen and Sheng

(2016) conducted experiments with CO_2 and CH4 injection into the Eagle Ford cores. They found that higher concentrations of injected gas caused more precipitation and growth in asphaltene aggregates' size. Furthermore, Shen and Sheng (2017) reported a more than one-third permeability reduction due to asphaltene deposition in the Eagle Ford cores and the plugging of pores smaller than 800 nm. Compared to the pre-injection measured permeability of 126 nD, the experimental results showed a 47.5 nD permeability reduction after six cycles of the CO_2 huff-and-puff process. Mohammad et al. (2017) investigated the asphaltene deposition by conducting a compositional reservoir simulation. They pointed out that when the bottom hole pressure drops below saturation pressure, gas comes out of the solution (compositional change), which reduces the solubility of the asphaltene and induces precipitation. To reduce asphaltene deposition, the reservoir pressure must be maintained above the Asphaltene Onset Pressure (AOP). Shen and Sheng (2019) conducted a numerical study to understand better the physical mechanisms and key parameters affecting asphaltene deposition. They found that the asphaltene precipitation and deposition behavior differ in the matrix and the fracture network. In the matrix, the asphaltene deposition occurs during both the huff and puff cycles, while in the fracture network, it is primarily in the puff cycle. Reducing huff cycle time and increasing puff cycle time were reported as favorable strategies for reducing asphaltene deposition. Additionally, higher pressure during the huff cycle and lower pressure during the puff cycle were preferred, although they seemed to promote asphaltene deposition. Li et al. (2020) conducted experiments to simulate the CO_2 huff-and-puff process using outcrop samples. They found that the maximum asphaltene deposition occurs during the first huff-and-puff cycle. Also, after seven cycles of huff-and-puff, the cumulative oil recovery was 21.5% lower with the asphaltene deposition than without any deposition.

The laboratory-scale experiments by Elturki and Imqam (2022) on the Eagle Ford cores with CO_2 huff-and-puff found the asphaltene deposition to be a function of injection pressure, miscibility, and soaking duration. As reported in other studies, pressures higher than the MMP resulted in improved oil recovery as CO_2 in a miscible state has good solubility with oil. However, below MMP, the asphaltene clusters are deposited primarily in the larger pores. After a few cycles, as the pressure reaches above MMP, the asphaltenes fill both the large and small pores, resulting in decreased oil recovery from subsequent cycles. Although this is preliminary laboratory work that has not yet been scaled to field pilots, it could be a factor showing a decreasing oil rate in the subsequent huff-and-puff cycles after the initial boost in oil rate from the first cycle. Additionally, the authors pointed out that shorter soaking times yielded better oil recovery as it reduced the time for asphaltene accumulation within the cores before switching to the puff cycle. Finally, CO_2 was found to be a better injectant for huff-and-puff than N_2 for the first five cycles; however, additional huff-and-puff cycles with CO_2 resulted in an increased asphaltene deposition within the core.

Although some research has been carried out in recent years to investigate the factors promoting asphaltene instability during the miscible gas injection in shale reservoirs, the mechanism still needs to be fully understood. Upscaling these results to the field scale could help better understand the asphaltene deposition mechanism and minimize the permeability reduction that impedes additional oil recovery.

5.3 Case Studies from Two Huff-and-Puff Pilots in the Eagle Ford

EP Energy (now Verdun Oil Company) developed two natural gas miscible cyclic huff-and-puff EOR projects in the Eagle Ford in 2018 – Maltsberger and Richie Farms lease – located in the gas condensate and volatile oil windows, respectively. Each of these leases was first modeled

in a reservoir simulator to characterize the subsurface and understand the recovery uplift expected from the huff-and-puff EOR process before implementing it in the field, as detailed and explored further in this section.

Although the two leases were located only a few miles away, the injection of available produced gas resulted in higher incremental oil recovery in the gas condensate pilot compared to the volatile oil. As part of the robust characterization, both the leases were found to have severe inter-well communication, which resulted in a limited miscibility downhole, thereby reducing the effectiveness of the huff-and-puff process. Additionally, the recovery uplift from the huff-and-puff EOR process depends on the composition of the injectant gas and the reservoir pressure, which have a first-order impact on the mixing/miscibility of the fluids in the formation.

5.3.1 Pilot in the Eagle Ford Gas Condensate Window

The Maltsberger EOR project consisted of 13 horizontal producing wells (three parent wells and ten child/infill wells) in LaSalle County, Texas, with a well spacing of 550 ft. Because of the difference in the development timing of the wells on the lease, the completion design varied across the wells. The cluster spacing in the wells varies from 22 to 49 ft, with wider cluster spacing in the parent wells developed earlier. The production history ranges from 4 to 8 years, with the parent wells producing for about eight years while the newest child wells had four years of production, and each well was producing less than 10 barrels of oil per day at the time of the study in 2018.

Ganjdanesh et al. (2019a), Ganjdanesh et al. (2019b), and Carlsen et al. (2019) describe the compositional reservoir simulation model developed and the production stream tracking to predict the performance of huff-and-puff EOR. The fracture hits observed on the parent wells during the

hydraulic fracture stimulation of child wells and the well-to-well communication observed during the depletion phase were critical in characterizing the subsurface in the sector model. The image logs from the offset wells showed high fracture intensity and were used to build an Embedded Discrete Fracture Model (EDFM). Several long fractures connecting the different producers had to be added to the sector model to history match the pressure and production data responses. The field production data for the depletion phase was initially used to history match the sector model. Then, the field data from the initial huff-and-puff cycles were incorporated to fine-tune the model further. The pressure history matching showed that the interwell fractures could be as long as 2,500 ft. **Figure 5.1** shows the history-matched sector model, including the multiple long interwell fractures. In the model, these fractures resulted in the migration of the injected gas away from the injector, thereby bypassing most of the remaining oil in the matrix, hindering pressure buildup in the reservoir, gas containment, and limiting the efficacy of the huff-and-puff EOR process.

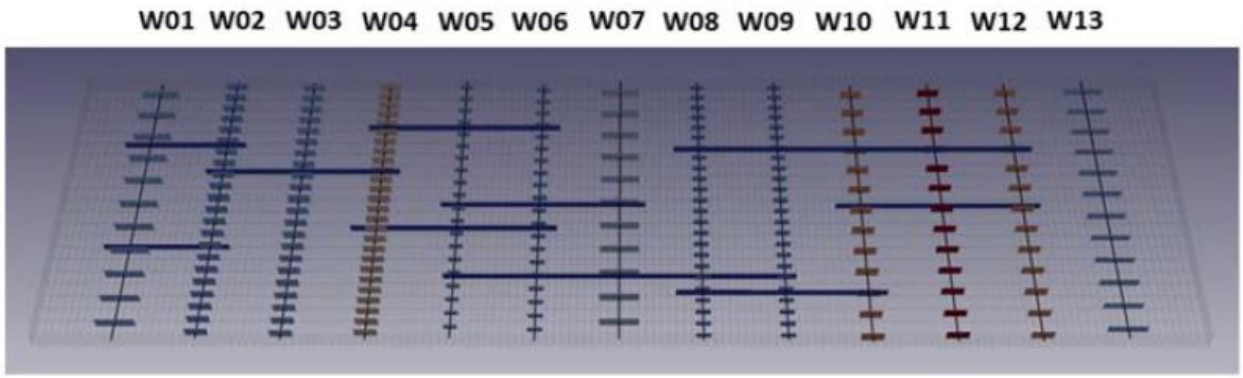
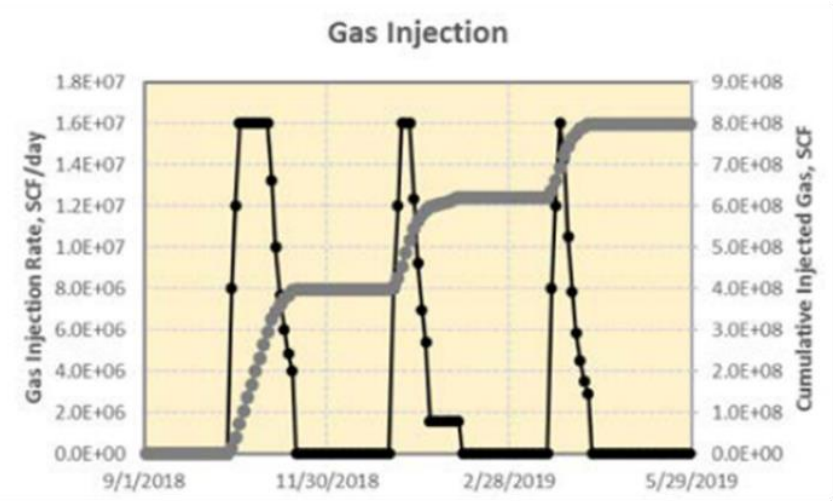
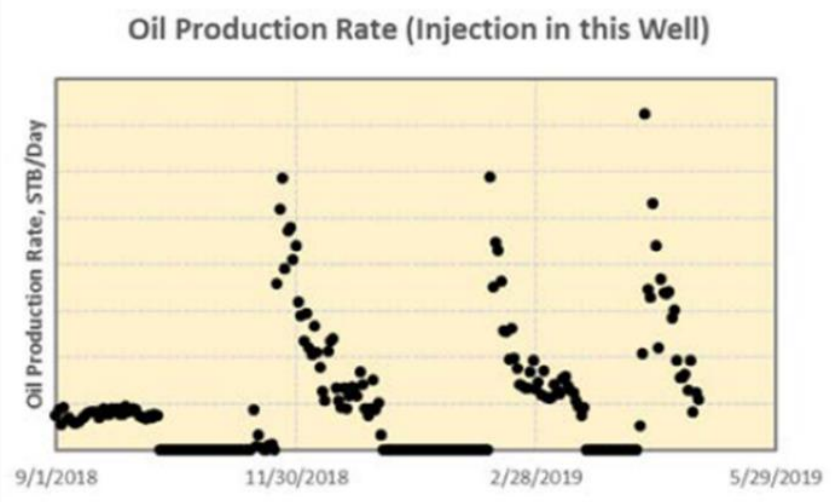


Figure 5.1: Reservoir simulation history-matched model for EP Energy's Maltsberger EOR project consists of 13 horizontal wells and multiple long interwell fractures (Ganjdanesh et al., 2019b).

Based on the results from this composition model, the huff-and-puff process was implemented in two cycles. For the first cycle, the produced gas was injected into well W09 (**Figure 5.1**) while the four offset wells (W07, W08, W10, and W11) were shut in for pressure containment and to minimize the escape of the injected gas through long connecting fractures. **Figure 5.2** shows the observed and simulated results for the first three huff-and-puff cycles for the well W09. 400 mmscf of field gas (76.8% C1, 19% C2/C3, 4.2% C4/C5/C6) was injected for the first injection cycle of 32 days, followed by 200 mmscf of gas for the second and third cycles, all with a maximum injection pressure and gas injection rate of 7,500 psi and 16 mmscf/d. A sharp six-fold increase in the oil rate was observed during the production phase compared to the pre-huff-and-puff oil rate (**Figure 5.2b**). Due to the differences in the injection schemes and volumes for the three cycles, the oil production rate response differed after each cycle. The model outputs for bottom hole pressure matched the observed pressures closely (**Figure 5.2c**), which built confidence in the calibrated model. After the first injection cycle in well W09, the gas was injected into well W02 while the three offset wells (W01, W03, and W04) were shut in. The calibrated model was run for five years to simulate 15 huff-and-puff cycles in each well, and the results show about 20 and 15 percent increase in cumulative oil production for the W09 and W02 wells, respectively (Ganjdanesh et al., 2019a; Ganjdanesh et al., 2019b). This was followed by optimizing the injectant composition, where a rich gas (70% C2, 30% C3) was evaluated. As discussed in Section 2.1.2.1, injecting rich gas in a condensate reservoir shrinks the phase diagram and decreases the dew-point pressure, resulting in incremental oil recovery of greater than 25 percent (compared to 15-20% with the field gas).





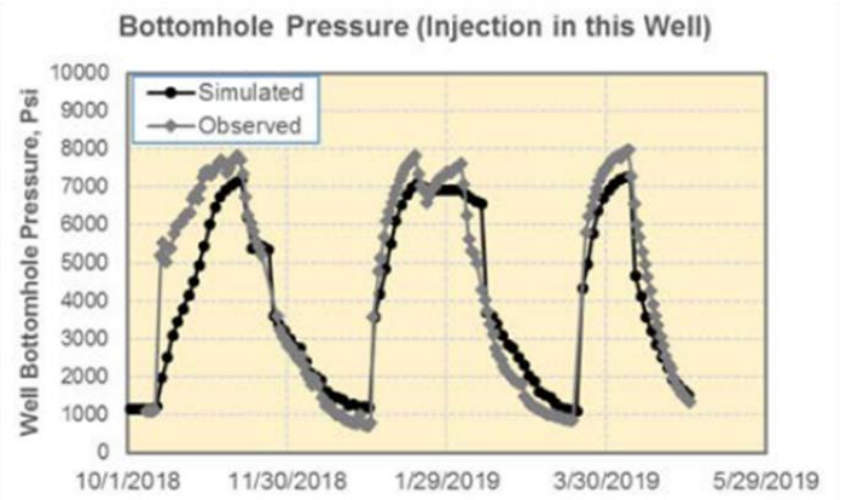


Figure 5.2: Observed and simulated results for three initial huff-and-puff cycles for EP Energy's Maltsberger W09 well – a) Gas Injection Rates and Cumulative Injected Gas Volume, b) Oil Production Rate, and c) Bottomhole Pressures(Ganjdanesh et al., 2019b).

5.3.2 Pilot in the Eagle Ford Volatile Oil Window

Compared to the Maltsberger EOR project, the Richie Farms EOR project consisted of only three horizontal wells in the volatile oil window of Eagle Ford in La Salle County, Texas. Learnings and takeaways from the Maltsberger simulation project were utilized to evaluate the Richie Farms lease for huff-and-puff potential. The original model consisted of over two dozen wells; however, the Ritchie Farms lease was selected because it showed the highest huff-and-puff potential in the numerical model (Kerr, 2024).

The Ritchie Farms lease was developed with a well spacing of approx. 440ft, a slightly tighter well spacing than the Maltsberger lease in the Gas Condensate area. All three wells were co-developed, with an average lateral length of about 5,850 ft. The easternmost well (158H) was a child well, offsetting a parent well developed in 2011. Each well consisted of 16 stages and was completed using a hybrid crosslink/linear gel fluid system, with 40 ft cluster spacing, 9 clusters per stage, and 360 ft stage length at ~30 bbl/ft fluid intensity (Enverus Prism, 2024; Kerr et al., 2020). The wells started production in March 2017, and each well was producing 50-100 barrels of oil per day a year later at the time of the EOR study. Similar to the Maltsberger EOR project, the produced gas from the field was used for cyclic natural gas injection.

Kerr et al. (2020) describe the simulation study that was carried out to optimize the injection pressure and slug sizes. Significant pressure communication between the wells was observed via natural and induced fractures during the huff-and-puff pilot, which caused a loss of injected gas to offset wells. The two exterior wells on the lease (or the “edge wells”) were converted into water injectors to mitigate the containment issue, and the field results showed an additional 7-12% recovery with this approach (Venepalli et al., 2021).

For this research, the efficacy of the different injectants in the huff-and-puff process is evaluated through a reservoir simulation model for the Ritchie Farms EOR pilot. Section 5.4 describes the model construction and history match results for the primary depletion phase and the initial huff-and-puff cycles modeled using the produced gas. In Section 5.5, the calibrated reservoir model is used to run sensitivities for the different injectants, where the model results for the field gas are compared to carbon dioxide and dimethyl ether as two other possible injectants.

5.4 Numerical Modeling of the Ritchie Farms Huff-and-Puff EOR Pilot

This section replicates the history-matching previously completed on the EP Energy (now Verdun Oil Company) Ritchie Farms natural gas huff-and-puff EOR pilot using GEM modeling software by Computer Modeling Group (CMG), followed by running various scenarios to evaluate the efficacy of huff-and-puff scenarios. Publicly available data (as referenced) and personal communication with the operator were utilized for research, data gathering, and initial model building.

Reservoir Characterization

Bustin et al. (2022) conducted laboratory analyses of the Eagle Ford core from the Ritchie Farms lease. The cores showed two distinct reservoir facies, both primarily consisting of limestones, and were found to be highly laminated and very thinly bedded. The mineralogy of EF 1/2 facies comprised 62% calcite, 26% quartz, 6% clay, 3% feldspar, pyrite traces, and a 9-11% porosity. In contrast, the EF 3/6 facies comprised 88% calcite and 11% quartz, with a lower porosity of 3-7%. The pore size distribution for both facies had a uni-modal distribution and was found to be in the range of 15-40 nm, and effective permeability to gas was found to be about 200 nD at in situ reservoir stress.

Fiallos et al. (2019) and Torres et al. (2019) described the natural fracture characterization completed for the area. Similar to the Maltsberger lease, fracture hits during hydraulic fracture stimulation and inter-well communication during the depletion phase have also been observed in the Ritchie Farms area. Ultrasonic wellbore image (WBI) logs were analyzed for fracture detection around the wellbore, and the severity of existing fractures ranged from very weak to significant. An EDFM model was built and history-matched to help characterize the inter-well communication and match the empirical observations from the field. Long inter-well fractures reached up to 3,500 ft in length and often promoted bottom-hole pressure equalization among the connected wells.

Fluid Characterization

A twelve-component Peng Robinson Equation of State (EOS) model was developed by Kerr et al. (2020) to characterize the PVT surface samples collected from two nearby Eagle Ford wells (5H and 92H). The composition of the two recombined fluid samples is shown in **Table 5.1**, with a C7+ mole fraction greater than 40% for both wells, indicating both wells to be black oil fluid samples. The initial reservoir pressure is about 4,900 psi, and the reservoir temperature is 215 °F. **Table 5.2** and **Table 5.3** show the EOS parameters and Binary Interaction Coefficients (BICs) for the fluid model after tuning. **Table 5.3** shows the BICs for non-hydrocarbon and hydrocarbon pairs, and zero values of BICs were assumed for the hydrocarbon-hydrocarbon pairs. The oil and gas phase viscosities were calculated using the Jossi, Stiel, and Thodos correlation with the low-pressure mixture viscosity evaluated using the Herning-Zipperer & Yoon-Thodos (HZYT) formulas. The comparison of the experimental data to the EOS model for Constant Mass Expansion, Viscosity, Slim tube, and Differential Liberation experiments are included in Kerr et al. (2020).

Table 5.1: 12-Component Composition for the Two Nearby Eagle Ford Wells, 5H and 92H (modified from Kerr et al., 2020)

Component	Ritchie Farms 5H	Ritchie Farms 92H
	mol %	mol %
C1	32.472	32.497
C2	8.756	8.275
C3	5.747	5.569
iC4 + nC4	4.139	4.281
iC5 + nC5	3.287	3.404
C6	2.876	2.950
C7-C10	14.634	15.159
C11-C20	19.183	18.605
C21-C45	7.997	8.266
C46-C80	0.427	0.501
N_2	0.078	0.077
$CO_2 + H_2S$	0.403	0.416

Table 5.2: EOS Parameters of the 12-Component Fluid Model (modified from Kerr et al., 2020)

Component	Critical Pressure Pc	Critical Temp Tc	Molecular Weight	Density	Acentric Factor	Critical Volume Vc	Peneloux Volume Shift Parameter Cpen
	psig	°F	g/mol	g/cm^3	unitless	ft^3/lb-mol	ft^3/lb-mol
C1	652.502	-116.590	16.04		0.008	1.586	-0.083
C2	693.651	90.050	30.07		0.098	2.371	-0.093
C3	601.066	205.970	44.10		0.152	3.252	-0.102
iC4 + nC4	530.514	297.465	58.12		0.188	4.119	-0.107
iC5 + nC5	475.396	377.547	72.15		0.239	4.885	-0.090
C6	415.897	453.650	86.18	0.6640	0.296	5.927	0.022
C7-C10	355.488	508.891	114.08	0.7498	0.418	8.134	0.075
C11-C20	246.601	840.512	199.00	0.8097	0.760	10.895	0.493
C21-C45	185.994	1,057.333	383.37	0.8793	1.239	29.971	-0.437
C46-C80	161.148	1,553.583	745.23	0.9498	1.145	40.518	-2.774
N_2	477.620	-232.510	28.01		0.040	1.438	-0.068
$CO_2 + H_2S$	1,066.538	94.127	43.38		0.219	1.509	-0.029

Table 5.3: Binary Interaction Coefficients for the Different Components

Component	N_2	$CO_2 + H_2S$
C1	3.1100E-02	1.1744E-01
C2	5.1500E-02	1.1765E-01
C3	8.5200E-02	1.1794E-01
iC4 + nC4	8.6226E-02	1.1595E-01
iC5 + nC5	9.6202E-02	1.1626E-01
C6	8.0000E-02	1.1553E-01

C7-C10	8.0000E-02	9.3608E-02
C11-C20	8.0000E-02	9.3608E-02
C21-C45	8.0000E-02	9.3608E-02
C46-C80	8.0000E-02	9.3608E-02
N_2	-	-4.6196E-03
$CO_2 + H_2S$	-4.6196E-03	-

Model Description

A compositional, single-porosity reservoir simulation model was created to match the production data from an Eagle Ford Pilot in the volatile oil window, based on the project description in Fiallos et al. (2019), Torres et al. (2019), and Kerr et al. (2020).

A coarse model was built first to compare the history match results with the published literature (Kerr et al., 2020). Although the lease consisted of three wells, the sector model consisted of modeling one stage per well. An element of symmetry approach was used rather than modeling the entire lateral since the hydraulic fracture design was the same along the laterals, as shown in **Figure 5.3**. A grid block size of 40 ft in the x- and y-directions was created to accommodate the cluster spacing of 40 ft. The top of the grid block was defined at 7,930 ft depth, with seven layers of variable grid thickness based on log and core data from nearby pilots (total pay thickness of 130 ft). The initial reservoir pressure is about 4,900 psi, and the reservoir temperature is 215 °F. The absolute permeability of the grid block in the x- and y-directions was defined as 788 nD, and the permeability in the z-direction was assumed to be $1/10^{th}$ of the horizontal permeability or 78.8 nD. The porosity and water saturation for the matrix were defined as 9% and 35.28%, respectively, based on the petrophysical analysis.

For the single stage modeled for each well, three different asymmetric fracture geometries were defined to capture the uneven fracture distribution and conductivity typically observed in the field (**Table 5.4**). Rather than discretizing the hydraulic fractures individually, the hydraulic

fractures were modeled using logarithmically-spaced, locally-refined (LS-LR) grid blocks to reduce the computational time as well as being able to capture the movement of the pressure transients in the tight shale matrix. The fracture orientations were in line with the Microseismic mapping observations and wellbore downhole imaging, and the effective fracture half-lengths were modeled to vary from 65 to 150 ft (Kerr et al., 2020). Additionally, to history match the water production without modeling water injection, the water saturation values in the primary hydraulic fracture (referred to as Fractured Zone in CMG) and surrounding SRV (Non-Fractured Zone) were increased to higher values than the water saturation in the matrix (**Table 5.4**).

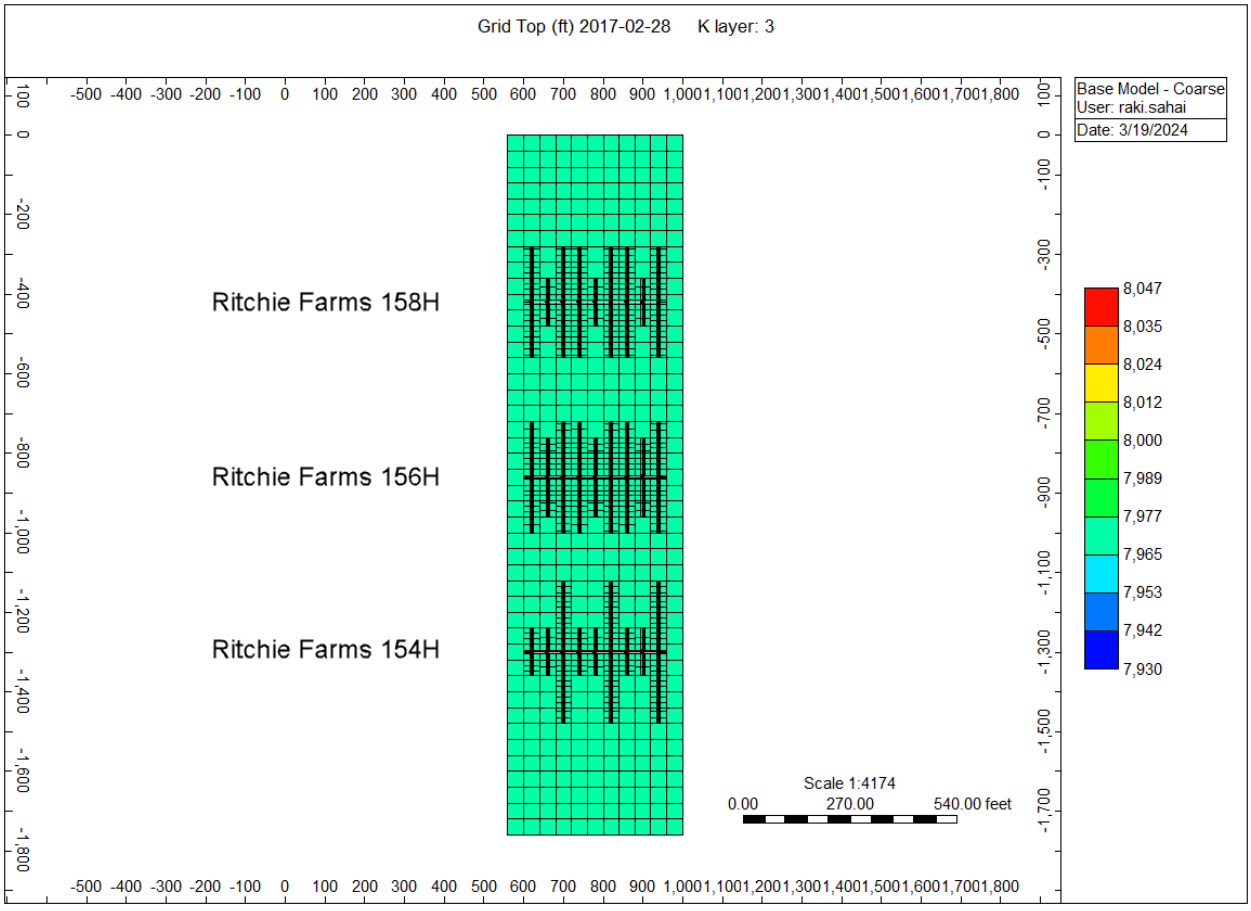


Figure 5.3: Reservoir simulation grid for the Ritchie Farm pilot, showing a single stage for the three wells (154H, 156H, and 158H), each with nine clusters with asymmetric fracture geometries.

5.4.1 History Matching

The model was history-matched using the CMG's CMOST automated history-matching tool by tuning the matrix (matrix permeability and relative permeability) and hydraulic fracture (hydraulic fracture half-length, hydraulic fracture height, and fracture conductivity) properties. The ranges for the tuning parameters were picked based on the info provided by Bustin et al. (2022), Torres et al. (2019), and Kerr et al. (2020).

Since the wells were completed with 16 stages each, the actual production for each well was scaled to represent the production from a single stage and used for the history matching. Although a history match with reasonable history match error was obtained using CMOST, the hydraulic fracture properties were hard coded to those reported by Kerr et al. (2020), shown in **Table 5.4**, and were held constant for the sensitivities.

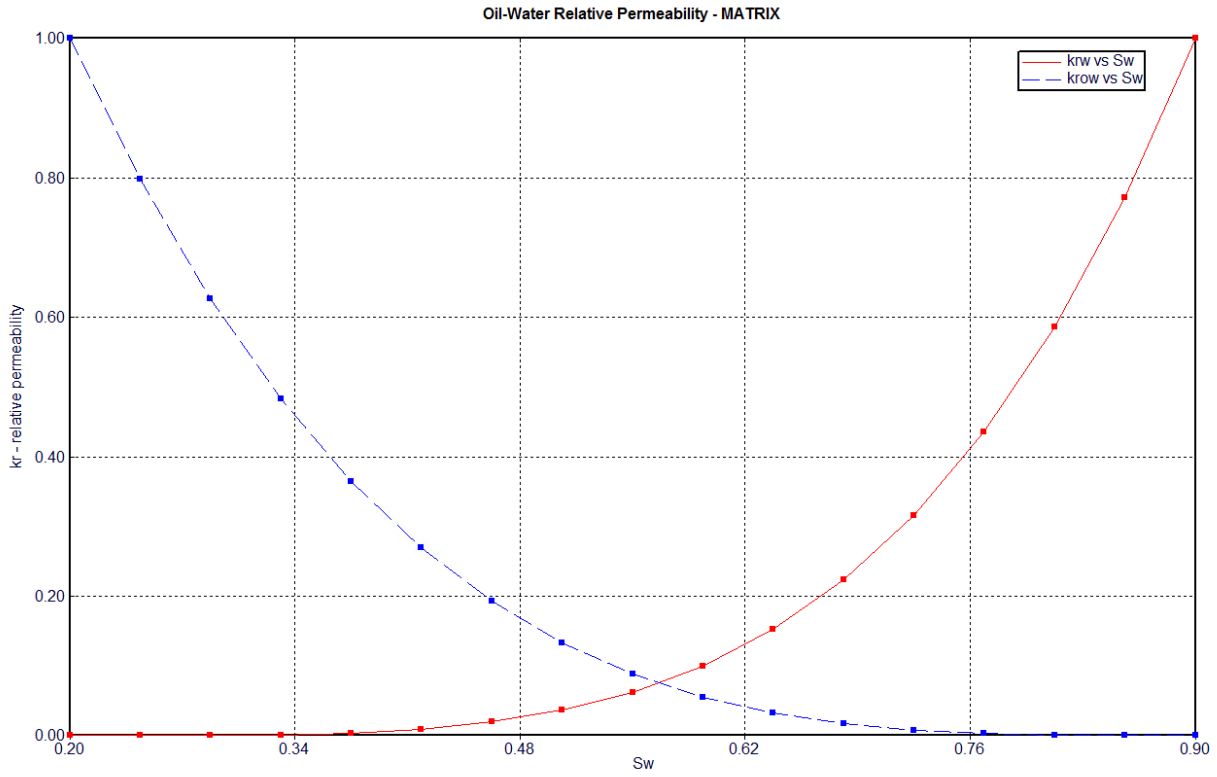
Figure 5.4 shows the oil-water and gas-liquid relative permeability curves used for the matrix, while straight-line relative permeability curves were used for the hydraulic fractures. **Figure 5.5** through **Figure 5.7** show the history match results for the three wells, which used total fluid as the constraint while matching the bottom hole pressure. **Figure 5.8** shows the pressure distribution with the coarse model at the end of the history match.

Table 5.4: Hydraulic fracture properties used for the three wells (154H, 156H, and 158H), with three different fracture geometries per well (Kerr et al., 2020)

Hydraulic Fracture Properties		Ritchie Farms 154H			Ritchie Farms 156H			Ritchie Farms 158H		
		Design 1	Design 2	Design 3	Design 1	Design 2	Design 3	Design 1	Design 2	Design 3
Xf (ft)	FZ	147	59	35.125	133.5	118	64	131.25	131	37.75
Frac Height Above (layers)		1	1	0	0	0	0	1	0	0
Frac Height Below (layers)		0	4	3	3	0	1	0	2	3
Perm (mD)	FZ	77.675	30.175	85.75	58.2	26.375	94.775	62	17.825	85.75
	NFZ	0.3817	0.305	0.3817	0.154	0.0867	0.1457	0.1103	0.069	0.246
Sw (%)	FZ	44.25	52.25	69.50	74.00	80.75	58.00	57.75	54.50	84.25
	NFZ	43.50	40.80	57.60	45.40	45.90	56.40	53.90	49.60	48.30

where,

FZ represents the Fractured Zone or the primary hydraulic fracture
NFZ represents the Non-Fractured Zone or the SRV surrounding the primary hydraulic fracture



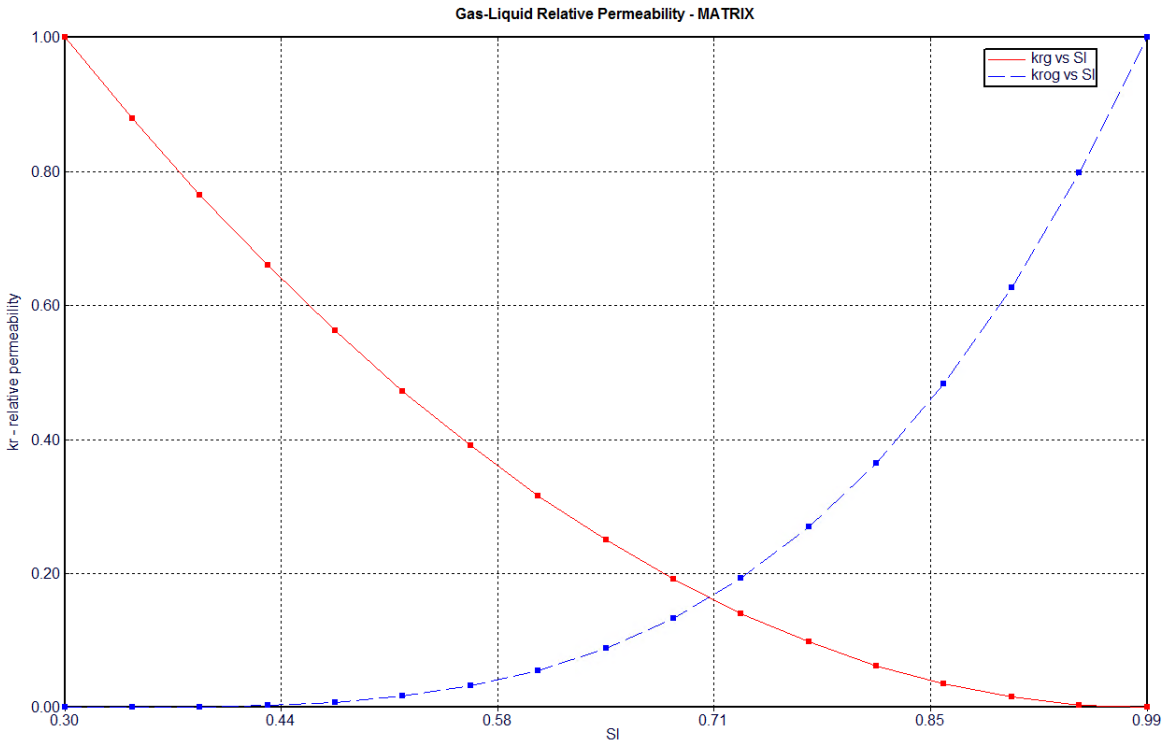


Figure 5.4: Oil-Water and Gas-Liquid Relative Permeability curves used for the matrix.

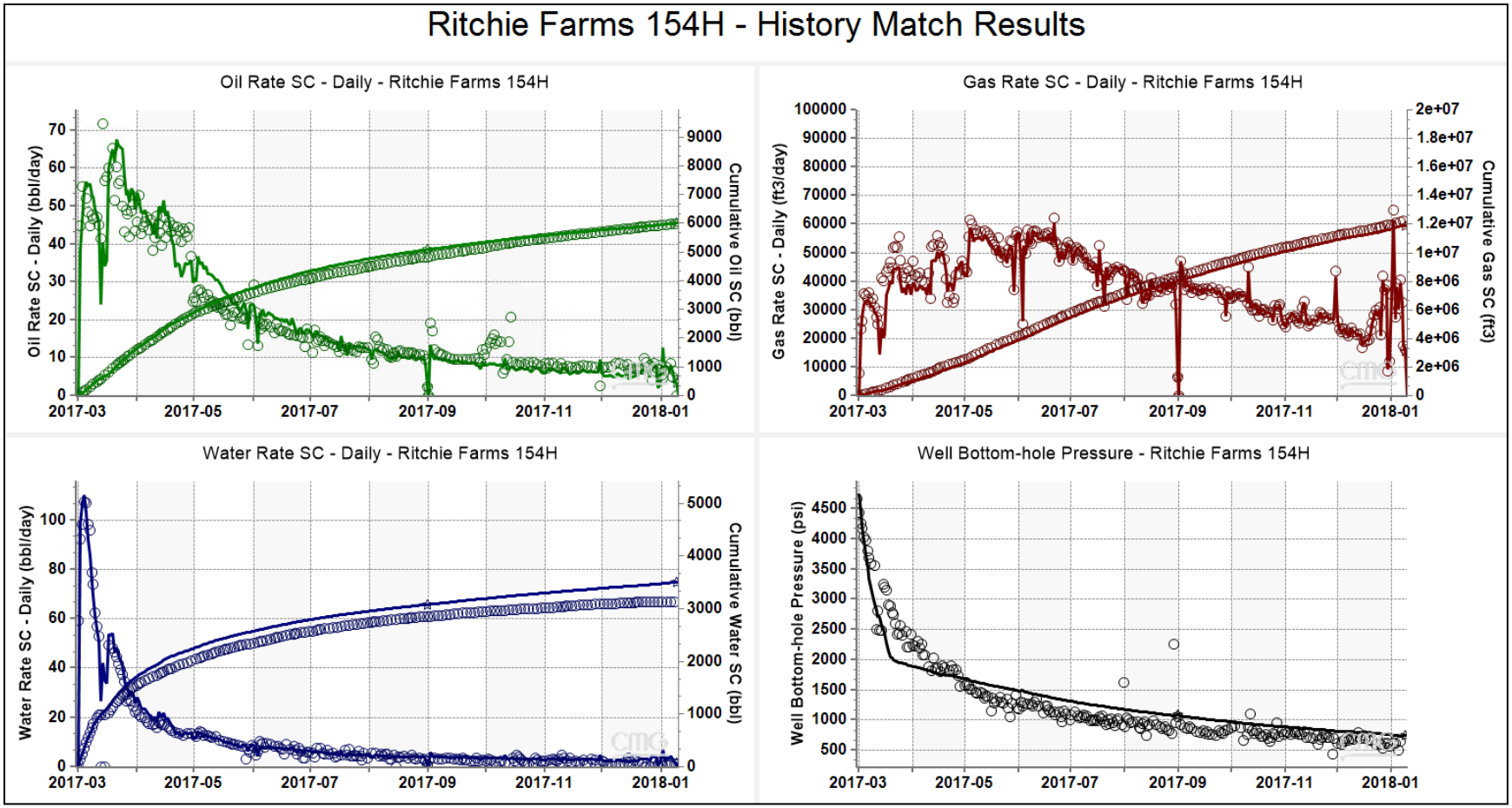


Figure 5.5: History match results for 154H – oil rate and cumulative oil production comparison (top left), gas rate and cumulative gas comparison (top right), water rate and cumulative water production comparison (bottom left), and bottom hole pressure comparison (bottom right).

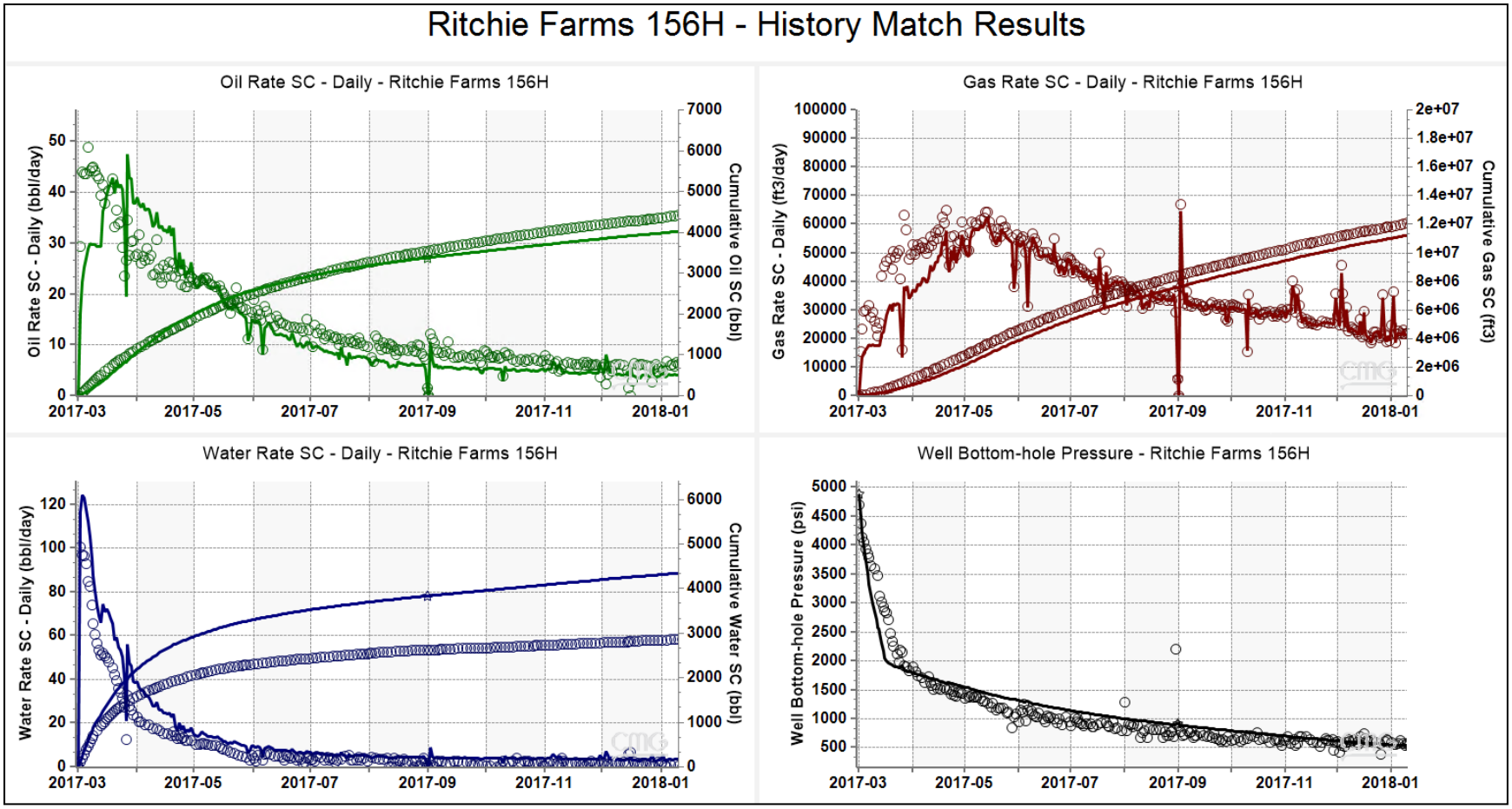


Figure 5.6: History match results for 156H – oil rate and cumulative oil production comparison (top left), gas rate and cumulative gas comparison (top right), water rate and cumulative water production comparison (bottom left), and bottom hole pressure comparison (bottom right).

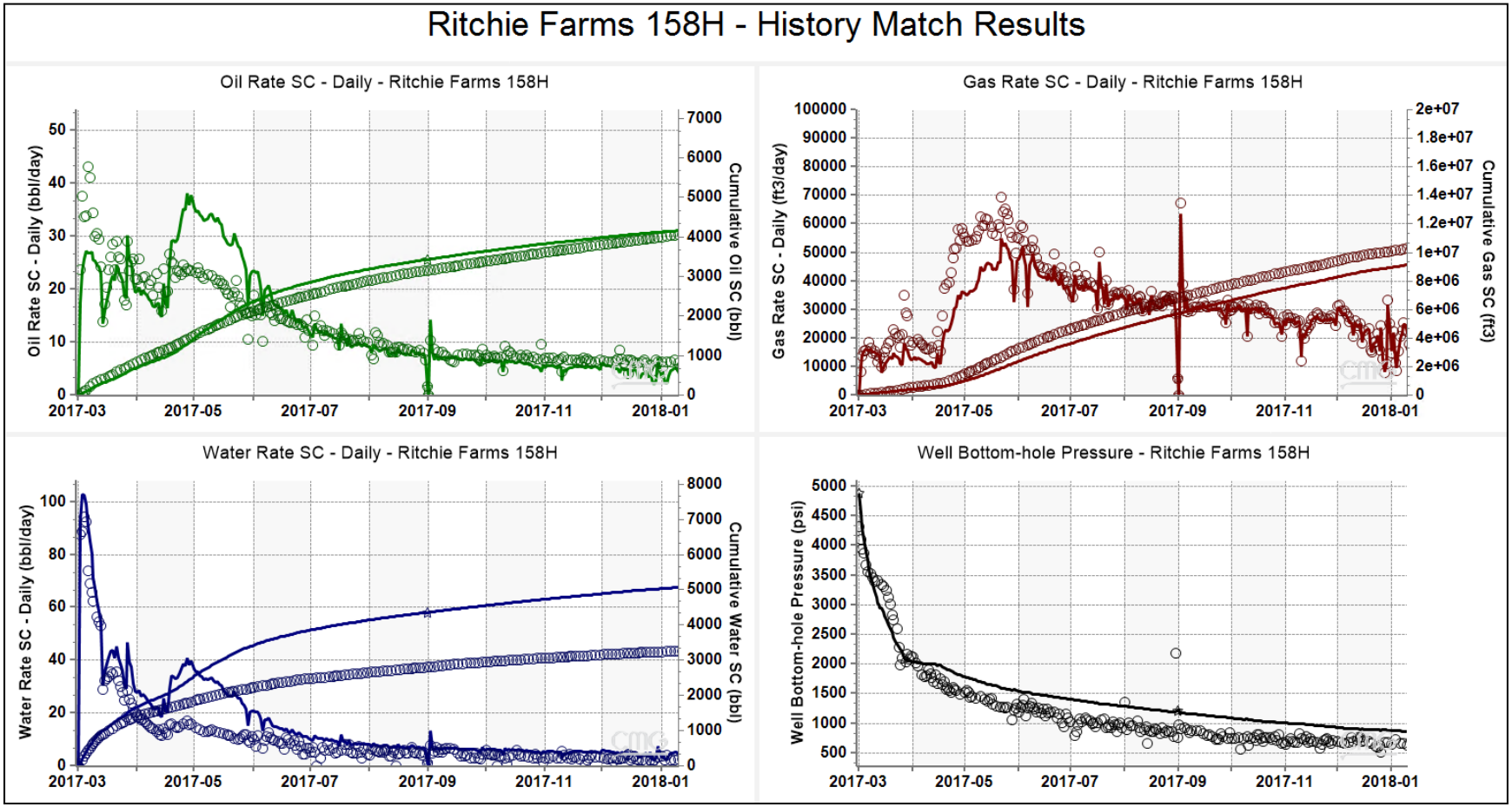


Figure 5.7: History match results for 158H – oil rate and cumulative oil production comparison (top left), gas rate and cumulative gas comparison (top right), water rate and cumulative water production comparison (bottom left), and bottom hole pressure comparison (bottom right).

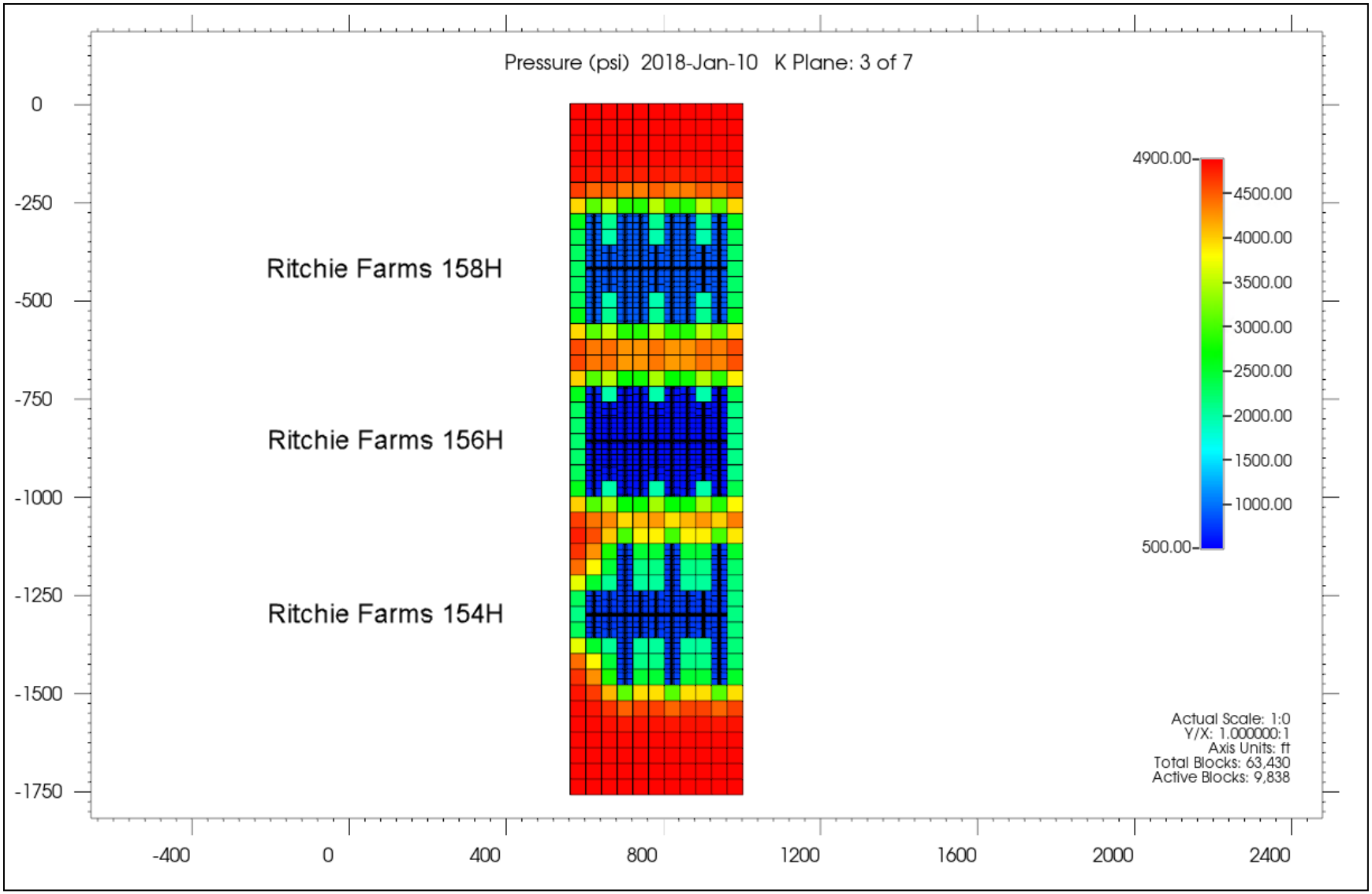


Figure 5.8: Pressure distribution at the end of history match, with 1 stage modeled for each of the three wells (coarse grid model).

5.4.2 Forecast with Miscible Cyclic Huff-and-Puff EOR

Following the history match, the model was run to simulate the huff-and-puff process with produced gas from the field, as it was readily available in large volumes. CO_2 is another common choice for huff-and-puff pilots; however, the choice of injectant gas was based on the availability of the gas. The composition of the field gas is included in **Table 5.5**. Although C2 through C6 are present in small quantities, the composition of the field gas is primarily lean, as C1 makes up the majority of the gas. C1 has the lowest critical temperature (**Table 5.2**) compared to other hydrocarbon gases, so it has the highest MMP. Small quantities of ethane, propane, and butane reduce the MMP of the overall field gas with the remaining oil in the reservoir. Injecting the gas at or above the First Contact Miscibility (FCM) pressure would maximize the recovery efficiency and uplift.

Table 5.5: Composition of the Field Gas

Component	Mol %
C1	73.43%
C2	15.12%
C3	7.12%
iC4 + nC4	3.15%
iC5 + nC5	0.88%
C6	0.30%

For forecasting and running sensitivities, the existing reservoir simulation grid with a grid block size of 40 ft in the x- and y-directions (excluding the LS-LR grid blocks for the hydraulic fractures) was refined to study the complex fluid phenomenon in the matrix blocks during the cyclic process. Compared to the pressure distribution shown in **Figure 5.8** with a coarse grid, **Figure 5.9** shows the pressure distribution with the finer grid at the end of the history match. Additionally, methane solubility in water was modeled using Henry's law, where CMG GEM uses Harvey's correlation to predict Henry's constant.

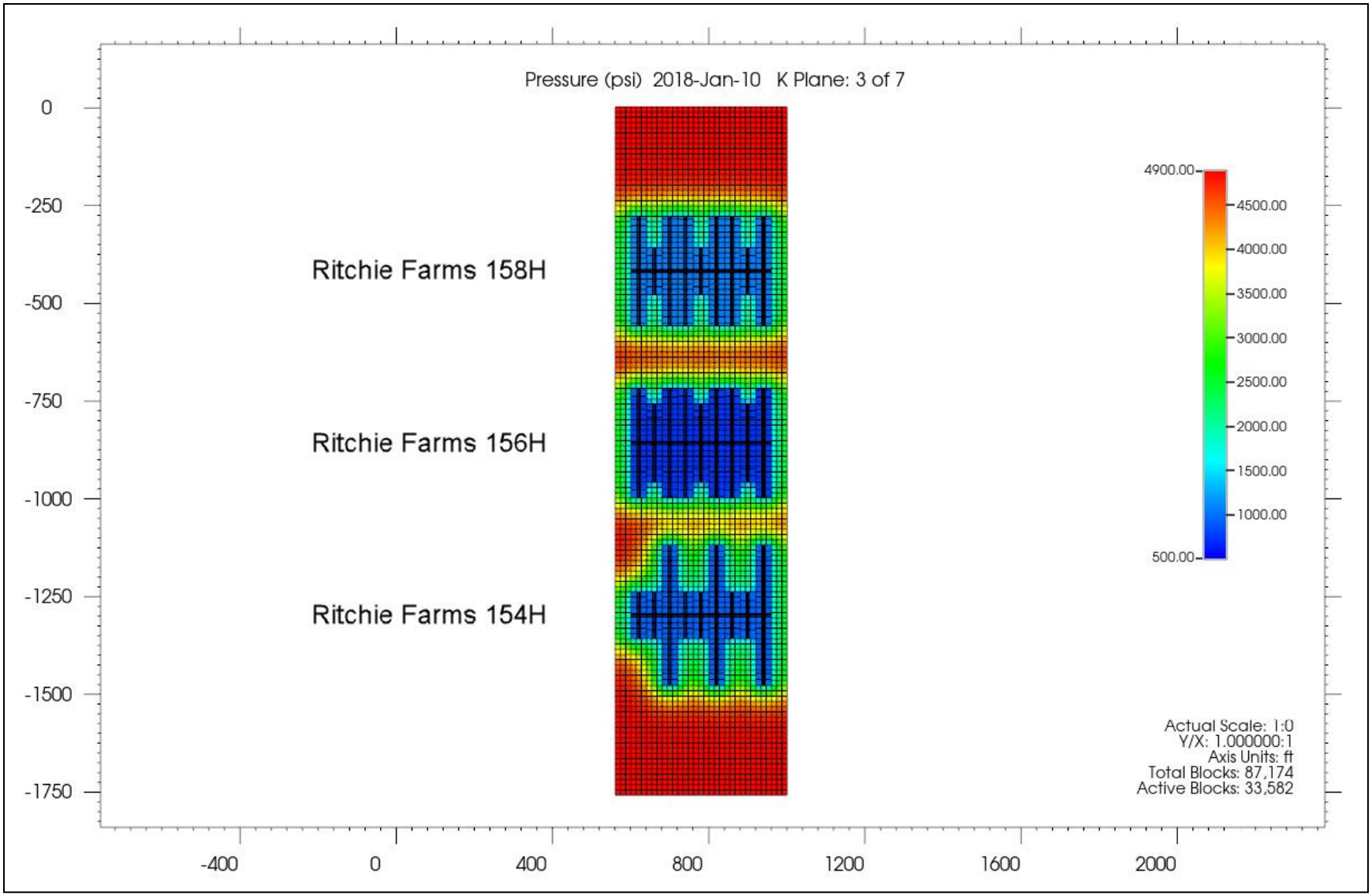


Figure 5.9: Pressure distribution at the end of history match, with 1 stage modeled for each of the three wells (fine grid model).

Effect of Cycle Times

In an ideal scenario where the injected gas is well contained within the drainage area of the well, the hydrocarbon pore volume lost with primary depletion is replaced with the injected volumes to build pressure. As the pressure increases and reaches MMP, the injected gas becomes miscible with the oil, resulting in oil swelling, viscosity reduction, and additional oil recovery. Once the injection gas is selected (produced gas in this case), the duration of each cycle (injection, soaking, and production) is often chosen based on simulation runs. It requires a balance of maximizing the duration of the injection cycle (to build pressure, which is also a function of the injection rate) and minimizing the loss in production. So, four different cycle time scenarios were run to evaluate the effect on oil recovery (**Table 5.6**). Since the effect of soaking time is not well understood, the operator decided to skip the soaking stage altogether, so the soaking stages are excluded from these sensitivities for cycle time optimization. A separate sensitivity for soaking stages is included at the end of this section.

Table 5.6: Scenarios to Evaluate the Effect of Different Cycle Times

Scenario	Injection Cycle Time (days)	Soaking Cycle Time (days)	Production Cycle Time (days)	Total Cycle Time (days)
1	15	-	30	45
2	30	-	30	60
3	30	-	45	75
4	45	-	45	90

For this project, two different compressor options were available to the operator, which could deliver surface gas rates of ~4.8 mmscf/d and ~5.7 mmscf/d per well. Based on the facility constraints and gas availability, the operator picked one that could deliver 4.8 MMscf/d (300 Mcf/d per stage) and allow a maximum bottom-hole injection pressure of 4,500 psi (Kerr et al., 2020).

The gas injection rate for these sensitivities was kept constant at 300 Mcf/d. For the production cycle, a minimum oil rate constraint of 4.5 barrels per day (average pre-huff-and-puff oil rate per stage for the Ritchie Farms lease) was applied to switch to the injection cycle if the oil rate falls below.

Regarding the sensitivity results, **Figure 5.10** shows a plot of oil swelling (using 'C1 mole fraction in oil phase' as a proxy for oil swelling) and oil viscosity changes for scenario 2 at a grid block in the SRV. After the primary depletion ended in January 2018, for scenario 2, the huff-and-puff cycles were modeled with 30 days of injection and 30 days of production (no soaking phase modeled for this scenario). The top-right plot shows the oil production rate in green and the gas injection in red. The middle-right plot shows the C1 mole fraction in the oil phase as a proxy for oil swelling increasing with gas injection, and the bottom-right plot shows the oil viscosity decreasing with gas injection. **Figure 5.11** shows the same plots for a matrix grid block just outside the SRV, and it shows the limited reach of the injectant outside the SRV during the injection phases. Lastly, **Figure 5.12** shows the same plots for a grid block in the matrix, with no changes to oil swelling or oil viscosity observed during the injection phases.

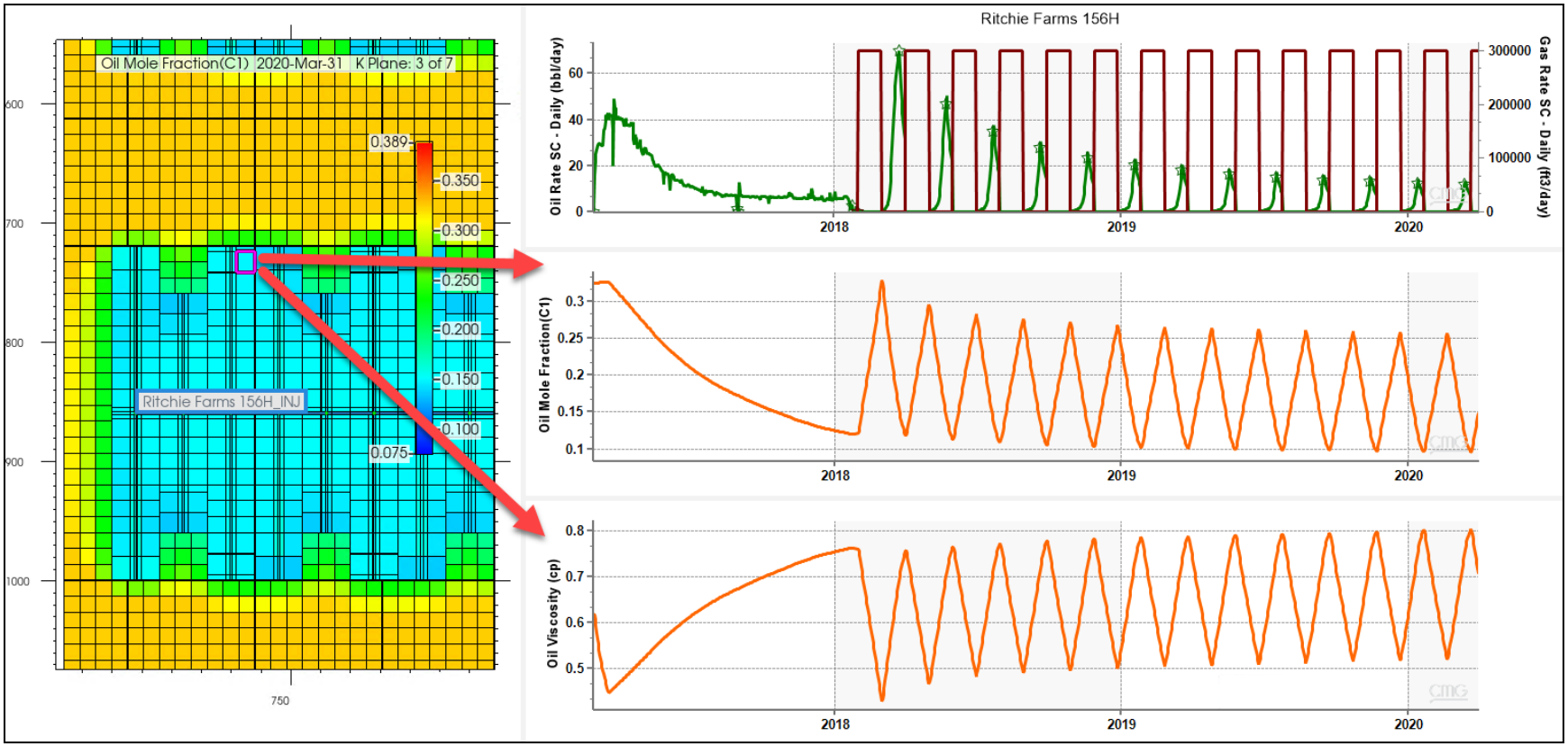


Figure 5.10: Oil mole fraction at the end of scenario 2 (left), oil production rate & gas injection rate for the single stage (top right), C1 mole fraction in the oil phase (middle right), and oil viscosity for a grid block (pink square grid block) within the SRV.

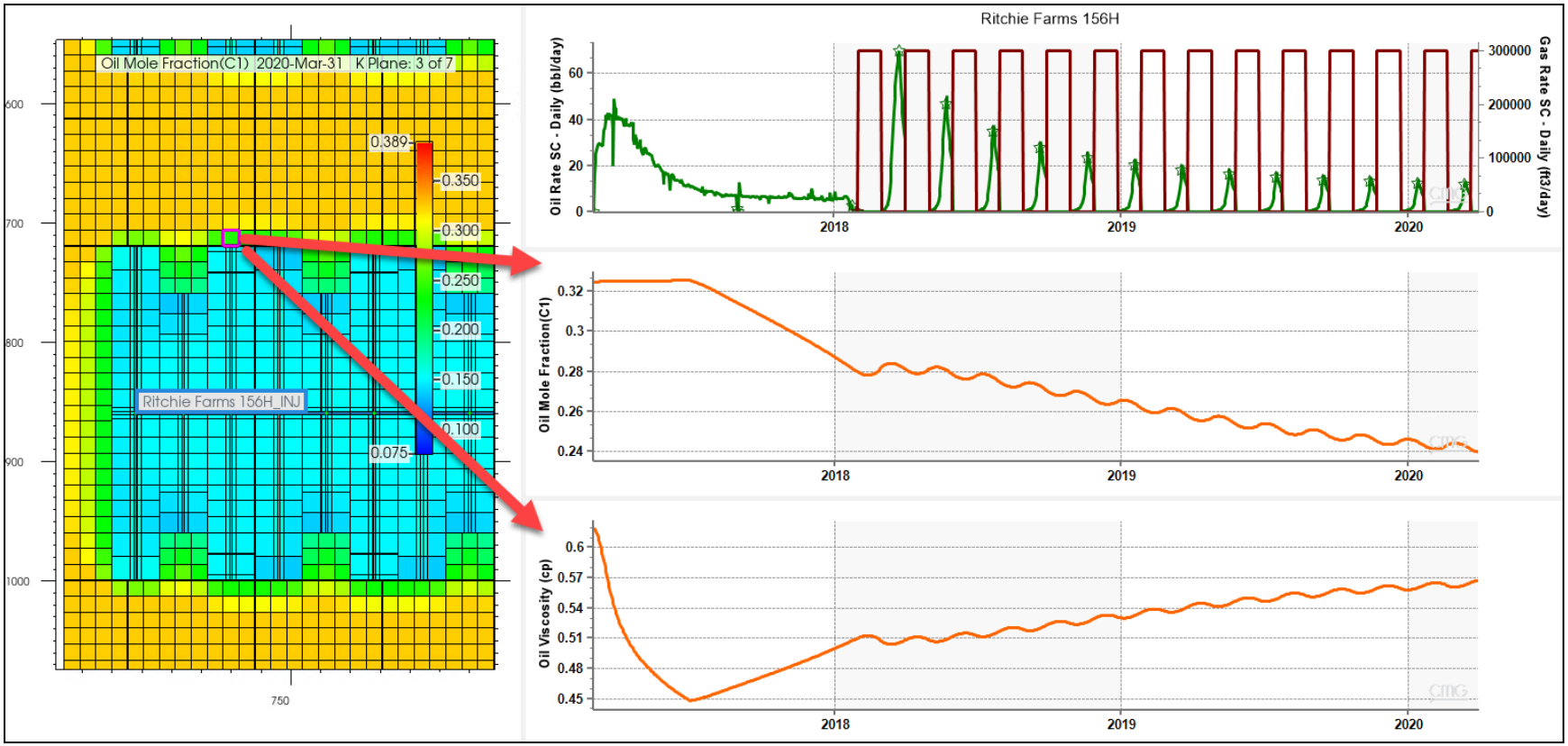


Figure 5.11: Oil mole fraction at the end of scenario 2 (left), oil production rate & gas injection rate for the single stage (top right), C1 mole fraction in the oil phase (middle right), and oil viscosity for a grid block (pink square grid block) just outside the SRV.

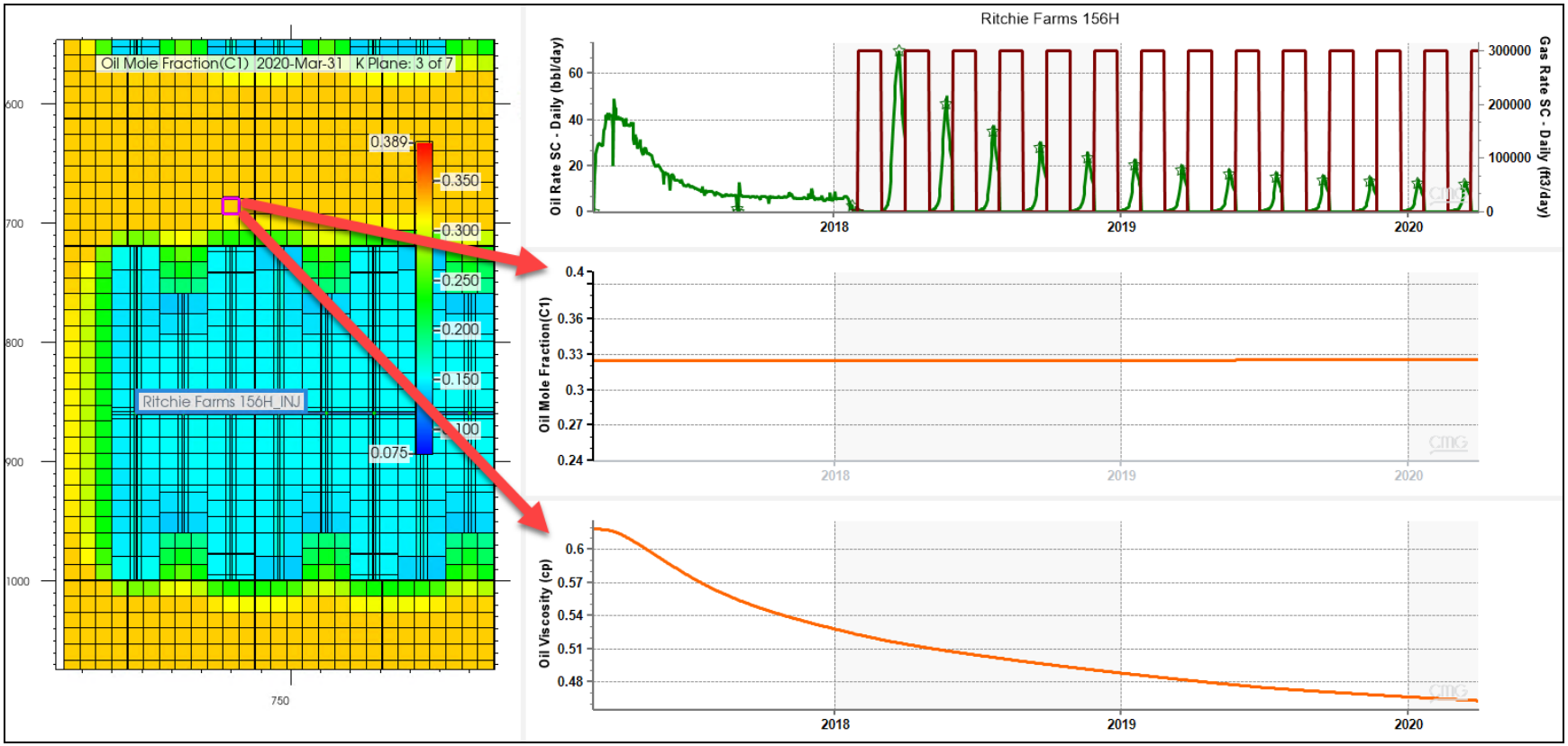


Figure 5.12: Oil mole fraction at the end of scenario 2 (left), oil production rate & gas injection rate for the single stage (top right), C1 mole fraction in the oil phase (middle right), and oil viscosity for a grid block (pink square grid block) in the matrix.

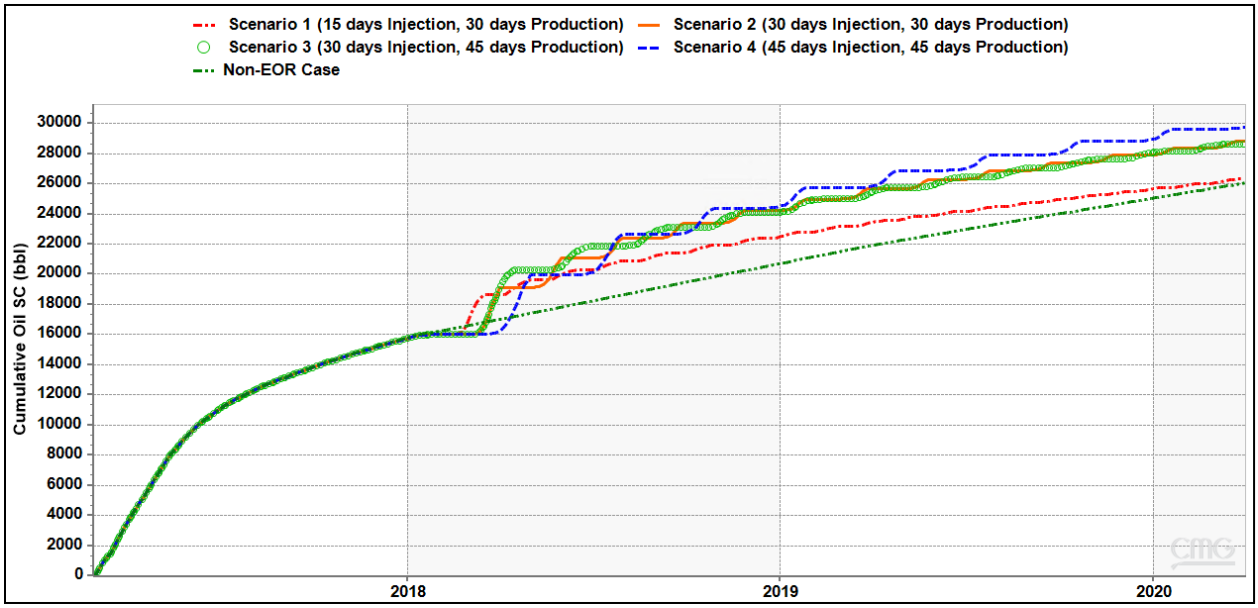


Figure 5.13: Cumulative oil production for the different scenarios.

Table 5.7: Results for the Different Scenarios for One Stage Modeled for the Three Wells

Scenario	Number of Cycles Fully Completed in 26 months	Total Gas Volume Injected (MMcf)	Maximum BHP Reached for Different Wells (psi)	Cumulative Oil Volume (Mbo)	Oil Recovery Uplift Relative to Non-EOR Scenario after 1 year	Oil Recovery Uplift Relative to Non-EOR Scenario after 26 Months	Huff-and-Puff Efficiency (stb/MMcf)
1	20	270.0	1,442 - 1,780	26.362	8.0%	1.2%	1.1
2	13	360.0	2,220 - 2,728	28.814	18.3%	10.6%	7.7
3	11	319.8	2,220 - 2,728	28.642	18.0%	9.9%	8.1
4	8	364.5	3,714 - 4,444	29.774	21.8%	14.3%	10.2

Figure 5.13 and **Table 5.7** summarize the results for these sensitivities. At the end of the depletion phase, the bottom hole pressures for the three wells ranged from 707 to 1,058 psi. The cumulative oil volume for the non-EOR scenario for all three wells after 26 months is 26.058 Mbo, which could be slightly optimistic as it does not factor in periodic shut-ins for well maintenance, artificial lift installation/repairs, etc.

To benchmark different scenarios, the Huff-and-Puff Efficiency (HPE) metric is defined as the ratio of incremental oil recovered with the huff-and-puff process to the total gas injected.

This efficiency metric is inversely related to the Gas Utilization Factor (GUF) reported for conventional flooding EOR projects (Maffeis et al., 2015). For comparison, the Huff-and-Puff Efficiency has been reported to be 10-50 stb/MMcf for successful Eagle Ford Pilots (Carlsen et al., 2020).

- For scenario 1, the shorter injection cycle times help with additional oil recovery. However, when coupled with the well shut-ins for the gas injection, the cumulative oil recovery after 26 months is only 1% higher than the non-EOR scenario. When looking at the results on the cumulative oil production plot and comparing it to the non-EOR case, it could lead one to believe that the huff-and-puff results in an acceleration of oil volumes only, which could be likely because the pressure buildup was very minimal compared to other scenarios. Additionally, with the cost of the injected gas and additional surface facilities, the economics do not look attractive compared to the non-EOR case.
- For scenarios 2 and 3, with the same injection cycle time of 30 days but different production cycle times, the oil recovery uplift is only 0.7% higher for scenario 2. However, it required 12.6% (or 40.2 MMcf) of additional gas. At the end of the 26 months, the bottom hole pressures cannot be easily compared since the two scenarios were at different stages of their respective cycles. However, the variance in the oil recovery uplift year-over-year is widening between the two scenarios, which could lead to better long-term recovery with scenario 2.
- For scenario 4, the total gas volume injected is almost the same as in scenario 2; however, the oil recovery uplift is 3.7% higher. This scenario with an extended injection cycle time has the highest huff-and-puff efficiency metric, which could be explained by the BHP approaching the expected MMP values, unlike the other three scenarios.

Although the bottom hole pressure did not reach the MMP for most scenarios, an increasing trend in oil recoveries with injected volumes was observed. This corroborates the laboratory findings of EERC with the Bakken oils, where the higher pressures were found to mobilize more oil regardless of MMP (Hawthorne et al., 2018).

The maximum bottom hole pressure was achieved after the first injection cycle for all the scenarios. Since the maximum oil rate increase was also observed after the first cycle, it begs the question of whether the injection cycle times should be extended for subsequent cycles. Note that the effect of asphaltene deposition was not modeled separately for these sensitivities, as Fragoso et al. (2019) did for history-matching one of the Eagle Ford pilots, which could further reduce the oil rate uplift observed for the subsequent cycle.

Overall, comparing the huff-and-puff efficiency (HPE) for the different scenarios, longer injection cycle times are better as they could lead to higher pressure buildup in the reservoir and better oil recovery. Over 3-5 years, the difference in the recoveries could be significant.

In the pilot, the operator experimented with the various cycle times to better understand the response. However, it was found that when the bottom hole pressure reached 3,500 psi, a gas breakthrough occurred, and a significant amount of injected gas was recorded in the offset wells. To mitigate the leakage of the injected gas beyond the 3-well lease, a model was run where the two exterior wells on the lease (or the “edge wells”) were converted into water injectors and re-pressurized with 2 bpm of water injection. The model predicted an 8% additional recovery from the 156H well over the seven months. When this approach for gas containment was implemented in the field, it was found that a further 7-12% oil recovery was achievable (Venepalli et al., 2021). The field results were within 10% of the simulation recovery predictions (Kerr et al., 2020).

Effect of Injection Rate

Amongst other factors, the economic success of the huff-and-puff process is dependent on the availability and cost of the injectant gas. The facility design is a function of the facility cost (compressor horsepower, infrastructure, pad location, etc.), the expected hydrocarbon recovery uplift, and the associated economics. As mentioned, achieving reservoir pressures higher than the First Contact Miscibility pressure would maximize the recovery efficiency and uplift.

In the previous sensitivities, the injection rate was kept constant, and the injection time varied. In this section, sensitivities were carried out to evaluate the effect of the injection rate if the operator had chosen to go with a compressor that could deliver surface gas rates of 5.7 mmscf/d with a maximum bottom-hole injection pressure of 5,500 psi. Scenarios 2 and 4 were re-evaluated with an injection rate of 358 Mcf/d (**Table 5.8**).

Table 5.8: Scenarios to Evaluate the Effect of Injection Rate

Scenario	Injection Cycle Time (days)	Soaking Cycle Time (days)	Production Cycle Time (days)	Total Cycle Time (days)	Injection Rate (Mcf/d)
2	30	-	30	60	300
4	45	-	45	90	300
5	30	-	30	60	358
6	45	-	45	90	358

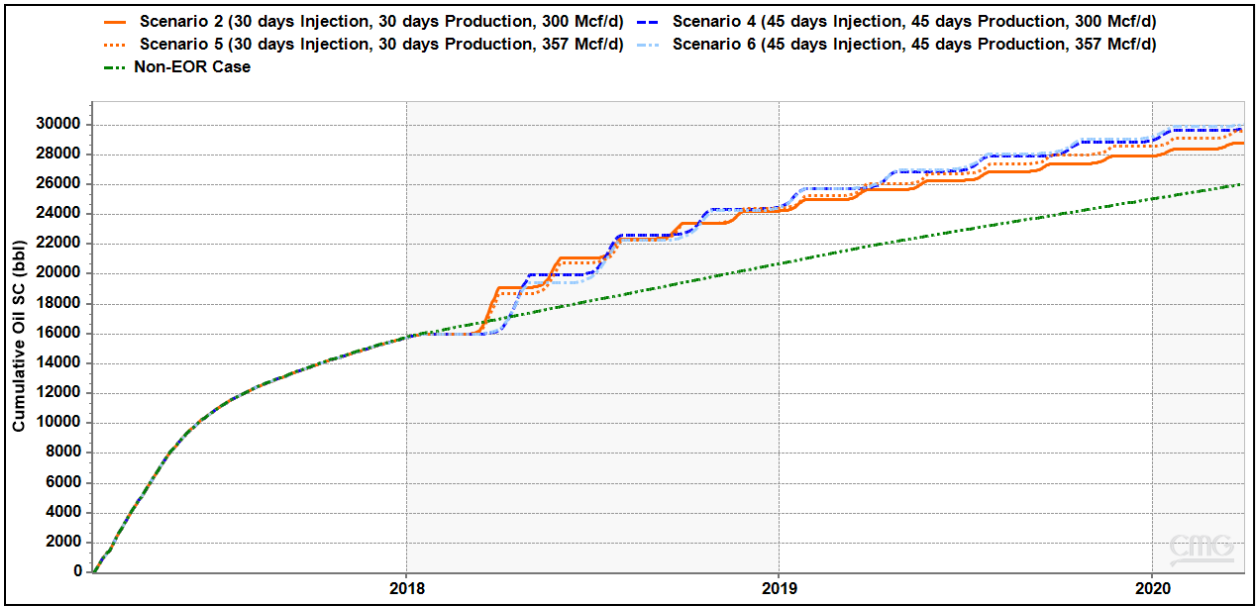


Figure 5.14: Cumulative oil production for the different scenarios.

Table 5.9: Scenarios to Evaluate the Effect of Injection Rates

Scenario	Number of Cycles Fully Completed in 26 months	Total Gas Volume Injected (MMcf)	Maximum BHP Reached for Different Wells (psi)	Cumulative Oil Volume (Mbo)	Oil Recovery Uplift Relative to Non-EOR Scenario after 1 year	Oil Recovery Uplift Relative to Non-EOR Scenario after 26 Months	Huff-and-Puff Efficiency (STB/MMcf)
2	13	360.0	2,220 - 2,728	28.814	18.3%	10.6%	7.7
4	8	364.5	3,714 - 4,444	29.774	21.8%	14.3%	10.2
5	13	429.1	2,697 - 3,334	29.600	19.6%	13.6%	8.3
6	8	431.1	4500	30.070	21.9%	15.4%	9.3

Figure 5.14 and **Table 5.9** summarize the results for these sensitivities. As expected, with a higher injection rate, more gas volume is injected while keeping the duration of the injection cycle unchanged. It achieved higher bottom hole pressures, and the oil recovery over the longer term (26 months) was higher than near-term (12 months) for both scenarios 5 and 6. Although 18-19% additional gas volumes were injected at a higher rate for scenarios 5 and 6, the oil recovery

uplift was higher in scenario 5 than scenario 6 (relative to scenarios 2 and 4). As a result, the HPE increased slightly from Scenario 2 to 5 but saw a reduction in HPE from Scenario 4 to 6.

Effect of Soaking Time

To evaluate the effect of soaking time, scenario 2 (with no soaking) was compared to two new scenarios with 15 and 30 days of soaking time (**Table 5.10**).

Table 5.10: Scenarios to Evaluate the Effect of Soaking Time

Scenario	Injection Cycle Time (days)	Soaking Cycle Time (days)	Production Cycle Time (days)	Total Cycle Time (days)
2	30	-	30	60
7	30	15	30	75
8	30	30	30	90

Figure 5.15 through **Figure 5.17** compare the oil viscosity, oil production rates, and cumulative oil production for the three scenarios. For scenarios 7 and 8, with different soaking times, longer runs were made to keep the number of cycles unchanged from scenario 2, and the results are included in **Table 5.11**. However, **Table 5.12** compares the results with different numbers of cycles completed within the same 26-month period for the three scenarios.

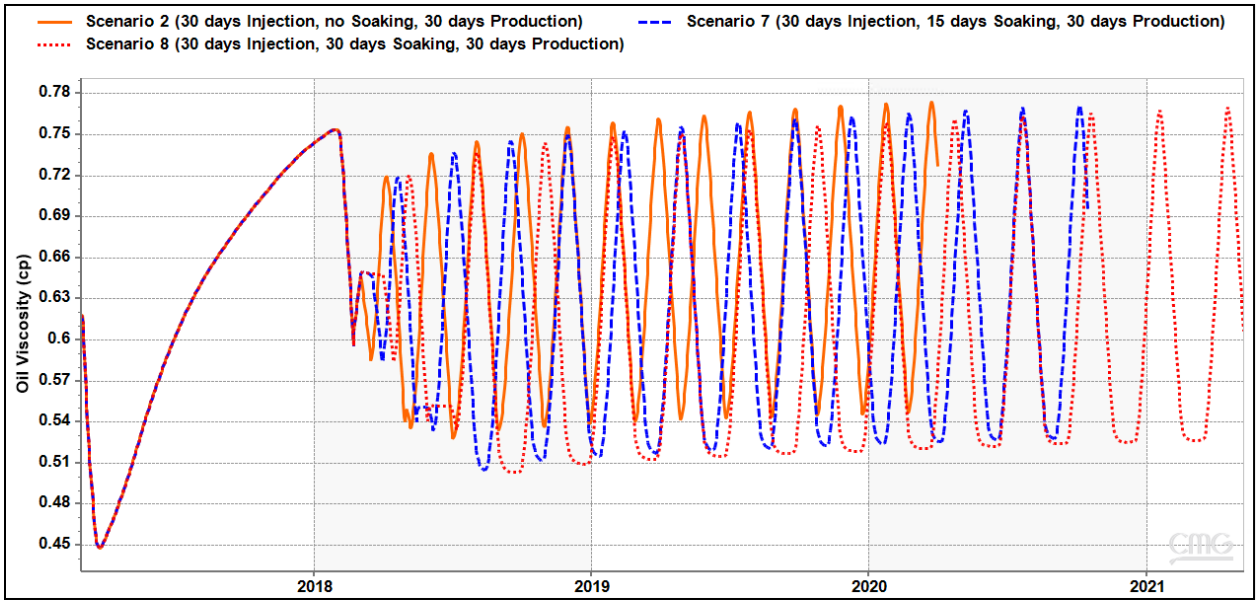


Figure 5.15: Oil viscosity changes for the different scenarios.

Figure 5.15 shows that the soaking phase significantly lowers the oil viscosity with the well shut-in between the injection and production phases. The oil viscosity reduction is the same for the initial two cycles, with or without soaking. However, in the third cycle, we observe a higher viscosity reduction with the soaking phase for scenarios 7 and 8. Although the viscosity reduction is the same for scenarios 7 and 8, the extended shut-in with scenario 8 allows the fluids to mix for longer. Over time, with the subsequent cycles, the viscosity reduction with no soaking continues to decrease. The soaking period, especially the extended mixing of fluids with scenario 8, results in better peak oil rates for each production cycle than without soaking (**Figure 5.16**). This translates into higher cumulative oil production after 13 huff-and-puff cycles for the scenarios with soaking (**Figure 5.17**), with cumulative production for scenarios 7 and 8 being 2.7% and 5.1% higher than scenario 2, respectively (**Table 5.11**). As the oil rate after 13 cycles is still higher than the pre-huff-and-puff oil rates, the variance between these scenarios would continue to widen as the cycles are repeated. However, adding the soaking phase comes with the issue of shutting in the

well longer, i.e., with “lost” or “deferral” of production. Factoring in the shut-in periods for the soaking phase, the cumulative production for scenarios 7 and 8 is 2.9% and 5.7% lower than scenario 2, respectively, over a fixed 26-month period (**Table 5.12**).

Even though we observe higher viscosity reduction with the soaking phases, we do observe that the peak oil rates decline for subsequent cycles even with soaking. With the injection rates and the cycle time for the soaking phase unchanged for subsequent cycles, the pressure build-up is not enough to bring the bottom hole/reservoir pressure up to miscibility conditions.

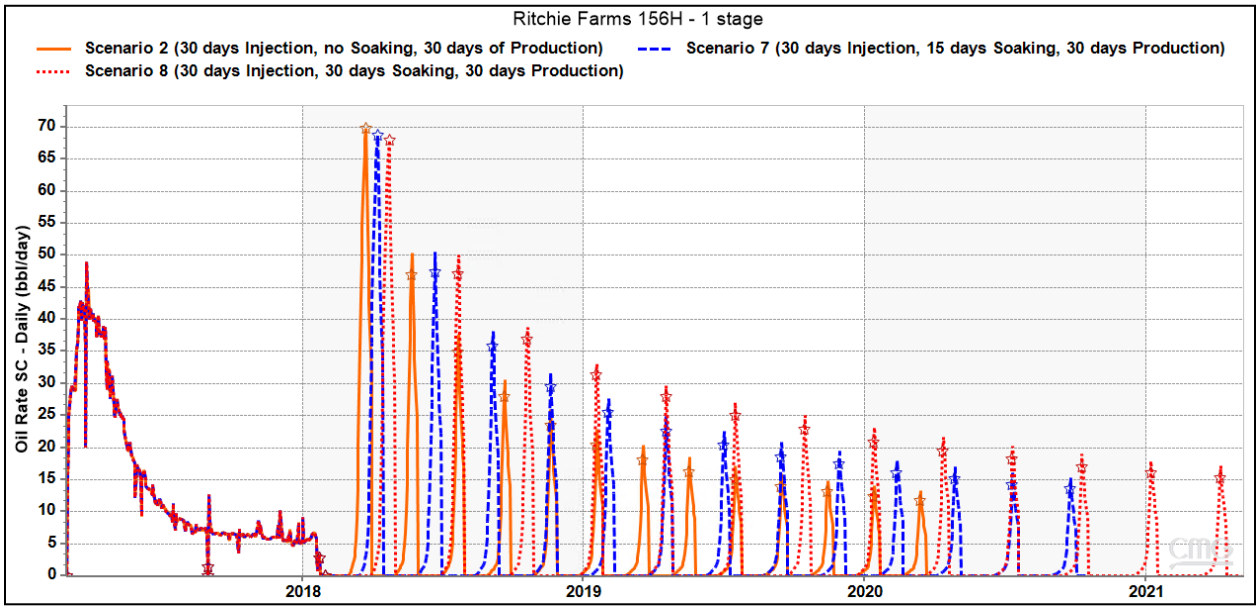


Figure 5.16: Oil Rate for Ritchie Farms (1 stage) for the different scenarios.

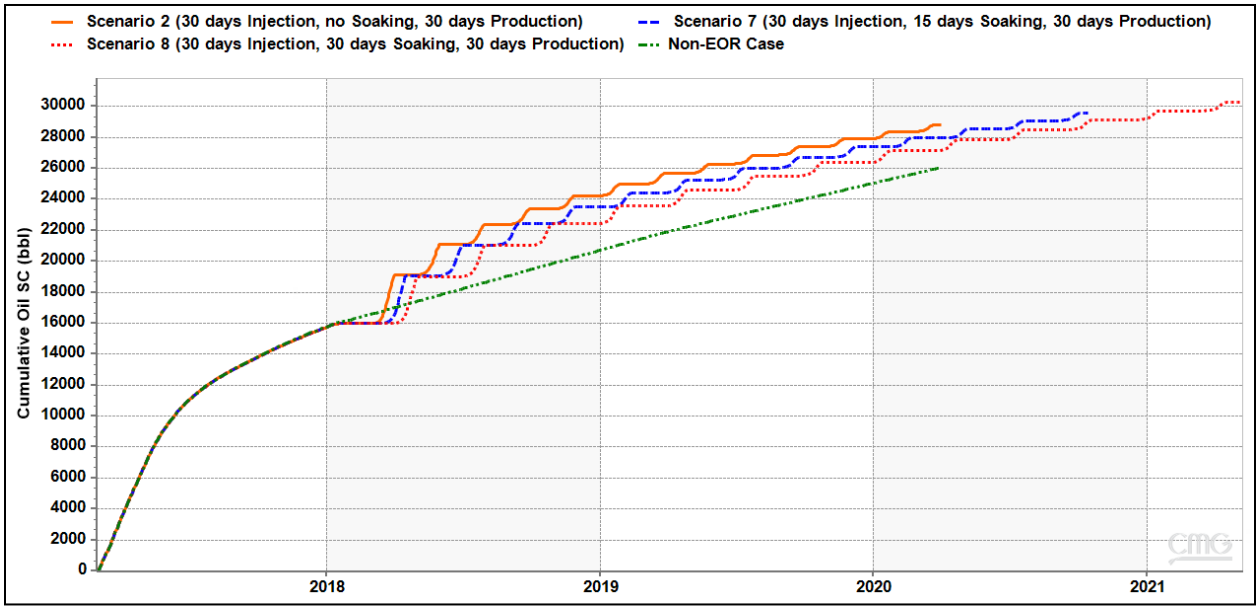


Figure 5.17: Cumulative oil production for the different scenarios.

Table 5.11: Results for the Different Scenarios to Evaluate the Effect of Soaking Time – same number of cycles

Scenario	Number of Cycles Fully Completed	Total Gas Volume Injected (MMcf)	Maximum BHP Reached for Different Wells (psi)	Cumulative Oil Volume (Mbo)	Oil Recovery Uplift Relative to Non-EOR Scenario after 1 year	Oil Recovery Uplift Relative to Non-EOR Scenario after 13 Cycles	Huff-and-Puff Efficiency (stb/MMcf)
2	13	360.0	2,220 - 2,728	28.814	18.3%	10.6%	7.7
7	13	360.0	2,220 - 2,728	29.593	12.8%	13.6%	9.8
8	13	360.0	2,220 - 2,728	30.293	11.6%	16.3%	11.8

Table 5.12: Results for the Different Scenarios to Evaluate the Effect of Soaking Time – same 26 months of total huff-and-puff duration; different number of cycles

Scenario	Number of Cycles Fully Completed in 26 months	Total Gas Volume Injected (MMcf)	Maximum BHP Reached for Different Wells (psi)	Cumulative Oil Volume (Mbo)	Oil Recovery Uplift Relative to Non-EOR Scenario after 1 year	Oil Recovery Uplift Relative to Non-EOR Scenario after 26 Months	Huff-and-Puff Efficiency (stb/MMcf)
2	13	360.0	2,220 - 2,728	28.814	18.3%	10.6%	7.7
7	10	297.0	2,220 - 2,728	27.986	12.8%	7.4%	6.5
8	8	243.0	2,220 - 2,728	27.163	11.6%	4.2%	4.5

Figure 5.18 shows the oil production by puff cycle for the three scenarios for Ritchie Farms 156H. The volume produced for the first two cycles is about the same for the three scenarios; however, the volume variance between the different scenarios starts to diverge following the second cycle. The modeling results, with additional recovery observed from the well shut-in for soaking, suggest that the huff-and-puff cycles should be tailored to include soaking following the initial few cycles. The soaking stage adds to the downtime during which the well will be offline, making it unpopular amongst the operators unless the long-term benefits can be justified.

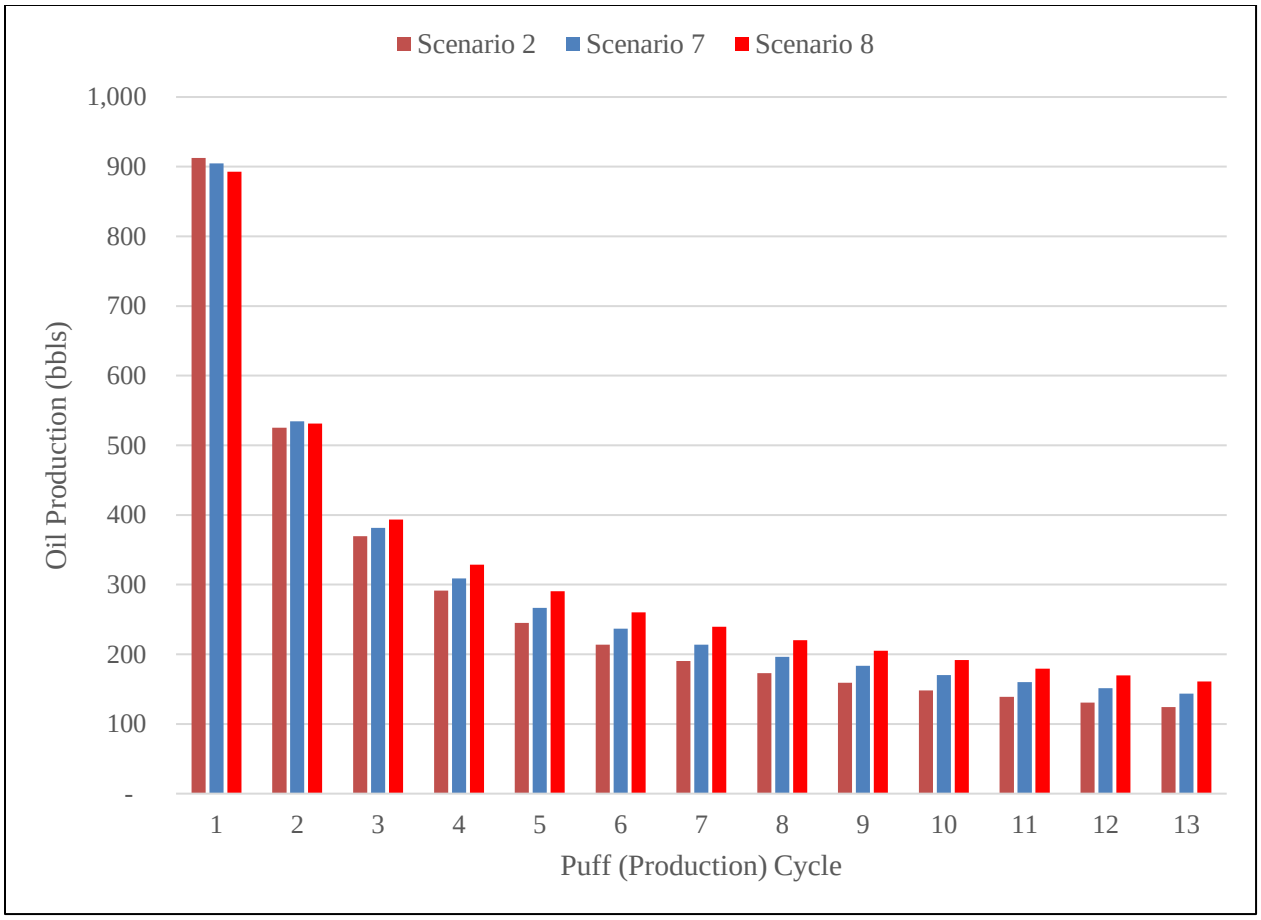


Figure 5.18: Oil production by puff cycle for the different scenarios for Ritchie Farms 156H.

To summarize, if gas containment is not an issue, increasing the soaking period (assuming the injection rate is fixed and cannot be increased further) with every subsequent cycle to increase the overall oil recovery would be prudent. Also, this corroborates the findings and recommendations for optimizing the soaking phase in Chapter 4, where the initial cycles were found to be tapping into smaller matrix blocks closer to the wellbore, but soaking is needed in the subsequent cycles to tap into larger matrix blocks.

5.5 Sensitivities

The history-matched reservoir simulation model for the Ritchie Farms lease was used to compare the results against CO_2 gas and a novel liquid solvent, Dimethyl Ether (DME).

5.5.1 Carbon Dioxide (CO_2)

The CO_2 has been widely used in the oil industry for EOR since the early 1970s in West Texas. A few characteristics of CO_2 that have made it a preferred choice as an injectant for miscible gas flooding over the years are being readily available, having a lower cost, and having a relatively lower MMP than other gases, especially lean gases such as methane.

Regarding the recovery mechanism, the miscibility occurs through multiple contacts when the CO_2 is injected above MMP. The lighter and intermediate components of the oil vaporize into the CO_2 through the vaporization gas-drive process, while part of the injected CO_2 dissolves into the oil through the condensation gas-drive process. This mass transfer allows the fluids to become completely miscible and results in swelling of the oil and oil viscosity reduction. This exchange is accelerated with oils containing a significant amount of lighter and intermediate hydrocarbons and high CO_2 density as it is injected in a compressed state. CO_2 can easily reach the supercritical state, where its density is nearly identical to that of a liquid, and its viscosity is comparable to that of gas. Additionally, the diffusion coefficient of CO_2 is up to two orders of magnitude higher than that of liquid solvents due to its high solubility characteristics with oil (Sofla et al., 2024).

Although CO_2 is reported to have high sweep efficiency during the EOR process under miscibility conditions, below MMP, the CO_2 is in a gaseous state and suffers from gravity override, viscous fingering, and channeling, resulting in early gas breakthroughs into offset wells. As discussed in Chapter 2, several early field tests in Bakken were carried out with CO_2; however,

early breakthroughs resulted in a lack of pressure buildup to achieve miscibility conditions. Being corrosive, the injection of CO_2 requires the wellbore tubulars to be rated for sour service. Additionally, as discussed in Section 5.2, asphaltene precipitation with CO_2 injection is well documented in conventional reservoirs and results in pore plugging and permeability reduction.

5.5.2 Dimethyl Ether (DME)

Dimethyl Ether (DME) is an industrial chemical widely used as a liquid refrigerant and aerosol propellant. In recent years, it has been used as a replacement for transport fuels and, with characteristics similar to liquified petroleum gas (LPG), in domestic applications for cooking and heating (Chernetsky et al., 2015). It is used extensively in the chemical industry because it is miscible with most organic solvents and has a high solubility in water.

Under normal atmospheric conditions, DME is a colorless gas and can be liquified at low pressures. Under reservoir conditions, the DME exists as a liquified gas and shows liquid-vapor equilibrium characteristics similar to n-propane and n-butane (**Figure 5.19**). Due to its polarity, DME is partially soluble in water, and under moderate temperature and pressure conditions, it is fully miscible with oil (Chahardowli et al., 2016). Like other solvents, the oil-recovery mechanism with DME is also dictated by the phase behavior and distribution of DME among the fluid phases in the reservoir. Experimental and simulation results of coreflood tests have confirmed the robustness of the DME-based EOR application for different rock types (Chernetsky et al., 2015). Experimental work by Salimi et al. (2022) showed that the oil viscosity is significantly reduced when DME mixes with oil at low DME ratios. In their work, the oil viscosity of 100 cP at 212 °F was decreased to 24 cP and 1 cP by mixing it with 5% and 30% by weight of DME, respectively. The viscosity of the aqueous phase was also reduced due to DME dissolution.

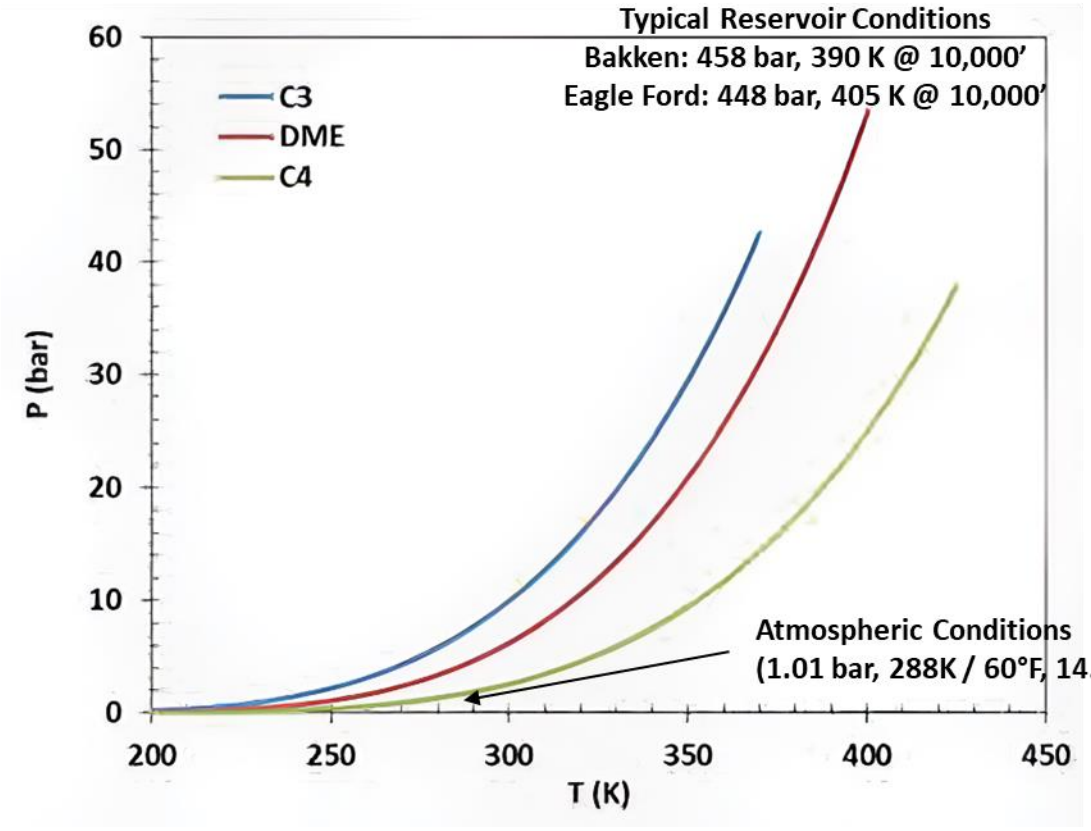


Figure 5.19: Pressure-Temperature diagram for DME, n-propane, and n-butane (modified from Salimi et al., 2022).

Experimental work by Salimi et al. (2022) has shown no asphaltene precipitation (with asphaltene content of 6.4% by weight) when oil was mixed with DME at increasing ratios up to 80% v/v. Compatibility tests with formation water with a salinity of 9.2 wt.% showed that DME is soluble in formation water without any incompatibility or salting-out effect. The DME partitioning into the oleic phase improved with increased temperature and salinity.

In the petroleum industry, DME is applied as a water-soluble solvent for EOR applications to enhance the performance of waterfloods in conventional reservoirs. Shell originally developed the DME Enhanced Waterflooding (DEW) technique (Cho et al., 2018; Parsons et al., 2019;

Ratnakar et al., 2016) in which DME was utilized as a miscible solvent in conjunction with conventional waterflooding to increase the oil recovery. The application of DEW takes advantage of DME's solubility in both water and hydrocarbons. The water pumped during the injection phase of the waterflooding application is used as a carrier for transporting DME. Upon contact with the remaining oil in the reservoir, DME preferentially partitions into the hydrocarbon phase, thereby swelling and mobilizing the oil phase. This is followed by the freshwater injection to recover the remaining mobile oil and DME. Residual oil saturation through DEW sweep is reduced significantly below that typically achieved by waterflooding alone. Finally, the DME can be easily extracted from the produced well stream fluids by distillation or absorption process, then re-used for injection, thereby reducing the project costs (Cho et al., 2018; Parsons et al., 2019).

Significant research has been conducted to understand the pressure-volume-temperature (PVT) behavior of DME and DME/crude oil mixtures, with a focus on the partitioning behavior of DME (Chernetsky et al., 2015; Ratnakar et al., 2016; Salimi et al., 2022). The efficacy of the DME-based EOR process is primarily controlled by the mass transfer of DME into the aqueous and oleic phases. DME transfers to both oleic and aqueous phases because of its polarity, with preference to the oleic phase. The DME concentration in the oil affects the extent of oil swelling and viscosity reduction, ultimately increasing the oil mobility. With DME injection, the first contact miscibility occurs under the reservoir conditions (Cho et al., 2018). Partitioning of DME between the two phases is influenced by temperature, salinity, pH of the aqueous phase, and oil composition (Salimi et al., 2022).

Having similar physical properties, including molecular weight, the DME is often compared to LPG. DME has a water solubility of three orders of magnitude greater than LPG

(Parsons et al., 2016). Additionally, the DME has the advantages of lower cost, higher efficiency, and easily extracted from produced well stream fluid for re-injection (Cho et al., 2018).

5.5.3 Sensitivities with CO_2 and DME

This section includes the additional sensitivities performed to test the efficacies of both CO_2 and DME in the Ritchie Farms pilot in the Eagle Ford.

Effect of Injectant Type

Using Scenario 2 as the base case to compare the results, sensitivities were carried out to evaluate the performance of two alternate solvents (**Table 5.13**). The properties of CO_2 were readily available in the CMG WinProp fluid library. In the case of DME, the phase change data was taken from the NIST Chemistry WebBook and Wu et al. (2011) and are summarized below:

- Molecular weight: 46.0684 g/mole
- Critical Pressure: 52.6701209 atm
- Critical Temperature: 400.378 K
- Acentric Factor: 0.196
- Critical Volume: 0.164 m^3/kg-mole
- Average normal boiling point: -12.6076 °F
- Parachor: 132

The Binary Interaction Coefficients were taken from Cho et al. (2018) and are included in **Table 5.14**.

Table 5.13: Scenarios to Evaluate the Effect of Soaking Time

Scenario	Injection Cycle Time (days)	Soaking Cycle Time (days)	Production Cycle Time (days)	Total Cycle Time (days)	Injectant Type
2	30	-	30	60	Field Gas
9	30	-	30	60	CO_2
10	30	-	30	60	Dimethyl Ether

Table 5.14: Binary Interaction Coefficients between DME and other components (Cho et al. (2018))

Component	DME
C1	0.29
C2	0.25
C3	0.25
C4	0.25
C5	0.25
C6	0.20
C6-C9	0.20
C10-C27	0.08
C18-C27	0.08
C28+	0.08
N_2	0.10
CO_2	0.00
H_2S	0.00

Figure 5.20 compares the oil rate, cumulative oil production, bottom hole pressure for Ritchie Farms 158H, and cumulative water production for the different scenarios. Although the bottom hole pressure was observed to be the lowest with DME, the oil rate was highest with DME. The DME has a higher preferential solubility in the oleic phase at intermediate pressures than other injectants. The water production was observed to be the lowest for the DME due to partial

solubility. However, the water production was the highest with the CO_2 due to higher water solubility than light hydrocarbon gases like C1.

Figure 5.21 and **Figure 5.22** show the mole fraction of the injectant in the oil phase (a proxy for oil swelling) and oil viscosity changes at the six different grid blocks shown in **Figure 5.21 – left**. For the two scenarios of field gas and CO_2, the oil swelling and corresponding oil viscosity reduction were observed to decrease with distance away from the primary hydraulic fracture. The reversal in oil viscosity trend at ~0.45 cP for the different grid blocks is due to the grid block pressure decreasing below the bubble point pressure. In the case of DME (**Figure 5.22 – right**), both the oil swelling (DME mole fraction in the oil phase) and oil viscosity reduction with time indicate greater penetration within the SRV. This suggests that the DME is more effective than other injectants at oil recovery due to higher solubility at intermediate pressures with deeper penetration.

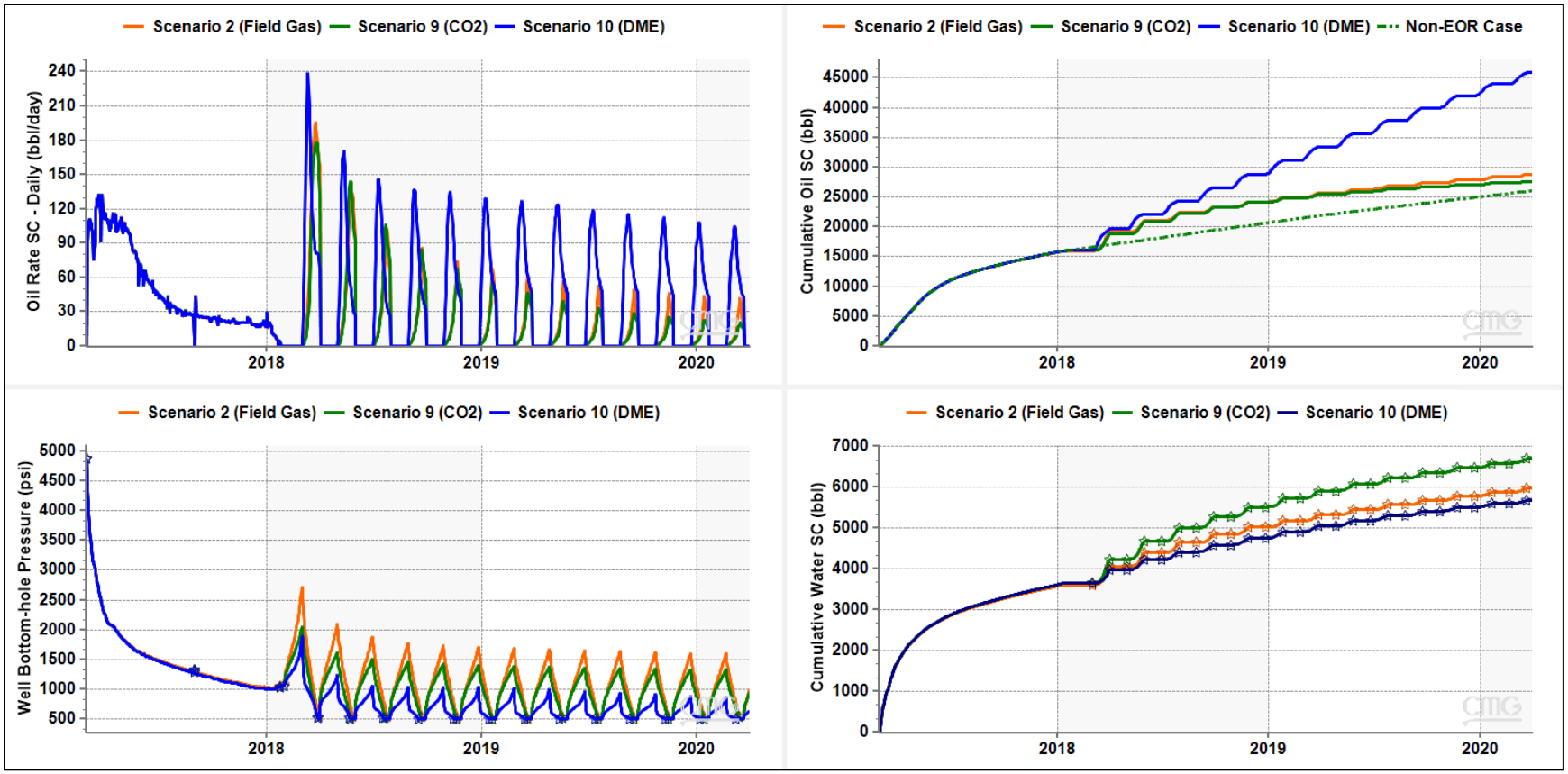


Figure 5.20: Oil rate, cumulative oil production, bottom hole pressure for Ritchie Farms 158H, and cumulative water production for the different scenarios.

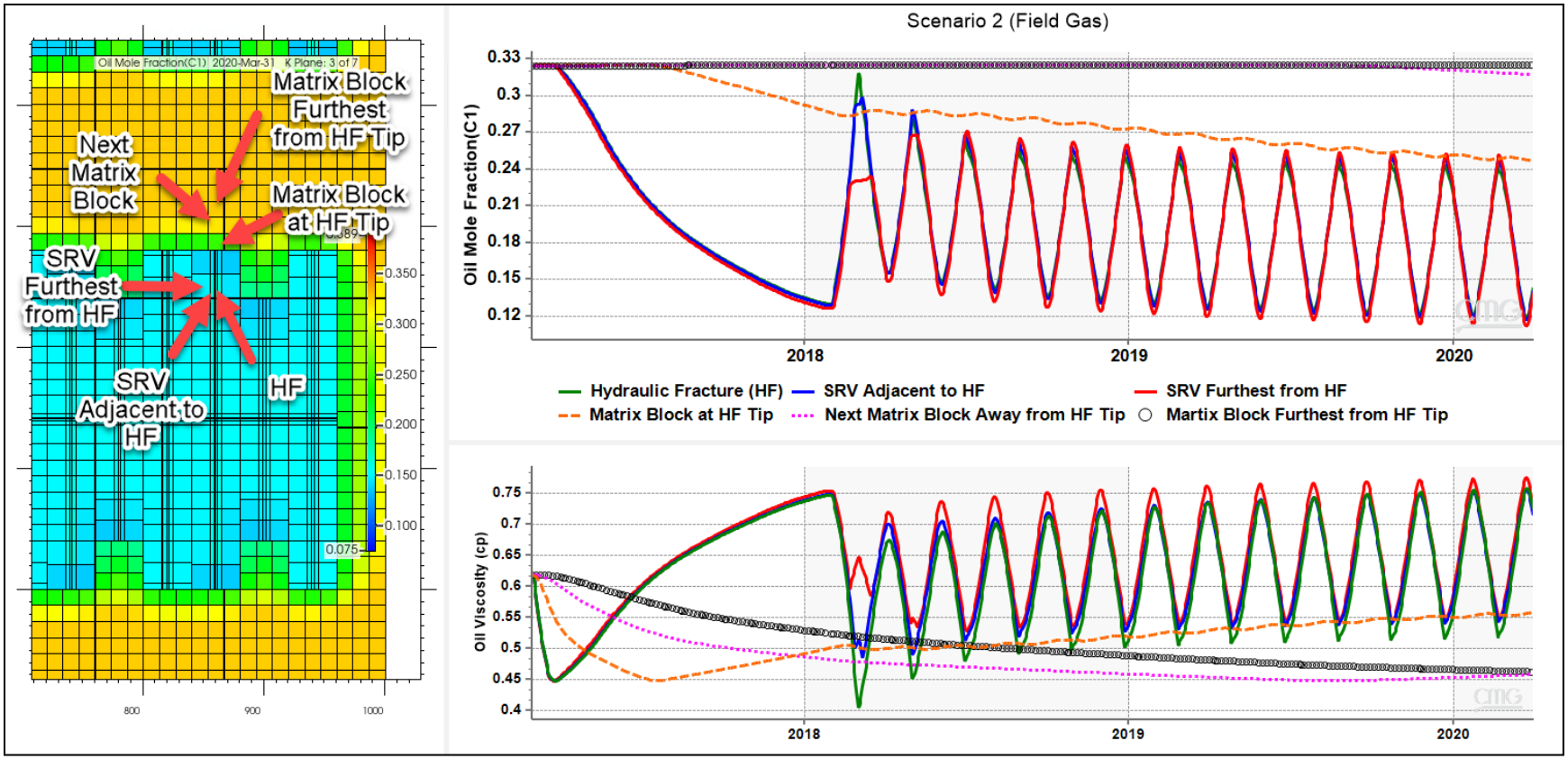


Figure 5.21: C1 mole fraction in oil (top right) and oil viscosity (bottom right) at six different grid blocks (left) for scenario 2 (Field Gas).

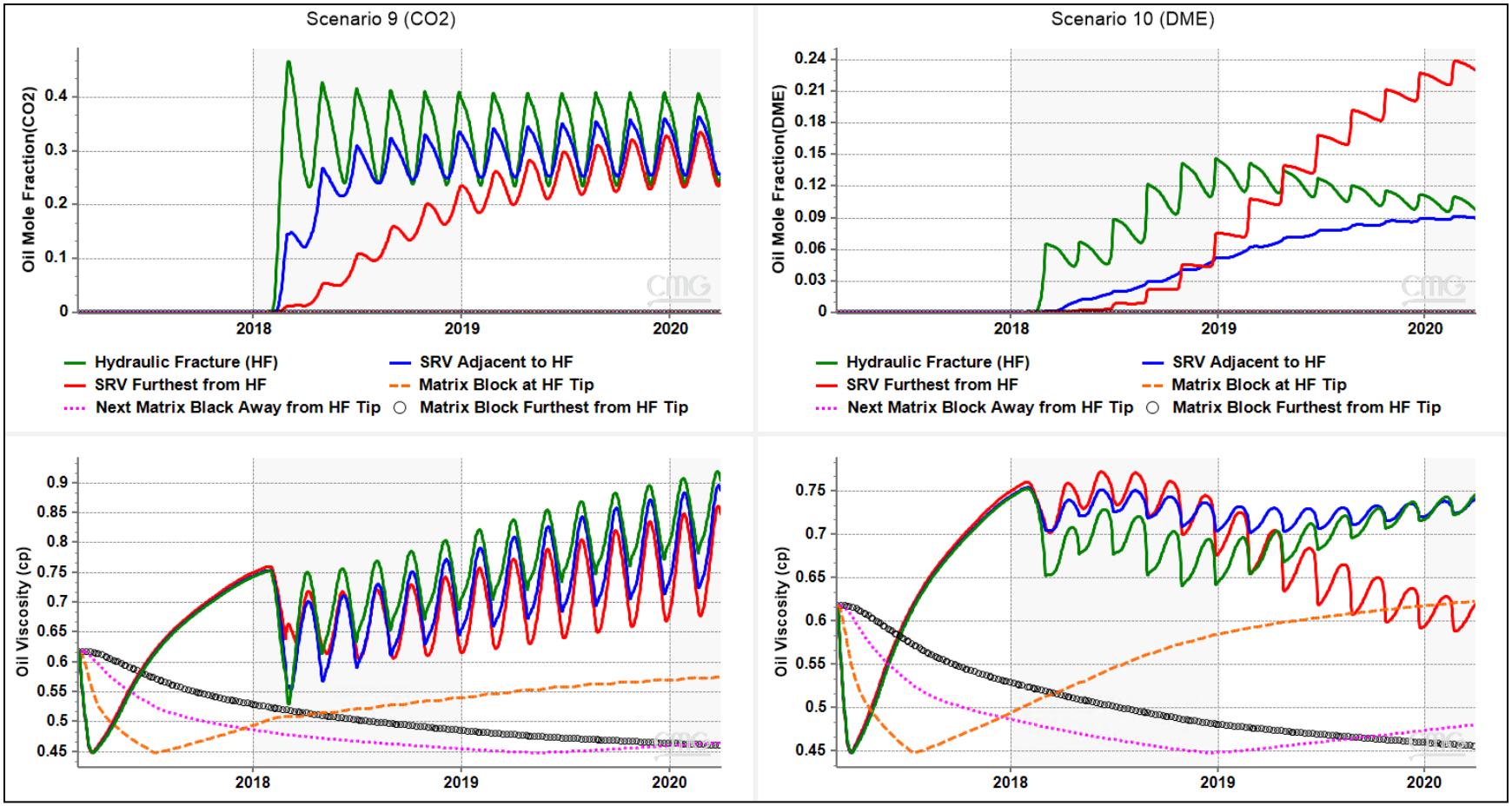


Figure 5.22: CO_2 mole fraction in oil and oil viscosity at six different grid blocks for scenario 9 (CO_2) (left), and DME mole fraction in oil and oil viscosity at six different grid blocks for scenario 10 (DME) (right).

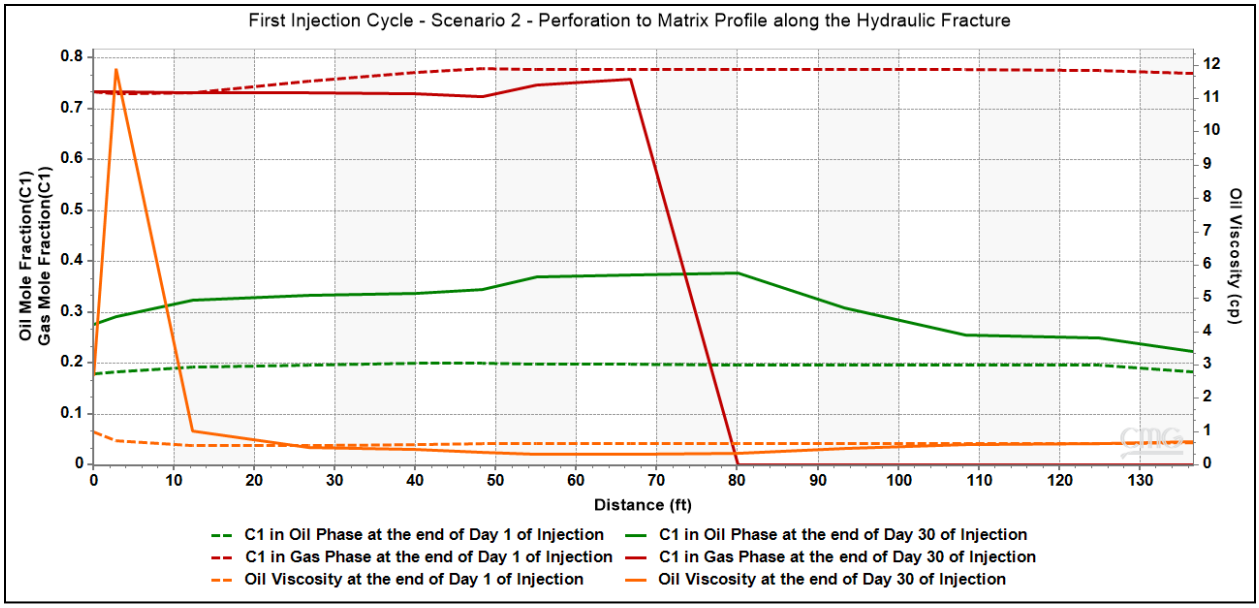


Figure 5.23: C1 mole fraction in oil and gas phases and oil viscosity for the first Field Gas injection cycle from perforation (distance = 0) to matrix (distance = 135 ft).

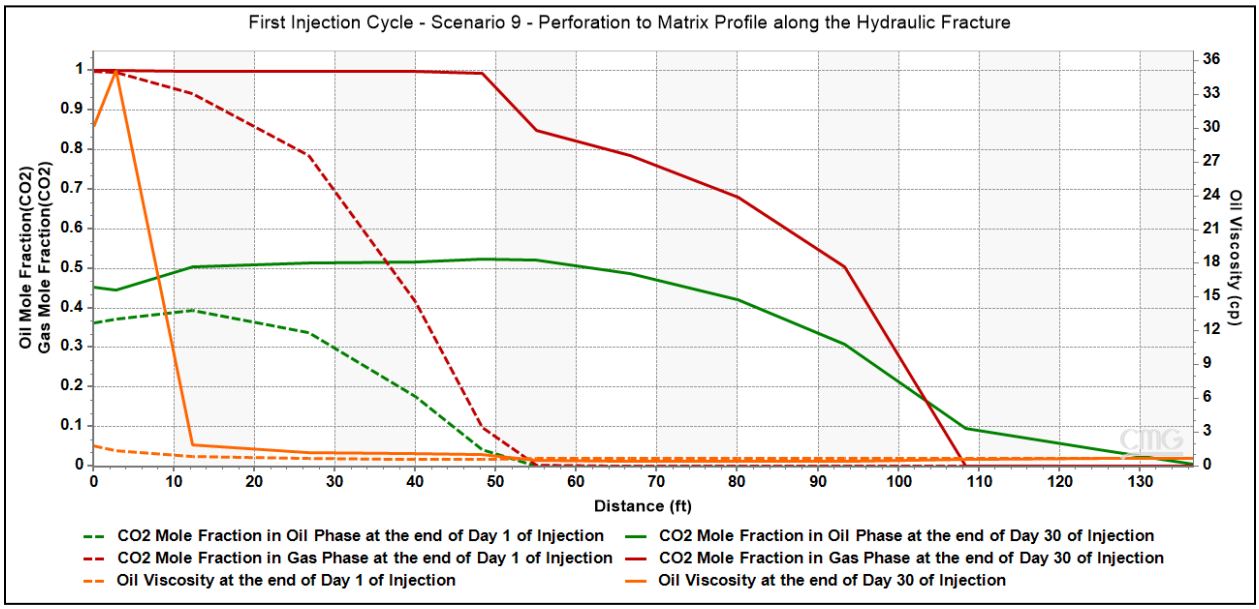


Figure 5.24: CO_2 mole fraction in oil and gas phases and oil viscosity for the first CO_2 injection cycle from perforation (distance = 0) to matrix (distance = 135 ft).

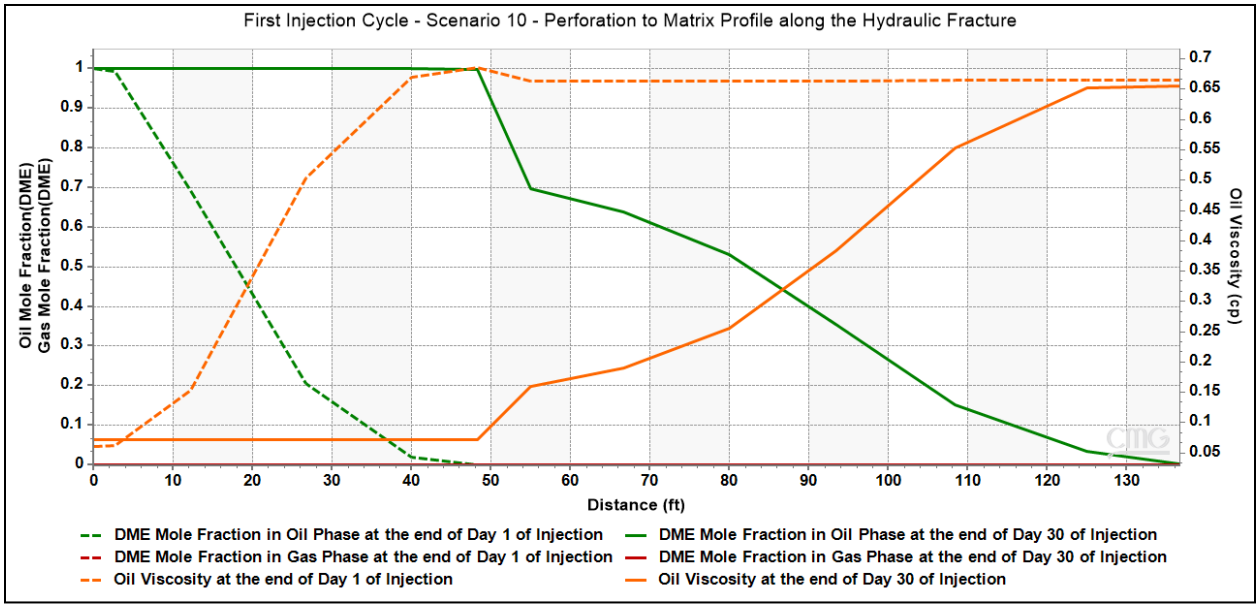


Figure 5.25: DME mole fraction in oil and gas phases and oil viscosity for the first DME injection cycle from perforation (distance = 0) to matrix (distance = 135 ft).

Figure 5.23 through **Figure 5.25** show the profile of the field gas, CO_2, and DME for the first injection cycle, as the bottom hole pressures were usually the highest during the first injection cycle for the three injectants (**Figure 5.20**). The field gas and CO_2 stayed in the gas phase for the duration of the injection cycle as the miscibility conditions were not achieved, making both sub-optimal injectants. At a reservoir temperature of 215 °F, the bottom hole pressure was high for CO_2 to be in the supercritical state for some time towards the end of the injection phase. Methane, which makes most of the field gas (**Table 5.5**), is a poor hydrocarbon solvent. It can only dissolve light hydrocarbons (up to about C12) and has a low propensity towards dissolving intermediate and heavier molecular weight hydrocarbons.

In contrast, CO_2 is better at dissolving the light and intermediate components (up to C16) (Hawthorne & Miller, 2019). The mass transfer of the lighter and/or intermediate components with the injected gas results in higher viscosity and density of residual oil after injection. In Sensitivities

2 and 9, with the selective mass transfer for the field gas and CO_2, an increase in the oil viscosity was observed near-wellbore, up to 10-15 feet from the perforation, which could cause further restriction for lighter oil stranded deeper in the reservoir.

Even though the bottom hole pressures of DME were lower than those of the other two injectants, DME was injected in the liquid phase as it can be liquified at low pressures with its favorable liquid-vapor equilibrium characteristics (**Figure 5.19**). When DME is injected into the reservoir and comes in contact with the remaining mobile oil, the first-contact miscibility process occurs, leading to oil swelling and viscosity reduction. Significant oil viscosity reduction was observed ~50 feet into the reservoir compared to the other two injectants.

Table 5.15 summarizes the results for these sensitivities, with DME resulting in ~60% higher cumulative oil production after 26 months and a much favorable HPE. Additional sensitivities are included in the following sections to evaluate the impact of varying interaction/solubility with oil and water.

Table 5.15: Scenarios to Evaluate the Effect of Injectant Type

Scenario	Number of Cycles Fully Completed in 26 months	Total Gas Volume Injected (MMcf)	Maximum BHP Reached for Different Wells (psi)	Cumulative Oil Volume (Mbo)	Oil Recovery Uplift Relative to Non-EOR Scenario after 1 year	Oil Recovery Uplift Relative to Non-EOR Scenario after 26 Months	Huff-and-Puff Efficiency (STB/MMcf)
2	13	360.0	2,220 - 2,728	28.814	18.3%	10.6%	7.7
9	13	360.0	1,656 - 2.063	27.668	17.8%	6.2%	4.5
10	13	360.0	1,287 - 1,914	45.855	47.5%	76.0%	55.0

Effect of Water Solubility

Water is abundant in hydrocarbon reservoirs and exists as fluid initially in place or injected as part of the hydraulic fracture treatment. In CMG, the cubic EOS models are used to model the oil and gas phase interaction, and the solubility of gases in water is handled separately. Like methane, the solubility of CO_2 in water was modeled using Henry's law. Henry's constant is a function of pressure, temperature, and salinity, and is inversely proportional to the solubility of the gas in a liquid. The Henry's constant for CO_2 is in the order of ten to the power of three (in units of atmosphere), an order of magnitude smaller than that of light hydrocarbon gases like C1 and C2, indicating higher solubility of CO_2 in water (**Figure 5.26**).

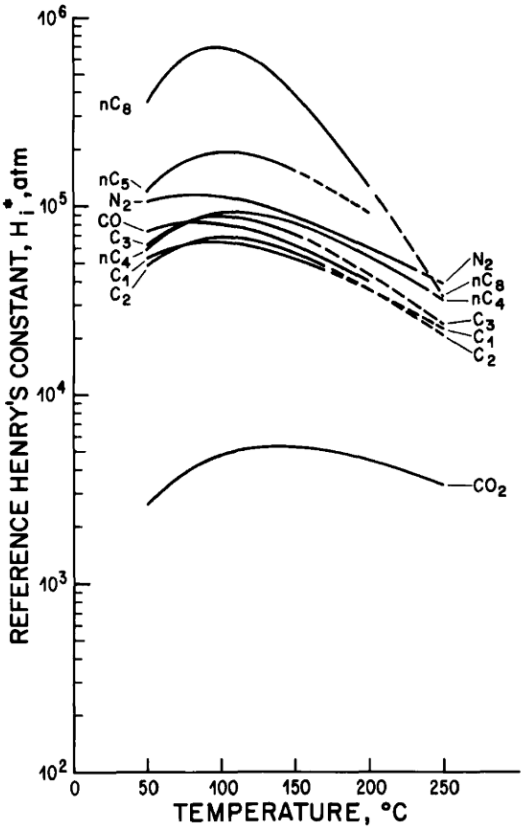


Figure 5.26: Variation of the reference Henry's Law Constant with temperature for various gases (Li & Nghiem, 1986).

In the case of DME, due to its polarity, it is partially soluble in water and fully miscible with oil under reservoir conditions. Since DME does not exist in the fluid libraries of the various PVT modeling software, based on the available literature (Cho et al., 2018), the solubility of pure DME in water under reservoir conditions is assumed to be the same as that of CO_2 (Scenario 2). However, two new scenarios are run in which the DME solubility in water is varied up to two orders of magnitude (**Table 5.16**).

Table 5.16: Scenarios to Evaluate the Effect of Water Solubility

Scenario	Injection Cycle Time (days)	Soaking Cycle Time (days)	Production Cycle Time (days)	Total Cycle Time (days)	Solubility
10	30	-	30	60	Base
11	30	-	30	60	10x Solubility
12	30	-	30	60	100x Solubility

Figure 5.27 and **Table 5.17** summarize the results for the different scenarios, with the same volume of DME injected for the various scenarios. As expected, the cumulative water production was the highest for Scenario 12 with 100x solubility. The DME mole fraction in the oil phase was initially zero until the cyclic huff-and-puff started, as DME does not occur naturally in the reservoirs. After a cyclic process for 26 months, the DME mole fraction was the highest for Scenario 10, with the lowest water solubility, as more DME was available to mix with the remaining oil in the reservoir. As a result, the oil viscosity reduction was the highest for Scenario 10. The DME mole fraction in the oil phase and oil viscosity are plotted for a grid block within the SRV but do not directly offset the hydraulic fracture. Finally, the cumulative oil production was the highest for Scenario 10. With differences in oil recovery, a wide range of HPE values were observed for the three scenarios.

Table 5.17: Results for the Different Scenarios

Scenario	Number of Cycles Fully Completed in 26 months	Total Gas Volume Injected (MMcf)	Maximum BHP Reached for Different Wells (psi)	Cumulative Oil Volume (Mbo)	Oil Recovery Uplift Relative to Non-EOR Scenario after 1 year	Oil Recovery Uplift Relative to Non-EOR Scenario after 26 Months	Huff-and-Puff Efficiency (STB/MMcf)
10	13	360.0	1,287 - 1,914	45.855	47.5%	76.0%	55.0
11	13	360.0	1,305 - 1668	43.631	37.1%	67.4%	48.8
12	13	360.0	1,215 - 1,621	31.624	11.8%	21.4%	15.5

According to Parsons et al. (2016), DME has a water solubility of three orders of magnitude greater than that of LPG (Parsons et al., 2016). If that applies under the reservoir conditions, the DME solubility would mimic Scenario 12. Even in that case, the HPE for Scenario 12 (15.5) is significantly higher than that with field gas (Scenario 2 with HPE of 7.7) and CO_2 (Scenario 9 with HPE of 4.5). Additionally, experimental work with DME has shown no asphaltene precipitation (Salimi et al., 2022), but it could lower the HPE for field gas and CO_2.

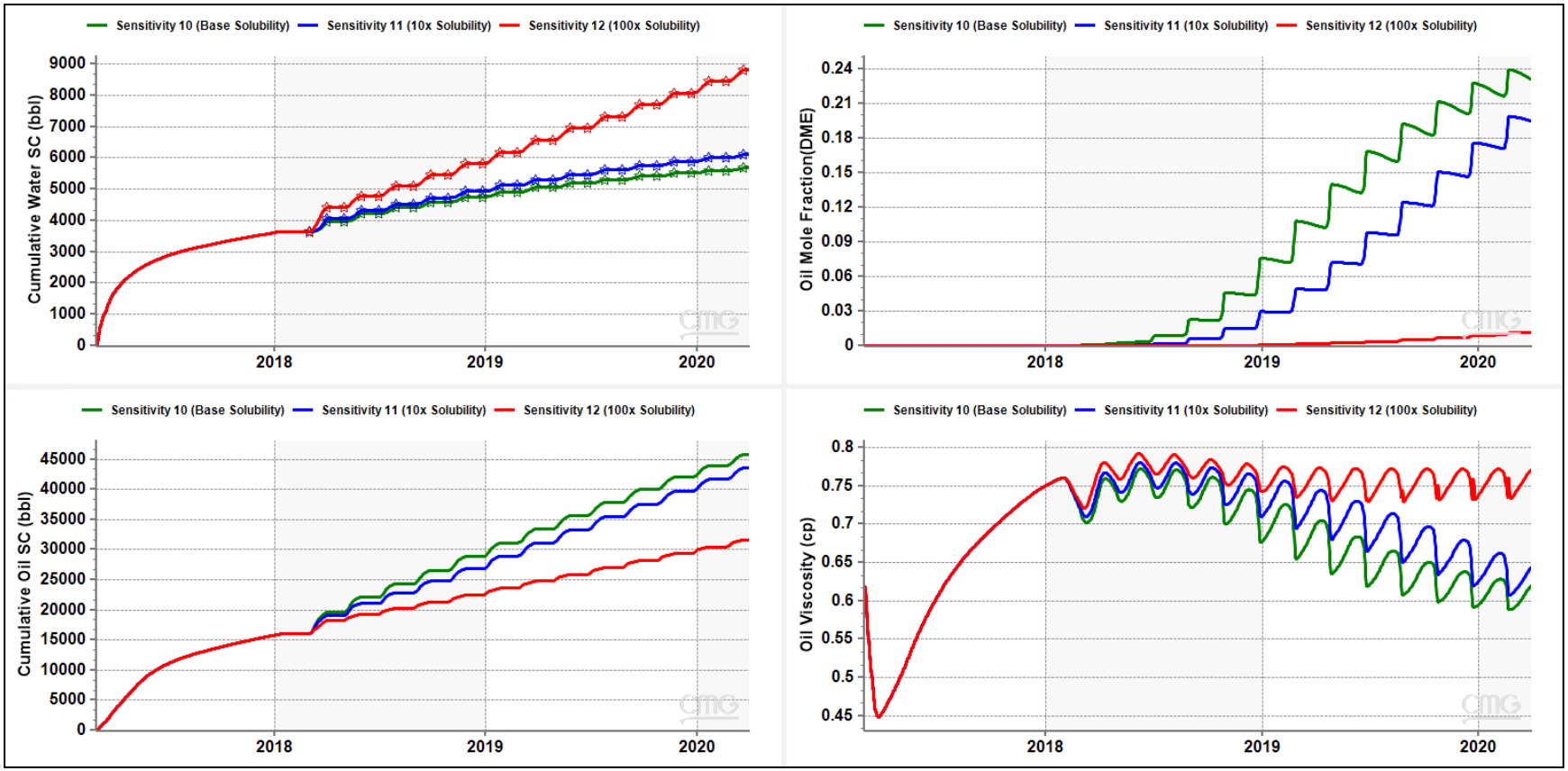


Figure 5.27: Cumulative water production, cumulative oil production, DME mole fraction in oil, and oil viscosity for scenarios 10, 11, and 12.

Effect of Binary Interaction Coefficients for DME

The Binary Interaction Coefficients (BICs) are a set of correction terms to the mixing rule for the model parameter 'a' in the cubic equation of state models. Typically, the BICs range from -0.1 to 0.2 and are computed by using correlations, tuning the fluid model to the experimental data, or a combination of both, and have been shown to impact the phase behavior calculations significantly. The history matching process used a twelve-component Peng Robinson EOS model developed using the two oil samples from Eagle Ford. **Table 5.3** includes the Binary Interaction Coefficients for the fluid model after tuning.

For DME, the BICs in the sensitivities so far have been based on the phase equilibrium modeling published by Cho et al. (2018) (**Table 5.14**). A sensitivity was performed using work by Tsanas (2018), in which the BICs were computed for the binary systems of water, hydrocarbons, and inert gases (**Table 5.18**). The oil composition used for the experiments consisted of a mixture of methane, n-butane, and n-decane, and the results were slightly different from Cho et al. (2018). A sensitivity was performed with these values (**Table 5.19**).

Table 5.18: Binary Interaction Coefficients between DME and other components (Tsanas (2018))

Component	**DME**
C1	0.0401
C3	0.0486
nC4	0.0425
nC5	0.0402
n-C10	0.0174
nC12	0.0091
CO_2	-0.0066
N_2	0.1063

Table 5.19: Scenarios to Evaluate the Effect of BICs

Scenario	Injection Cycle Time (days)	Soaking Cycle Time (days)	Production Cycle Time (days)	Total Cycle Time (days)	BIC Source
10	30	-	30	60	Base
13	30	-	30	60	DTU

Table 5.20 and **Figure 5.28** summarize the results for this sensitivity, with the same volume of DME injected in the two scenarios. The updated BIC values showed a significantly higher DME mole fraction in the oil phase, resulting in a higher oil viscosity reduction. The cumulative oil production was ~20% higher, with a much higher HPE.

Table 5.20: Results for the Different Scenarios

Scenario	Number of Cycles Fully Completed in 26 months	Total Gas Volume Injected (MMcf)	Maximum BHP Reached for Different Wells (psi)	Cumulative Oil Volume (Mbo)	Oil Recovery Uplift Relative to Non-EOR Scenario after 1 year	Oil Recovery Uplift Relative to Non-EOR Scenario after 26 Months	Huff-and-Puff Efficiency (STB/MMcf)
10	13	360.0	1,287 - 1,914	45.855	47.5%	76.0%	55.0
13	13	360.0	1,337 - 1,883	54.946	71.3%	110.9%	80.2

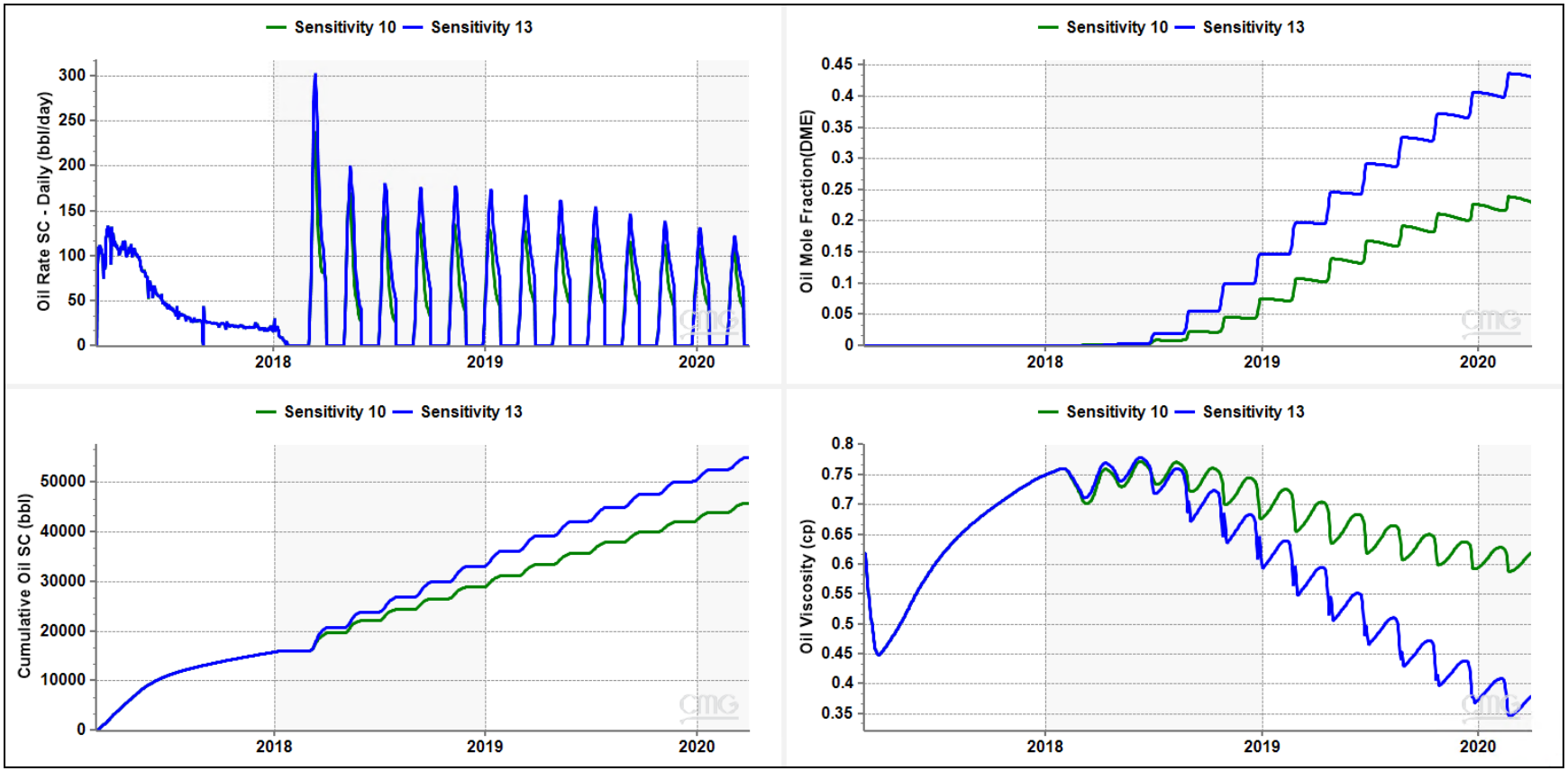


Figure 5.28: Oil rate, cumulative oil production, DME mole fraction in oil, and oil viscosity for scenarios 10 and 13.

Effect of Soaking Time

To evaluate the effect of soaking time with different injectants, scenarios 2 and 8 (field gas without and with soaking) were compared to CO_2 and DME with 30 days of soaking (**Table 5.21**).

Table 5.21: Scenarios to Evaluate the Effect of Soaking Time

Scenario	Injection Cycle Time (days)	Soaking Cycle Time (days)	Production Cycle Time (days)	Total Cycle Time (days)	Injectant Type
2	30	-	30	60	Field Gas
8	30	30	30	90	Field Gas
9	30	-	30	60	CO_2
14	30	30	30	90	CO_2
10	30	-	30	60	DME
15	30	30	30	90	DME

Figure 5.29, **Table 5.22** and **Table 5.23** summarize the results. For scenarios 14 and 15 with soaking times added, the duration of the runs was extended to keep the number of cycles unchanged from scenarios 9 and 10, respectively. The results are included in **Table 5.22**. Although the bottom hole pressures for the scenarios with soaking were similar to those without, additional cumulative oil recovery and improved HPE were observed due to the extended mixing of the fluid allowed during soaking.

Table 5.23 compares the results with different numbers of cycles completed within the same 26-month period for the different scenarios. Although the cumulative oil production was lower due to the addition of soaking stages, the HPE was comparable to slightly better for the CO_2 and DME cases.

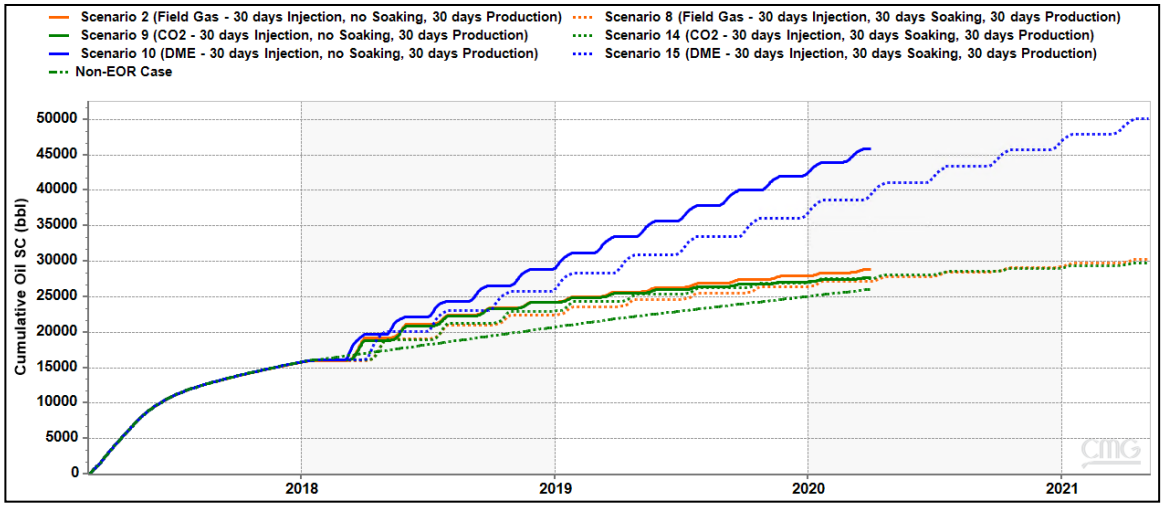


Figure 5.29: Cumulative oil production for the different scenarios.

Table 5.22: Results for the Different Scenarios to Evaluate the Effect of Soaking Time – same number of cycles

Scenario	Number of Cycles Fully Completed	Total Gas Volume Injected (MMcf)	Maximum BHP Reached for Different Wells (psi)	Cumulative Oil Volume (Mbo)	Oil Recovery Uplift Relative to Non-EOR Scenario after 1 year	Oil Recovery Uplift Relative to Non-EOR Scenario after 13 Cycles	Huff-and-Puff Efficiency (stb/MMcf)
2	13	360.0	2,220 - 2,728	28.814	18.3%	10.6%	7.7
8	13	360.0	2,220 - 2,728	30.293	11.6%	16.3%	11.8
9	13	360.0	1,656 - 2,063	27.668	17.8%	6.2%	4.5
14	13	360.0	1,656 - 2,063	29.779	15.0%	14.3%	10.3
10	13	360.0	1,287 - 1,914	45.855	47.5%	76.0%	55.0
15	13	360.0	1,287 - 1,914	50.038	34.1%	92.0%	66.6

Table 5.23: Results for the Different Scenarios to Evaluate the Effect of Soaking Time – same 26 months of total huff-and-puff duration; different number of cycles

Scenario	Number of Cycles Fully Completed in 26 months	Total Gas Volume Injected (MMcf)	Maximum BHP Reached for Different Wells (psi)	Cumulative Oil Volume (Mbo)	Oil Recovery Uplift Relative to Non-EOR Scenario after 1 year	Oil Recovery Uplift Relative to Non-EOR Scenario after 26 Months	Huff-and-Puff Efficiency (stb/MMcf)
2	13	360.0	2,220 - 2,728	28.814	18.3%	10.6%	7.7
8	8	243.0	2,220 - 2,728	27.163	11.6%	4.2%	4.5
9	13	360.0	1,656 - 2,063	27.668	17.8%	6.2%	4.5
14	8	243.0	1,656 - 2,063	27.584	15.0%	5.9%	6.3
10	13	360.0	1,287 - 1,914	45.855	47.5%	76%	55.0
15	8	243.0	1,287 - 1,914	39.391	34.1%	51.1%	54.8

5.6 Discussion

Compared to the produced gas (rich in C1) typically used as an injectant in the huff-and-puff pilots, CO_2 is often discussed as an alternative due to its long history of being used in the conventional EOR with reduced MMP, as well as having higher sweep efficiency under miscibility conditions. A new liquid injectant, DME, is presented, which shows encouraging modeling results and provides several benefits compared to both the produced gas and CO_2:

1) At the surface, the unique property of DME being liquified at low pressures makes it easier to handle and inject using a triplex pump. It does not require high horsepower compressors needed with gas injectants, thereby reducing the overall project costs by an order of magnitude, making DME a significantly cost-effective injectant.
2) Regarding the recovery mechanism, DME has a higher preferential solubility in the oleic phase at intermediate pressures than other injectants. Under reservoir

conditions, first contact miscibility occurs, thereby reducing the viscosity of the contacted oil, enhancing oil mobility, and ultimately resulting in a higher oil recovery

   a. In the case of CO_2, the vaporizing mechanisms lead to reduced intermediate hydrocarbon components in the contacted oil, leaving behind a heavier residual oil with increasing viscosity over time.

3) At reservoir conditions, the DME exists in a liquid state, making it a more efficient solvent promoting single-phase flow. As a result, DME shows a greater penetration distance compared to the other two gas injectants (**Figure 5.21** through **Figure 5.25**).

   a. For the cases studied here, at reservoir conditions, both produced gas and CO_2 existed in a gaseous phase, increasing gas saturation and promoting two-phase flow (inefficient process).

   b. Based on the experimental work by Salimi et al. (2022), the DME is an efficient solvent, and as it mixes with remaining oil (even) at low DME ratios, it reduces oil viscosity significantly.

   c. Since DME exists in a liquid state under reservoir conditions, it is not expected to show the gravity override issues typically seen with gas injectants, which have lower densities than oil.

4) Based on the experimental work published in the literature, no asphaltene deposition has been reported when oil was mixed with DME at increasing ratios up to 80% v/v.

5) Because of its low boiling point, DME can be easily extracted from the produced wellstream fluid by distillation and reused for injection. Unlike CO_2, DME will not contaminate the produced wellstream.

6) Additionally, since the DME does not occur naturally, it can be easily tagged and used as a tracer, helping understand inter-well connectivity. In the case of containment issues, the DME injection (rate and volume) can be controlled/optimized, which cannot be done with the hydrocarbon injectants that occur naturally.
7) The DME is not corrosive like CO_2, so it does not need wellbore tubulars to be rated for sour service.

Although gas injectants are being commonly used for huff-and-puff EOR applications in shale reservoirs, Venepalli et al. (2021) and Alinejad & Dehghanpour (2023) have presented advantages of using NGL as an injectant. Like DME, the NGL can be injected as a liquid using a triplex pump. The NGLs contain intermediate components, which have been observed to drop with every subsequent huff-and-puff cycle, making the NGLs difficult to reuse. Since NGLs occur naturally in the reservoirs, it cannot be traced or tracked easily. In contrast, the DME has the advantages of lower cost and higher efficiency and can be easily extracted from the produced well stream fluid for re-injection (Cho et al., 2018).

While several advantages are presented of using DME as a liquid solvent for the huff-and-puff process, the impact of HSE (Health, Safety and Environmental) should be carefully evaluated during field implementation. DME is a highly flammable fluid and a dangerous fire hazard, and safe work practices should always be followed. Instead of using pure DME, it can be mixed with 10-20% volume of water to reduce the reactive nature of DME.

5.6.1 Schematic of cyclic process with DME

After the first three steps of injection, soaking, and production, the cyclic process is modified to include the separation of the DME at the flash tank, and then re-injecting of the produced DME for the next cycle (**Figure 5.30**). For step 4, since the DME boils at a much lower temperature compared to other hydrocarbons, it is easier to extract DME from the produced well stream compared to the other injectants, especially CO_2. Due to its chemical structure, the DME has weak intermolecular Van der Waal's forces and no hydrogen bonding, causing it to boil at a lower temperature and can be recovered by distillation.

The reuse of the DME reduces the overall project costs, thereby making the modified cyclic process more efficient than currently available technology.

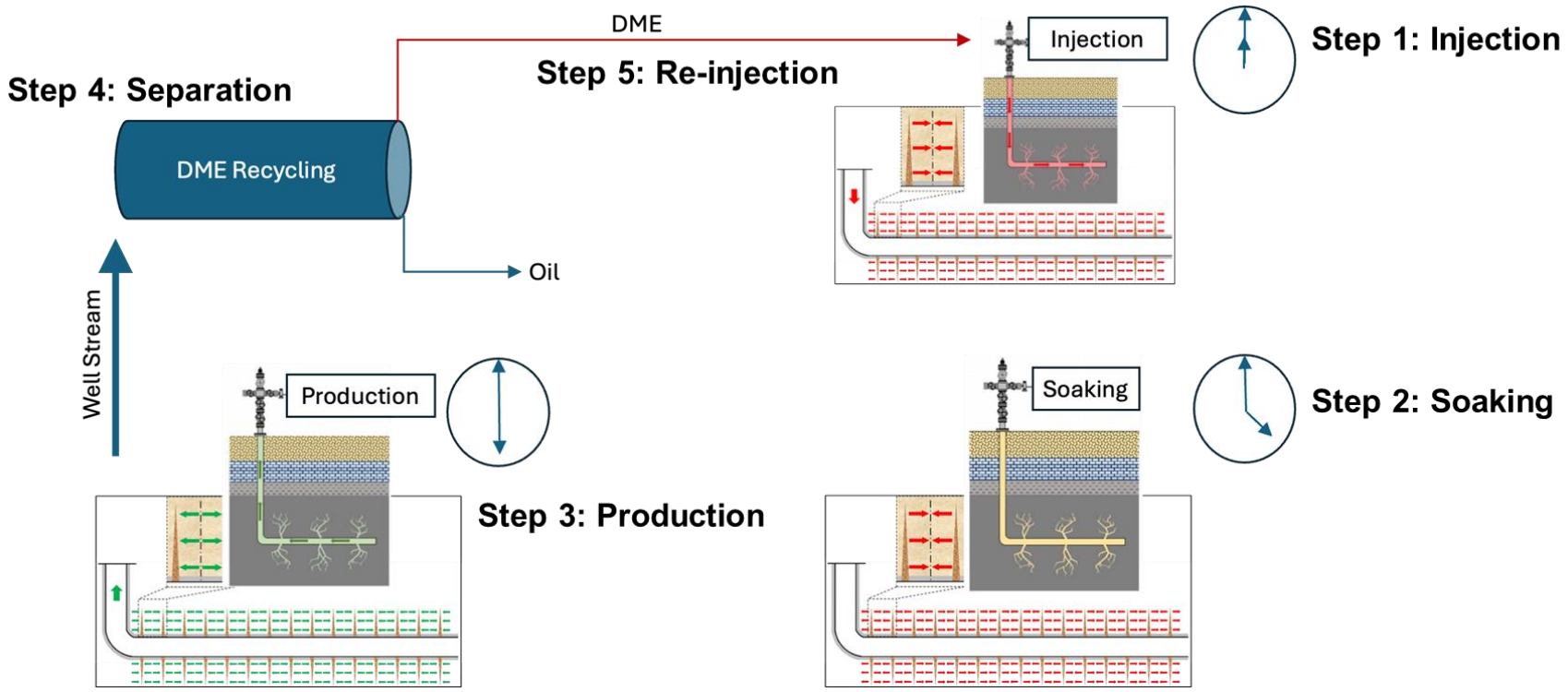


Figure 5.30: Schematic of the cyclic process with DME

5.7 Key Takeaways

A novel liquid injectant, DME, is presented, which shows promising modeling results and provides several potential transformative benefits compared to the two gas injectants (produced gas and CO_2):

- The unique characteristic of DME being liquified at low pressures makes it suitable and cost-effective as an injectant.
- Preferentially partitions into the oleic phase at intermediate pressures, thereby swelling and mobilizing the oil phase. The oil recovery with the huff-and-puff process with DME is much higher than that with the two other gas injectants.
- DME shows a greater penetration distance as it stays in the liquid phase at reservoir conditions, promoting single-phase flow (efficient process). The two gas injectants at reservoir conditions (at least in cases studied here) existed in a gaseous phase, increasing gas saturation and promoting two-phase flow (inefficient process).
- No evidence in the literature claiming DME interference with the resident oil chemistry resulting in asphaltene deposition. However, the issues of asphaltene deposition and permeability impairment are well documented with other gas injectants such as CO_2.
- Since DME does not occur naturally in petroleum reservoirs, it can be used as a tracer to understand inter-well connectivity. In the case of containment issues, the DME injection rate and volumes can be controlled/optimized.
- Because of its low boiling point, the DME can be easily extracted from the produced wellstream fluid by distillation and reused for injection, thereby reducing project costs.

Building on the work in Chapter 4, where the effect of the soaking phase was investigated analytically, the soaking phase is explored further using a numerical simulation model and three different injectants.

- Although the addition of the soaking phase extends the duration of each huff-and-puff cycle, it allows the extended mixing of the fluids, resulting in additional cumulative oil recovery and an improved Huff-and-Puff Efficiency (HPE) metric.
- The oil viscosity reduction is the same for the initial two cycles, with or without soaking. However, the addition of the soaking phase results in higher viscosity reduction from the third cycle onwards and higher peak oil rates for subsequent cycles, compared to no soaking. In contrast, the viscosity reduction mechanism with no soaking continues to become less effective in subsequent cycles.
- Overall, the huff-and-puff cycles should be tailored to increase the soaking period (assuming the injection rate is fixed) with every subsequent cycle to increase the penetration and oil recovery. This corroborates the findings from Chapter 4, where the initial cycles were found to be tapping into smaller matrix blocks closer to the wellbore, but soaking is needed in subsequent cycles to tap into larger matrix blocks away from the wellbore.

Chapter 6

Conclusions and Recommendations

This chapter focuses on the conclusions drawn from this research. Recommendations for field operations and future work are also included.

6.1 Conclusions

The project objectives are re-stated along with the conclusions made from the research work and observations:

1) *Develop a mathematical model to simulate the huff-and-puff process*
    a. A 1-D mathematical model is developed leveraging the classical analytic equations to understand recoveries at the core and reservoir scales. Based on the Peclet number criterion, mass transfer in the shale matrix is modeled to be diffusion-dominated. The model represents the diffusion of a limited volume of a well-stirred fluid into a porous medium (matrix). To better represent field conditions, the matrix is characterized as an ensemble of randomly distributed rock pillars separated by fracture discontinuities, and the recovery is explored as a function of the micro-fracture distribution.
2) *Evaluate the accessibility of the injected gas during the injection, soaking, and production cycles in the presence of natural and hydraulic fractures*
    a. The penetration of the injectant into the matrix during the injection, soaking, and production phases are evaluated and compared as a function of

parameters such as diffusion coefficient, matrix block size, and duration of the different phases of the cyclic process.

b. The impact of complex fracture networks created during hydraulic fracturing on the efficacy of the huff-and-puff EOR process is investigated by modeling matrix blocks of different lengths:

    i. The Lorenz/Cauchy distribution observed in the laboratory experiments by Damani et al. (2018) for fracture density can be scaled to the field using the 1:50 upscaling relationship.

    ii. Secondary fractures emanating from the primary fracture follow a Lorenz/Cauchy distribution and result in decreasing recoveries away from the wellbore. Initial cycles appear to tap into the tightly spaced fractures/smaller matrix blocks near the wellbore. As cycles are repeated, the larger blocks away from the wellbore are accessed with comparatively slower recovery. To optimize the recovery/process, the operators should look into extending the injectant-remaining oil contact time by modifying the duration of injection/soaking/production phases in subsequent cycles.

3) *Based on the results from the model, develop a correlation or series of correlations that help to understand the recoveries at the field scale. Such a correlation(s) can help with better candidate selection and a more accurate technical evaluation during the feasibility and post-treatment lookback evaluation.*

a. Discrepancies in the recoveries between the lab and field scales can be resolved by incorporating the two scaling parameters, Alpha α and Mass Transfer Coefficient B_i.

b. An upscaling equation is derived in terms of $\frac{B_i}{\alpha}$ to predict recovery factors better

c. Two upscaling schemes are identified to translate recovery factors from core to reservoir scale based on the values of α, and exponential and logarithmic trends were observed for α = 0.1 and α > 0.1, respectively.

    i. The implication of these two upscaling schemes could help explain the perception of why the wells with better primary recovery (larger contact area, larger fracture volumes, larger α) make better candidates for huff-and-puff application.

4) Evaluate the role of soaking time as a function of stimulated reservoir volume

a. The soaking phase was found to be significantly less impactful on the smaller matrix blocks closer to the wellbore. However, larger matrix blocks away from the wellbore show increasing penetration lengths with longer soaking times.

    i. In the field, as the subsequent cycles are repeated, usually keeping the duration or cycle times of the phase unchanged, the larger matrix blocks away from the wellbore are accessed with comparatively slower recovery. This explains the reduced recovery observed from the subsequent cycles in the field pilots.

b. Additionally, the addition of the soaking phase allows the extended mixing of the fluids, resulting in higher oil viscosity reduction and additional cumulative oil recovery compared to no soaking. The addition of the soaking phase also improved the Huff-and-Puff Efficiency (HPE).

c. Since the initial huff-and-puff cycles are suspected to be tapping into and recovering the remaining oil from smaller matrix blocks near the wellbore, to optimize the process, the huff-and-puff cycles should be tailored to increase the soaking period with every subsequent cycle. Operators can possibly skip or limit the soaking phases from the initial cycles. However, as the large matrix blocks away from the wellbore are the main contributor to production in subsequent cycles, increasing the duration of soaking stages for the subsequent cycles is recommended.

    i. The initial cycles tapping into smaller matrix blocks near the wellbore help explain the industry's perception, with some claiming that the soaking phase does not add any additional recovery.

5) *To investigate the feasibility of other injectants, such as liquid solvents, that could eliminate one or more issues realized with the gas-based cyclic miscible huff-and-puff process.*

    a. The cyclic miscible gas injection field pilots have highlighted two complex issues: (i) the containment of the injected gas, and (ii) asphaltene deposition, which results in permeability impairment.

b. A novel liquid injectant, DME, is presented, which can mitigate these two issues and provide several benefits to gas injectants.
    i. DME's unique property of being liquified at low pressures makes it suitable and cost-effective as an injectant.
    ii. Preferentially partitions into the oleic phase at intermediate pressures, thereby swelling and mobilizing the oil phase. The oil recovery with the huff-and-puff process with DME is much higher than that with the two other gas injectants.
    iii. DME shows a greater penetration distance as it stays in the liquid phase at reservoir conditions, promoting single-phase flow (efficient process). The two gas injectants at reservoir conditions (at least in cases studied here) existed in a gaseous phase, increasing gas saturation and promoting two-phase flow (inefficient process).
    iv. The literature does not provide evidence of DME interference with the resident oil chemistry resulting in asphaltene deposition. However, the issues of asphaltene deposition and permeability impairment are well documented with other gas injectants, such as CO_2.
    v. Since DME does not occur naturally in petroleum reservoirs, it can be used as a tracer to understand inter-well connectivity. In the case of containment issues, the DME injection rate and volumes can be controlled/optimized.

vi. Because of its low boiling point, the DME can be easily extracted from the produced wellstream fluid by distillation and reused for injection, thereby reducing project costs.

Although significant work has been completed in the last 15 years by the combined efforts of academia and industry, the mechanics of huff-and-puff application in shale reservoirs are not well understood. The results and recommendations from this research provide a better understanding of the huff-and-puff process. They can thus be used to assist with the feasibility studies and optimize the field implementation of the huff-and-puff EOR.

6.2 Recommendations for Future Work

The results from this research work have provided additional insights to understand the huff-and-puff process better. Additional studies are recommended to expand this understanding further. With all the knowledge acquired during this research, the recommendations for potential future work are:

- The mathematical model can be extended to include the effect of advection, as the Peclet number is not constant and could vary due to lithology and fabric changes within the rock.
    - The upscaling schemes identified using the current mathematical model can be validated using numerical methods/simulation

- The compositional modeling and simulation can be enhanced by:
    - Modeling asphaltene precipitation with field gas and CO_2 to improve the model forecast
    - Although smaller grids and local grid refinement were used to represent the matrix and the hydraulic fracture, respectively, the overmixing of the fluids and penetration of the injected fluid into the reservoir should be evaluated with finer grids.
    - Characterizing natural and hydraulic fractures is of utmost importance, as a lack of injectant containment could impact the overall project outcome. Future work should model natural fractures to capture the injection patterns better and to estimate recovery uplift more accurately.

Nomenclature

α = scaling parameter, dimensionless

δ = Pore Constrictivity, dimensionless

ε_t = Effective transport-through porosity, dimensionless

γ = scale parameter for Lorenz/Cauchy distribution

τ_f = Toruosity, dimensionless

j = diffusive flux

k_c = convective mass transfer coefficient, dimensionless

u = bulk velocity due to advection in the control volume, m/s

x = space coordinate measured normal to the section

x_0 = location of the peak of the Lorenz/Cauchy distribution

B_i = Mass transfer coefficient, dimensionless

C = concentration of diffusing substance

D = Diffusion coefficient, m^2/s

D_e = Effective Diffusion Coefficient, m^2/s

F = Waxman-Smits Formation Resistance Factor

F = rate of transfer per unit area of section

F_x = rate of transfer through the unit area of the corresponding plane through the center point P (x,y,z)

L_c = Characteristic length available for flow, m

L = half of cluster spacing, m

L_p = Penetration Length, m

K = inverse of α, defined in the heat and mass transfer equations

M_t = total amount of gas diffused, moles

References

Afari, S., Ling, K., Sennaoui, B., Demetrius, M., Oguntade, T., and Porlles, J., (2022). *Optimization of CO_2 huff-n-puff EOR in the Bakken Formation using numerical simulation and response surface methodology*, Journal of Petroleum Science and Engineering, Volume 215, Part A, August 2022. DOI: https://doi.org/10.1016/j.petrol.2022.110552.

Akita, E., and Moghanloo, R.G., (2018). *A Systematic Approach for Upscaling of the EOR Results from Lab-Scale to Well-Scale in Liquids-Rich Shale Plays*, SPE paper 190188, presented at SPE Improved Oil Recovery Conference held in Tulsa, Oklahoma, USA, April 14-18, 2018. DOI: https://doi.org/10.2118/190188-MS.

Alfarge, D., Wei, M, and Bai, B. (2017). *IOR Methods in Unconventional Reservoirs of North America: Comprehensive Review*, SPE paper 185640, presented at the 2017 SPE Western Regional Meeting held in Bakersfield, California, USA, April 23, 2017. DOI: https://doi.org/10.2118/185640-MS.

Alfarge, D., Alsaba, M., Wei, M., Bai, B., (2018). *Miscible Gases Based EOR in Unconventional Liquids Rich Reservoirs: What We Can Learn*, SPE paper 193748, presented at the SPE International Heavy Oil Conference and Exhibition held in Kuwait City, Kuwait, December 10-12, 2018. DOI: https://doi.org/10.2118/193748-MS.

Alharty, N., Teklu, T., Kazemi, H., Graves, R., Hawthorne, S., Braunberger, J., and Kurtoglu, B. (2015). *Enhanced Oil Recovery in Liquids-Rich Shale Reservoirs: Laboratory to Field*, SPE paper 175034, SPE Res Eval & Eng 21(01): 137-159, February 2018, DOI: https://doi.org/10.2118/175034-PA.

Alinejad, A., and Dehghanpour, (2023). *Using Natural Gas Liquid for EOR in a Huff-N-Puff Process – A Feasibility Study*, SPE paper 214825, presented at the SPE Annual Technical Conference and Exhibition, held in San Antonio, Texas, USA, October 16-18, 2023. DOI: https://doi.org/10.2118/214825-MS.

Ashoori, S., Sharifi, M., Masoumi, M., Salehi, M.M., (2017). *The relationship between SARA fractions and crude oil stability*, *Egyptian Journal of Petroleum*, Volume 26, Issue 1, 2017, Pages 209-213, DOI: https://doi.org/10.1016/j.ejpe.2016.04.002.

Ataceri, I.Z., Sapotra, I.W.R., Bagareddy, A.R., Elkady, M.H., Schechter, D.S., Haddix, G.W., Brock, V.A., Raney, K.H., Strickland, C.W., and Morris, G.R., (2023). *Surfactant Enhanced Oil Recovery Improves Oil Recovery in a Depleted Eagle Ford Unconventional Well: A Case Study*, SPE-215827-PA, SPE Journal 28 (06): 3180-3191. DOI: https://doi.org/10.15530/urtec-2023-3831548.

Atan, S., Ajayi, A., Honarpour, M., Turek, E., Dillenbeck, E., Mock, C., Ahmadi, M., and Pereira, C., (2018). *The Viability of Gas Injection EOR in Eagle Ford Shale Reservoirs*, SPE

paper 191673, presented at the 2018 SPE Annual Technical Conference and Exhibition held in Dallas, Texas, September 24-26, 2018. DOI: https://doi.org/10.2118/191673-MS.

Backeberg, N.R., Iacoviello, F., Rittner, M., Mitchell, T.M., Jones, A.P., Day, R., Wheeler, J., Shearing, P.R., Vermeesch, P., Striolo, A., (2017). *Quantifying the anisotropy and tortuosity of permeable pathways in clay-rich mudstones using models based on X-ray tomography*, Scientific Reports, 7: 14838, 2017. DOI: https://doi.org/10.1038/s41598-017-14810-1.

Baldwin, A., Lasecki, L., Mohrbacher, D., Porter, L., Tatarin, T., Nicoud, B., Taylor, G., Zaghloul, J., Basbug, B., Firincioglu, T., and Ghahfarokhi, R.B., (2020). *A Methodological Workflow for Assessment and Design of a Huff-N-Puff Hydrocarbon Gas Injection Pilot Test as an EOR Technique for Eagle Ford Shale Oil Reservoirs*, SPE paper 200415, presented at the SPE Improved Oil Recovery Conference, held virtually, August 31 – September 4, 2020. DOI: https://doi.org/10.2118/200415-MS.

Behbahani, T.J., Ghotbi, C., Taghikhani, V., and Shahrabadi, A., (2013), *Asphaltene Deposition under Dynamic Conditions in Porous Media: Theoretical and Experimental Investigation*, Energy Fuels 2013, 27, 2, 622-639, January 9, 2013. DOI: https://doi.org/10.1021/ef3017255.

Behbahani, T.J., Ghotbi, C., Taghikhani, V., and Shahrabadi, A. (2014). *Investigation of asphaltene adsorption in sandstone core sample during CO_2 injection: Experimental and modified modeling*, Fuel 2014, 133, 63-72, October 1, 2014. DOI: https://doi.org/10.1016/j.fuel.2014.04.079.

Bhagat, A., (2012). *Analysis of hydraulic fracture in Lyons sandstone using SEM*, USGS Consortium presentation, University of Oklahoma.

Bin, M., Mamoudou, S., Dang, S., Tinni, A., Sondergeld, C., and Rai, C., (2020). *Comprehensive Experimental Study of Huff-n-Puff Enhanced Oil Recovery in Eagle Ford: Key Parameters and Recovery Mechanism*, SPE paper 200436, presented at the SPE Improved Oil Recovery Conference, held virtually, August 31 – September 4, 2020. DOI: https://doi.org/10.2118/200436-MS.

Cander, H., (2012). *What are unconventional resources? A simple definition using viscosity and permeability*, AAPG Annual Convention and Exhibition, held at Long Beach, California, USA, April 22-25, 2012.

Carlsen, M.L., Whitson, C.H., Dahouk, M.M., Younus, B., Yusra, I., Kerr, E., Nohavitza, J., Thuesen, M., Drozd, J.H., Ambrose, R., and Mydland, S., (2019), *Compositional Tracking of a Huff-n-Puff Project in the Eagle Ford*, URTeC paper 539, presented at the Unconventional Resources Technology Conference, held in Denver, Colorado, USA, July 22-24, 2019. DOI: https://doi.org/10.15530/urtec-2019-539.

Carlsen, M.L., Mydland, S., and Whitson, C.H., (2020). *Gas EOR in Tight Unconventionals*, SPE Short Course, Unconventional Resources Technology Conference held virtually, July 20-22, 2020.

Carslaw, H. S. and Jaeger, J. C., (1959). *Conduction of Heat in Solids*, Clarendon Press, Oxford, United Kingdom.

Chahardowli, M.; Farajzadeh, R.; Bruining, H., (2016). *Experimental investigation of the use of the dimethyl ether/polymer hybrid as a novel enhanced oil recovery method*, J. Ind. Eng. Chem. 2016, 38, 50–60. DOI: https://doi.org/10.1016/j.jiec.2016.04.008.

Chernetsky, A., Masalmeh, S., Eikmans, D., Boerrigter, P.M., Fadili, A., Parsons, C.A., Parker, A., Boersma, D.M., Cui, J., Dindoruk, B., te Riele, P.M., Alkindi, A., and Azri, N., (2015). *A Novel Enhanced Oil Recovery Technique: Experimental Results and Modelling Workflow of the DME Enhanced Waterflood Technology*, SPE paper 177919, presented at the Abu Dhabi International Petroleum Exhibition and Conference, held in Abu Dhabi, UAE, November 9-12, 2015. DOI: https://doi.org/10.2118/177919-MS.

Cho, J., Kim, T.H., and Lee, K.S. (2018). *Compositional modeling and simulation of dimethyl ether (DME)-enhanced waterflood to investigate oil mobility improvement*, Pet. Sci. 15, 297–304, 2018. DOI: https://doi.org/10.1007/s12182-017-0212-z.

Clark, A. J., (2009). *Determination of Recovery Factor in the Bakken Formation, Mountrail County, ND*, SPE paper 133719, presented at the SPE Annual Technical Conference and Exhibition held in New Orleans, Louisiana, USA, 4-7 October 2009. DOI: https://doi.org/10.2118/133719-STU.

Crank, J., (1975). *The Mathematics of Diffusion*, Clarendon Press, Oxford.

Cronin, M., (2020). *Cyclic Solvent Injection in Ultratight Reservoirs Based on the Diffusion Process*, Ph.D. Dissertation, The Pennsylvania State University, December 2020. DOI: https://etda.libraries.psu.edu/files/final_submissions/22636.

Cronin, M., Emami-Meybodi, H., and Johns, R.T., (2019). *Diffusion-Dominated Proxy Model for Solvent Injection in Ultratight Oil Reservoirs*, SPE paper 190305, SPE Journal 24(02): 660-680, April 2019. DOI: https://doi.org/10.2118/190305-PA.

Damani, A., Sondergeld, C. H., and Rai, C.S., (2017). *Experimental investigation of the effect of in situ and injection fluids on hydraulic fractures in Tennessee sandstone*, Journal of Petroleum Science and Engineering. DOI: 10.1016/j.petrol.2018.07.027.

Dang, S., (2019). *Understanding The Fundamental Drive Mechanisms For Huff-N-Puff Enhanced Oil Recovery In Tight Formations*, Doctoral dissertation, The University of Oklahoma.

Dang, S., Mamoudou, S., Rai, C., and Sondergeld, C., (2023). *Experimental Observation of Diffusion as the Main Drive Mechanism in Unconventional Shales*, URTEC-3864848-MS, presented at the SPE/AAPG/SEG Unconventional Resources Technology Conference, June 13–15, 2023. DOI: https://doi.org/10.15530/urtec-2023-3864848.

Davudov, D., and Moghanloo, R.G., (2018). *Impact of Pore Compressibility and Connectivity Loss on Shale Permeability*, Internation Journal of Coal Geology, Volume 187, Pages 98-113, February 15, 2018. DOI:10.1016/j.coal.2018.01.008.

de Boer, R.B., Leeriooyer, K., Eigner, M.R.P., and van Bergen, A. R. D., (1995). *Screening of Crude Oils for Asphalt Precipitation: Theory, Practice, and the Selection of Inhibitors*, SPE paper 24987-PA, SPE Prod & Fac 10 (1): 55–61. DOI: https://doi.org/10.2118/24987-PA.

EIA, (2023). *US EIA Annual Energy Outlook 2023*, https://www.eia.gov/outlooks/aeo/ (accessed: March 30, 2024).

Eltahan, E., Ganjdanesh, R., Yu, W., Sepehrnoori, K., Drozd, H., and Ambrose, R., (2020). *Assisted History Matching Using Bayesian Inference: Application to Multi-Well Simulation of a Huff-N-Puff Pilot Test in the Permian Basin*, URTeC paper 2787, presented at the Unconventional Resources Technology Conference held virtually, July 20-22, 2020. DOI: https://doi.org/10.15530/urtec-2020-2787.

Evans, S., Siddiqui, S., and Magness, J., (2018). *Impact of Cluster Spacing on Infill Completions in the Eagle Ford*, URTEC paper 2899323, presented at the Unconventional Resources Technology Conference, held in Houston, Texas, USA, July 23-2, 2018. DOI: https://doi.org/10.15530/URTEC-2018-2899323.

Enverus Prism, (2024). *Lower Eagle Ford EOR Projects*, https://www.enverus.com/ (accessed March 26, 2024).

Fiallos, M.X., Yu, W., Ganjdanesh, R., Kerr, E., Sepehrnoori, K., Miao, J., and Ambrose, R., (2019). *Modeling Interwell Interference Due to Complex Fracture Hits in Eagle Ford Using EDFM*, IPTC paper 19468, presented at the International Petroleum Technology Conference, held in Beijing, China, March 26-28, 2019. DOI: https://doi.org/10.2523/IPTC-19468-MS.

Fu, Q., Cudjoe, S., Barati, R., Tsau, J., Li, X., Peltier, K., Mohrbacher, D., Baldwin, A., Nicoud, B., and Bradford, K., (2019). *Experimental and Numerical Investigation of the Diffusion-Based Huff-n-Puff Gas Injection into Lower Eagle Ford Shale Samples*, URTeC

paper 402, presented at the Unconventional Resources Technology Conference held in Denver, Colorado, USA, July 22-24, 2019. DOI: https://doi.org/10.15530/urtec-2019-402.

Fragoso, A., Lopez, B.A., Aguilera, R., and Noble, G., (2019). *Matching of Pilot Huff-and-Puff Gas Injection Project in the Eagle Ford Shale Using a 3D 3-Phase Multiporosity Numerical Simulation Model*, SPE paper 195822, presented at the SPE Annual Technical Conference and Exhibition, held in Calgary, Alberta, Canada, September 30 – October 2, 2019. DOI: https://doi.org/10.2118/195822-MS.

Ganjdanesh, R., Yu, W., Fiallos, M.X., Kerr, E., Sepehrnoori, K., and Ambrose, R., (2019a). *Gas Injection EOR in Eagle Ford Shale Gas Condensate Reservoirs*, URTeC paper 987, presented at the Unconventional Resources Technology Conference held in Denver, Colorado, USA, July 22-24, 2019. DOI: https://doi.org/10.15530/urtec-2019-987.

Ganjdanesh, R., Yu, W., Torres, M. X. F., and Sepehrnoori, K., (2019b). *Huff-N-Puff Gas Injection for Enhanced Condensate Recovery in Eagle Ford*, SPE paper 195996, presented at the SPE Annual Technical Conference and Exhibition held in Calgary, Alberta, Canada, September 30 – October 2, 2019. DOI: https://doi.org/10.2118/195996-MS.

Ghasemi, M., Astutik, W., Alavian, S.A., Whitson, C.H., Sigalas, L., Olsen, V., Suicmez, V.S., (2017). *Determining Diffusion Coefficients for Carbon Dioxide Injection in Oil-Saturated Chalk by Use of a Constant-Volume-Diffusion Method*, SPE paper 179550, SPE Journal, 22 (02): 505 – 520, April 2017. DOI: https://doi.org/10.2118/179550-PA.

Grathwohl, P., (2012). *Diffusion in Natural Porous Media: Contaminant Transport, Sorption/Desorption and Dissolution Kinetics*, Springer US (Reprint). ISBN: 9781461556831.

Grinestaff, G., (2019). *Eagle Ford Shale Cyclic Gas Injection – Evaluation of Field Results and Economics*, Shale IOR presentation at the 25th Annual Conference in Midland, TX, December 12, 2019.

Grinestaff, G., Barden, C., Miller, J., Franklin, W., and Ding, E., (2020). *Evaluation of Eagle Ford Cyclic Gas Injection EOR: Feld Results and Economics*, SPE paper 200427, presented at the SPE Improved Oil Recovery Conference held virtually, August 31 – September 4, 2020. DOI: https://doi.org/10.2118/200427-MS.

Hamadou, R., Khodja, M., Kartout, M., and Jada, A., (2008). *Permeability reduction by asphaltenes and resins deposition in porous media*, Fuel 87, 10-11, 2178-2185, August 2008. DOI: https://doi.org/10.1016/j.fuel.2007.12.009.

Hamling, J., Sorensen, J., Guillot, S., Jin, L., Dalkhaa, C., (2021), *2021 Bakken EOR Topical Report – Findings and Conclusions Derived from Several Bakken Enhanced Oil Recovery Studies*, Bakken Production Optimization Program, April 30, 2021.

Hawthorne, S. B., Gorecki, C. D., Sorensen, J. A., Steadman, E. N., Harju, J. A., and Melzer, S., (2013). *Hydrocarbon mobilization mechanisms from Upper, Middle, and Lower Bakken reservoir rocks exposed to CO_2*, SPE paper 167200, presented at the SPE Unconventional Resources Conference Canada, Calgary, Alberta, Canada, November 5, 2013. DOI: https://doi.org/10.2118/167200-MS.

Hawthorne, S.B., Miller, D., Jin, L., and Gorecki, C.D., (2016). *Rapid and simple capillary-rise/Vanishing Interfacial Tension method to determine crude oil Minimum Miscibility Pressure: Pure and mixed CO2, methane, and ethane*, Energy & Fuels, 30(8), 6365-6372. DOI: 10.1021/acs.energyfuels.6b01151.

Hawthorne, S., Sorensen, J., Kurz, B., Gorecki, C., and Harju, J., (2018). *Lab Comparisons: Methane, Ethane, Propane, CO_2 and Produced Gas for Hydrocarbon Mobilization*, presented at the 24th Annual *CO_2* & ROZ Conference, December 6, 2018. DOI: https://www.CO2conference.net/wp-content/uploads/2018/12/Th9-Hawthorne-EERC-Lab-Gas-Studies-Update-12-6-18.pdf.

Hawthorne, S.B., Sorensen, J.A., Miller, D.J., Gorecki, C.D., Harju, J. A., and Pospisil, G., (2019). *Laboratory Studies of Rich Gas Interactions with Bakken Crude Oil to Support Enhanced Oil Recovery*, URTeC paper 961, presented at the Unconventional Resources Technology Conference held in Denver, Colorado, USA, July 22-24, 2019. DOI: https://doi.org/10.15530/urtec-2019-961.

Hawthorne, S.B., and Miller, D., (2019). *A comparison of crude oil hydrocarbon mobilization by vaporization gas drive into methane, ethane, and carbon dioxide at 15.6 MPa and 42°C*, Fuel 249 (2019) 392-399, August 1, 2019. DOI: https://doi.org/10.1016/j.fuel.2019.03.118.

Hawthorne, S.B., Grabanski, C.B., Miller, D.J., Kurz, B.A., and Sorensen, J.A., (2019). *Hydrocarbon Recovery from Williston Basin Shale and Mudrock Cores with Supercritical CO_2: Part 2. Mechanisms that Control Oil Recovery Rates and CO_2 Permeation*, Energy & Fuels 2019 33 (8), 6867-6877, August 1, 2019. DOI: https://pubs.acs.org/doi/10.1021/acs.energyfuels.9b01180.

Hoffman, B. T., and Evans J. G., (2016). *Improved Oil Recovery IOR Pilot Projects in the Bakken Formation*, SPE paper 180270, presented at the SPE Low Perm Symposium held in Denver, Colorado, USA, 5-6 May 2016. DOI: https://doi.org/10.2118/180270-MS.

Hoffman, B. T., (2018). *Huff-N-Puff Injection Pilot Projects in the Eagle Ford*, SPE paper 189816, presented at the SPE Canada Unconventional Resources Conference held in Calgary, Alberta, Canada, March 13-14, 2018. DOI: https://doi.org/10.2118/189816-MS.

Jacobs, T., (2019). *Shale EOR Delivers, So Why Won't the Sector Go Big?*, SPE Journal of Petroleum Technology, April 30, 2019. DOI: https://jpt.spe.org/shale-eor-delivers-so-why-wont-sector-go-big.

Jeffrey, R.G., and Settari, A., (1995). *A Comparison of Hydraulic Fracture Field Experiments, Including Mineback Geometry Data, with Numerical Fracture Model Simulations*, SPE paper 30508, presented at the SPE Annual Technical Conference and Exhibition, Dallas, Texas, October 22, 1995. DOI: https://doi.org/10.2118/30508-MS.

Jin, X., Pavia, M., Samuel, M., Shah, S., Zhang, R., and Thompson, J., (2019). *Field Pilots of Unconventional Shale EOR in the Permian Basin*, URTeC paper 506, presented at the SPE/AAPG/SEC Unconventional Resources Technology Conference, held in Denver, Colorado, USA, July 22-24, 2019. DOI: https://doi.org/10.15530/urtec-2019-506.

Kerr, E., Venepalli, K.K., Patel, K., Ambrose, R., and Erdle, J., (2020). *Use of Reservoir Simulation to Forecast Field EOR Response – An Eagle Ford Gas Injection Huff-N-Puff Application*, SPE paper 199722, presented at the SPE Hydraulic Fracturing Technology Conference and Exhibition held in The Woodlands, Texas, USA, February 4-6, 2020. DOI: https://doi.org/10.2118/199722-MS.

Kerr, E., (2024). *Personal Communication*.

Kostarelos, K., (2019). *Opportunities for CO_2 EOR in Unconventional Reservoirs*, 2019 Interdisciplinary CCUS Workshop, September 23-24, 2019.

Kovscek, A. R., Tang, G. Q., and Vega, B., (2008). *Experimental investigation of oil recovery from siliceous shale by CO_2 injection*, SPE paper 115679, presented at the SPE Annual Technical Conference and Exhibition, Denver, Colorado, USA, September 21, 2008. DOI: https://doi.org/10.2118/115679-MS.

Leahey, H., Thoms, M., Volkmer, N., McNamara, J., Koo, D., and Taylor, P., (2020). *Eagle Ford Enhanced Oil Recovery – Is there Enough Huff in This Puff*, Enverus Report, June 10, 2020.

Li, Y., and Nghiem, L.X., (2016). *Phase Equilibria of Oil, Gas and Water/Brine Mixtures from a Cubic Equation of State and Henry's Law*, The Canadian Journal of Chemical Engineering, Vol. 64, 3, June 1986, 486-496. DOI: https://doi.org/10.1002/cjce.5450640319.

Li, L., Su, Y., Lv, Y, and Tu, J., (2020). *Asphaltene deposition and permeability impairment in shale reservoirs during CO_2 huff-n-puff EOR process*, Petroleum Science and Technology, Vol. 38:4, 384–390. DOI: https://doi.org/10.1080/10916466.2019.1705855.

Liu, J., Li, H., Liu, S., Xu, J., Wang, X., and Tan, Q., (2023). *Investigating the Impact of Aqueous Phase on CO_2 Huff 'n' Puff in Tight Oil Reservoirs Using Nuclear Magnetic*

Resonance Technology: Stimulation Measures and Mechanisms, SPE-217978-PA, SPE Journal 28 (06): 3324-3340. DOI: https://doi.org/10.2118/217978-PA.

Mamoudou, S., Tinni, A., Curtis, M., Sondergeld, C.H., and Rai, C.S., (2021), *Impact of EOR Huff-n-Puff on Rock Microstructure*, URTEC-2021-5664-MS, presented at the SPE/AAPG/SEG Unconventional Resources Technology Conference, July 26–28, 2021. DOI: https://doi.org/10.15530/urtec-2021-5664.

Maroudas, A., (1996). *Particles Deposition in Granular Filter Media-2*, Filtration and separation, Vol 3, 2, March/April 1996, 115-121.

Merchant, D., (2017). *Enhanced Oil Recovery – The History of CO_2 Conventional WAG Injection Techniques developed from Lab in the 1950s to 2017*, CMTC paper 502866, presented at the Carbon Management Technology Conference, held in Houston, Texas, USA, July 17-19, 2017. DOI: https://doi.org/10.7122/502866-MS.

Min, B., Mamoudou, S., Dang, S., Tinni, A., Sondergeld, C., and Rai, C., (2020). *Comprehensive Experimental Study of Huff-n-Puff Enhanced Oil Recovery in Eagle Ford: Key Parameters and Recovery Mechanism*, SPE-200436-MS, presented at the virtual SPE Improved Oil Recovery Conference held August 31-September 4, 2020. DOI: https://doi.org/10.2118/200436-MS.

Mikhailov, M. D., and Ozisik, M. N., (1984). *Unified Analysis and Solutions of Heat and Mass Diffusion*, John Wiley and Sons, New York, NY, USA.

Mohammad, R.S., Zhang, S., Lu, S., Jamad-Ud-Din, S., and Zhao, X. (2017). *Simulation Study of Asphaltene Deposition and Solubility of CO_2 in the Brine during Cyclic CO_2 Injection Process in Unconventional Tight Reservoirs*, International Journal of Earth, Energy and Environmental Sciences, 10.0(6), 2017. DOI: https://doi.org/10.5281/zenodo.1340202.

Mukherjee, S., (2020). *Measurement and Analysis of Oil-Gs Diffusion at Reservoir Conditions: Application to Huff-n-Puff EOR in Unconventional Reservoirs*, M.S. Thesis, 2020. DOI: https://hdl.handle.net/11244/326601.

Mydland, S., Yusra, I., Whitson, C.H., Dahouk, M.M., and Carlsen, M. L., (2020). *Gas EOR Processes in Tight Unconventionals*, SPE paper 200396 presented at the SPE Improved Oil Recovery Conference, Virtual, August 30, 2020. DOI: https://doi.org/10.2118/200396-MS.

Orangi, A., Nagarajan, N.R., Honarpour, M.M., and Rosenzweig, J., (2011). *Unconventional Shale Oil and Gas-Condensate Reservoir Production, Impact of Rock, Fluid, and Hydraulic Fractures*, SPE paper 140536, presented at the SPE Hydraulic Fracturing Technology Conference held in The Woodlands, Texas, USA, January 14, 2011. DOI: https://doi.org/10.2118/140536-MS.

Parsons, C., Chernetsky, A., Eikmans, D., te Riele, P., Boersma, D., Sersic, I., and Broos, R., (2016), *Introducing a Novel Enhanced Oil Recovery Technology*, SPE paper 179560, presented at the SPE Improved Oil Recovery Conference, held in Tulsa, Oklahoma, USA, April 11-13, 2016. DOI: https://doi.org/10.2118/179560-MS.

Pautz, J.F., Crocker, M.E., and Walton, C.G., (1989). *Relating Water Quality and Formation Permeability to Loss of Injectivity*, SPE paper 18888, presented at the SPE Production Operations Symposium, held at Oklahoma City, Oklahoma, March 13-14, 1989. DOI: https://doi.org/10.2118/18888-MS.

Perez, F., and Devegowda, D., (2020). *How Far Does EOR Solvent Penetrate Kerogen in Shales?*, URTeC paper 2913, presented at the Unconventional Resources Technology Conference held in Austin, Texas, USA, July 20-22, 2020. DOI: https://doi.org/10.15530/urtec-2020-2913.

Pospisil, G., Weddle, P., Strickland, S., McChesney, J., Tompkins, K., Neuroth, T., Pearson, C. M., Griffin, L., Kaier, T., Sorensen, J., and Jin, L., (2020). *Report on the First Rich Gas EOR Cyclic Multiwell Huff N Puff Pilot in The Bakken Tight Oil Play*, SPE paper 201471 presented at the SPE Virtual Annual Technical Conference and Exhibition, October 26–29, 2020. DOI: https://doi.org/10.2118/201471-MS.

Pospisil, G., Griffin, L., Southern, T., Strickland, S., McChesney, J., Pearson, C.M., Dalkhaa, C., Sorensen, J., Hamling, J., Kurz, B., Bosshart, N., Warmack, M., Assady, A., Zhao, J., Schwanitz, B., Williams, A., Schechter, D., and Sarmah, A., (2022). *East Nesson Bakken Enhanced Oil Recovery Pilot: Coinjection of Produced Gas and a Water-Surfactant Mixture*, URTec paper 3722974, presented at the Unconventional Resources Technology Conference held in Houston, Texas, USA, June 20-22, 2022. DOI: https://doi.org/10.15530/urtec-2022-3722974.

Rapp, B.E., (2017). *Microfluidics: Modeling, Mechanics and Mathematics*, Chapter 9 – Fluids, Elsevier, 2017: 243-263. DOI: https://doi.org/10.1016/B978-1-4557-3141-1.50009-5.

Ratnakar, R.R., Dindoruk, B., and Wilson, L.C., (2016). *Phase behavior experiments and PVT modeling of DME-brine-crude oil mixtures based on Huron-Vidal mixing rules for EOR applications*, Fluid Phase Equilibria 434, 49-62, 2017. DOI: https://doi.org/10.1016/j.fluid.2016.11.021.

Raterman, K. T., Farrell, H. E., Mora, O. S., Janssen, A. L., Gomez, G. A., Busetti, S., McEwen, J., Davidson, M., Friehauf, K., Rutherford, J., Reid, R., Jin, G., Roy, B., and Warren, M., (2018). *Sampling a stimulated rock volume: An Eagle Ford example*, SPE paper 191375, SPE Res Eval & Eng 21 (04): 927–941, November 2018. DOI: https://doi.org/10.2118/191375-PA.

Rogers, J.B., Basbug, B., Firincioglu, T., and Ozgen, C., (2020). *A Simulation Case Study of Gas Injection Pilot in Eagle Ford*, SPE paper 200430 presented at the SPE Improved Oil Recovery Conference held virtually, August 31 – September 4, 2020. DOI: https://doi.org/10.2118/200430-MS.

Sahai, R., (2022). *Field Development and Asset Management*, Unconventional Shale Gas Development - Lessons Learned, Chapter 1, Pages 1-31, Elsevier, Oxford, United Kingdon.

Salahshoor, S., and Ciezobka, J., (2020). *Hydraulic Fracturing Test Site HFTS Phase-2 EOR Pilot: Huff-n-Puff Pilot in the Permian-Midland Basin*, SPE paper 200468, presented virtually at the SPE Improved Oil Recovery Conference, August 31-September 4, 2020. DOI: https://doi.org/10.2118/200468-MS.

Salimi, H., Ameri, A., and Nieuwerf, (2022). *Dimethyl Ether DME Solvent Based Enhanced-Oil Recovery Technology – A Laboratory and Subsurface Study*, SPE paper 200223, presented at the SPE Oman Petroleum & Energy Show, held in Muscat, Oman, March 21-23, 2022. DOI: https://doi.org/10.2118/200223-MS.

Shale Ingenuity, 2022, *Shale Oil EOR*, https://www.shaleingenuity.com/ (accessed March 31, 2022).

Shen, Z., and Sheng, J.J., (2016). *Experimental Study of Asphaltene Aggregation during CO_2 and CH4 Injection in Shale Oil Reservoirs*, SPE paper 179675, presented at the SPE Improved Oil Recovery Conference, Tulsa, Oklahoma, USA, April 11-13, 2016. DOI: https://doi.org/10.2118/179675-MS.

Shen, Z., and Sheng, J.J., (2017). *Experimental Study of Permeability Reduction and Pore Size Distribution Change due to Asphaltene Deposition during CO_2 Huff and Puff Injection in Eagle Ford Shale*, Asia-Pacific Journal of Chemical Engineering, vol. 12, issue 3, March 14, 2017. DOI: https://doi.org/10.1002/apj.2080.

Shen, Z., and Sheng, J.J., (2019). *Optimization Strategy to Reduce Asphaltene Deposition-Associated Damage During CO_2 Huff-n-Puff Injection in Shale*, Arab J Sci Eng 44, 6179–6193 (2019). DOI: https://doi.org/10.1007/s13369-018-03701-w.

Sheng, J. J., and Chen K., (2014). *Evaluation of the EOR potential of gas and water injection in shale oil reservoirs*, Journal of Unconventional Oil Gas Resources 5, 1–9. DOI: https://doi.org/10.1016/j.juogr.2013.12.001.

Sheng, J. J., (2015). *Enhanced oil recovery in shale reservoirs by gas injection*, Journal of Natural Gas Science & Engineering 22, 252–259.

Sheng, J. J., (2018). *Technology 101: EOR Methods for Shale and Tight Formations*, SPE The Way Ahead article, April 5, 2018.

Sim, S.S., Takabayashi, K., Okatsu, K., and Fisher, D., (2005). *Asphaltene-Induced Formation Damage: Effect of Asphaltene Particle Size and Core Permeability*, SPE paper 95515, presented at the SPE Annual Technical Conference and Exhibition, Dallas, Texas, October 9-12, 2005. DOI: https://doi.org/10.2118/95515-MS.

Sofla, M. J. D., Farahani, Z.D., Ghorbanizadeh, S., and Namdar, H., (2024). *Experimental study of asphaltene deposition during CO_2 and flue gas injection EOR methods employing a long core*, Sci Rep 14, 3772, 2024. DOI: https://doi.org/10.1038/s41598-024-54395-0.

Song, C., Yang, D., (2013), *Performance Evaluation of CO_2 Huff-n-puff Processes in Tight Oil Formations*, SPE paper 167217, presented at the SPE Unconventional Resources Conference Canada, Calgary, Alberta, Canada, November 5-7, 2013. DOI: https://doi.org/10.2118/167217-MS.

Song, C., Clarkson, C.R., Hamdi, H., and Ghanizadeh, A., (2021). *Comparison of CO_2 and Lean Gas Cyclic Injection ("Huff-n-Puff") in Artificially Fractured Shale Core Samples*, URTEC-2021-5309-MS, presented at the SPE/AAPG/SEG Unconventional Resources Technology Conference, July 26–28, 2021. DOI: https://doi.org/10.15530/urtec-2021-5309.

Song, C., Ghanizadeh, A., Younis, A., and Clarkson, C.R., (2023). *Experimental evaluation of the impact of induced fractures on cyclic solvent injection performance in low-permeability hydrocarbon reservoirs*, Fuel, Volume 354, 2023: 129327. DOI: https://doi.org/10.1016/j.fuel.2023.129327.

Sorensen, J., (2022). *Bakken Production Optimization Program (BPOP) Update*, EERC, February 23, 2022.

Srivastava, R.K., and Huang, S.S., (1997). *Asphaltene Deposition During CO_2 Flooding: A Laboratory Assessment*, SPE paper 37468, presented at the SPE Production Operations Symposium, held in Oklahoma City, Oklahoma, March 9-11, 1997. DOI: https://doi.org/10.2118/37468-MS.

Sun, J., Zou, A., Schechter, D., (2016). *Experimental and Numerical Studies of CO_2 EOR in Unconventional Liquid Reservoirs with Complex Fracture Networks*, SPE paper 179634, presented at the SPE Improved Oil Recovery Conference, Tulsa, Oklahoma, USA, April 11, 2016. DOI: https://doi.org/10.2118/179634-MS.

Thomas, W. R., Helms, L. W., Driggers T. K., Trice, D. W., Thomas, G. L., (2016). *EOG Resources (EOG) Earnings Call*, May 6, 2016.

Thoms, M., (2020). *Enhancing Data to Drive Eagle Ford EOR Value*, Enverus Post, July 7, 2020.

Torres, M. X. F., Yu, W., Ganjdanesh, R., Kerr, E., Sepehrnoori, K., Miao, J., and Ambrose, R. (2019). *Modeling Interwell Fracture Interference and Huff-N-Puff Pressure Containment*

in Eagle Ford Using EDFM, SPE paper 195240, presented at the SPE Oklahoma City Oil and Gas Symposium held in Oklahoma City, Oklahoma, USA, April 9-10, 2019. DOI: https://doi.org/10.2118/195240-MS.

Tovar, F. D., Eide, O., Graue, A., and Schechter, D. S., (2014). *Experimental Investigation of Enhanced Recovery in Unconventional Liquid Reservoirs using CO_2: A Look Ahead to the Future of Unconventional EOR*, SPE paper 169022, presented at the SPE Unconventional Resources Conference, The Woodlands, Texas, USA, April 1, 2014. DOI: https://doi.org/10.2118/169022-MS.

Turta, A.T., Najman, J., Singhal, A.K., Leggitt, S., and Fisher, D., (1997). *Permeability Impairment due to Asphaltenes During Gas Miscible Flooding and its Mitigation*, SPE paper 37287, presented at the International Symposium on Oilfield Chemistry, held in Houston, Texas, February 18-21, 1997. DOI: https://doi.org/10.2118/37287-MS.

van Brakel, J., and Heertjes, P. M., (1974). *Analysis of diffusion in macroporous media in terms of a porosity, a tortuosity and a constrictivity factor*, Int. J. Heat Mass Transfer, 17: 1093–1103, September 1, 1974.

Vega, B., O'Brien, W.J., and Kovescek, A.R., (2010). *Experimental Investigation of Oil Recovery From Siliceous Shale by Miscible CO_2 Injection*, SPE paper 135627, presented at the SPE Annual Technical Conference and Exhibition held in Florence, Italy, September 19-22, 2010. DOI: https://doi.org/10.2118/135627-MS.

Vermilye, J. M., and C. H. Scholz, (1998). *The process zone: A microstructural view of fault growth*, J. Geophys. Res. 103, 12,223-12,237.

Venepalli, K.K., Downey, R.A., Erdle, J.C., and Nohavitza, J., (2021). *Evaluation of a Superior Shale EOR Application in the Eagle Ford Shale*, URTeC paper 208312, presented at the SPE/AAPG/SEG Asia Pacific Unconventional Resources Technology Conference, held virtually, November 16-18, 2021. DOI: https://doi.org/10.15530/AP-URTEC-2021-208312.

Wan T., (2015). *Investigation of EOR performance in shale oil reservoirs by cyclic gas injection*, Doctoral dissertation, Texas Tech University.

Warpinski, N.R. and Teufel, L.W., (1987). *Influence of Geologic Discontinuities on Hydraulic Fracture Propagation*, Journal of Petroleum Technology, 1987, vol. 39, no. 2, pg. 209-220. DOI: https://doi.org/10.2118/13224-PA.

Warpinski, N.R., Mayerhofer, M.J., Vincent, M.C., Cipolla, C.L., and Lolon, E.P., (2008). *Stimulating Unconventional Reservoirs: Maximizing Network Growth while Optimizing Fracture Conductivity*, SPE paper 114173, presented at 2008 SPE Unconventional

Reservoirs Conference held in Keystone, Colorado, U.S.A., February 10-12, 2008. DOI: https://doi.org/10.2118/114173-MS.

Warpinski, N.R., (2009). *Stress Amplification and Arch Dimensions in Proppant Beds Deposited by Waterfracs*, SPE paper 119350, presented at 2009 SPE Hydraulic Fracturing Technology Conference held in The Woodlands, Texas, USA, January 19-21, 2009. DOI: https://doi.org/10.2118/119350-MS.

Wu, J., Zhou, Y., and Lemmon, E.W., (2011). *An Equation of State for the Thermodynamic Properties of Dimethyl Ether*, J. Phys. Chem. Ref. Data, Vol. 40, No. 2, 2011. DOI: https://doi.org/10.1063/1.3582533.

Xiong, R., Guo, J., Kiyingi, W., Luo, H., and Li, S., (2023). *Asphaltene deposition under different injection gases and reservoir conditions*, Journal of Chemical Engineering Research and Design, Volume 194, 2023, Pages 87-94, DOI: https://doi.org/10.1016/j.cherd.2023.03.036.

Yu, Y., Li, L., and Sheng, J.J., (2016). *Further Discuss the Roles of Soaking Time and Pressure Depletion Rate in Gas Huff-n-Puff Process in Fractured Liquid-Rich Shale Reservoirs*, SPE paper 181471, presented at the SPE Annual Technical Conference and Exhibition held in Dubai, UAE, September 26-28, 2016. DOI: https://doi.org/10.2118/181471-MS.

Yu, W., Zhang, Y., Varavei, A., Sepehrnoori, K., and Zhang, T., (2018). *Compositional Simulation of CO_2 Huff-n-Puff in Eagle Ford Tight Oil Reservoirs with CO_2 Molecular Diffusion, Nanopore Confinement and Complex Natural Fractures*, SPE paper 190325, SPE Res Eval & Eng 22 (02): 492–508. March 20, 2019. DOI: https://doi.org/10.2118/190325-PA.

Zang, A. and Stephansson, O., (2010). *Stress Field of the Earth's Crust*, Springer, Berlin, Germany.

Ziarani, A.S., and Aguilera, R., (2012). *Pore-throat radius and tortuosity estimation from formation resistivity data for tight-gas sandstone reservoirs*, Journal of Applied Geophysics, 83:65-73. DOI: https://doi.org/10.1016/j.jappgeo.2012.05.008.

Ziarani, A.S., Aguilera, R., and Cui, A.X., (2020). *Permeability of Tight Sand and Shale Formations: A Dual Mechanism Approach for Micro and Nanodarcy Reservoirs*, SPE paper 200010, presented at the SPE Canada Unconventional Resources Conference held in Calgary, Alberta, Canada, March 18-19, 2020. DOI: https://doi.org/10.2118/200010-MS.